

**Ministry of Higher Education and Scientific Research  
University of Baghdad  
Institute of Laser for Postgraduate Studies**



# **Design of Compact Subwavelength Grating-Assisted (De)Multiplexer for Mode Division Multiplexing Systems**

**A Thesis Submitted to the Institute of Laser for  
Postgraduate Studies, University of Baghdad in Partial  
Fulfillment of the Requirements for the Degree of  
Doctor of Philosophy in Laser / Electronic and  
Communication Engineering**

**By  
Zaid Lateef Hussain**

**B.Sc. Laser and Optoelectronics Engineering- 2002  
M. Sc. Laser and Optoelectronics Engineering -2005**

**Supervisor  
Prof. Dr. Raad Sami Fyath**

**2022 AD**

**1443 AH**

## Certification

I certify that this thesis was prepared under our supervision at the Institute of Laser for Postgraduate Studies, University of Baghdad, in a partial fulfillment of requirements for the degree of a Doctor of Philosophy in Laser/ Electronic and Communication Engineering.

Signature:

Name: **Dr. Raad Sami Fyath**

Title: Professor

Address: Department of Computer  
Engineering, Al-Nahrain  
University.

Date: 17/03/ 2022

(Supervisor)

In view of the available recommendation, I forward this thesis for debate by Examining Committee.

Signature:

Name: **Hanan Jaafar Taher**

Title: **Asst. Prof.**

Address: Head of scientific committee,  
Institute of Laser for Postgraduate  
Studies, University of Baghdad.

Date: 17/03/ 2022

## Examination Committee Certificate

We certify that we have read this thesis “Design of Compact Subwavelength Grating-Assisted (De)Multiplexer for Mode Division Multiplexing Systems” and as examination committee we examined the student in its contents and in our opinion it is adequate with standards as a thesis for the degree of Doctor of Philosophy in Laser/ Electronic and Communication Engineering.

Signature:

Name: **Dr. Abdul Hadi M. Al-Janabi**

Title: Professor

Address: Institute of Laser for  
Postgraduate Studies, University of  
Baghdad.

Date: / / 2022

(Chairman)

Signature:

Name: **Dr. Jassim Kadhim Hmood**

Title: Professor

Address: Department of Laser and  
Optoelectronics Engineering, University  
of Technology.

Date: / / 2022

(Member)

Signature:

Name: **Dr. Shelan Khasro Tawfeeq**

Title: Assistant professor

Address: Institute of Laser for  
Postgraduate Studies, University of  
Baghdad.

Date: / / 2022

(Member)

Signature:

Name: **Dr. Anwaar Abdul Satar A. Al-Dergazly**

Title: Assistant professor

Address: Department of Laser and  
Optoelectronics Engineering, Al-Nahrain  
University.

Date: / / 2022

(Member)

Signature:

Name: **Dr. Tahreer S. Mansour**

Title: Assistant professor

Address: Institute of Laser for  
Postgraduate Studies, University of  
Baghdad.

Date: / / 2022

(Member)

Signature:

Name: **Dr. Raad Sami Fyath**

Title: Professor

Address: Department of Computer  
Engineering, Al-Nahrain University.

Date: / / 2022

(Supervisor)

Approved by the deanship of Institute of Laser for Postgraduate Studies, University of  
Baghdad,

Signature:

Name: **Prof. Dr. Hussein A. Jawad**

Title: Dean

Address: of Institute of Laser for Postgraduate Studies, University of Baghdad.

Date: / / 2022

## **Acknowledgement**

I would like to thank my supervisor **Prof. Dr. Raad Sami Fyath** who gave me the opportunity to join in the fiber laser group and work on such an active area. I own the deepest gratitude for his superb guidance, support and constant encouragement throughout my research work and thesis writing.

I would like to express my sincere gratitude to **Prof. Dr. Hussein A. Jawad**, Dean of Institute of Laser for Postgraduate Studies, for his advice, help and encouragement during my research work. Special thanks to **Dr. Jawad K. Hasan**, Asst. Dean of the institute of Laser for Postgraduate Studies, **Asst. Prof. Dr. Tahreer Safa'a Mansour**, head of the engineering and Industrial Application Dept. for their advice, help and support.

I would also like to acknowledge and give thanks to all the faculty member of Institute of Laser for Postgraduate Studies, especially to **Prof. Dr. Abdul Hadi M. Al-Janabi**, **Asst. Prof. Dr. Mohammed K. Thaher**, **Asst. Prof. Dr. Shelan Khasro Tawfeeq**, and **Dr. Hanan Jafar Tahir** for their valuable suggestions and advice.

I am grateful for the funding support from the Iraqi Ministry of Higher Education and Scientific Research; University of Baghdad; Institute of Laser for Postgraduate Studies.

Many thanks to all my friends and colleagues in the Institute of Laser for Postgraduate Studies.

Finally, big thanks to my entire family especially, my mother and my wife for helping me to get through the difficult times, for all their emotional support, understanding, and care they provided.

Zaid

## Abstract

Silicon photonics based on Silicon-On-Insulator (SOI) has become the perfect solution to design photonic integrated circuits (PICs). Utilizing the SOI platform, optical devices with low loss, compact size, and wide operating bandwidth can be obtained. Recently, new technologies have attracted great attention in the design of photonic structures for their abilities to enhance the performance and footprint of the already existing devices and introduce new devices with new forms. One of these technologies is the subwavelength grating (SWG) technology.

The work in this thesis consists of two main parts. In the first part, multimode interferometer MMI-based (de)multiplexers are designed using the SWG technology. First, a 3-TE mode (de)multiplexer is designed using SWG in the MMI section. Then the device design is modified to a 3-TE mode all-SWG (de)multiplexer. The performance of both devices is compared to each other in addition to comparison to their conventional counterpart. It is noticed that the SWG devices showed wider operating bandwidth ( $>160$  nm) (1.470 to 1.630)  $\mu\text{m}$ , and more compactness ( $\approx 70\%$  footprint reduction) compared to the conventional waveguide-based device. Second, two 4-TE modes (de)multiplexers are designed using conventional and SWG-assisted MMI coupler. A significant enhancement is observed in the performance of the device through maintaining low losses ( $> -0.5$  dB) performance with wider operating bandwidth (140 nm) (1.480–1.620)  $\mu\text{m}$ , and the footprint shrank about 30% compared to the conventional waveguide-based device.

In the second part of the thesis, a new scheme of (de)multiplexers based on SWG-assisted cascaded asymmetric directional couplers (SWG-ADC). Three SWG-ADC-based devices are designed, a 12-TE mode, 12-TM mode, and 24-mode (de)multiplexers. The 12-modes device is a six-stage structure and each stage supports a certain number of high-order modes based on the desired design. The results showed higher-order mode excitation with low

insertion loss, crosstalk, and broad operating bandwidth. Finally, both TE- and TM-mode devices are connected through polarization splitters for mode guidance purposes, leading to a new device of double mode number of multiplexing.

All the proposed (de)multiplexers are designed and simulated using Rsoft photonics CAD ver. 2020.03 software package described in appendix A.

## LIST OF CONTENTS

CONTENTS	PAGE
<b>Abstract</b>	I
<b>List of Contents</b>	III
<b>List of Symbols</b>	V
<b>List of Abbreviations</b>	IX
<b>List of Tables</b>	XI
<b>List of Figures</b>	XIII
<b>Chapter One: Introduction</b>	
1.1 General Introduction	1
1.2 Optical Multiplexing Techniques	3
1.3 Concept of Waveguide Modes	6
1.4 Fundamentals of Subwavelength Grating (SWG) Technology	12
1.4.1 Introduction to The Periodic Structures	13
1.4.2 Principle of SWG Waveguides	15
1.5 Multimode Interference Coupler	16
1.5.1 MMI Principle of Operation	17
1.5.2 SWG-MMI Coupler	20
1.6 Optical Phase Shifters	21
1.6.1 Passive Phase-Shifting Technique	21
1.6.2 Theoretical Analysis of a Passive Phase Shifter	22
i. Conventional Passive Phase Shifter	22
ii SWG-assisted Passive Phase Shifter	24
1.7 Asymmetric Directional Coupler	25
1.8 Literature Survey	26
1.9 Aim of The Thesis	29
1.10 Contributions	29
<b>Chapter Two: Design of Multimode interferometer-based (De)Multiplexers Using SWG Technology</b>	
2.1 Introduction	30
2.2 N-mode (De)multiplexer	30
2.3 Three-Mode (De)multiplexer	33

2.3.1 Subwavelength Grating Assisted (De)multiplexer	33
2.3.1.1 General Description	33
2.3.1.2 Device Dimensional Parameters Selection	39
2.3.1.3 Device Performance Evaluation	45
2.3.2 All-Subwavelength Grating Three-Mode (De)multiplexer	51
2.3.2.1 Device Dimensional Parameters Selection	51
2.3.2.2 Device Performance Evaluation	57
2.3.3 Operation Bandwidth Extension	62
2.3.3.1 O+C/C+L Band Operating (De)multiplexer	62
2.3.3.2 C+L Band Operating All-SWG (De)multiplexer	63
2.4 Proposed Four-TE Mode Demultiplexer	70
2.4.1 Conventional Four-TE Mode (De)multiplexer	70
2.4.2 SWG-assisted (De)multiplexer	77
<b>Chapter Three: Design of High-Order Mode (De)Multiplexers Using Cascaded Subwavelength Gratings</b>	
3.1 Introduction	82
3.2 Twelve-TE mode SWG-assisted ADC (De)multiplexer	82
3.2.1 General Description and Parameters Selection	82
3.2.2 Performance Evaluation of the Proposed Device	87
3.3 Fourteen-TE mode SWG-assisted (De)multiplexer	92
3.4 Twelve-TM-mode SWG-assisted ADC (De)multiplexer	96
3.4.1 Device Performance Evaluation	98
3.5 Dual-polarization SWG-assisted ADC (De)multiplexer	104
<b>Chapter Four: Conclusions and Suggestions for Future Work</b>	
4.1 Conclusions	110
4.2 Suggestions for Future Work	112
<b>References</b>	113
<b>Publications</b>	122
<b>APPENDIX A</b>	123

## LIST OF SYMBOLS

SYMBOLS	DESCRIPTION	UNITS
$A_{ij}$	Coupler matrices element	-
$a$	Subwavelength grating segment thickness	$\mu\text{m}$
$c$	Speed of light in vacuum	$\text{ms}^{-1}$
$c_\nu$	Excitation coefficient of the $\nu$ -th mode	-
$D$	Coupling gap function	-
$D.C$	Duty cycle	$\mu\text{m}$
$D.C_{MMI}$	MMI coupler duty cycle	$\mu\text{m}$
$D.C_{ps}$	Phase shifter duty cycle	$\mu\text{m}$
$D.C_{SWG}$	Subwavelength grating section duty cycle	$\mu\text{m}$
$D.C_T$	Trident duty cycle	$\mu\text{m}$
$d$	Core thickness	$\mu\text{m}$
$\mathbf{E}$	Electric field	$\text{Vm}^{-1}$
$\vec{\mathbf{E}}_B$	Bloch electric field	$\text{Vm}^{-1}$
$\mathbf{E}_i$	Input electric field amplitude	$\text{Vm}^{-1}$
$\mathbf{E}_o$	Output electric field amplitude	$\text{Vm}^{-1}$
$E_x$	Electric field in the x-axis	$\text{Vm}^{-1}$
$E_y$	Electric field in the y-axis	$\text{Vm}^{-1}$
$E_z$	Electric field in the z-axis	$\text{Vm}^{-1}$
$g_i$	Coupling gap	$\mu\text{m}$
$\mathbf{H}$	Magnetic field	$\text{Am}^{-1}$
$H_x$	Magnetic field in the x-axis	$\text{Am}^{-1}$
$H_y$	Magnetic field in the y-axis	$\text{Am}^{-1}$
$H_z$	Magnetic field in the z-axis	$\text{Am}^{-1}$
$h$	Rib waveguide slab height	$\mu\text{m}$
$k_o$	Wavenumber of the propagating wave in a vacuum	-
$\kappa$	Coupling Coefficient	-
$k_{x\nu}$	Mode wavenumber	-
$L_\pi$	Beat length	$\mu\text{m}$
$L_a$	Coupler ports length	$\mu\text{m}$
$L_b$	Arm length	$\mu\text{m}$
$L_c$	Coupling length	$\mu\text{m}$
$L_{MMI}$	MMI physical length	$\mu\text{m}$

$L_{pbs}$	Polarization beam splitter length	$\mu\text{m}$
$L_{ps}$	Phase-shifting waveguide length	$\mu\text{m}$
$L_t$	Tri-junction arm length	$\mu\text{m}$
$L_s$	Straight waveguide length	$\mu\text{m}$
$N$	Number of images (ports)	-
$n$	Material refractive index	-
$n_1$	Core material refractive index	-
$n_2$	Cover material refractive index	-
$n_3$	Substrate material refractive index	-
$n_{co}$	Core index	-
$n_{cl}$	Cladding index	-
$n_{cover}$	Cover index	-
$n_{eff-B}$	Bloch complex effective index	-
$n_{eff,B,i}$	Bloch imaginary effective index	-
$n_{eff,B,r}$	Bloch real effective index	-
$n_{eff\_L}$	Fundamental mode effective refractive index of the lower waveguide	-
$n_{eff\_U}$	Fundamental mode effective refractive index of the upper waveguide	-
$n_{eff\_TE0}$	Fundamental mode effective refractive index	-
$n_{eff\_TEm}$	Excited high-order mode effective refractive index	-
$n_{xx}$	Subwavelength grating effective index in x-direction	-
$n_{zz}$	Subwavelength grating effective index in z-direction	-
$P$	Periodic coefficient	-
$P_{in}$	Input power	dBm
$P_{out\,desired}$	Desired output power	dBm
$P_{out\,undesired}$	Undesired output power	dBm
$p_{MMI}$	Periodicity integer	-
$\mathbf{T}_{cn}$	1xN coupler transfer matrix	-
$\mathbf{T}_d$	Mode total transfer matrix	-
$\mathbf{T}_{MMI}$	NxN MMI coupler transfer matrix	-
$\mathbf{T}_\Phi$	Phase shifter transfer matrix	-
$w_a$	Access waveguide width	$\mu\text{m}$
$w_{b1}$	Outer arm width	$\mu\text{m}$

$w_{b2}$	Inner arm width	$\mu\text{m}$
$w_c$	Central arm width	$\mu\text{m}$
$w_e$	MMI effective width	$\mu\text{m}$
$w_{gi}$	Access waveguide width	$\mu\text{m}$
$w_i$	SWG-assisted ADC section width	$\mu\text{m}$
$w_{in}$	Input stem waveguide width	$\mu\text{m}$
$w_{MMI}$	MMI physical width	$\mu\text{m}$
$w_{ps}$	Phase-shifting waveguide width	$\mu\text{m}$
$w_{ps1}$	Phase shifter1 width	$\mu\text{m}$
$w_{ps2}$	Phase shifter2 width	$\mu\text{m}$
$w_{pbs}$	Polarization beam splitter width	$\mu\text{m}$
$w_o$	Outer arm width	$\mu\text{m}$
$w_s$	Straight waveguide width	$\mu\text{m}$
$x_i$	MMI coupler location parameter	-
$\alpha_B$	Bloch attenuation constant	$\text{dB}\mu\text{m}^{-1}$
$\beta$	Propagation constant	-
$\beta_0$	Propagation constant of the fundamental mode	-
$\beta_1$	Propagation constant of the 1 <sup>st</sup> order mode	-
$\beta_B$	Bloch propagation constant	-
$\beta_v$	Mode propagation constant	-
$\beta_L$	Lower waveguide fundamental mode propagation constant	-
$\beta_U$	Upper waveguide fundamental mode propagation constant	-
$\gamma_B$	Bloch complex propagation constant	-
$\epsilon$	Electric permittivity of the material	$\text{Fm}^{-1}$
$\epsilon_0$	Electric permittivity of vacuum	$\text{Fm}^{-1}$
$\theta$	Accumulation phase	degree
$\Lambda$	Period	$\mu\text{m}$
$\Lambda_{MMI}$	MMI coupler pitch	$\mu\text{m}$
$\Lambda_{ps}$	Phase shifter pitch	$\mu\text{m}$
$\Lambda_T$	Trident pitch	$\mu\text{m}$
$\lambda$	Light wavelength	$\mu\text{m}$
$\lambda_0$	Light wavelength in vacuum	$\mu\text{m}$
$\mu_0$	Magnetic permeability of vacuum	$\text{Hm}^{-1}$
$\nu$	Mode number	-
$\xi$	Stationary state	-

$\Phi$	Phase	degree
$\Phi_o$	Initial phase	degree
$\Phi_U$	Upper waveguide phase	degree
$\Phi_L$	Lower waveguide phase	degree
$\Delta\Phi$	Total phase shift	degree
$\varphi_\nu$	Distribution of the $\nu$ -th mode	-
$\varphi_{ij}$	The phase of the input imaging	degree
$\psi$	MMI field function	-
$\omega$	Frequency	rad/sec

## LIST OF ABBREVIATIONS

ABBREVIATION	DESCRIPTION
ADC	Asymmetric directional coupler
B.W	Bandwidth
C.T	Crosstalk
CMOS	Complementary metal-oxide-semiconductor
CWDM	Coarse wavelength division multiplexing
D.C	Duty cycle
DWDM	Dense wavelength-division multiplexing
EM	Electromagnetic
EMT	Effective medium theorem
FB	Floquet-Bloch theorem
FMF	Few-mode fiber
GI	General interference
I.L	Insertion loss
IoT	Internet of things
MDM	Mode-division multiplexing
MMI	Multimode interferometer
ODL	Optical delay line
OPS	Optical phase shifter
PBS	Polarization beam splitter
PDM	Polarization-division multiplexing
PI	Paired interference
PIC	Photonic Integrated Circuit
PS	Phase shifter
SDC	Symmetric directional coupler

SDM	Space-division multiplexing
Si	Silicon
SI	Symmetric interference
SiO <sub>2</sub>	Silicon dioxide
SMF	Single-mode fiber
SOI	Silicon on insulator
SWG	Subwavelength grating
TE	Transverse electric
TM	Transverse magnetic
WDM	Wavelength-division multiplexing

## LIST OF TABLES

TABEL NO.	TITLE	PAGE
1.1	Mode (de)multiplexer's structures.	6
1.2	Literature survey summary	29
2.1	Device main geometrical parameters for the designed SWG-MMI (de)multiplexer.	45
2.2	Device insertion loss and total crosstalk at $\lambda = 1.55 \mu\text{m}$ .	48
2.3	Performance comparison of the designed device with the previously reported one.	49
2.4	Device main geometrical parameters for the proposed all-SWG (de)multiplexer.	57
2.5	(de)multiplexer insertion loss and total crosstalk at $\lambda = 1.55 \mu\text{m}$ .	60
2.6	Performance comparison of the designed device with the previously reported devices.	60
2.7	Device performance indicators for the C+L band all-SWG (de)multiplexer.	69
2.8	Conventional device geometrical and performance parameters.	76
2.9	SWG-assisted device geometrical and performance parameters.	80
2.10	Performance comparison of the designed device with the previously reported devices.	81
3.1	SWG-bus sections widths for the 12-TE mode device.	86
3.2	Access waveguide geometrical parameters for the 12-TE mode.	87
3.3	Device insertion loss (dB) at $1.55 \mu\text{m}$ .	89
3.4	12-TE mode device operating bandwidths.	91

3.5	Geometrical parameters of the added sections 14-TE mode device.	92
3.6	Added section performance parameters.	93
3.7	SWG-bus sections widths of the proposed 12-TM device.	97
3.8	Access waveguide geometrical parameters of the proposed 12-TM device.	97
3.9	12-TM device insertion loss (dB) at 1.55 $\mu\text{m}$ .	100
3.10	12-TM mode device 1-dB/3-dB designed device operating bandwidths.	103
3.11	Performance comparison of the designed devices with the previously reported ones.	103

## LIST OF FIGURES

FIGURE NO.	TITLE	PAGE
1.1	Internet traffic as a function of time reported by Cisco.	3
1.2	Basic scheme of mode (de)multiplexing operation in MDM systems.	5
1.3	Types of waveguides: (a) Planar waveguide (b) Nonplanar waveguide.	7
1.4	Representative channel waveguides.	8
1.5	Planar waveguide scheme.	9
1.6	Schematic diagram of a periodic waveguide.	14
1.7	FB real refractive index as a function of the wavelength-to-pitch ratio.	15
1.8	Basic scheme of the MMI coupler.	17
1.9	MMI optical field distributions for: (a) General Interference; (b) Symmetric Interference; (c) Paired Interference.	20
1.10	Schematic passive phase shifting structure.	22
1.11	Schematic of conventional width-based passive phase-shifting structure.	23
1.12	Schematic of SWG passive phase shifting structure.	24
1.13	Scheme of directional couplers (a) Symmetric (SDC) (b) Asymmetric ADC.	25
1.14	Simulated light propagation in an ADC for different excited high-order modes.	26
2.1	Simplified block diagram of N-mode (de)multiplexer.	31
2.2	Schematic of 1×3 mode (de)multiplexer.	34
2.3	A simplified 3-mode (de)multiplexer for TE <sub>0</sub> and TE <sub>1</sub> modes excitation.	35

2.4	Schematic of the 3-TE mode SWG-MMI (de)multiplexer.	38
2.5	Effective refractive index vs. width of the input of tri-junction.	40
2.6	Variation of the tri-junction output power with branch width.	40
2.7	Variation of the tri-junction output power with branch length.	41
2.8	Optical field distribution along the SWG-MMI coupler (a) upper edge (b) lower edge (c) center.	42
2.9	Dependence of the SWG-MMI output on port adjustment parameter.	43
2.10	Dependence of the phase shift induced by the PS as a function of its width and length $w_{ps}$ and $L_{ps}$ , respectively.	44
2.11	Optical intensity distribution of the guided mode along the device when the input is (a) TE <sub>0</sub> , (b) TE <sub>1</sub> , (c) TE <sub>2</sub> , and (d) all three.	46
2.12	Transverse field profile of the input field (left) and output field (right) for (a) TE <sub>0</sub> , (b) TE <sub>1</sub> , (c) TE <sub>2</sub> .	47
2.13	Insertion Loss of the proposed structure performance.	49
2.14	Crosstalk of the proposed structure, (a) TE <sub>0</sub> , (b) TE <sub>1</sub> , (c) TE <sub>2</sub> .	50
2.15	Schematic of the all-SWG 3-TE mode (de)multiplexer. The inset represents the waveguide cross-section.	51
2.16	The Trident normalized output power vs. $\Lambda_t$ and $D.C_t$ .	53
2.17	Trident normalized output power as a function of arm width.	53
2.18	Trident normalized output power as a function of arm's length.	54
2.19	Phase shift difference variation of the SWG-PS with its width and length $w_{ps}$ and $L_{ps}$ , respectively.	55

2.20	Coupler output variation in response to the change in coupler length $L_{MMI}$ .	56
2.21	Optical field distribution along the SWG-MMI coupler: (a) upper edge (b) lower edge (c) center.	56
2.22	Optical field distribution of the proposed device when operating as a demultiplexer for the input mode (a) $TE_0$ , (b) $TE_1$ , (c) $TE_2$ .	58
2.23	Optical field distribution of the proposed device when operating as a multiplexer for the input mode (a) $TE_0$ , (b) $TE_1$ , (c) $TE_2$ .	58
2.24	Transverse field profile of all-SWG (a) demultiplexer, (b) multiplexer.	59
2.25	Insertion loss spectrum of the proposed all-SWG (de)multiplexer.	61
2.26	Crosstalk per port of the proposed all-SWG (de)multiplexer when excited by: (a) $TE_0$ , (b) $TE_1$ , (c) $TE_2$ .	61
2.27	Optical field distribution of the guided mode along the O+C (de)multiplexer when the input mode is (a) $TE_0$ , (b) $TE_1$ , (c) $TE_2$ .	62
2.28	Optical field distribution of the guided mode along the C+L (de)multiplexer when the input mode is (a) $TE_0$ , (b) $TE_1$ , (c) $TE_2$ .	63
2.29	Schematic diagram of the C+L Band all-SWG (de)multiplexer. The inset is waveguide cross-section and SWG details.	64
2.30	Splitter transmission as a function of arms (a) width (b) length (c) duty cycle.	65
2.31	Phase difference as a function of shifter width $w_{ps}$ .	66
2.32	Coupler transmission as a function of the length $L_{MMI}$ .	67
2.33	Intensity distribution across the C+L band all-SWG (de)multiplexer at $1.5696 \mu\text{m}$ for input mode (a) $TE_0$ , (b) $TE_1$ , (c) $TE_2$ .	67

2.34	Intensity distribution across the C+L band all-SWG (de)multiplexer at 1.5303 $\mu\text{m}$ for input mode (a) $\text{TE}_0$ , (b) $\text{TE}_1$ , (c) $\text{TE}_2$ .	68
2.35	Intensity distribution across the C+L band all-SWG (de)multiplexer at 1.6118 $\mu\text{m}$ for input mode (a) $\text{TE}_0$ , (b) $\text{TE}_1$ , (c) $\text{TE}_2$ .	68
2.36	Device performance dependency on operating wavelength.	69
2.37	Conventional 4-TE mode (de)multiplexer scheme.	70
2.38	Splitter transmission evolution as a function of the branch (a) width (b) length.	72
2.39	Phase difference as a function of the width $w_{ps}$ for a phase shifter designed with $L_{ps} = 3 \mu\text{m}$ .	73
2.40	Conventional MMI coupler transmission as a function of $L_{MMI}$ .	74
2.41	Intensity distribution of the guided mode along the (de)multiplexer with conventional MMI coupler.	74
2.42	Conventional device performance as a function of wavelength (a) I. L (b) C. T.	75
2.43	SWG-assisted 4-TE mode (de)multiplexer scheme.	77
2.44	SWG-MMI coupler transmission as a function of $L_{MMI(SWG)}$ .	78
2.45	Intensity distribution of the guided mode along the (de)multiplexer with SWG MMI coupler.	78
2.46	SWG-assisted device performance as a function of wavelength (a) I. L (b) C. T.	79
3.1	Schematic of the proposed 12-mode multiplexer. The inset shows the waveguide, input and output modes transverse cross-sections, the SWG, and coupling parameters.	83
3.2	Normalized transmission as a function of $\Lambda$ and $D.C$ at 1.55 $\mu\text{m}$ .	85

3.3	Effective index of the guided TE-mode as a function of waveguide width.	85
3.4	Intensity distribution across the 12-TE mode (a) TE <sub>0</sub> -TE <sub>3</sub> , (b) TE <sub>4</sub> -TE <sub>7</sub> , (c) TE <sub>8</sub> -TE <sub>11</sub> . The inset shows the output modes transverse cross-sections.	88
3.5	Crosstalk of the proposed 12-TE mode device for demultiplexing operation.	89
3.6	Insertion loss of the proposed 12-TE mode device as a function of wavelength TE <sub>0</sub> -TE <sub>6</sub> , (b) TE <sub>7</sub> -TE <sub>11</sub> .	90
3.7	Effect of fabrication error on the insertion loss of the 12-TE modes device.	92
3.8	Effective index of the TE <sub>12</sub> and TE <sub>13</sub> modes as a function of waveguide width.	93
3.9	Intensity distribution across the device when exciting (left) TE <sub>12</sub> , (right) TE <sub>13</sub> .	94
3.10	Insertion loss of the proposed 14-TE device as a function of wavelength.	94
3.11	Crosstalk of the proposed 14-TE device as a function of wavelength.	95
3.12	Effect of fabrication on the insertion loss of the 14-TE device.	95
3.13	Schematic configuration of the proposed 12-TM mode multiplexer. The inset shows the input and output modes transverse cross-sections.	96
3.14	Effective index of the guided TM-modes as a function of waveguide width.	98
3.15	Intensity distribution across the 12 TM-mode device for each case of excited high-order mode.	99
3.16	Excited high-order mode cross-section detected at the output end of the 12 TM-mode designed device.	100
3.17	The proposed device crosstalk for demultiplexing operation.	101

3.18	Insertion loss spectrum of the 12-TM mode device operating bandwidth (a) $TM_0$ - $TM_6$ , (b) $TM_7$ - $TM_{11}$ .	102
3.19	Schematic configuration of the proposed 24-mode multiplexer.	104
3.20	Field propagation of the proposed 24 modes across the designed structure (a) $TE_1/TM_1$ to $TE_6/TM_6$ , (b) $TE_7/TM_7$ to $TE_{10}/TM_{10}$ , (c) $TE_{11}/TM_{11}$ .	105
3.21	Schematic configuration of the polarization beam splitter.	106
3.22	Splitter port#1 normalized transmission for the case of (a) TE modes, (b) TM modes.	107
3.23	Splitter port#2 normalized transmission for the case of (a) TE modes, (b) TM modes.	108
3.24	Field propagation of the proposed polarization beam splitter. The left for TE mode and the right for TM-mode.	109

# Chapter One

## Introduction

1.1 General Introduction
1.2 Optical Multiplexing Techniques
1.3 Concept of Waveguide Modes
1.4 Fundamentals of Subwavelength Grating (SWG) Technology
1.4.1 Introduction to The Periodic Structures
1.4.2 Principle of SWG Waveguides
1.5 Multimode Interference Coupler
1.5.1 MMI Principle of Operation
1.5.2 SWG-MMI Coupler
1.8 Optical Phase Shifters
1.6.1 Passive Phase-Shifting Technique
1.6.2 Theoretical Analysis of a Passive Phase Shifter
ii. Conventional Passive Phase Shifter
ii SWG-assisted Passive Phase Shifter
1.9 Asymmetric Directional Coupler
1.8 Literature Survey
1.9 Aim of The Thesis
1.10 Contributions

# CHAPTER ONE

## Introduction

### 1.1 General Introduction

Due to the rapid growth in the telecommunication networks as a result of the increase in the number of users, applications, and services connected through it, many needs are required to maintain the quality of the services such as speed, flexibility, and reconfigurability which are the most important requirements. For that reason, optical communication thrived in solving many issues through the use of light for data transmission where the information must be sent in the near infrared spectrum extending from 0.85 to 1.65  $\mu\text{m}$  wavelength. Photonics term was introduced in the '60s to designate the manipulation of light as the generation, emission, transmission, modulation, signal processing, switching, amplification, or detection/sensing. Manipulating the light requires the use of some optical/photonic elements such as waveguides made from a dielectric material with high permittivity which means a high refractive index that produces total internal reflection to guide the light as required. Thus, Photonic Integrated Circuits (PICs) are required to be used, where several functions are integrated into these devices for optical communication to be achievable [1].

In 1969 Stewart E. Miller introduced the first PIC used in optical communications and signal processing where the capability of the dielectric waveguide to steer the laser and the implementation of the circuitry for an integrated laser were discussed [1]. PICs have several advantages, such as mechanical, thermal, and acoustic isolation eased by the miniaturization of the circuit besides the low consumption of the power. Devices like frequency filters, couplers, and phase modulators, are also investigated, and thus the basis for contemporary PIC was laid. Photonics has become essential in

many applications of everyday life. Optical fibers are the backbone of every communication network [2], and for energy and capacity enhancement, the copper interconnects were replaced with integrated optics [3,4]. Additionally, due to photonics potential in developing solutions in both telecommunications and Datacom, it is considered as the main technology of the H2020 program of the European Commission and is used in many applications e.g. energy generation [5,6], metrology [7], spectrometry [8], and sensing [9].

Many materials with a variety of advantages have been used for PICs design and fabrication. Silicon was the dominant one due to its unique characteristics as a semiconductor material. It can be extracted from silica which is greatly abundant and overcomes the fact that silicon is not found as a pure element on earth's crust. In addition to the capability of manufacturing silicon wafers with high purity to be considered an economical material for PIC's fabrication. The challenges in the use of Si in optical interconnects are propagation losses resulting from scattering of the light from waveguides sidewalls, high fiber-to-waveguide coupling losses, and low electro-optic coefficient. These were overcome by the use of new nanofabrication techniques, leading to a huge number of ultra-compact high-performance photonic devices [10]. Thus, for these reasons, silicon is an attractive material that is intensively employed in the industry of microelectronics. As silicon integration capacity is significantly increasing, this led to one of the most important technical challenges is tackled which is the steadily growing data traffic flowing across the global network. Also due to the growth in the number of connected internet services resulting from 5G technology and Internet of Things (IoT) services and the demands for new services such as cloud computing, big data, and streaming requires enormous data management. Figure 1.1 depicts the annual growth in internet traffic inside data centers from 2010 to 2025 exceeding the 100 zettabytes (1 zettabyte =  $10^{21}$  bytes) threshold in 2021.

Since that data traffic is exponentially increasing, the data centers are consuming the energy in the same manner, so their operator is aiming to reduce the energy required for single-bit transmission and thus costs and environmental effect is reduced accordingly [11]. For the huge demand for faster data rates and wider bandwidth, it is important to utilize the potential of silicon photonics in improving the energy consumption and performance inside and outside these data centers.

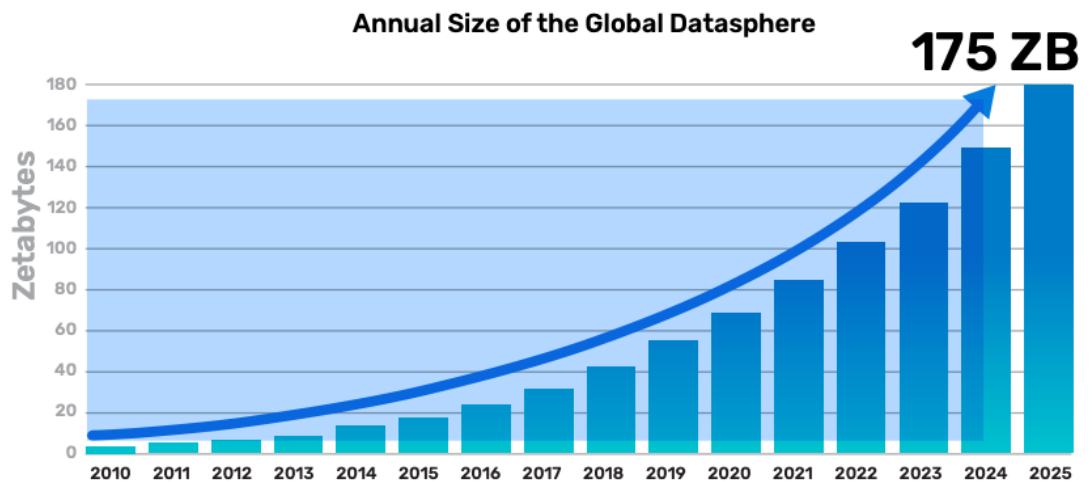


**Figure 1.1:** Internet traffic as a function of time reported by Cisco [12].

## 1.2 Optical Multiplexing Techniques

To handle huge capacity demands, optical interconnects that are silicon-based are evolved using several multiplexing techniques which allow multi-channel transmission/reception over a single waveguide. Wavelength-division multiplexing (WDM) is a widely employed technique, through the utilization of silicon high-bandwidth density of silicon which as a result allows data transmission over different wavelengths [13]. In the dense wavelength division multiplexing (DWDM) category, the wavelength spacing is about 100 GHz or less which provides channels to be multiplexed in the wavelength domain [14]. Each wavelength is represented by a laser

source, thus high stabilization and careful alignment of these sources are required which implicates additional cost and system complexity [15]. Another category of WDM is the coarse wavelength division multiplexing (CWDM) which supports 18 wavelength channels with 20nm spacing. This category offers relaxation in limitations presented in DWDM [16]. The second technique for capacity expansion is the polarization division multiplexing (PDM) in which the two states of polarization of light are used as different transmission channels which in the end doubles the current number of channels from a single wavelength source [17]. Solving Maxwell equations gives sets of solutions in a planar waveguide which are the transverse electric (TE) mode and transverse magnetic (TM) mode. These modes are orthogonal to each other. In combination with other multiplexing techniques such as WDM, the bandwidth of the optical system can be expanded considerably [18]. For a higher capacity, physical channels are spatially distributed and placed together on a single chip giving rise to what is called the space-division multiplexing technique (SDM). This technique can combine other techniques in one system. The main drawback of this technique is the complexity in design, where several photonic components and waveguides are employed [19]. Finally, with the rapid development of the platforms based on refractive index contrast, light modes selection and manipulation became easy leading to the use of these modes as discrete transmission channels. This technique is called mode division multiplexing (MDM) [20]. In this technique, the capacity of the optical system is expanded using multimode waveguides which are capable to support several modes (or spatial Eigen modes). Again, Maxwell equations are solved under certain boundary conditions of the multimode waveguide, and the result is translated as eigenmodes, these modes are orthogonal and they do not interfere [21]. Thus, the capacity of the optical system is expanded directly proportional to the number of these modes. WDM and PDM are considered as already well-developed mature techniques for optical capacity enhancement whereas

MDM and SDM are promisingly developing. All these techniques are complementing each other adding extra degrees toward the higher capacity of the optical systems. Currently, MDM attracts much attention due to its low losses and high integration level.

Mode (de)multiplexers, depicted in Figure 1.2, are the key element in most MDM designs. Their function is to separate and combine the optical modes at the input and output of the system [22].

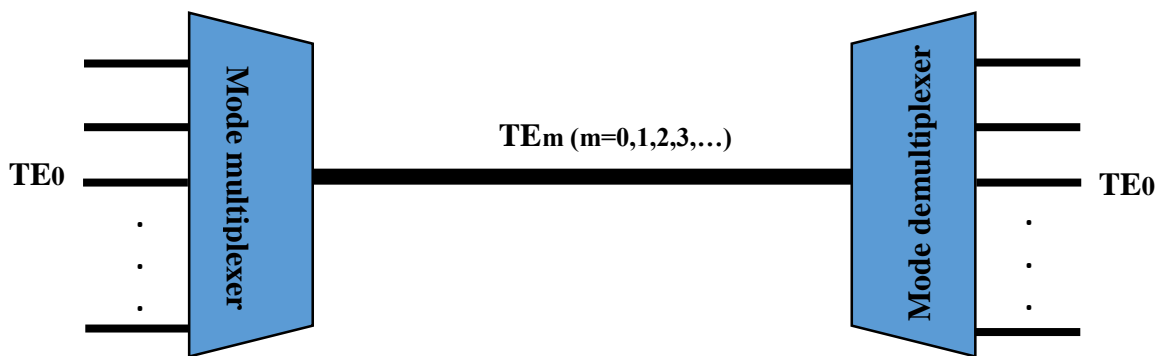


**Figure 1.2:** Basic scheme of mode (de)multiplexing operation in MDM systems.

Several mode (de)multiplexers are designed based on bulk-optics, fibers, and waveguides [23, 24] as presented in Table 1.1. The bulk-optics multiplexers are built with spatial light modulators or phase plates [25–28], which offer efficient spatial mode separation and high selectivity. The main drawbacks of this type come from the fact that these devices are of high losses, bulk size, and are difficult to align. For fiber-based mode (de)multiplexers, photonic lanterns are utilized using few-mode fiber (FMF) with single-mode fibers (SMFs) attached to them [29–30]. This type of multiplexing offers compact size and low losses advantages accompanied by poor mode selection and fabrication difficulty disadvantages.

Finally, to achieve a high degree of compactness, low losses, ease of fabrication, and integration capability, waveguide-based mode (de)multiplexers are considered. This type can be built using coupler-based

structures which nowadays are the key components in PICs that are employed in several optical signal processing and routing such as multimode interferometers (MMIs) couplers [31,32], and directional couplers [33-38]. The MMIs have the advantages of low losses, wide operating bandwidth, compactness, and flexible fabrication tolerance [39,40]; thus, making them the right choice for optical systems capacity enhancements. In contrast, the directional couplers are attractive for their capability to produce devices with a high output number, scalability, and flexibility to generate any high-order mode based on phase match condition satisfaction between a multimode and a single-mode waveguide [41].

**Table1.1** Mode (de)multiplexer's structures [24].

<b>Setup</b>	<b>Advantages</b>	<b>Disadvantages</b>
Bulk-optic	Low crosstalk	Bulky; Difficult to align
Fiber	Small size; Low loss	High crosstalk; Difficult to fabricate "excluding FBG"
Planar-waveguide	Small size; Low crosstalk	Need mode rotators

### 1.3 Concept of Waveguide Modes

The dielectric waveguide comprises two main layers, the core which is a high index layer covered with a low index layer called cladding. The optical wave is mainly confined and propagates along with the longitudinally extended core. The propagation characteristics of a waveguide with an optically isotropic material are expressed through specific parameters, the dielectric constant  $\varepsilon(x,y)/\varepsilon_0$  which is independent of the z-direction, and the transverse profile of the material refractive index  $n(x,y)$ . There are two main types of waveguides as shown in Figure 1.3. First, the planar waveguide in which the cladding sections (normally the lower layer called film and the upper as cover) form a sandwich shape around the core layer in a specific plane, for example, x -plane having an index profile  $n(x)$  and thus

the optical field is confined in one-dimension accordingly. The second, is the nonplanar waveguide where the cladding is surrounding the core in all transverse directions which means  $n(x, y)$ , and thus this waveguide has two-dimensions optical field confinement, examples of this type are optical fiber and channel waveguide [42].

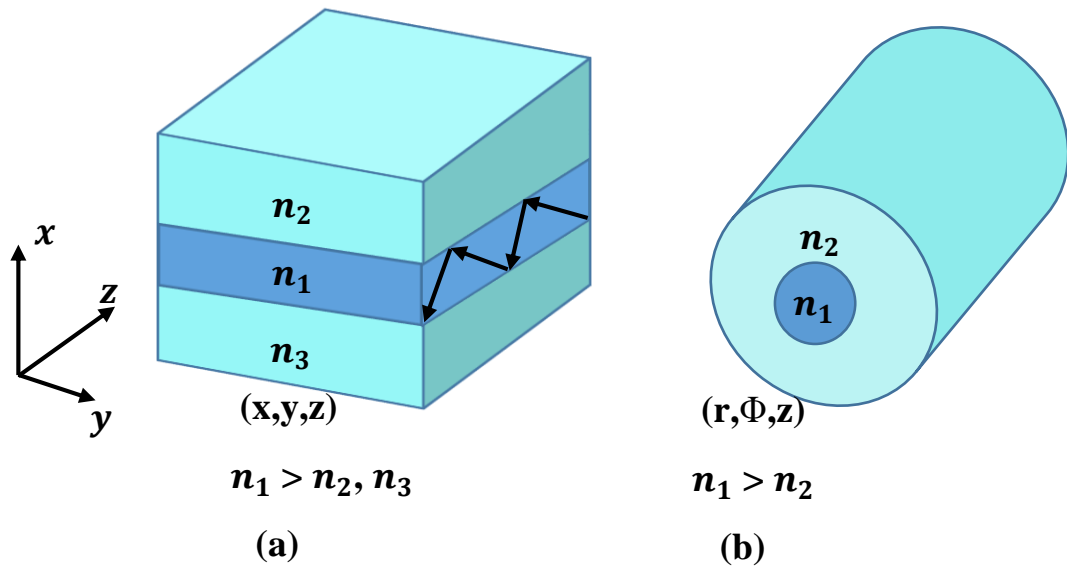


**Figure 1.3:** Types of waveguides: (a) Planar waveguide (b) Nonplanar waveguide [42].

As a nonplanar type, the channel waveguide can be categorized into subtypes shown in Figure 1.4 which include [42]:

1. *The buried waveguide* in which the high refractive index core is buried into a low index medium. Normally, in this type, the core has a rectangular cross-section.
2. *The strip-loaded waveguide* is formed by loading a dielectric strip of low refractive index into a planer waveguide that already has optical field confinement in the x-direction. The function of the strip is to provide optical field confinement in the y-direction. Note that the loaded strip of thickness and index d,  $n_3$ , respectively; placed above the guiding core of the index  $n_1$ , so that  $n_3 < n_1$ .

3. *The ridge waveguide* this waveguide has a similar structure to the strip-loaded one, except the guiding core is the ridge (or the strip) which is of a high index. This type has the property of strong optical field confinement since the core is surrounded by a low index cladding from three directions.
4. *The rib waveguide*, again this type is similar to the strip or ridge one, the difference is both the planar layer and the strip layer are forming the guiding core of high index.
5. *The diffused waveguide*, where the high index area is created within the substrate by dopants diffusion, for example, doping LiNbO<sub>3</sub> waveguide with Ti diffusion. In this type, the core and substrate boundaries are not clearly defined because of the diffusion process, also the core is not of symmetrical dimensions, i.e. has  $d$  thickness in the x-direction and  $w$  width in the y-direction.

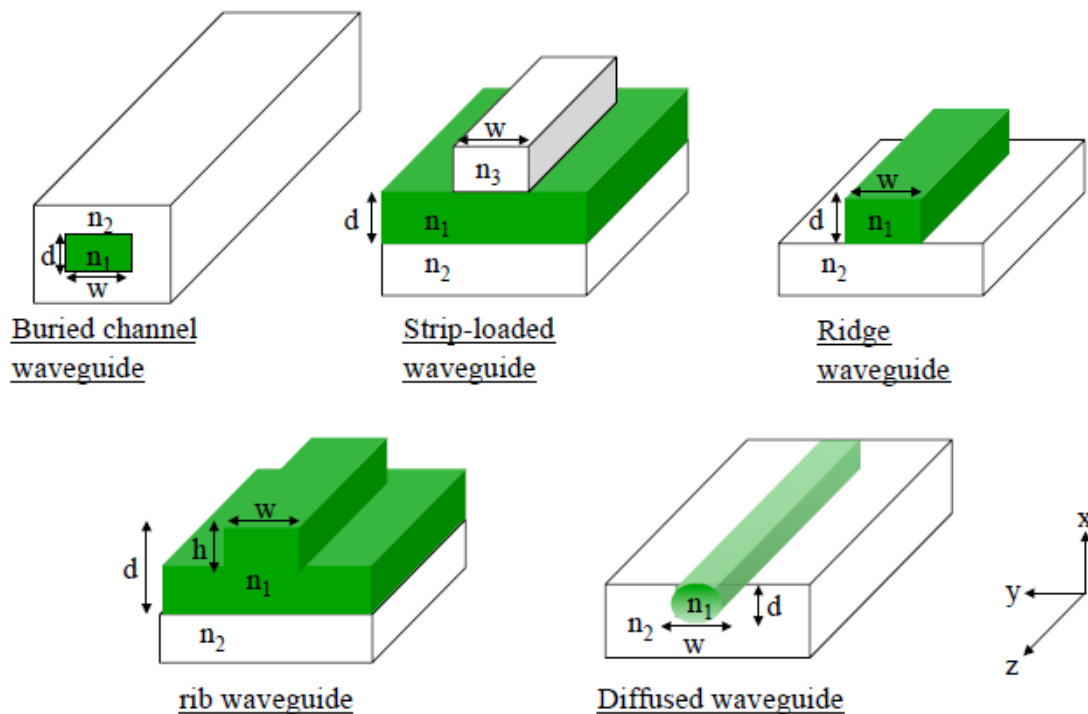


**Figure 1.4:** Representative channel waveguides [42].

To have an idea about optical waveguide modes, consider a planar step-index waveguide shown in Figure 1.5, which is comprised of three dielectric layers, the core, the cover, and the cladding of refractive indices  $n_1$ ,  $n_2$ , and  $n_3$ , respectively. Note that  $n_2, n_3 < n_1$ , and when  $n_2 = n_3$  is a symmetric waveguide, whereas  $n_2 \neq n_3$  is an asymmetric waveguide [43].

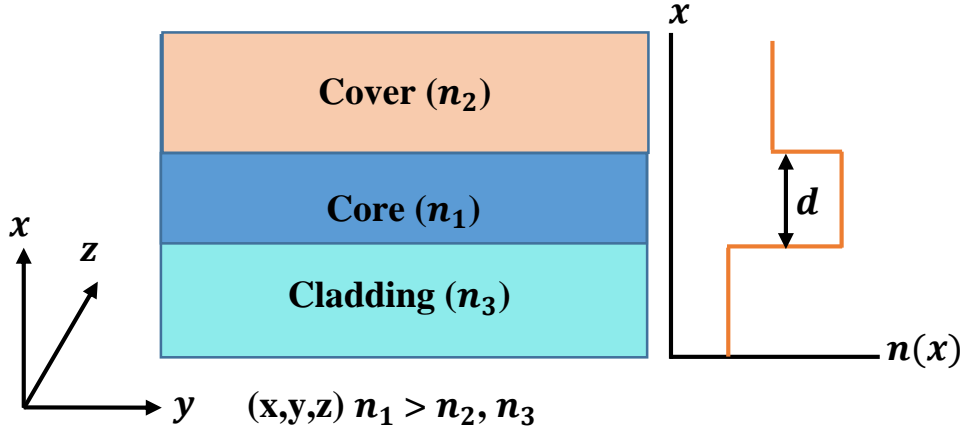


**Figure 1.5:** Planar waveguide scheme [42].

The term optical mode refers to the solution of Maxwell's equations satisfying certain boundary conditions and does not change its spatial distribution while propagating through the medium. By solving the below curl equations in each layer, modes can be obtained by imposing the boundary conditions where tangential components of  $\mathbf{E}$  and  $\mathbf{H}$  are continuous across the interfaces [44, 45]

$$\nabla \times \mathbf{E} = i\omega\mu_o\mathbf{H} \quad (1.1)$$

$$\nabla \times \mathbf{H} = -i\omega\varepsilon_o n^2 \mathbf{E} \quad (1.2)$$

These equations give two linearly polarized sets of solutions, the transverse electric (TE), and the transverse magnetic (TM) modes [44,45].

*i. Transverse Electric (TE) modes*

In this case, the field components  $E_x = E_z = 0$ , whereas  $E_y$  satisfy the following equation [45]

$$\frac{d^2 E_y}{dy^2} + (n^2 k_o^2 - \beta^2) E_y = 0 \quad (1.3)$$

$$k_o = \omega \sqrt{\epsilon_o \mu_o} = \omega / c$$

And the magnetic field components can be related to the  $E_y$  component as follows

$$H_x = -\frac{\beta}{\omega \mu_o} E_y, \quad H_y = 0, \quad H_z = -\frac{i}{\omega \mu_o} \frac{dE_y}{dx} \quad (1.4)$$

Equation (1.3) can be solved for each layer by substituting the refractive index  $n_1$ ,  $n_2$ , and  $n_3$  for the core, cover, and cladding layer, respectively. and since these indices are fixed, a general solution can be written as:

$$E_y = \begin{cases} B_c \exp[-q_1(x - d)]; & x > d \\ A \cos[px - \Phi]; & |x| \leq d \\ B_s \exp[q_2(x + d)]; & x < -d \end{cases} \quad (1.5)$$

where the constants  $p$ ,  $q_1$ , and  $q_2$  are wavenumbers at the core, cladding, and cover, respectively. these constants have the following formulas [43]

$$p = n_1^2 k_o^2 - \beta^2, \quad q_1^2 = \beta^2 - n_2^2 k_o^2, \quad q_2^2 = \beta^2 - n_3^2 k_o^2 \quad (1.6)$$

The rest of the constants are determined by the boundary conditions at the interfaces at which previously mentioned the tangential components of E and H are continuous with index discontinuous. From a mathematical point of view,  $E_y$  and  $H_z$  are continuous at  $x = \pm d$ .  $E_y$  is continuous when

$$B_c = A \cos[px - \Phi]; \quad B_s = A \cos[px + \Phi] \quad (1.7)$$

As  $H_z \propto \frac{dE_y}{dx}$ ,  $\frac{dE_y}{dx}$  must be continuous at  $x = \pm d$ , which is only satisfied if

$$pA \sin[pd - \Phi] = B_c q_1; pA \sin[pd + \Phi] = B_s q_2 \quad (1.8)$$

Assuming  $A = 1$ , yields  $\Phi$  must satisfy the following

$$\tan[pd - \Phi] = q_1/p; \tan[pd + \Phi] = q_2/p \quad (1.9)$$

Solving equation (1.9) gives

$$2\Phi = m\pi - \tan^{-1}(q_1/p) + \tan^{-1}(q_2/p) \quad (1.10)$$

$$2pd = m\pi + \tan^{-1}(q_1/p) + \tan^{-1}(q_2/p) \quad (1.11)$$

where  $m=0,1,2,..$  is an integer. Equation (1.11) represents the eigenvalue equation. Several solutions of  $m$  represent TEm modes. Note that these modes can be divided into odd and even ones [43]

### *ii. Transverse Magnetic (TM) modes*

In this case, the field components  $H_x = H_z = 0$ , whereas  $H_y$  satisfy the following [45]

$$\frac{d^2 H_y}{dy^2} + (n^2 k_o^2 - \beta^2) H_y = 0 \quad (1.12)$$

and the electric field components can be related to the  $H_y$  component as follows

$$E_x = -\frac{\beta}{\omega \mu_o} H_y, \quad E_y = 0, \quad E_z = -\frac{i}{\omega \mu_o} \frac{dH_y}{dx} \quad (1.13)$$

For TM modes, a similar procedure followed for TE mode can be followed here solving equation (1.12). Here,  $E_z$  need to be continuous at the boundaries, thus  $n^{-2} \frac{dH_y}{dx}$  is continuous at  $x = \pm d$ . The eigenvalues are having the following form

$$2pd = m\pi + \tan^{-1}(n_1^2 q_1/n_2^2 p) + \tan^{-1}(n_1^2 q_2/n_3^2 p) \quad (1.14)$$

taking into account the indices of all layers since  $n_2 \neq n_3$ .

Similarly, the TM modes can be divided into odd and even modes.

## 1.4 Fundamentals of Subwavelength Grating (SWG) Technology

As mentioned earlier, silicon (Si) has attracted much interest in several photonic applications due to its high compatibility with complementary metal-oxide-semiconductor (CMOS) technology. As a core material, its high refractive index offers a degree of contrast compared to the cladding layers, and thus the propagating light is highly confined [46]. Yet, the refractive index of Si is fixed which limits the design flexibility that might be required in the design of certain components such as multiplexers and couplers where refractive index matching needs to be satisfied.

To overcome this limitation, certain technology to manipulate and engineer the refractive index became a need which is found through the subwavelength grating (SWG) technology [47].

The term subwavelength grating refers to a periodic structure of dimensions that are less than the wavelength of the light propagating smoothly in the form of Bloch mode through them so that there is no reflection or diffraction to occur [48]. This can be achieved by the adjustment of certain parameters of the SWG structure and thus, a waveguide with enhanced optical properties is obtained compared to the conventional counterpart which interns greatly affects the design of low loss, highly compact, ultra-broad bandwidth optical devices [49]. Thus, SWG has been employed in the design and fabrication of a wide spectrum of photonic based on SOI platforms, such as beam power splitters [50,51], polarization beam splitters [52-55], optical phase shifters [56,57], Y-junctions [58], adiabatic couplers, directional couplers [59], micro-ring resonators [60], and MMI couplers [61-63]. In particular, the operating bandwidth of directional couplers and MMI couplers acting as optical 3-dB couplers has been expanded by SWG [62].

### 1.4.1 Introduction to The Periodic Structures

The periodic structures are analyzed using a theorem found by G. Floquet developed by F. Bloch which is called the Floquet-Bloch (FB) theorem. First, Floquet found the solution of a linear differential equation with periodic coefficients [64]. Later, Bloch generalized Floquet results as he studied the electron propagation in the periodic crystal structures [65]. To introduce the Floquet-Bloch theorem, consider a differential equation that has a stationary state  $\xi(z)$ , and a periodic coefficient  $P(z)$  with a period  $\Lambda$ , so that  $P(z \pm \Lambda) = P(z)$  [66]

$$\frac{d^2\xi}{dz^2} + P(z)\xi(z) = 0 \quad (1.15)$$

Using the FB theorem to solve the above equation, yields a linear combination form

$$\xi(z) = e^{ikz}u(z) \quad (1.16)$$

where  $u(z)$  is a periodic function satisfying the condition  $u(z \pm \Lambda) = u(z)$  [66].

One of the major applications of the FB theorem is to solve the equations of the EM field propagating in an optical periodic waveguide. The scheme of such a waveguide is shown in Figure 1.6, which depicts a segmented core, cover, and substrate of refractive index  $n_1$ ,  $n_2$ , and  $n_3$ , respectively. The extending core in the  $z$ -direction of segment thickness  $a$ , period or pitch denoted by  $\Lambda$ , and duty cycle  $D.C = a/\Lambda$  [67]. Note that the periodically varying refractive index of the structure has the following mathematical formula [68,69]

$$n(x, y, z) = n(x, y, z \pm \Lambda) \quad (1.17)$$

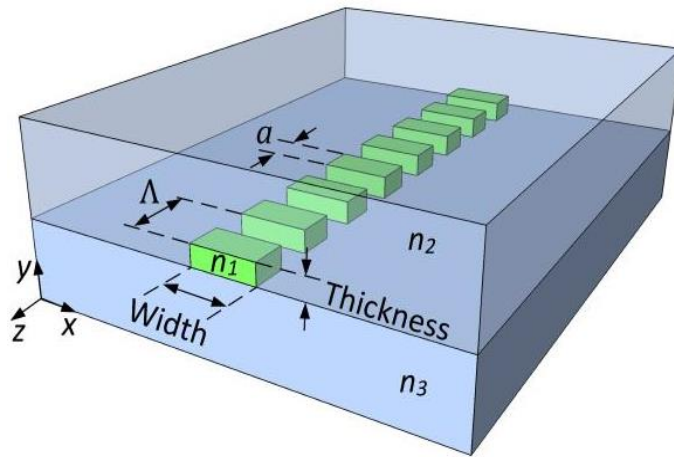


**Figure 1.6:** Schematic diagram of a periodic waveguide [68].

The field of the structure can be expressed as the FB theorem states [68]

$$\vec{E}(x, y, z) = \vec{E}_B(x, y, z)e^{-z\gamma_B} \quad (1.18)$$

where  $\vec{E}_B$  represents the periodic part of the formula of period  $\Lambda$  along the  $z$ -direction that satisfies the condition  $\vec{E}_B(x, y, z) = \vec{E}_B(x, y, z \pm \Lambda)$ . Also, the same procedure applies to the magnetic part of the field. Note that, the transmission properties are expressed by the exponent term of equation (1.18). Here  $\gamma_B$  is the complex propagation constant which can be expressed as a complex quantity with  $\alpha_B$  the attenuation constant as the real part which is related to the length of the path, and  $\beta_B$  the propagation constant the phase changes along with the periodic structure. Thus,

$$\gamma_B = \alpha_B + i\beta_B \quad (1.19)$$

The complex effective index of the structure can be expressed as [68]

$$n_{eff-B} = n_{eff,B,r} + in_{eff,B,i} = -i\frac{\gamma_B}{k_0} = \frac{\beta_B}{k_0} - i\frac{\alpha_B}{k_0} \quad (1.20)$$

where  $k_0$  is the free space wavenumber,  $k_0 = 2\pi/\lambda_0$ ,  $\lambda_0$  is the wavelength of the light in free space. Normally only the real part of the effective index is considered.

### 1.4.2 Principle of SWG Waveguides

Generally, as presented in Figure 1.7 below, the operation of the periodic waveguide can be classified into three main regions: radiation, Bragg reflection, and subwavelength dispersion-less regions based on the ratio of the wavelength of the propagating light  $\lambda$  to the pitch length  $\Lambda$  of the structure [70]. In the radiation region, where  $\lambda/\Lambda$  is low, the propagating light through the waveguide is diffracted. In the second region of the Bragg reflection region where the pitch length is a multiple of  $1/2$  of the wavelength of the light satisfying the Bragg condition, here the real effective index follows a linear relation to the  $\lambda/\Lambda$  ratio. The third region which is the focus of the work is the subwavelength grating region, where the pitch is too short compared to the wavelength ( $\Lambda \ll \lambda$ ) so that the diffraction effects are completely suppressed [68]. In the subwavelength grating region, the structures can be considered as a new homogenous medium with an effective index and optical properties that can be adjusted through manipulating the parameters of the SWG geometry, thus completely new design approaches are in hand [68,71].

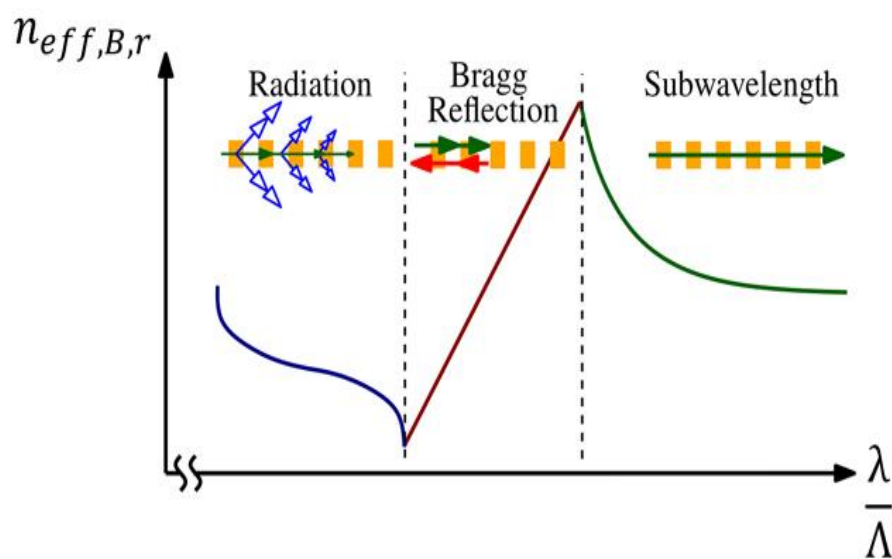


**Figure 1.7:** FB real refractive index as a function of the wavelength-to-pitch ratio [72].

Modeling of subwavelength structure as an equivalent homogeneous medium was done using effective medium theory (EMT). Rytov was the first who studied the EM properties of a medium with  $\Lambda \ll \lambda$  and found approximated formulas for the refractive indices (in  $x$  and  $z$ -direction) of the equivalent medium known as Rytov's formulas [69,72]

$$n_{xx}^2 = D.C.n_1^2 + (1 - D.C).n_2^2 \quad (1.21)$$

$$n_{zz}^{-2} = D.C.n_1^{-2} + (1 - D.C).n_2^{-2} \quad (1.22)$$

where  $n_1$  and  $n_2$  are the refractive indices of the core and cladding layers, respectively. Note that, both indices are greater than 1, and  $n_{xx} \gg n_{zz}$  for  $D.C$  range (0-1). These indices can be adjusted by manipulating the  $D.C$ , thus controlling the guidance and the confinement of the modes through the structure accordingly [68].

### 1.5 Multimode Interference Coupler

The multimode interference (MMI) coupler has been developed in recent years to be one of the main components in MDM applications for its capability to design devices of low losses, compact in size, low power imbalance, and the fact of no need for cascading topology for higher ports number [73]. The operation of the MMI is based on the concept of self-images where the input field profile is regenerated as single or multiple images over periodic intervals along the propagation direction of the waveguide [74]. A multimode waveguide supports a certain number of guided modes when the light enters the MMI section. It excites high-order modes, and with the interference of these modes, self-images of the input light are generated along the MMI section. The quality of the image can be enhanced through large mode counters and small phase errors [74, 75].

### 1.5.1 MMI Principle of Operation

The basic scheme of an MMI coupler is shown in Figure 1.8. It comprises a multimode section with single-mode input/output waveguides (ports) located at specific positions. The refractive indices of the core and the cladding layers are denoted by  $n_1$  and  $n_2$ , respectively. The coupler is distinguished by a set of parameters which are the length and the width denoted by  $L_{MMI}$ , and  $w_{MMI}$ , respectively.

Assume the multimode section supports  $m$  modes of mode number  $\nu=0, 1, \dots, (m-1)$  at the designed wavelength  $\lambda$ . The propagation constant  $\beta_\nu$  and the wavenumber  $k_{x\nu}$  are related by the following dispersion formula [75,76]:

$$\beta_\nu^2 + k_{z\nu}^2 = k_0^2 n_1^2 \quad (1.23)$$

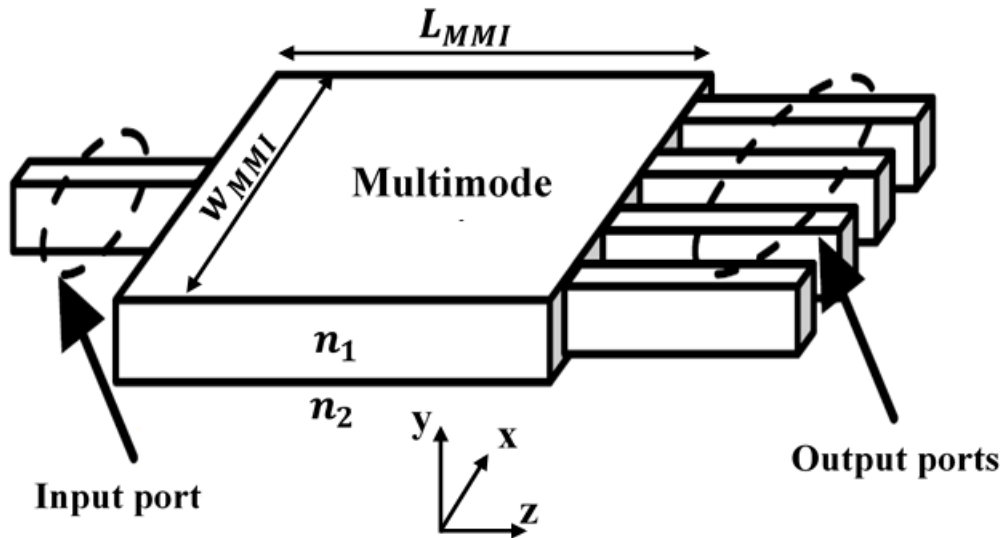


**Figure 1.8:** Basic scheme of the MMI coupler [75].

where  $k_{z\nu} = (v - 1)\pi/w_e$ ,  $w_e$  is the effective width of the MMI section given as [78]

$$w_e = w_{MMI} + \frac{\lambda}{\pi} (n_1^2 - n_2^2)^{-1/2} \quad (1.24)$$

Normally,  $w_e \simeq w_{MMI}$ . Substituting  $k_{x\nu}$  in equation (1.23), one can get the propagation constant formula [76]

$$\beta_v = k_o n_1 - \frac{(v-1)^2 \pi \lambda}{4w_e^2 n_1} \quad (1.25)$$

The beat length is defined as the reciprocal of the difference between the propagation constant of the fundamental and the 1<sup>st</sup> order modes and has the following formula [76]

$$L_\pi = \frac{\pi}{\beta_0 - \beta_1} = \frac{4n_1 w_e^2}{3\lambda} \quad (1.26)$$

Assume the field at the entrance of the MMI coupler ( $z = 0$ ) is expressed in terms of the product of the  $v$ -th mode excitation coefficient given as  $c_v$  and its distribution  $\varphi_v$  as follows [77]

$$\psi(x, 0) = \sum_v c_v \varphi_v(x) \quad (1.27)$$

The excitation coefficient is given by

$$c_v = \frac{\int \psi(x, 0) \cdot \varphi_v(x) dx}{\sqrt{\int \varphi_v^2(x) dx}} \quad (1.28)$$

The field at any point along the coupler is expressed as

$$\psi(x, z) = \sum_v c_v \cdot \varphi_v(x) \cdot \exp(-j(\omega t - \beta_v z)) \quad (1.29)$$

Substituting  $\beta_v$  from equation (1.25) into (1.29), gives

$$\psi(x, z) = \sum_v c_v \cdot \varphi_v(x) \cdot \exp(-j \frac{v(v+2)\pi}{3L_\pi} z) \quad (1.30)$$

where the exponent part represents the phase term of the field. Under certain situations, at distance  $z = L$  even and odd field images  $\psi(x, L)$  of the input field  $\psi(x, 0)$  are produced with respect to the plane  $x = \pm w_e$ . Based on the above analysis, the self-imaging properties can be investigated using three interference mechanisms [78].

**a. General Interference mechanism (GI)**

In this mechanism, there is no restriction on mode excitation, i.e. all modes are allowed to interfere constructively ( $v=0,1,2,3\dots$ ). Also no restriction on the location of the exciting input field. The generated images are located at distances [78]

- for a single image  $L = p_{MMI}(3L_\pi)$  (1.31)

- for an N-fold image  $L = \frac{p_{MMI}}{N}(3L_\pi)$  (1.32)

where,  $p_{MMI}$  is a periodicity integer, normally ( $p_{MMI} = 1$ ).

**b. Restricted Symmetric Interference mechanism (SI)**

In this mechanism, the input field is placed at the center of the MMI coupler, i.e.  $x = 0$ , to obtain only evenly symmetric images ( $v = 0,2,4$ ) located at distances [78]

$$L = \frac{p_{MMI}}{N} \left( \frac{3L_\pi}{4} \right) \quad (1.33)$$

**c. Restricted Paired Interference mechanism (PI)**

In this mechanism, an even symmetric input field is fed to the MMI coupler at specific positions ( $x = \pm w_e/6$ ). The excitation coefficient for  $v = 2,5, 8, \dots$ , is zero due to their odd symmetry. The images of the input field are obtained at distances [78]

$$L = \frac{p_{MMI}}{N} L_\pi \quad (1.34)$$

Note that, the contributing modes that come in pairs are 0-1, 3-4, and 6-7..., which is the reason for the name of this mechanism. And thus, the number of input ports is limited to two.

Based on the above discussion, while keeping the width and beat length parameters of the MMI coupler fixed, the length in the SI mechanism is 4x shorter than that of the GI and PI mechanisms. For the PI mechanism, the length is three times shorter than that in the GI mechanism. Yet, the GI

mechanism offers flexibility in input field position, the number of ports, and the capability to produce single, and multiple images [78]. Figure 1.9 depicts field propagation and first image generation for each type of interference mechanism.

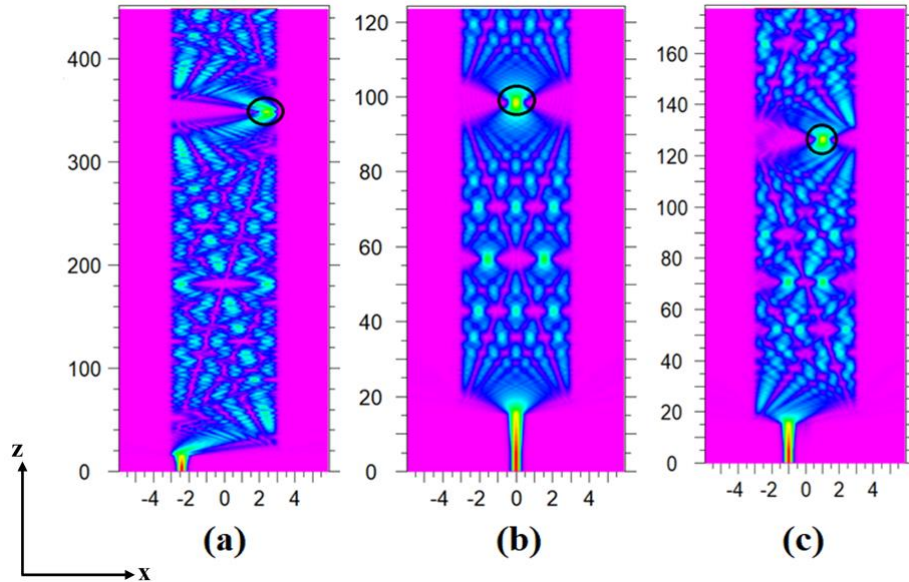


**Figure 1.9:** MMI optical field distributions for (a) General Interference; (b) Symmetric Interference; (c) Paired Interference. Values on both axes are in  $\mu\text{m}$ .

### 1.5.2 SWG-MMI Coupler

As introduced before, to improve the performance and overcome the bandwidth limitations of the conventional waveguides, a SWG section is introduced to replace that in the MMI section. The contribution of the SWG is interpreted as the modification of the refractive index part in equation (1.26) as follows [68]:

$$L_{\pi} = \frac{\pi}{\beta_0 - \beta_1} = \frac{n_{zz}^2}{n_{xx}} \frac{4w_e^2}{3\lambda} \quad (1.35)$$

with the proper adjustment of the term  $\frac{n_{zz}^2}{n_{xx}}$ , the beat length dependence on wavelength can be reduced considerably, and thus the operating bandwidth of the proper coupler expands accordingly. This adjustment is done by selecting the right pitch length and duty cycle of the SWG section.

## 1.6 Optical Phase Shifters

Optical phase shifters (OPS) are an essential part of a wide spectrum of MDM devices and applications. Their operation must not be confused with that of the optical delay line (ODL) which is distinguished as a time-domain delay, whereas the OPS adjusts the phase of the optical signal to a reference one by the change of the effective refractive index. The OPS can induce a phase shift from 0 to 360°. In OPS, the phase slightly changes along the optical path within the order of one wavelength, whereas in ODL, the time delay between optical signals requires that the optical path needs to be greater than one wavelength [79]. OPSs are categorized into two groups based on the inclusion of a control element or not to induce the required shift. the first one is the active phase shifter which requires a control element to induce the phase shift mainly using two mechanisms, the thermo-optic effect and the free-carrier plasma dispersion [80]. In contrast, for the passive phase shifter, no control element to induce the phase shift is required and it is only based on the path difference between two waveguides of different dimensions (length and width) [57].

### 1.6.1 Passive Phase-Shifting Technique

The commonly used scheme of the passive PSs shown in Figure 1.10, comprises, two parallel waveguides, a reference waveguide of length  $L_s$ , and width  $w_s$ , and another waveguide of length  $L_{ps}$ , and width  $w_{ps}$  whose geometrical dimensions are modified by the amount  $\Delta L_{ps}$  and/or  $\Delta w_{ps}$  to induce the desired phase difference at the output end. Generally, any waveguide produces a certain phase shift on the optical signal propagating through it given as [57]:

For the upper waveguide

$$\Phi_U(\lambda) = -\beta_U(\lambda, z) \cdot L_{ps} \quad (1.36)$$

For the lower reference waveguide:

$$\Phi_L(\lambda) = -\beta_L(z, \lambda) \cdot L_s \quad (1.37)$$

The total phase shift  $\Delta\Phi(\lambda)$  at the output end is

$$\Delta\Phi(\lambda) = \Phi_U(\lambda) - \Phi_L(\lambda) \quad (1.38)$$

where the  $\beta$ 's are the phase constants of the fundamental mode propagating across the corresponding waveguide.

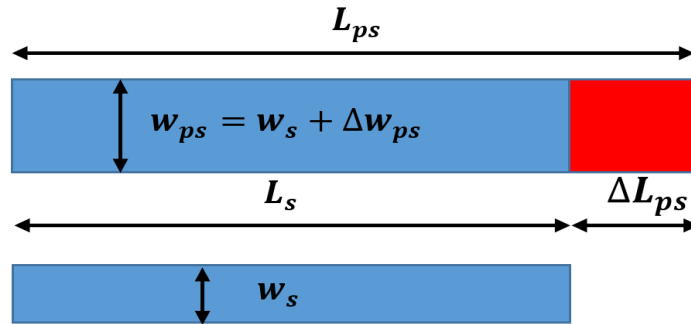


**Figure 1.10:** Schematic of passive phase-shifting structure.

## 1.6.2 Theoretical Analysis of a Passive Phase Shifter

This sub-section first presents the theoretical analysis of the operation of the passive PSs using the conventional waveguides. Later, with the use of SWG technology, a counterpart is designed to address and overcome the limitations observed in the conventional type.

### i. Conventional Passive Phase Shifter

Consider two parallel waveguides are shown in Figure 1.11, of equal length  $L_{ps}$  and different widths  $w_{ps}$ , and  $w_s$  corresponding to the upper and lower waveguides, respectively. These waveguides are placed at a certain separation so that to ensure no interference occurs between their optical signals. The desired phase shift  $\Delta\Phi(\lambda)$  is achieved through the width dissimilarity of the two waveguides. Using equations (1.36) to (1.38), yields [68]

$$\Delta\Phi(\lambda) = \Phi_L(\lambda) - \Phi_U(\lambda) = [\beta_U - \beta_L] \cdot L_{ps} \quad (1.39)$$

Substituting the difference in the propagation constants gives

$$\Delta\Phi(\lambda) = \frac{2\pi}{\lambda} (n_{eff\_U} - n_{eff\_L}) \cdot L_{ps} = \frac{2\pi}{\lambda} \Delta n_{eff} L_{ps} \quad (1.40)$$

where  $n_{eff}$  is the effective refractive index of the fundamental mode in the corresponding waveguide.

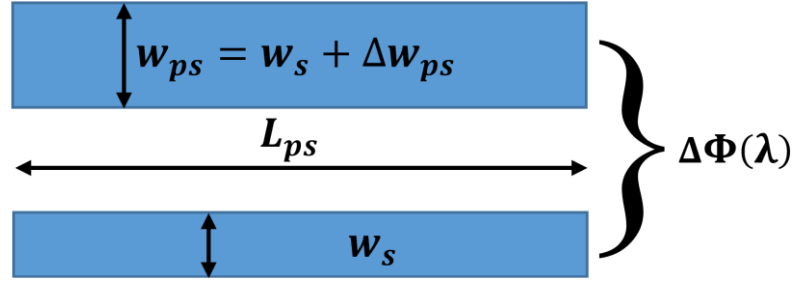


**Figure 1.11:** Schematic of conventional width-based passive phase-shifting structure [57].

The length of the waveguides  $L_{ps}$  is chosen so that initial phase shift  $\Delta\Phi_o$  at the desired wavelength ( $\lambda_o$ ) is generated. Thus the length can be calculated using a modified form equation (1.40) for the length as follows [57]:

$$L_{ps} = \Delta\Phi_o \frac{\lambda_o}{2\pi\Delta n_{eff}(\lambda_o)} \quad (1.41)$$

Again, equation (1.40) can be rewritten including the initial phase shift due to the selection of the phase shifter length as in equation (1.42), which shows that the phase shift contains two parts, a constant part at the designed wavelength and a variable part that changes with the wavelength.

$$\Delta\Phi(\lambda) = \Delta\Phi_o \frac{\lambda_o}{\Delta n_{eff}(\lambda_o)} \frac{\Delta n_{eff}(\lambda)}{\lambda} \quad (1.42)$$

Introducing the effect of effective index change in terms of the width change of the waveguides. The propagation constant  $\beta$  has the formula

$$\beta_v = k_o n_1 - \frac{\pi\lambda}{4w_e^2 n_1^2} \quad (1.43)$$

from equation (1.20), the effective index related to the propagation constant as [57]

$$n_{eff} = \frac{\beta}{k_o} = n_1 - \frac{\lambda^2}{8w_e^2 n_1} \quad (1.44)$$

Since  $\Delta n_{eff} = n_{eff\_U} - n_{eff\_L}$ , then

$$\Delta n_{eff} = \frac{\lambda^2}{8n_1} \left[ \frac{1}{w_{e\_L}^2} - \frac{1}{w_{e\_U}^2} \right] \quad (1.45)$$

Thus, equation (1.40), can be modified again including the waveguide width contribution as [57]

$$\Delta\Phi(\lambda) = \frac{\pi\lambda}{4n_1} \left[ \frac{1}{w_{e\_L}^2} - \frac{1}{w_{e\_U}^2} \right] L_{ps} \quad (1.46)$$

where  $n_1$  is the refractive index of the core material,  $w_e$ , is the effective width of the corresponding waveguide (with L for lower, U for upper).

## ii. SWG-assisted Passive Phase Shifter

For bandwidth and loss enhancement, the conventional waveguides considered in the previous section are replaced with a SWG alternative as shown in Figure 1.12. These waveguides consist of segments of thickness  $a$  arranged periodically with pitch length  $\Lambda$ . Both are of length  $L_{ps}$ , and widths  $w_{ps}$ , and  $w_s$  of the shifter and reference waveguide, respectively.

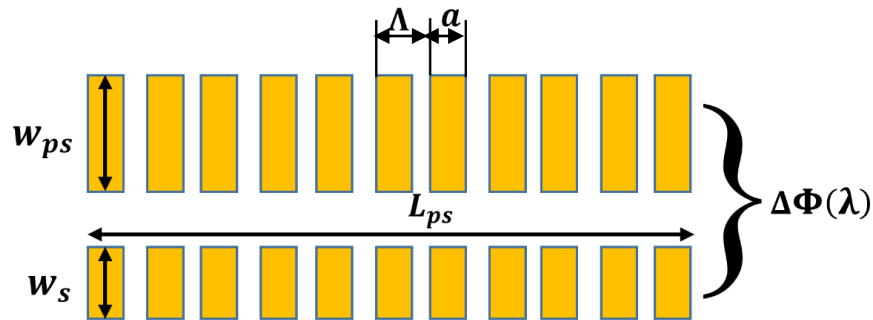


**Figure 1.12:** Schematic of SWG passive phase shifting structure [57].

Again, the SWG technology contribution is interpreted in terms of the refractive index modification of the new homogenous medium utilizing equations (1.21) and (1.22). The phase difference of equation (1.46) can be rewritten as [57]:

$$\Delta\Phi(\lambda) = \frac{\pi\lambda n_{xx}}{4 n_{zz}^2} \left[ \frac{1}{w_{e\_L}^2} - \frac{1}{w_{e\_U}^2} \right] L_{ps} \quad (1.47)$$

The wavelength dependence of equation (1.47) can be improved through proper selection for the values of SWG parameters  $D, C$  and  $\Lambda$  where the refractive index ratio changes accordingly.

### 1.7 Asymmetric Directional Coupler

The directional coupler is a PIC device that transfers the optical field between two closely placed waveguides. The basic scheme of a standard directional coupler is shown in Figure 1.13, where the evanescent wave extends from the first waveguide and is coupled into the second one. The directional couplers can be found in two structures, the symmetric directional coupler (SDC) whose waveguides are identical as shown in Figure (1.13-a), and the asymmetric directional coupler (ADCs), whose waveguides are of different dimensions “non-identical” as shown in Figure (1.13-b). The SDC type is used to build power and polarization splitters [81], whereas the ADC type is widely used in MDM (de)multiplexing techniques due to their flexibility, scalability, and structural simplicity for capacity enhancement and high-order mode excitation from an input fundamental mode [82,83].

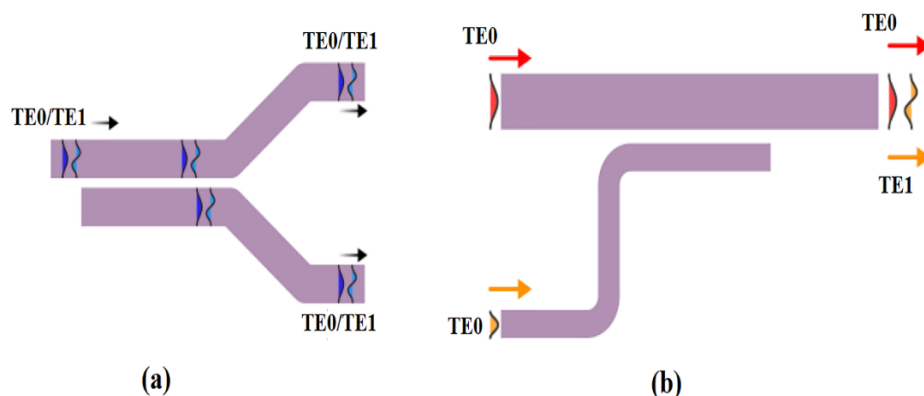


**Figure 1.13:** Scheme of directional couplers (a) SDC (b) ADC [83].

In the ADC multiplexer, efficient power transfer and high-order mode excitation is based on the satisfaction of the phase-matching condition  $[n_{eff\_TE0} - n_{eff\_TEm} \approx 0]$  between the single-mode access waveguide and the main multimode waveguide of effective indices  $n_{eff\_TE0}$ , and  $n_{eff\_TEm}$ , respectively. These waveguides are closely placed with certain coupling parameters (length and gap) and the excited modes can be observed at the output end as shown in Figure 1.14. The amount of the optical power coupled from the access waveguide to the main multimode waveguide can be expressed in terms of the coupling coefficient as [84]

$$\kappa^2 = \frac{P_{TEm}^{out}}{P_{TE0}^{in}} = \sin^2(D * L_c) \quad (1.48)$$

where  $P_{TEm}^{out}$ , and  $P_{TE0}^{in}$  are the power of the output TE<sub>n</sub> high-order mode, and the input TE<sub>0</sub> mode, respectively.  $D$  is the coupling gap and  $L_c$  is a coupling length.

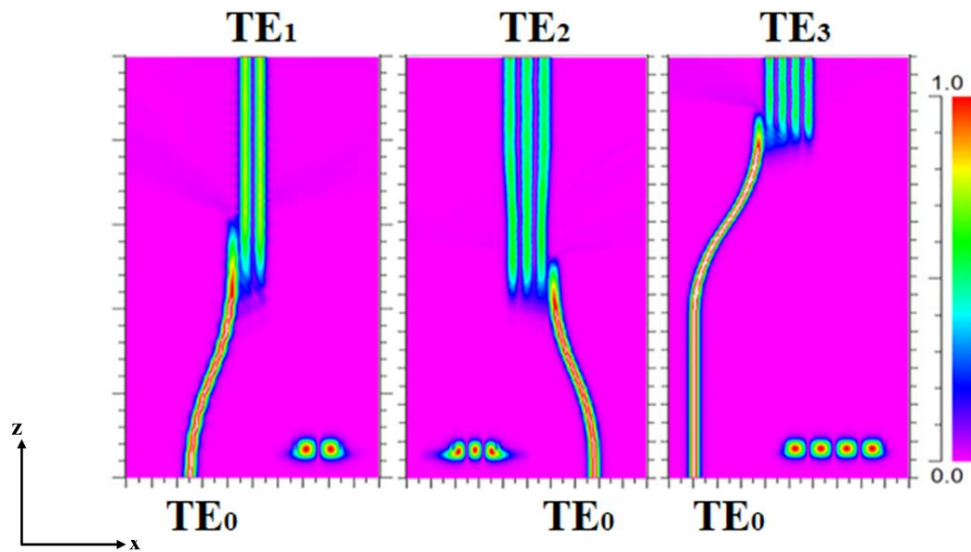


**Figure 1.14:** Simulated light propagation in an ADC for different excited high-order modes.

## 1.8 Literature Survey

This section presents a brief survey of related published work. It focuses on the use of MMI couplers and ADC couplers as mode (de)multiplexing

devices and the application of subwavelength grating technology in this field. Note that the operating wavelengths of the reported work are 1.55  $\mu\text{m}$ .

**In 2017, Jafari *et al.* [85]** proposed a two-mode SWG-assisted ADC-based (de)multiplexer. The losses of the proposed device are  $< 0.5$  dB, the crosstalk is  $< -15$  dB over an operating bandwidth of 65 nm extending over the range (1.5-1.565)  $\mu\text{m}$ .

**In 2017, Dai *et al.* [83]** proposed a 10-channel dual-polarization conventional ADC-based (de)multiplexer. It supports four TM and 6 TE polarized modes. This device shows worst-case losses of 1.8 dB and crosstalk of -15 dB over operating bandwidth -90 nm (1.52-1.6)  $\mu\text{m}$ .

**In 2018, Truong *et al.* [86]** proposed a three-mode conventional MMI-based (de)multiplexer. The designed device offers insertion loss  $> -0.9$  dB and crosstalk  $< -17$  dB over an operating bandwidth of 40 nm (1.525-1.565)  $\mu\text{m}$ . It features an overall footprint of (5 $\times$ 400  $\mu\text{m}^2$ ).

**In 2019, Herrero-Bermello *et al.* [87]** proposed an MMI-based polarization splitter using tilted SWG segments. The losses of the designed device are  $< 1$  dB and an extinction ratio  $> 20$  dB over an operating bandwidth of 131 nm (1.4-1.7)  $\mu\text{m}$ , also the device footprint is (4 x 100  $\mu\text{m}^2$ ).

**In 2020, Nath *et al.* [88]** proposed a five-mode ADC-based (de)multiplexer based on a conventional silicon-on-insulator (SOI) waveguide, for on-chip optical interconnects. The device exhibits an insertion loss of -0.24 dB and crosstalk of -33 dB with 40 nm (1.53-1.57)  $\mu\text{m}$  operating bandwidth. The overall coupling length of the device is about 40  $\mu\text{m}$ .

**In 2020, Zhou and Sun [73]** proposed a two-mode MMI-based (de)multiplexer using a conventional (SOI) platform. Device performance showed an insertion loss  $> -1$  dB, crosstalk  $< -15$  dB, 40 nm (1.53-1.57)  $\mu\text{m}$  operating bandwidth, and an overall footprint of (2.7 $\times$ 43.7  $\mu\text{m}^2$ ).

**In 2020, González-Andrade *et al.* [89]** experimentally demonstrated a two-mode MMI-based (de)multiplexer using subwavelength grating technology. The performance of the device showed an insertion loss  $> -1.1$  dB, crosstalk better than  $-18$  dB, and an operating bandwidth of 120 nm (1.52-1.64)  $\mu\text{m}$ . The total area of the device is  $(3.7 \times 38.6)$   $\mu\text{m}^2$ .

**In 2020, Chen and Xiao [82]** proposed a polarization beam splitter built using an SWG-assisted directional coupler. The device was characterized by an insertion loss  $> -0.13$  dB, an extinction ratio  $> 23$  dB, and an operating bandwidth of 40 nm (1.52-1.56)  $\mu\text{m}$ . The device has a coupling length of 10  $\mu\text{m}$ .

**In 2021, Shiran *et al.* [90]** designed and fabricated a dual-mode MMI splitter based on SWG technology. Experimental results of the device showed an insertion loss  $> -0.1$  dB, crosstalk better than  $-17$  dB, over an operating bandwidth of 100 nm (1.5-1.6)  $\mu\text{m}$ . The device footprint is  $5 \times 48$   $\mu\text{m}^2$ .

**In 2021, Jiang *et al.* [91]** proposed a four-mode ADC-based (de)multiplexer based on an SWG-assisted waveguide. The experimental results showed minimum operating bandwidths  $< 100$  nm (1.5-1.6)  $\mu\text{m}$ . The insertion loss is  $> -1.7$  dB, the crosstalk is always better than  $-15$  dB. The coupling length of the proposed device is about 50  $\mu\text{m}$ .

This survey shows that the conventional waveguide-based (de)multiplexers are high order devices but have limitations in operating bandwidth and losses, and those who use the subwavelength grating technology are limited in the number of high-order modes. Thus, this thesis combines the benefits of both fields, in designing higher-order mode capacity devices, with low losses, wider operating bandwidth, and higher compactness. Table 1.2 lists a summary of the devices reported in the literature with the main specifications and performance indicators.

**Table1.2** Literature survey summary

Ref#	Structure	Approach	I.L	C.T	B.W ( $\mu\text{m}$ )	Area
[85]	SWG-assisted ADC-based (de)multiplexer	Theoretical	-0.5	-15	1.500-1.565	-
[83]	Conventional ADC-based (de)multiplexer	Theoretical	-1.8	-15	1.52-1.60	-
[86]	Conventional MMI-based (de)multiplexer	Theoretical	-0.9	-17	1.525-1.565	5×400
[87]	SWG-assisted MMI-based polarization splitter	Theoretical	-1	-	1.400-1.700	4×100
[88]	Conventional ADC-based (de)multiplexer	Theoretical	-0.24	-33	1.530-1.570	-
[73]	Conventional MMI-based (de)multiplexer	Theoretical	-1	-15	1.530-1.570	2.7×43.7
[89]	SWG-assisted MMI-based (de)multiplexer	Experimental	-1.1	-18	1.520-1.640	3.7×38.6
[82]	SWG-assisted ADC-based polarization beam splitter	Experimental	-0.13	-23	1.520-1.560	-
[90]	SWG-assisted MMI-based splitter	Theoretical	-0.1	-17	1.500-1.600	5×48
[91]	SWG-assisted ADC-based (de)multiplexer	Theoretical	-1.7	-15	1.500-1.600	-

### 1.9 Aim of The Thesis

The thesis aims to design low loss, compact, wideband, and fabrication tolerant devices using subwavelength grating technology that can be used in advanced optical communication systems.

### 1.10 Contributions

The main contributions of this thesis are proposing, designing, and simulation of

- i. Three-TE mode MMI-based (de)multiplexer using subwavelength grating technology.
- ii. Four-TE mode MMI-based (de)multiplexer using both conventional and subwavelength grating-based technology Si/SiO<sub>2</sub> platform.
- iii. Twelve-TE mode SWG-assisted ADC (de)multiplexer.
- iv. Fourteen-TE mode SWG-assisted ADC (de)multiplexer.
- v. Twelve-TM mode SWG-assisted ADC (de)multiplexer.
- vi. Twenty Four Dual-polarization SWG-assisted ADC (de)multiplexer.

## Chapter Two

# Design of Multimode interferometer-based (De)Multiplexers Using SWG Technology

2.2 Introduction
2.2 N-mode (De)multiplexer
2.3 Three-Mode (De)multiplexer
2.3.1 Subwavelength Grating Assisted (De)multiplexer
2.3.1.1 General Description
2.3.1.2 Device Dimensional Parameters Selection
2.3.1.3 Device Performance Evaluation
2.3.2 All-Subwavelength Grating Three-Mode (De)multiplexer
2.3.2.1 Device Dimensional Parameters Selection
2.3.2.3 Device Performance Evaluation
2.3.3 Operation Bandwidth Extension
2.3.3.1 O+C/C+L Band Operating (De)multiplexer
2.3.3.2 C+L Band Operating All-SWG (De)multiplexer
2.4 Proposed Four-TE Mode Demultiplexer
2.4.1 Conventional Four-TE Mode (De)multiplexer
2.4.2 SWG-assisted (De)multiplexer

## CHAPTER TWO

### Design of Multimode interferometer-based (De)Multiplexers Using SWG Technology

#### 2.1 Introduction

This chapter introduces a general mathematical framework of an  $N \times N$  MMI-based mode (de)multiplexer, along with design and simulation results of a subwavelength grating assisted, and all-subwavelength grating  $3 \times 3$  (de)multiplexers. These devices are designed to operate at the standard optical communication wavelength of  $1.55 \mu\text{m}$ . The analysis introduced in this chapter can be considered as basic guidelines to implement an MMI-based (de)multiplexer with a desired number of ports.

#### 2.2 N-mode (De)multiplexer

The basic scheme of the MMI-based N-mode (de)multiplexer is presented in Figure 2.1. It acts as a  $1 \times N$ -port device that comprises three main parts cascaded sequentially which are a  $1 \times N$  power splitter, phase shifters, and  $N \times N$  MMI coupler. The splitter and the MMI parts are designed utilizing the concept of the transfer matrix which depends on the order of the input modes, whereas the phase shifter is designed so that certain demultiplexing operation is satisfied. Thus, each output port of the device is assigned for a given input mode with no or minimum output detected at other output ports. Note that the nonlinear optical effects in the optical components are negligible.

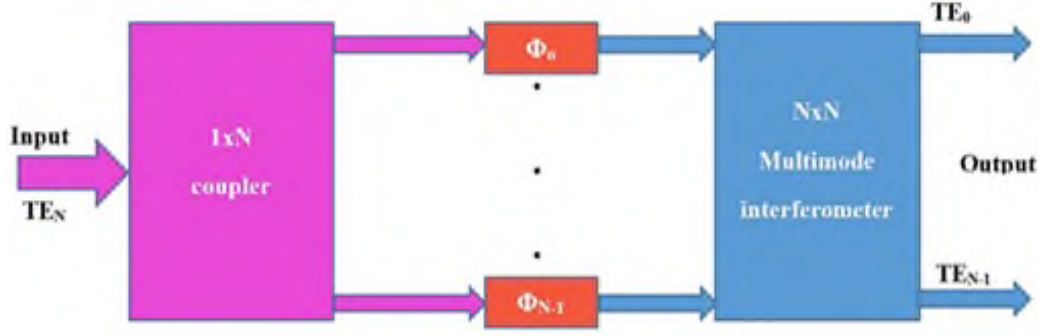


**Figure 2.1:** Simplified block diagram of N-mode (de)multiplexer.

Let the transfer matrices of the input coupler under the  $n$ -th mode excitation, phase-shift stage, and MMI are  $\mathbf{T}_{cn}$ ,  $\mathbf{T}_{\Phi}$ , and  $\mathbf{T}_{MMI}$ , respectively, generally described by equations (2.1-2.3). The elements of these matrices can be calculated from  $A_{ij} = 1/\sqrt{N} e^{j\varphi_{ij}}$ , where the phase  $\varphi_{ij}$  is given by [78]:

- If  $(i+j)$  even  $\varphi_{ij} = \varphi_o + \pi + \frac{\pi}{4N} (j - i)(2N - j + i)$
- If  $(i+j)$  odd  $\varphi_{ij} = \varphi_o + \frac{\pi}{4N} (j + i - 1)(2N - j - i + 1)$

where  $\varphi_o$  is a constant phase. Note that the  $\mathbf{T}_{cn}$  matrix is an input mode order  $TE_n$  mode, where  $n=0,1,\dots,N$ .

$$\mathbf{T}_{cn} \equiv [\mathbf{T}_{cn}]_{N \times 1} = \begin{bmatrix} c_{0,n} \\ \vdots \\ c_{N-1,n} \end{bmatrix} \quad (2.1)$$

$$\mathbf{T}_{\Phi} = [\mathbf{T}_{\Phi}]_{N \times N} = \begin{bmatrix} e^{j\Phi_0} & \dots & 0 \\ \vdots & \dots & \vdots \\ 0 & \dots & e^{j\Phi_{N-1}} \end{bmatrix} \quad (2.2)$$

$$\mathbf{T}_{MMI} \equiv [\mathbf{T}_{MMI}]_{N \times N} = \begin{bmatrix} m_{0,0} & m_{0,1} & \dots & m_{0,N-1} \\ m_{1,0} & m_{1,1} & \dots & m_{0,0} \\ \vdots & \vdots & \dots & \vdots \\ m_{N-1,0} & m_{N-1,1} & \dots & m_{N-1,N-1} \end{bmatrix} \quad (2.3)$$

The matrix corresponding to the  $n$ -th-order mode  $\mathbf{T}_{dn}$  of the device is given by:

$$\mathbf{T}_{\text{dn}} \equiv [\mathbf{T}_{\text{dn}}]_{N \times 1} = \mathbf{T}_{\text{MMI}} \cdot \mathbf{T}_{\Phi} \cdot \mathbf{T}_{\text{cn}} = \begin{bmatrix} (t_0)_n \\ (t_1)_n \\ \vdots \\ (t_{N-1})_n \end{bmatrix} \quad (2.4)$$

where the value of the matrix elements  $t_0, t_1, \dots, t_{N-1}$  depends on the order of the input field. Assume the input field is excited by  $N$  TE-modes having electric field amplitudes  $E_{i,0}, E_{i,1}, \dots$ , and  $E_{i,N-1}$ , and the field amplitudes at the  $N$  output ports are denoted by  $E_{o,0}, E_{o,1}, \dots$ , and  $E_{o,N-1}$ . Both parameters can be expressed in matrix form as:

$$\mathbf{E}_i \equiv [\mathbf{E}_i]_{N \times 1} = \begin{bmatrix} E_{i,0} \\ \vdots \\ E_{i,N-1} \end{bmatrix} \quad (2.5)$$

$$\mathbf{E}_o \equiv [\mathbf{E}_o]_{N \times 1} = \begin{bmatrix} E_{o,0} \\ \vdots \\ E_{o,N-1} \end{bmatrix} \quad (2.6)$$

Then

$$\mathbf{E}_o = \mathbf{T}_d \cdot \mathbf{E}_i \quad (2.7)$$

where

$$\mathbf{T}_d \equiv [\mathbf{T}_d]_{N \times N} = \begin{bmatrix} [\mathbf{T}_{d,0}] & [\mathbf{T}_{d,1}] & \dots & [\mathbf{T}_{d,N-1}] \end{bmatrix} \quad (2.8)$$

Combining equations (2.7) and (2.8) and using equations (2.4), (2.5), and (2.6) gives

$$\begin{aligned} E_{o,0} &= (t_0)_0 \cdot E_{i,0} + (t_0)_1 \cdot E_{i,1} + \dots + (t_0)_{N-1} \cdot E_{i,N-1} \\ E_{o,1} &= (t_1)_0 \cdot E_{i,0} + (t_1)_1 \cdot E_{i,1} + \dots + (t_1)_{N-1} \cdot E_{i,N-1} \\ &\vdots \\ &\vdots \\ E_{o,N-1} &= (t_{N-1})_0 \cdot E_{i,0} + (t_{N-1})_1 \cdot E_{i,1} + \dots + (t_{N-1})_{N-1} \cdot E_{i,N-1} \end{aligned} \quad (2.9)$$

## 2.3 Three-Mode (De)multiplexer

This section presents the mathematical framework and design steps of the three-mode (de)multiplexer for both SWG-assisted MMI coupler and the all-SWG coupler devices.

### 2.3.1. Subwavelength Grating Assisted (De)multiplexer

In this subsection, the design concept, parameters selection, and performance of the SWG-assisted (de)multiplexer are presented.

#### 2.3.1.1 General Description

First, using the analysis introduced in the previous section to obtain the matrices describing the performance of a  $1 \times 3$  mode (de)multiplexer whose output is excited using three input modes  $TE_0$ ,  $TE_1$ , and  $TE_2$ . The device consists of a  $1 \times 3$  trident splitter connected to a  $3 \times 3$  subwavelength grating +assisted MMI coupler with phase shifters placed at the arms of the splitter as shown in Figure 2.2. Equation (2.1) can be set based on design requirements for each case of input mode of this device as follows [86]:

$$\mathbf{T}_{c0} = \frac{1}{\sqrt{2}} [j \quad 0 \quad j]^T \quad (2.10)$$

$$\mathbf{T}_{c1} = \frac{1}{\sqrt{2}} [j \quad 0 \quad -j]^T \quad (2.11)$$

$$\mathbf{T}_{c2} = \frac{1}{\sqrt{2}} [0 \quad 1 \quad 0]^T \quad (2.12)$$

The subscripts 0,1, and 2 are used with a matrix  $\mathbf{T}_c$  to distinguish the three input modes  $TE_0$ ,  $TE_1$ , and  $TE_2$  respectively. Note that  $\pm j = e^{\pm j\frac{\pi}{2}}$  according to Euler's identity. Now, investigating equations (2.10-2.12), yield, the following findings:

- i. The trident splitter guides  $TE_0$  ( $TE_1$ ) mode through the outer arms with 50% amplitudes of the input field and is in phase (out of phase).
- ii. The trident splitter guides the input  $TE_2$  mode directly through the central arm with equal amplitude of the input field.

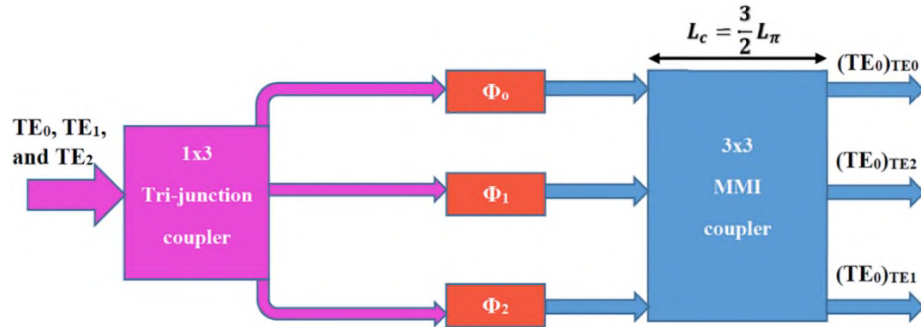


**Figure 2.2:** Schematic of  $1 \times 3$  mode (de)multiplexer.

The  $3 \times 3$  MMI coupler is designed to operate as a 3-dB splitter when the field is injected into either of the side input ports, i.e. the input power is split equally between the outer output ports and the MMI is acting as a  $2 \times 2$  coupler. Whereas for the case of field injection into the central port, the output is detected at the central output port only, which means in this case, the MMI is acting as a  $1 \times 1$  coupler with  $\Phi_1 = 0$ , the signal at the central input port is guided directly to the central output port. Thus, based on that analysis, for the case of  $TE_0$  ( $TE_1$ ) mode corresponding to the two outer input/output arms of the original MMI with the following transfer matrix [86]

$$\mathbf{T}_{\text{MMI}(0,1)} = \frac{1}{\sqrt{2}} \begin{bmatrix} j & j \\ -j & j \end{bmatrix} = \frac{j}{\sqrt{2}} \begin{bmatrix} 1 & 1 \\ -1 & 1 \end{bmatrix} \quad (2.13)$$

When  $\Phi_0$  and  $\Phi_2$  phases are introduced at the two outer inputs of the trident splitter, equation (2.13) is modified to

$$\mathbf{T}'_{\text{MMI}(0,1)} = \mathbf{T}_{\text{MMI}(0,1)} \begin{bmatrix} e^{j\Phi_0} & 0 \\ 0 & e^{j\Phi_2} \end{bmatrix} = \frac{j}{\sqrt{2}} \begin{bmatrix} e^{j\Phi_0} & e^{j\Phi_2} \\ -e^{j\Phi_0} & e^{j\Phi_2} \end{bmatrix} \quad (2.14)$$

similarly, the trident splitter can be treated as a 1X2 coupler corresponding to the outer arms transmission. Thus, for  $TE_0$  and  $TE_1$  in equations (2.10) and (2.11) can be modified to [86]

$$\mathbf{T}'_{c0} = \frac{1}{\sqrt{2}} \begin{bmatrix} j \\ j \end{bmatrix}, \quad \mathbf{T}'_{c1} = \frac{1}{\sqrt{2}} \begin{bmatrix} j \\ -j \end{bmatrix} \quad (2.15)$$

According to that, the (de)multiplexer can be modeled as shown in Figure 2.3.

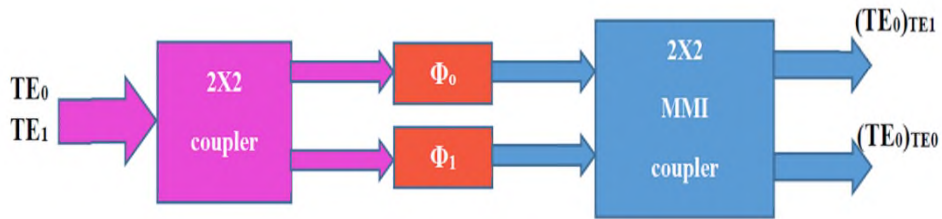


**Figure 2.3:** A simplified 3-mode (de)multiplexer for  $TE_0$  and  $TE_1$  modes excitation.

The outputs of the two outer ports of the (de)multiplexer can be calculated as

$$\begin{bmatrix} E_{o,0} \\ E_{o,1} \end{bmatrix} = \mathbf{T}_{MMI(0,1)} \begin{bmatrix} \mathbf{T}'_{c0} \\ \vdots \\ \mathbf{T}'_{c1} \end{bmatrix} \begin{bmatrix} E_{i,0} \\ E_{i,1} \end{bmatrix} \quad (2.16)$$

That analysis is utilized to obtain the output fields of the 2X2 MMI for the following two cases:

### 1. Case (a): Input Mode = $TE_0$

$$E_{o,0} = \frac{j}{2} \left[ e^{j\Phi_0} + e^{j(\frac{\pi}{2} + \Phi_1)} \right] \quad (2.17)$$

$$E_{o,1} = \frac{j}{2} \left[ -e^{j\Phi_0} + e^{j(\frac{\pi}{2} + \Phi_1)} \right] \quad (2.18)$$

Let the phase shifter be inserted at the output of the first outer arm of the trident to impose a  $\pi/2$  phase shift. Setting  $\Phi_0 = \pi/2$  and  $\Phi_1 = 0$  in equations (2.17) and (2.18) yields

$$E_{o,0} = \frac{j}{2} [e^{j\frac{\pi}{2}} + e^{j\frac{\pi}{2}}] = \frac{j}{2} [2j] = -1$$

$$E_{o,1} = \frac{j}{2} [-e^{j\frac{\pi}{2}} + e^{j\frac{\pi}{2}}] = 0$$

Thus, under that phase condition, the single output is detected at the outer ports of the  $3 \times 3$  MMI coupler.

## 2. Case (b): Input Mode = TE1

$$E_{o,0} = \frac{j}{2} [e^{j\Phi_0} + e^{j(-\frac{\pi}{2}+\Phi_1)}] \quad (2.19)$$

$$E_{o,1} = \frac{j}{2} [-e^{j\Phi_0} + e^{j(-\frac{\pi}{2}+\Phi_1)}] \quad (2.20)$$

setting  $\Phi_0 = \pi/2$  and  $\Phi_1 = 0$ , equations (2.19) and (2.20) yields

$$E_{o,0} = \frac{j}{2} [e^{j\frac{\pi}{2}} + e^{-j\frac{\pi}{2}}] = 0$$

$$E_{o,1} = \frac{j}{2} [-e^{j\frac{\pi}{2}} + e^{-j\frac{\pi}{2}}] = -1$$

This means that single output is also detected but on the other outer port of the (de)multiplexer. Important remarks related to the previous analysis are given in the following

1. When  $\Phi_0 = -\pi/2$  and  $\Phi_1 = 0$ , equations (2.17) and (2.18) become  $E_{o,0} = 0$  and  $E_{o,1} = 1$ , respectively, when TE<sub>0</sub> is excited at the (de)multiplexer input. Similarly for TE<sub>1</sub> mode, equations (2.19) and

(2.20) yield the two outputs  $E_{o,0} = 1$  and  $E_{o,1} = 0$ , respectively. Thus  $\Phi_0 = -\pi/2$  and  $\Phi_1 = 0$  condition is also useful to separate the input  $TE_0$  and  $TE_1$  modes into two individual output ports of the  $3 \times 3$  MMI coupler.

2. Considering the case of  $\Phi_0 = 0$  and  $\Phi_1 = \pi/2$  (i.e., the  $\pi/2$  phase shifter is placed at the other outer port of the tri-junction). Under these phase shifters, equations (2.17) and (2.18) become  $E_{o,0} = 0$  and  $E_{o,1} = -1$ , respectively. Also, equations (2.19) and (2.20) become  $E_{o,0} = j$  and  $E_{o,1} = 0$ , respectively.
3. When the accumulation phase  $\theta_a$  of the optical field of the guided modes propagating through the input  $1 \times 3$  coupler is taken into account, then the transfer matrix of this coupler is modified to [86]

$$\mathbf{T}'_{cn} = \mathbf{T}_{cn} e^{j\theta_a} \quad \text{for } n=0,1, \text{ and } 2$$

This makes each of the (de)multiplexer output fields is multiplied by the factor  $e^{j\theta_a}$ . Thus the phase  $\theta_a$  doesn't alter the function of the (de)multiplexer but introduces an extra phase shift for all the output fields.

Next, introduces the contribution of the subwavelength grating (SWG) effect in the MMI coupler of the designed device presented in Figure 2.4. As described in chapter 1, the SWG structure can be constructed as illustrated in Figure 1.6. which is the main concept of SWG, with two layers of refractive indices  $n_1$  and  $n_2$  are periodically arranged with pitch length denoted by  $\Lambda$ , where  $\Lambda \ll \lambda$  to ensure that the dispersion effect is suppressed and stratify that the structure serves as a homogeneous medium of an equivalent refractive index that can be expressed by equations (1.21 and 1.22), based on the polarization of the propagating E-field.

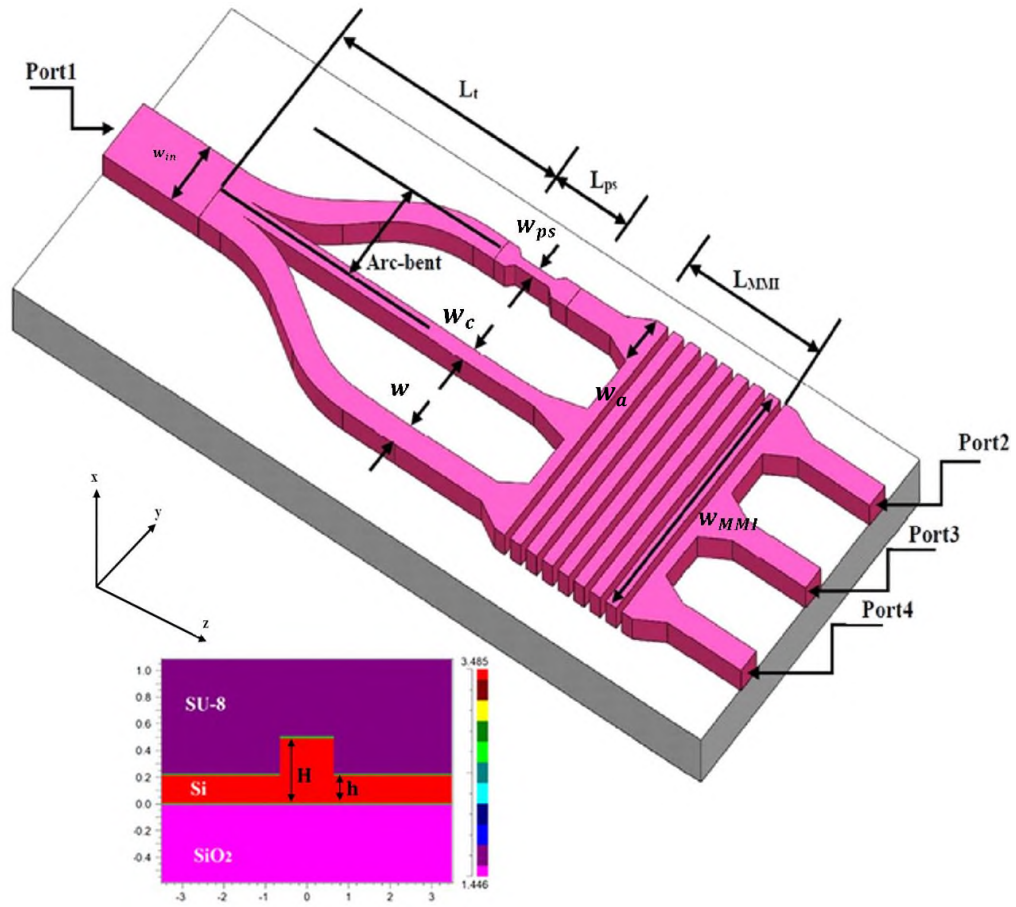


**Figure 2.4:** Schematic of the 3-TE mode SWG-MMI (de)multiplexer.

By introducing the SWG, the MMI coupler length formula to achieve the designed function of the coupler is described by equation (1.35). For a complete demultiplexing operation a  $\pi/2$  phase shift needs to be induced between the outer arms of the splitter before being connected to the SWG-MMI coupler. This phase shift is obtained through a passive phase shifter based on the difference between two waveguides of a certain length  $L_{ps}$  and different widths  $w_s$  and  $w_{ps}$  of straight and phase shifter, respectively. The induced phase shift can be expressed as in equation (1.46).

### 2.3.1.2 Device Dimensional Parameters Selection

Here, the dimensional parameters of each part of the (de)multiplexer should be carefully adjusted at the operating wavelength of  $1.55 \mu\text{m}$ . The device is designed on an SOI platform in the form of a rib waveguide with a height  $H = 500 \text{ nm}$  and a slab height  $h = 220 \text{ nm}$  [85]. The rib waveguide is composed of silicon (Si), silicon dioxide ( $\text{SiO}_2$ ), and SU-8 polymer layers with refractive indices of 3.476, 1.444, and 1.58, respectively, at  $1.55 \mu\text{m}$ . The Si is used to act as a core layer, the  $\text{SiO}_2$  of  $0.5 \mu\text{m}$  thickness as a cladding layer, and the  $0.5 \mu\text{m}$  thickness of a SU-8 polymer as a cover layer. The first part to design is the trident splitter which comprises three arms connected from their input end to a main stem of width  $w_{in}$ , which is wide enough to support high-order modes. The outer ones are S-bent arms identical to each other with equal widths and lengths denoted by  $w$  and  $L_t$ , respectively. The central arm is a straight waveguide with a width of  $w_c$ . The widths are chosen to support the fundamental mode ( $\text{TE}_0$ ) utilizing the effective index analysis of the guided modes through the rib waveguide, as shown in Figure 2.5. This Figure depicts the effective refractive index of the guided mode along the waveguide as a function of its width. The single-mode operation can be achieved for widths  $< 0.5 \mu\text{m}$ , and for a three modes operation, the width of the waveguide needs to be set to a value  $> 1 \mu\text{m}$ .

Simulation has been carried out to choose the proper values for the arms width  $w$  and  $w_c$  to achieve the desired operation of the splitter described in *i* and *ii* in section 2.3.1.1, and the result is shown in Figure 2.6, which depicts the change of the normalized transmission of the trident splitter as a function of the arm width. The red and black plots are corresponding to the outer and central arm widths, respectively. From this figure, it is obvious that maximum transmission and minimum crosstalk can be achieved when the widths are set to  $w > 0.4 \mu\text{m}$  and  $w_c < 0.3 \mu\text{m}$ . Thus, the widths  $w$  and  $w_c$  are set to  $0.5$  and  $0.2 \mu\text{m}$ , respectively. For the input stem waveguide, its

width  $w_{in}$  is set to  $1.2 \mu\text{m}$  so that the three arms fit exactly and can handle the three designed modes.

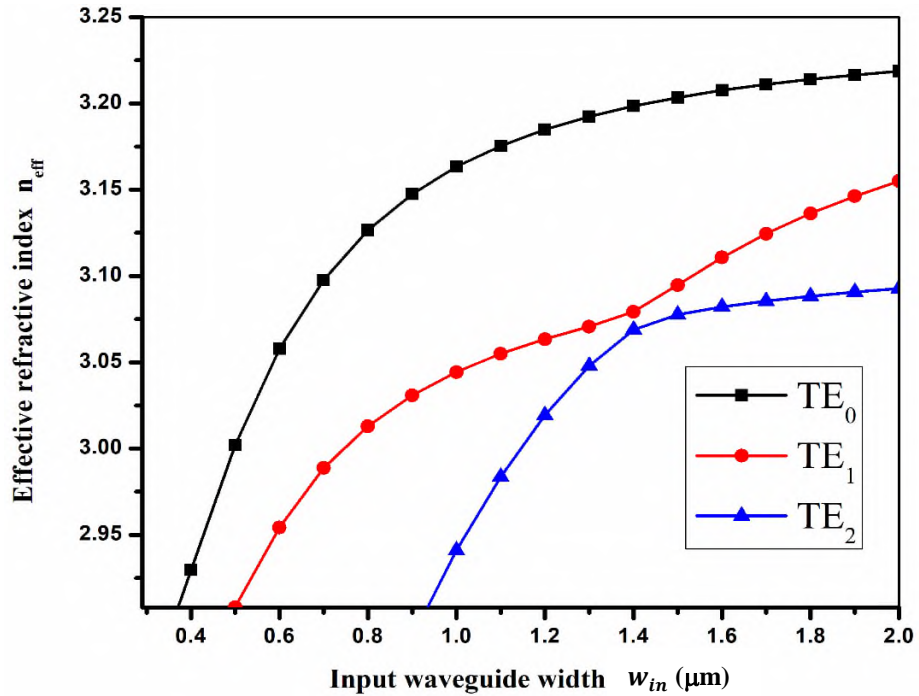


**Figure 2.5:** Effective refractive index vs. width of the input of tri-junction.

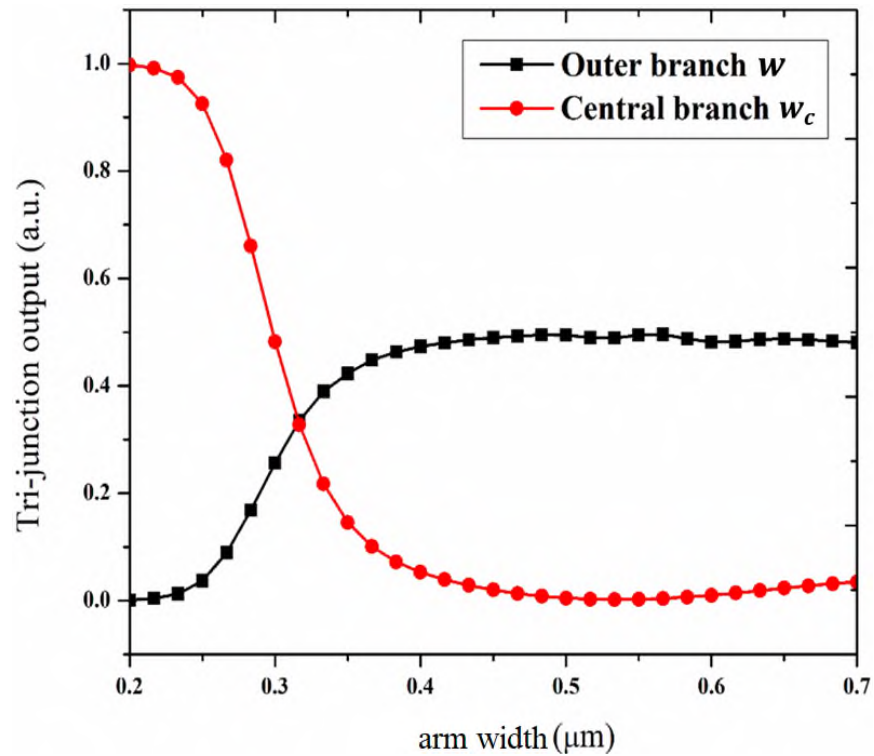


**Figure 2.6:** Variation of the tri-junction output power with branch width.

The next parameter to simulate is the arm length  $L_t$  and select the proper value to satisfy the designed splitting and guidance operation. Figure 2.7 depicts the simulation result presenting the normalized transmission of the splitter as a function of variation in arm's length. From this Figure, the desired operation can be achieved with a length ranging from (20-30  $\mu\text{m}$ ). Thus, in the design,  $L_t = 27\mu\text{m}$  is chosen as an acceptable value so that the trident splitter shows maximum transmission and minimum crosstalk for all three modes.

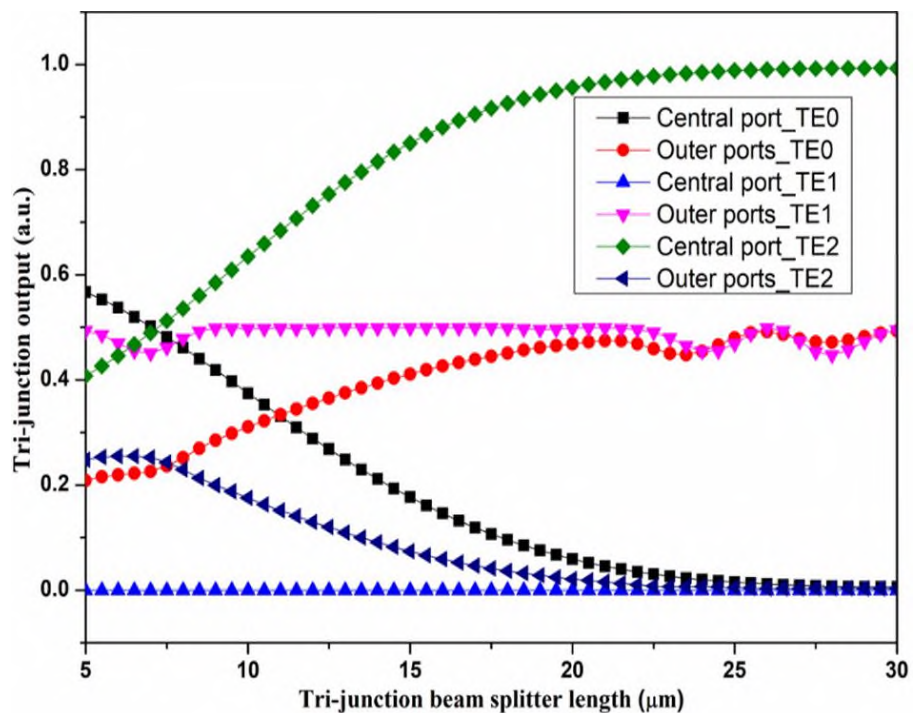


**Figure 2.7:** Variation of the tri-junction output power with branch length.

The second part to design is the SWG-MMI coupler. The main parameters for this part are the width, length, pitch length, and duty cycle denoted by  $w_{MMI}$ ,  $L_{MMI}$ ,  $\Lambda$ , and  $D.C$ , respectively. For compactness, flexibility, and high-performance purposes, the parameters  $w_{MMI}$ ,  $\Lambda$ , and  $D.C$  are set to 4.5  $\mu\text{m}$ , 0.2  $\mu\text{m}$ , and 50%, respectively. Regarding the desired operation of the SWG-MMI coupler explained earlier by the concept of self-imaging as a function of the length of the MMI section. The SWG-MMI length  $L_{MMI}$  is simulated around the theoretical value predicted by equations (1.31) and

(1.32) where both the two-folds and direct images (representing  $TE_0$  ( $TE_1$ ), and  $TE_2$  cases, respectively) appear at the same point on the output end. Figure 2.8 shows the simulation result which is the field distribution along the SWG-MMI coupler for the cases when the input field is side and center-injected into the MMI coupler, respectively. Based on this result, the desired images can be obtained when  $L_{MMI} = 57 \mu\text{m}$ , (excluding access waveguide length of  $5 \mu\text{m}$  length).

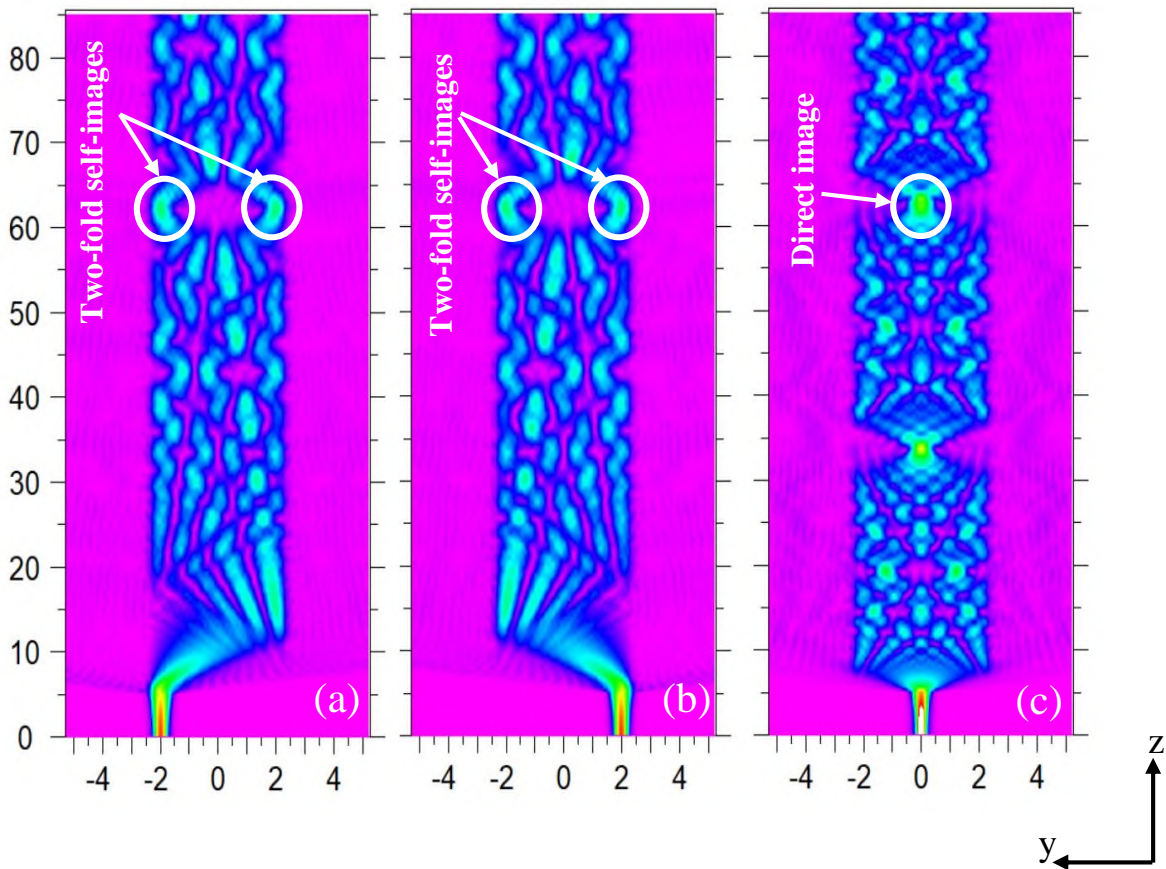


**Figure 2.8:** Optical field distribution along the SWG-MMI coupler (a) upper edge (b) lower edge (c) center. Values on both axes are in  $\mu\text{m}$ .

Note that ports with proper tapering for smooth field transition are located in the center of the SWG-MMI at ( $y=0$ ), while the side ports are initially at ( $y = \pm w_{MMI}/Y$ ), where  $Y$  is a *dimensionless integer* related to the number of the ports  $Y \leq N$ , and later adjusted to obtain the maximum output from the coupler. Thus, numerical simulation is conducted for this purpose and

the result is depicted in Figure 2.9 which shows the normalized transmission of the SWG-MMI coupler as a function of the change in the  $Y$ -parameter. From this Figure, it is obvious that the optimum value for port location is when  $Y = \pm 2.3$ .

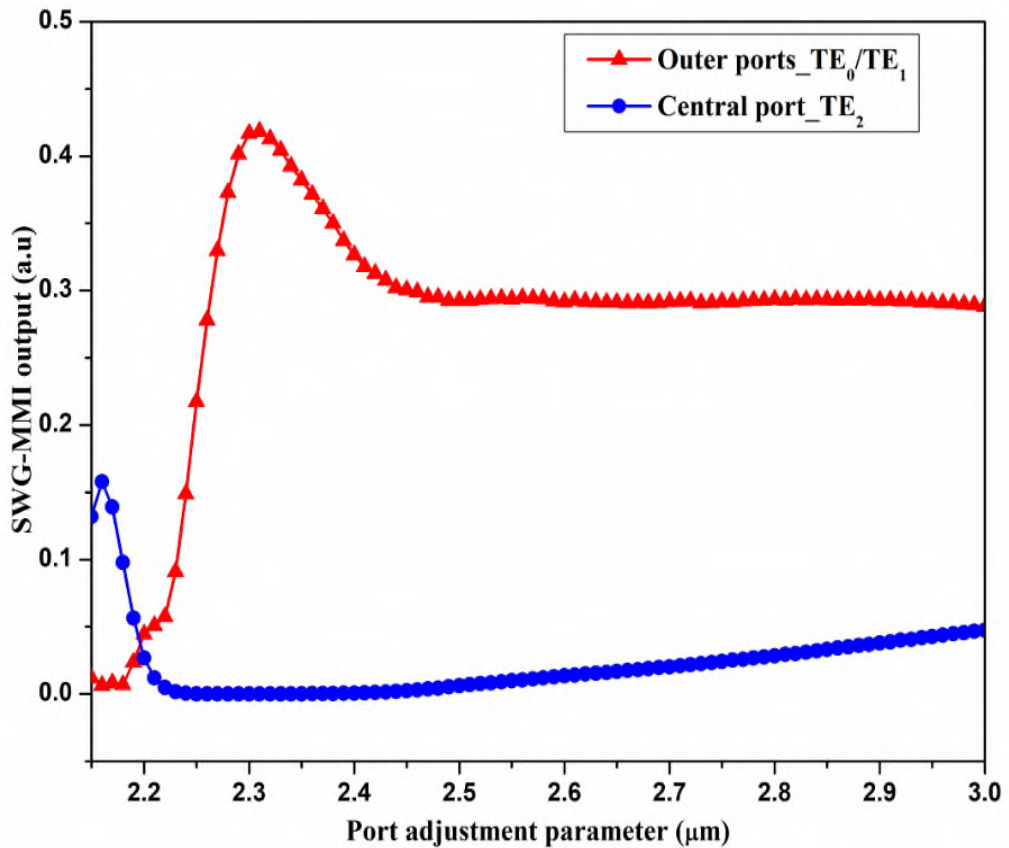


**Figure 2.9:** Dependence of the SWG-MMI output on port adjustment parameter.

Finally, designing the  $\pi/2$  phase shifter with main parameters the width and length denoted by  $w_{ps}$  and  $L_{ps}$ , respectively. A numerical simulation is conducted to design a tapered phase shifter and the result is depicted in figure (2.10) which represents the phase difference variation as a function of shifter width and length. During simulation, the width and length are ranged over the values (0.25-0.4)  $\mu\text{m}$  and (2.5-4.6)  $\mu\text{m}$ , respectively. The  $\pi/2$  phase difference can be obtained with several combinations of both parameters.

Again, for compactness and desired performance purposes,  $w_{ps}$  and  $L_{ps}$  of  $0.39 \mu\text{m}$  and  $2.5 \mu\text{m}$  are set, respectively. With that phase, the two components of  $\text{TE}_0$  ( $\text{TE}_1$ ) mode are interacted and guided to the designed structure output ports. Note that any parameter combination that satisfies the desired phase shift can be selected.

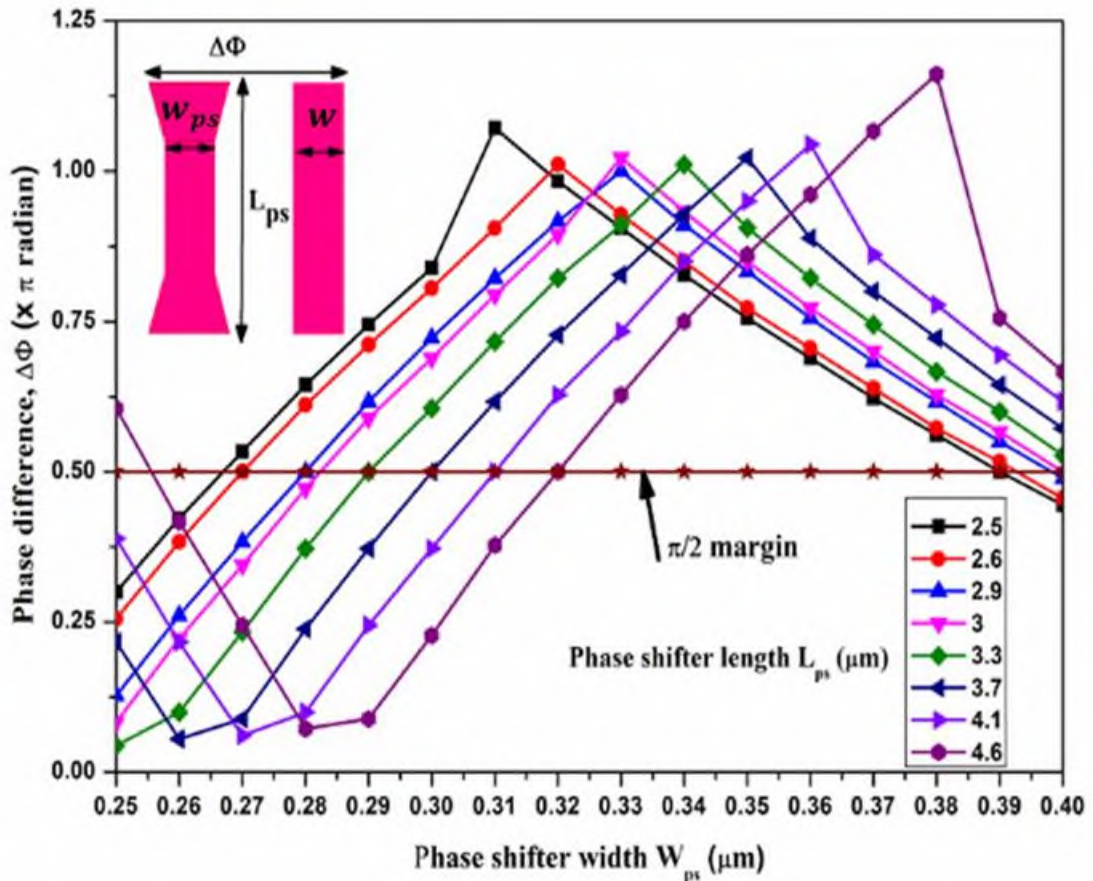


**Figure 2.10:** Dependence of the phase shift induced by the PS as a function of its width and length  $w_{ps}$  and  $L_{ps}$ , respectively.

A summary of the main geometrical parameter values is listed in Table 2.1 which are considered later to evaluate the performance of the designed device. Also, **the designed device's overall area is  $4.5 \times 120 \mu\text{m}^2$ .**

**Table 2.1.** Device main geometrical parameters for the designed SWG-MMI (de)multiplexer.

Section	Parameter	Value ( $\mu\text{m}$ )	Description
Tri-junction splitter	$w_{in}$	1.20	Input stem waveguide width
	$w$	0.50	Outer arm width
	$w_c$	0.20	Central arm width
	$L_t$	27	Tri-junction arm length
	S-bent	1.50	Outer arm bent
$\pi/2$ Phase shifter	$w_{ps}$	0.39	Phase shifter width
	$L_{ps}$	2.50	Phase shifter length
SWG-MMI coupler	$w_{MMI}$	4.50	SWG-MMI coupler width
	$w_a$	0.90	Access waveguide width
	$L_{MMI}$ (periods)	57 (285)	coupler length (segments)
	$\Lambda$ ( $D.C$ )	0.20 (50%)	Segments pitch (Duty cycle)

### 2.3.1.3 Device Performance Evaluation

The performance of the designed device is evaluated utilizing the Rsoft photonics suit through observation of the designed optical modes as they propagate across the device from the input to the output ports. Figure 2.11 depicts the optical intensity pattern for each case on the input modes at the designed wavelength of  $1.55 \mu\text{m}$  for (a)  $\text{TE}_0$ , (b)  $\text{TE}_1$ , (c)  $\text{TE}_2$ , and (d) all the three modes, which are injected into the device, respectively. It can be noticed that the  $\text{TE}_0$  ( $\text{TE}_1$ ) mode output is observed at the right (left) port, while the  $\text{TE}_2$  mode is guided to the central output port, respectively. This confirms the successful (de)multiplexing of the three modes  $\text{TE}_0$ ,  $\text{TE}_1$ , and  $\text{TE}_2$  as predicted over simulation and analysis.

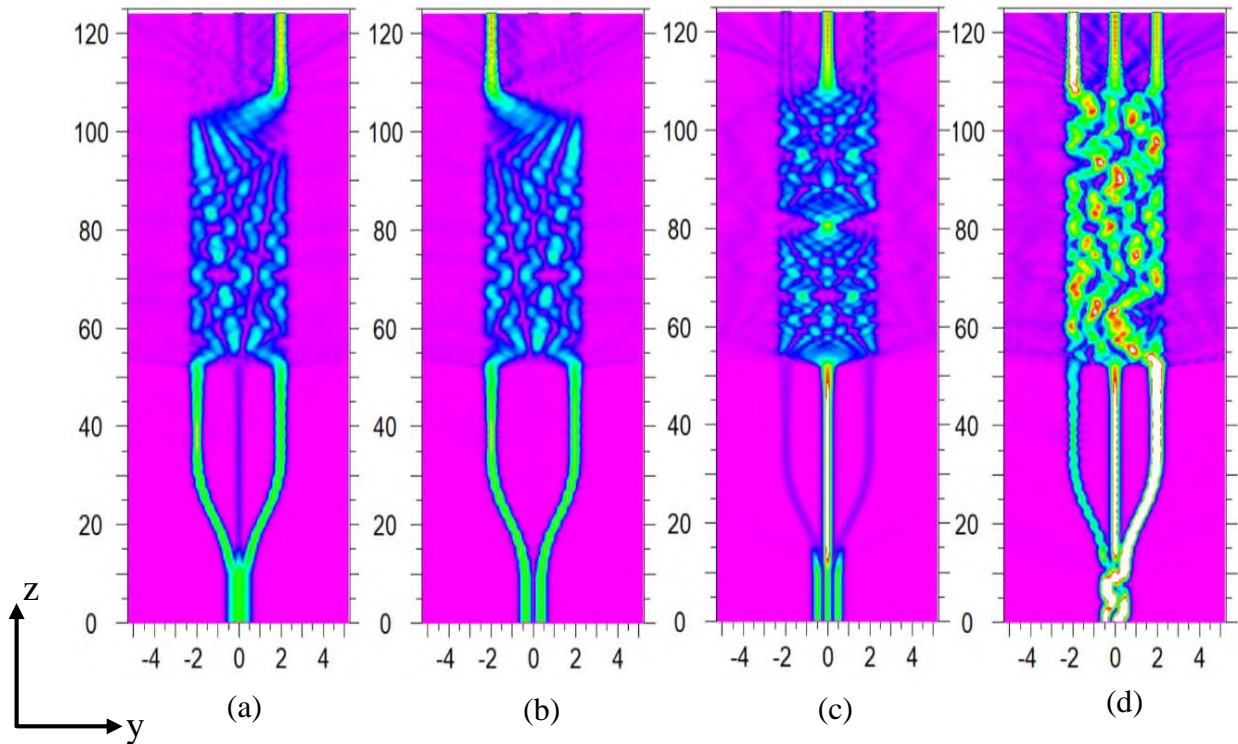


**Figure 2.11:** Optical intensity distribution of the guided mode along the device when the input is (a)  $TE_0$ , (b)  $TE_1$ , (c)  $TE_2$ , and (d) all three. Values on both axes are in  $\mu\text{m}$ .

It is worth mentioning that the proposed device is also capable to operate as a three-mode multiplexer with similar performance characteristics compared with demultiplexing operation state where the three output modes  $TE_0$ ,  $TE_1$ , and  $TE_2$  are obtained from the  $TE_0$  mode at the input end. This is illustrated in Figure 2.12 where the input and output transverse field profiles (x-y plane) are given for different input modes.

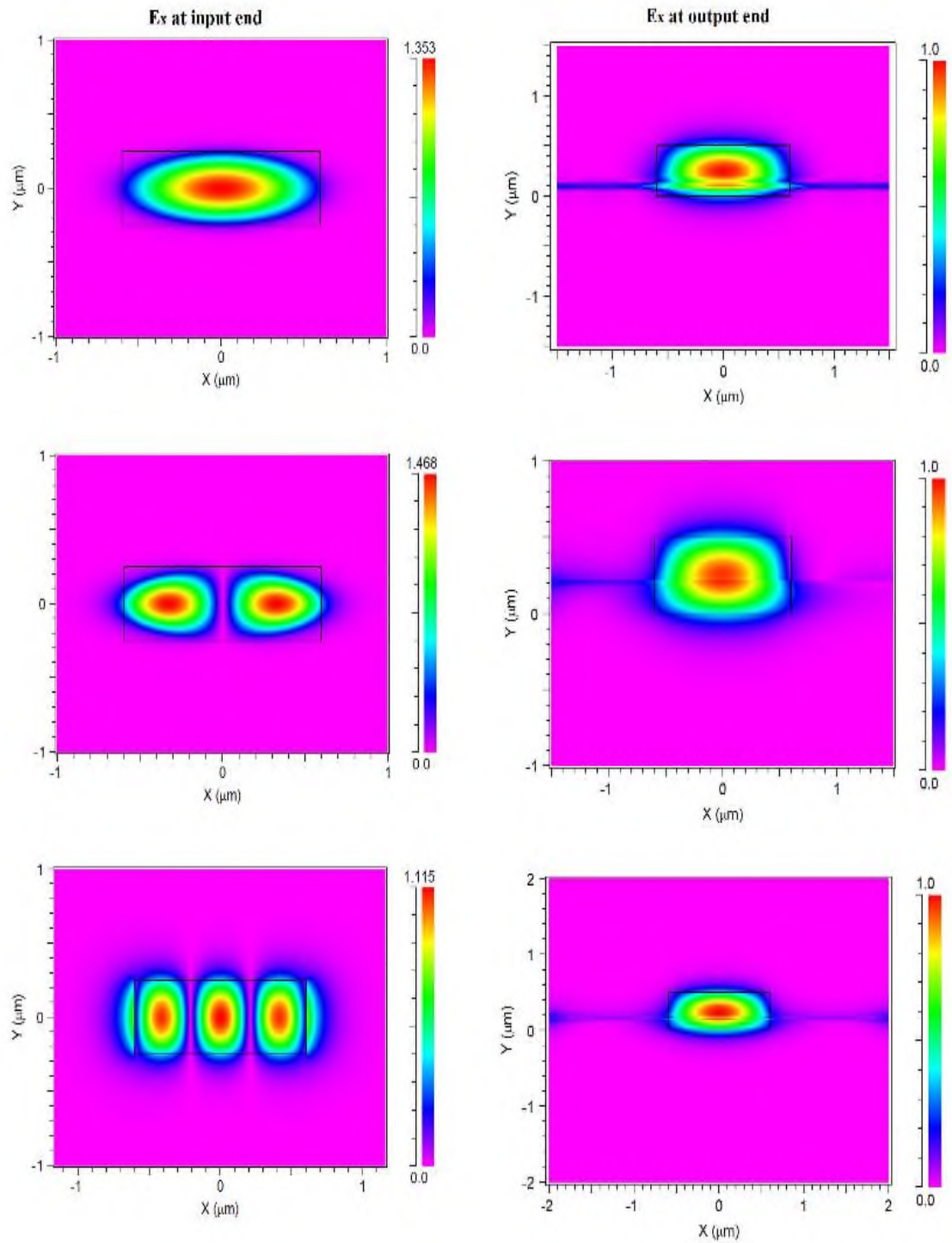


**Figure 2.12:** Transverse field profile of the input field (left) and output field (right) for (a)TE<sub>0</sub>, (b) TE<sub>1</sub>, and (c) TE<sub>2</sub>.

Second, evaluate the losses and operating bandwidth of the device by considering two essential parameters in multiplexing devices which are

insertion loss and crosstalk. The insertion loss denoted by I.L is the ratio of the desired output power  $(P_{out})_{desired}$  to the input power  $P_{in}$ , given by

$$I.L(dB) = 10 \log_{10} \frac{(P_{out})_{desired}}{P_{in}} \quad (2.21)$$

and the crosstalk denoted by  $C.T$  represents the ratio of the desired emitted power  $(P_{out})_{desired}$  to the undesired emitted output power  $(P_{out})_{undesired}$ , given by

$$C.T(dB) = -10 \log_{10} \frac{(P_{out})_{desired}}{(P_{out})_{undesired}} \quad (2.22)$$

The results of the calculations are shown in Figure 2.13 which are the insertion loss variation of the device as a function of the wavelength of the input light. The wavelength varies over the range (1.500-1.600)  $\mu\text{m}$ . From this Figure, it can be noticed that the device shows minimum loss at the designed wavelength of 1.55  $\mu\text{m}$  with an I.L of -0.8 dB. Further, the proposed device has 3-dB- and 1dB-bandwidths of 120 nm and 70 nm, respectively. Figure 2.14 shows the calculated crosstalk  $C.T$  of the device for each case of the input modes. Again, this Figure confirms the fact that minimum crosstalk is achieved at the operating wavelength with  $C.T$  lower than -18 dB. Table 2.2 lists the insertion loss and total crosstalk when the device operates at  $\lambda = 1.55 \mu\text{m}$ .

**Table 2.2.** Device insertion loss and total crosstalk at  $\lambda = 1.55 \mu\text{m}$ .

Parameter	TE <sub>0</sub> mode	TE <sub>1</sub> mode	TE <sub>2</sub> mode
I.L (dB)	-0.79	-0.85	-0.94
C.T (dB)	-17.9	-31.6	-19.8

A performance comparison between the proposed device with a related conventional 3×3 (de)multiplexer reported in [86] has been conducted. The

results are listed in Table 2.3. It can be noticed that the proposed device offers low losses similar to the conventional device. The operating bandwidth of the proposed device is 120 nm. Thus, the designed (de)multiplexer has 3 times wider bandwidth compared to that reported in [86]. Further, The footprint of the proposed device represents 27% of that of the conventional device.

**Table 2.3** Performance comparison of the designed device with the previously reported one.

Ref#	Structure	B.W( $\mu\text{m}$ )	C.T (dB)	I.L (dB)	Area ( $\mu\text{m}$ ) <sup>2</sup>
86	3-TE Conventional (de)multiplexer	(1.525-1.565)	< -17	> -0.9	5×400
This device	3-TE SWG-assisted (de)multiplexer	(1.490-1.610)	< -15	> -1.0	4.5×120

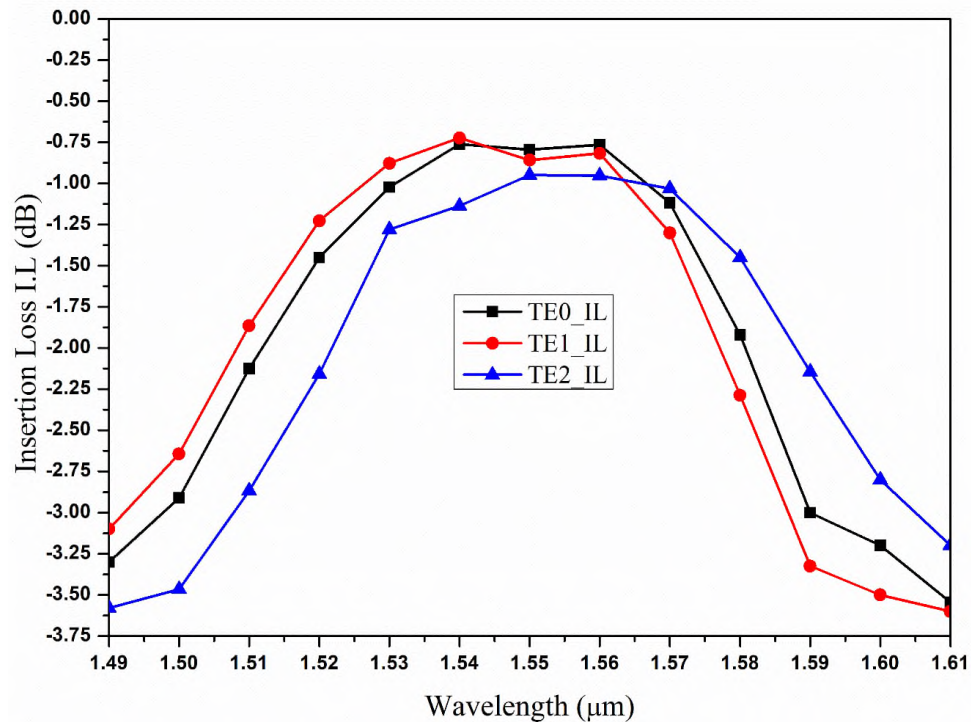


**Figure 2.13:** Insertion Loss of the proposed structure performance.

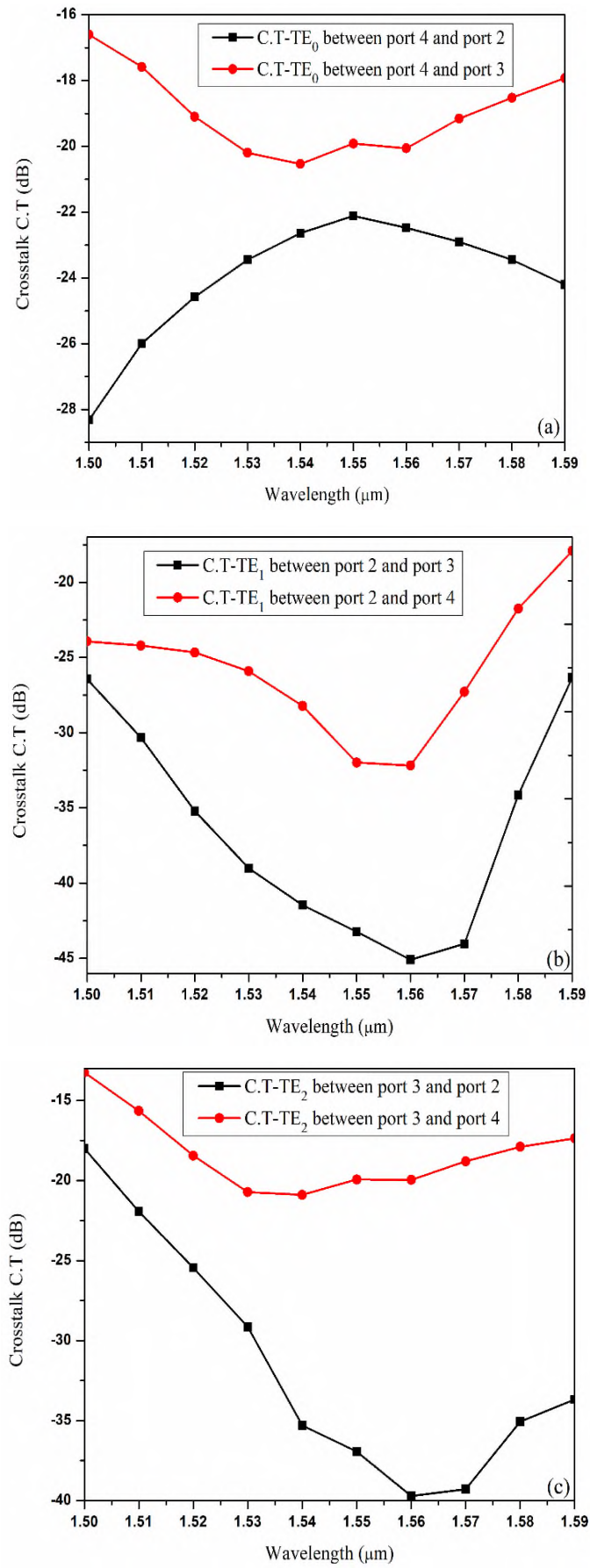


**Figure 2.14:** Crosstalk of the proposed structure, (a)TE<sub>0</sub>, (b) TE<sub>1</sub>, (c) TE<sub>2</sub>.

### 2.3.2. All-Subwavelength Grating Three-Mode (De)Multiplexer

In this subsection, the three-mode (de)multiplexer as shown in Figure 2.15 is designed and simulated completely utilizing subwavelength grating technology for further improvement in the performance to achieve wider bandwidth, while keeping control on the low loss compactness features obtained from the previously designed device. The proposed device is capable of the same demultiplexing operation described in the previous section. Note that the same waveguide structure is used in the design.

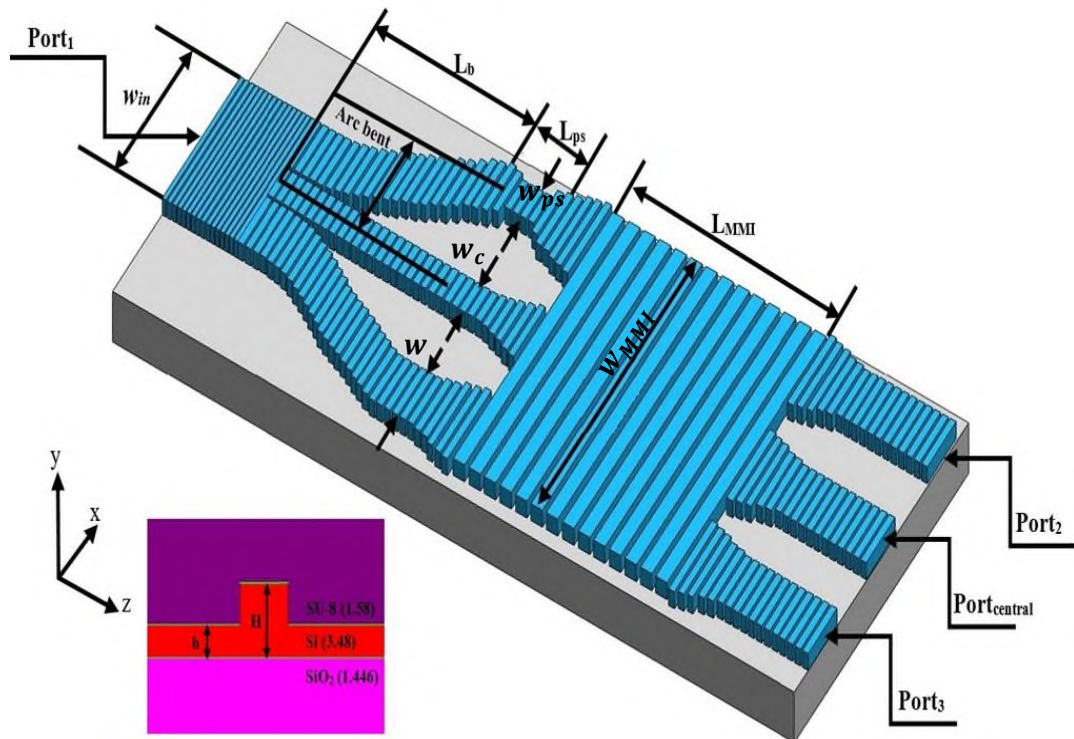


**Figure 2.15:** Schematic of the all-SWG 3-TE mode (de)multiplexer. The inset represents the waveguide cross-section.

#### 2.3.2.1 Device Dimensional Parameters Selection

Starting with the SWG-trident splitter to design wherein this device is identified by a set of parameters which are arms width, length, pitch length, and duty cycle denoted by  $w$ ,  $w_c$ ,  $L_t$ ,  $\Lambda_t$ , and  $D.C_t$ , respectively. To ensure

that mode splitting and guidance considered in the previously designed splitter are maintained, the widths of the splitter are set to  $0.5 \mu\text{m}$ , and  $0.25 \mu\text{m}$  corresponding to  $w$  and  $w_c$ , respectively. These values will be checked later after setting the SWG parameters of the splitter which are  $\Lambda_t$ , and  $D.C_t$ . The SWG parameters are chosen carefully so that smooth propagation of the optical field with maximum confinement within the waveguide, compactness, and ease of fabrication are guaranteed. Numerical simulation is conducted for this purpose and the result is depicted in Figure 2.16 which is the variation of the normalized transmission of the trident splitter in response to the variation of the duty cycle  $D.C_t$  for different values of pitch length  $\Lambda_t$ . From these results, it is clear that the desired splitter operation can be achieved when  $\Lambda_t$  is 150 or 160 nm with  $D.C_t$  extending over the range (60-75%), thus  $\Lambda_t$  and  $D.C_t$  are chosen to be 160nm, and 70%, respectively. Next, investigating the choice of arms width is serving the targeted operation through numerical simulation in each case of the input modes  $\text{TE}_0$  ( $\text{TE}_1$ ), and  $\text{TE}_2$ . The simulation result is shown in Figure 2.17 representing the normalized output power of the splitter as a function of arms width. This Figure confirms that the selected widths are perfect for the designed operation.

The final parameter to be selected is the arm's length  $L_t$  which needs to be set to a value where both compactness and the designed operation are guaranteed. A numerical simulation is conducted and the result is shown in Figure 2.18 which represents the variation of the normalized output power of the trident splitter as a function of arm's length changing over the range (5-30)  $\mu\text{m}$  for each case of the input modes, and it is clear that at  $L_t = 20 \mu\text{m}$  can be chosen since at this value the requirements mentioned earlier of compactness and good performance are satisfied.

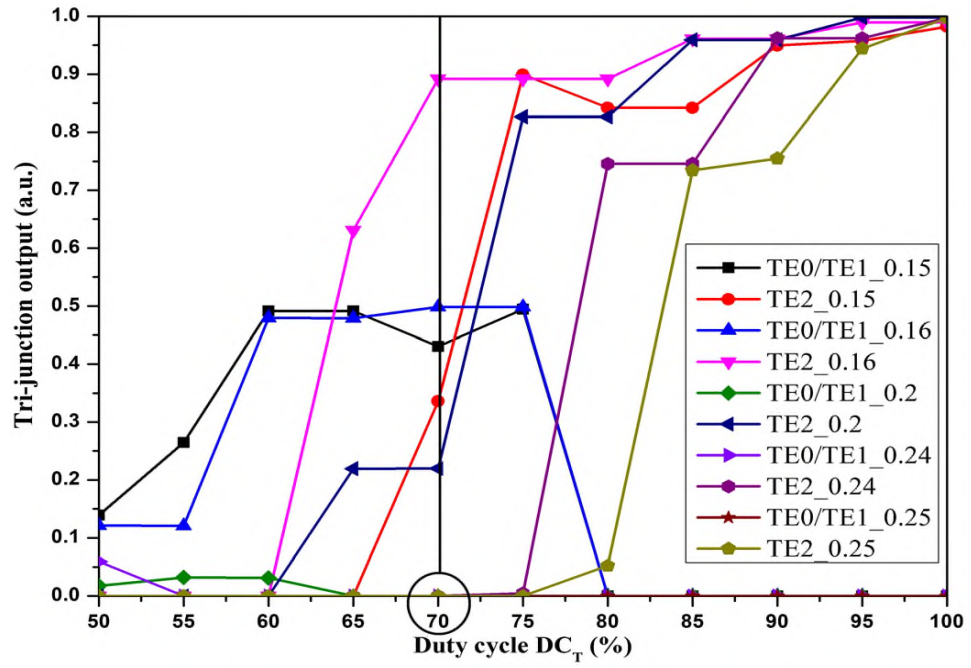


**Figure 2.16:** The Trident normalized output power vs.  $\Lambda_t$  and  $D.C_t$

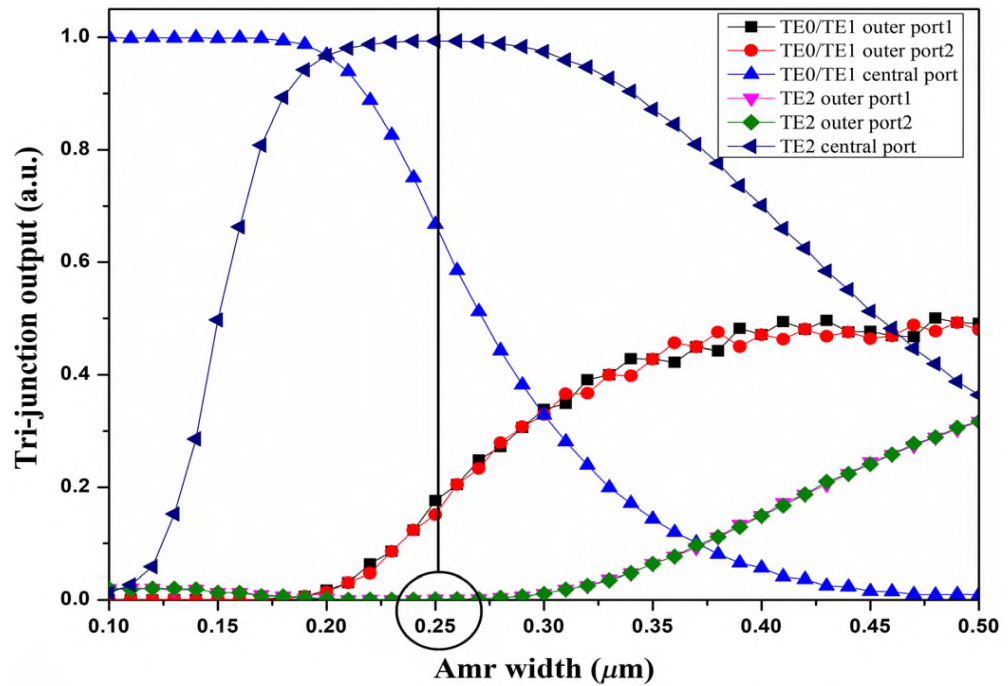


**Figure 2.17:** Trident normalized output power as a function of arm width.

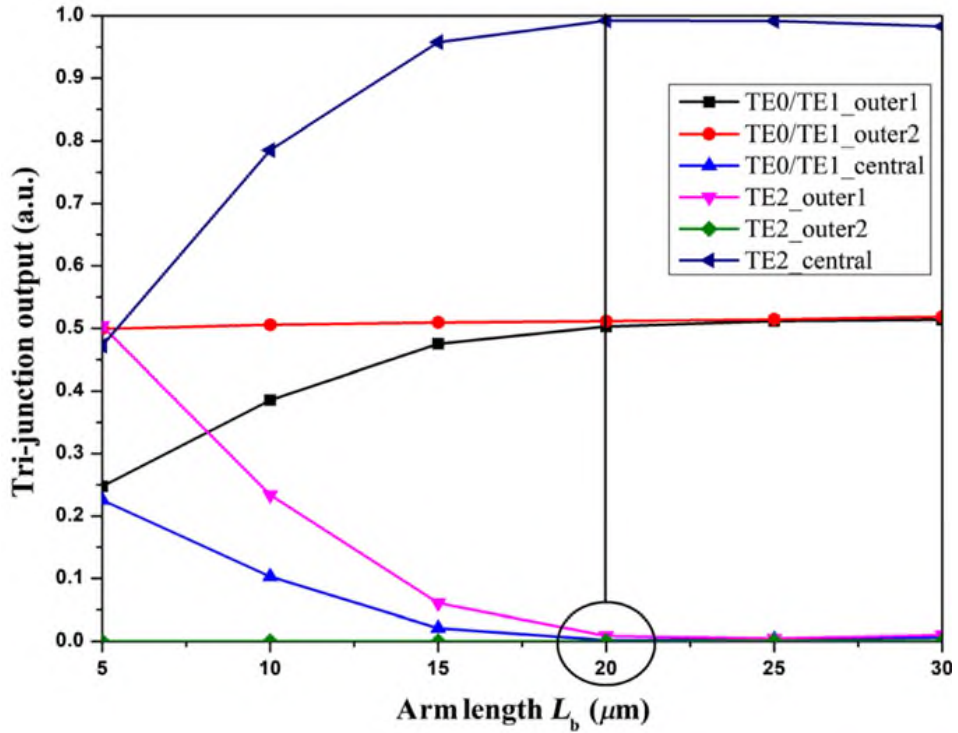


**Figure 2.18:** Trident normalized output power as a function of arm's length.

Moving forward to the next part of the device, which is the SWG-phase shifter. Note that in this device, the phase difference is given by equation (1.47). checking the formula, one can say that the main parameters representing such a phase shifter are the width, length, pitch length, and duty cycle denoted by  $w_{ps}$ ,  $L_{ps}$ ,  $\Lambda_{ps}$ , and  $D.C_{ps}$ , respectively. Note that the parameters  $\Lambda_{ps}$ , and  $D.C_{ps}$  are kept the same as that of the trident splitter for smooth field transition between device parts and design simplicity, and numerical simulation is conducted to design  $w_{ps}$  and  $L_{ps}$  only for the values to produce a  $\pi/2$  phase shift at the ends of the splitter. The simulation result is illustrated in Figure 2.19 where the phase difference as a function of  $w_{ps}$  for different values of  $L_{ps}$  is plotted and it shows clearly that there is flexibility in selecting these two parameters to achieve the target phase shift. In this device, it is suitable to set  $w_{ps}$ , and  $L_{ps}$  to 0.31 and 7  $\mu\text{m}$ , respectively. Another set of parameters can be considered for the  $\pi/2$  phase shift. For

example,  $w_{ps}$  and  $L_{ps}$  to 0.21 and 5  $\mu\text{m}$ , respectively, or  $w_{ps}$  and  $L_{ps}$  to 0.31 and 3  $\mu\text{m}$ , respectively, and so on.

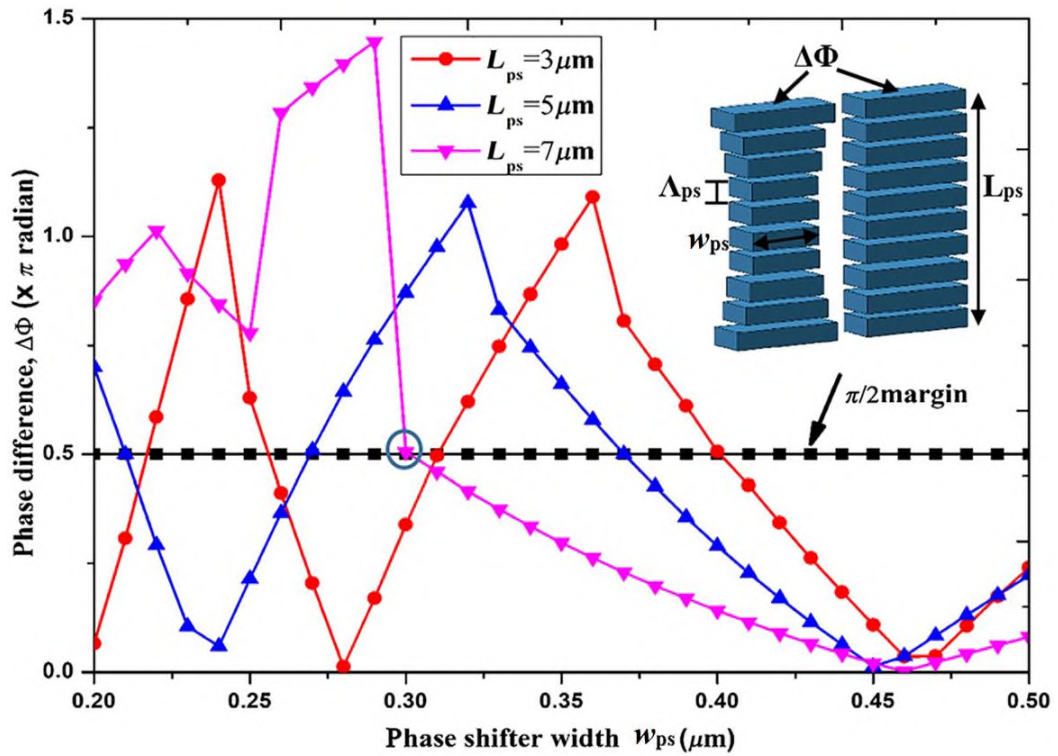


**Figure 2.19:** Phase shift difference variation of the SWG-PS with its width and length  $w_{ps}$  and  $L_{ps}$ , respectively.

The last part to design is the  $3 \times 3$  SWG-MMI coupler distinguished by its main parameters  $L_{MMI}$ ,  $w_{MMI}$ ,  $\Lambda_{MMI}$ , and  $D.C_{MMI}$ . The parameters  $w_{MMI}$ ,  $\Lambda_{MMI}$ , and  $D.C_{MMI}$  are set as 4  $\mu\text{m}$ , 0.2  $\mu\text{m}$ , and 50%, respectively. Numerical simulation is conducted to find the optimum value for the SWG-MMI length  $L_{MMI}$  at which the desired self-images described previously are obtained. The results presented in Figures 2.20 and 2.21 show the SWG-MMI coupler normalized output power variation as a function of the length  $L_{MMI}$  and the intensity distribution over the coupler for each case of input mode, respectively. These figures confirm that the desired coupler's operation is achieved at  $L_{MMI} = 45 \mu\text{m}$  (excluding access waveguides length).

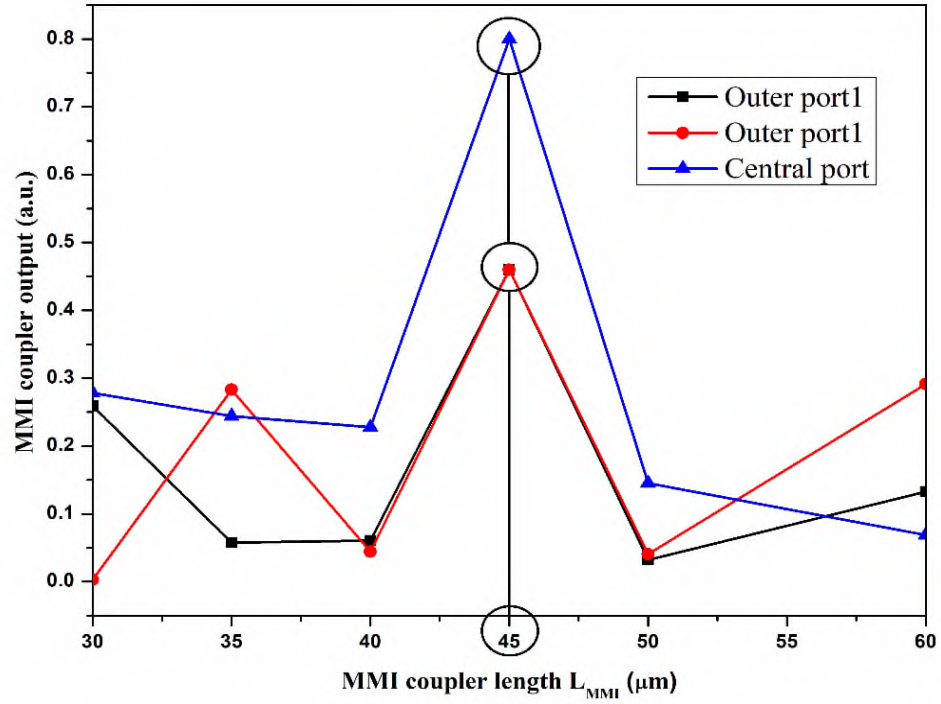


**Figure 2.20:** Coupler output variation in response to the change in coupler length  $L_{\text{MMI}}$ .

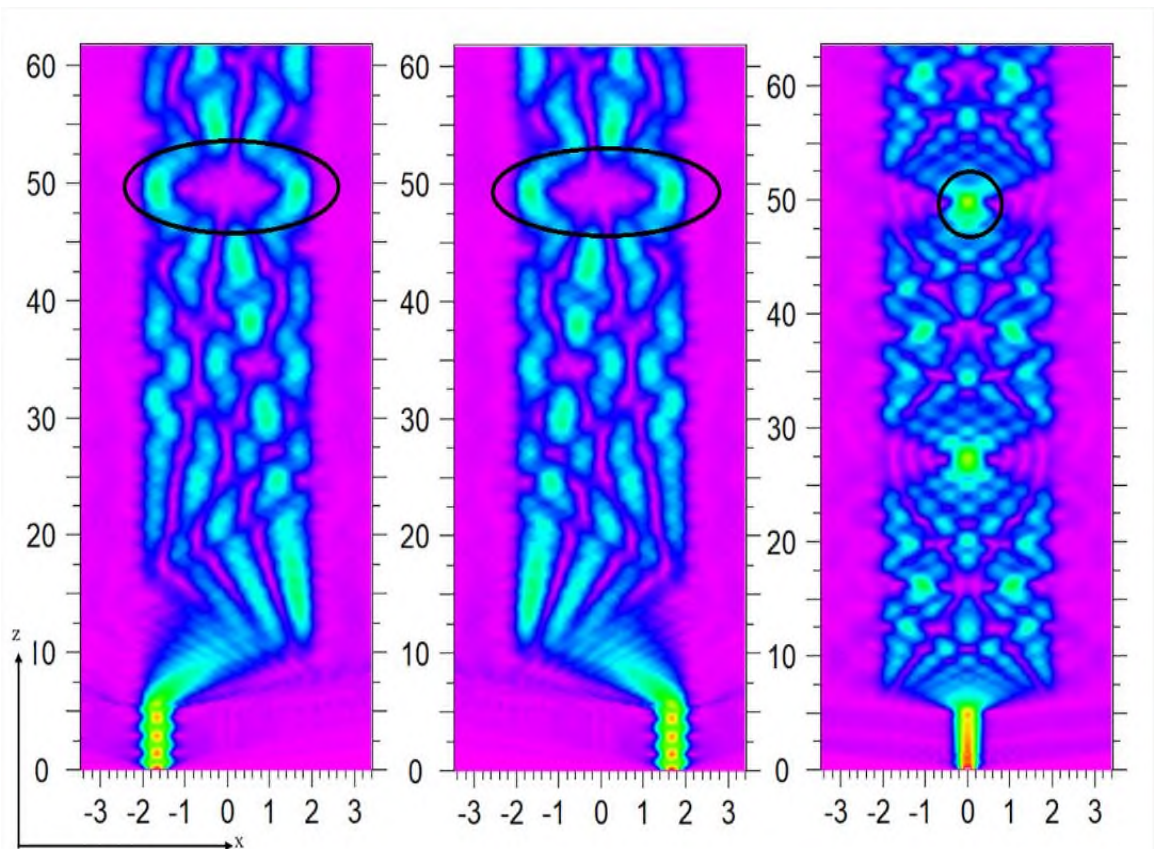


**Figure 2.21:** Optical field distribution along the SWG-MMI coupler: (a) upper edge (b) lower edge (c) center. Values on both axes are in  $\mu\text{m}$ .

A summary of the device's main geometrical parameters is given in Table 2.4. **The designed device's overall area is  $4 \times 95 \mu\text{m}^2$ .**

**Table 2.4.** Device main geometrical parameters for the proposed all-SWG (de)multiplexer.

Section	Parameter	Value ( $\mu\text{m}$ )	Description
Trident splitter	$w_{in}$	1.25	Input multimode waveguide width
	$w_o$	0.50	Outer arm width
	$w_c$	0.25	Central arm width
	$L_b$ (segments)	20 (125)	Arm length
	Arc bent	1.50	Bent
	$\Lambda_T$ ( $D.C_T$ )	0.16 (70%)	Trident pitch (Duty cycle)
Phase shifter	$w_{ps}$	0.31	Phase shifter width
	$L_{ps}$ (segments)	7 (40)	Phase shifter length
	$\Lambda_{ps}$ ( $D.C_{ps}$ )	0.16 (70%)	Shifter pitch (Duty cycle)
SWG-MMI coupler	$w_{MMI}$	4	Coupler width
	$w_a$	0.80	Access waveguide width
	$L_a$ (segments)	5 (25)	Coupler ports length (segments)
	$L_{MMI}$ (segments)	45 (225)	Coupler length (segments)
	$\Lambda_{MMI}$ ( $D.C_{MMI}$ )	0.20 (50%)	MMI pitch (Duty cycle)

### 2.3.2.2 Device Performance Evaluation

The optical conversion performance of the proposed device is verified using the Rsoft photonics CAD suit. Figure 2.22 depicts the demultiplexing operation for each of the input modes  $TE_0$ ,  $TE_1$ , and  $TE_2$  at the input end guided to the corresponding output port successfully. It is worth saying that the device can act as a multiplexer generating the designed modes from the fundamental mode  $TE_0$  as an input mode as shown in Figure 2.23.

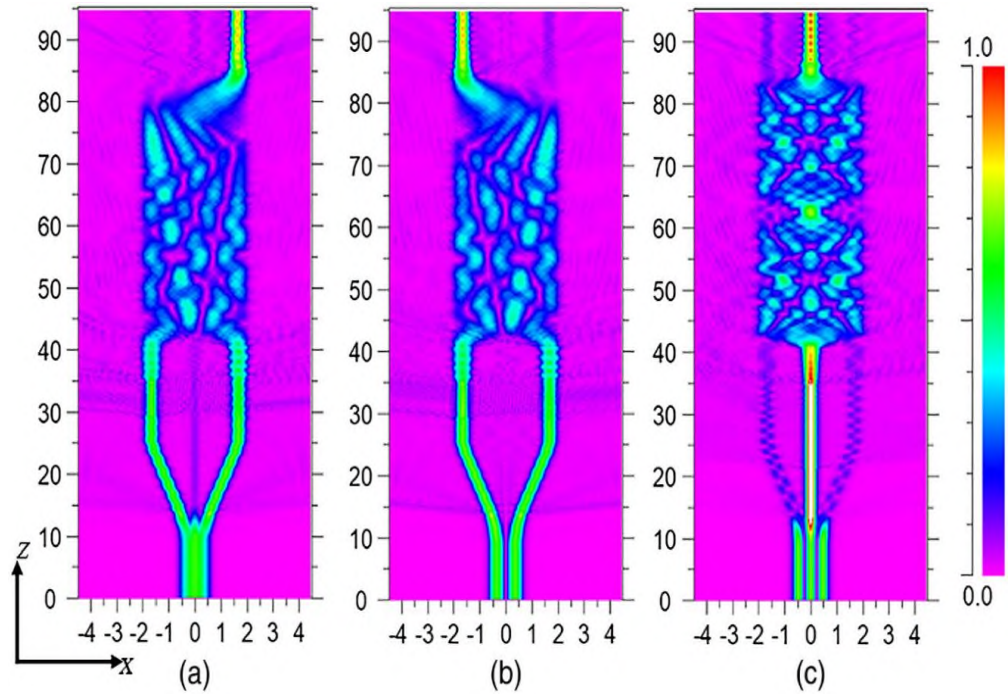


**Figure 2.22:** Optical field distribution of the proposed device when operating as a demultiplexer for the input mode (a) TE<sub>0</sub>, (b) TE<sub>1</sub>, (c) TE<sub>2</sub>. Values on both axes are in  $\mu\text{m}$ .

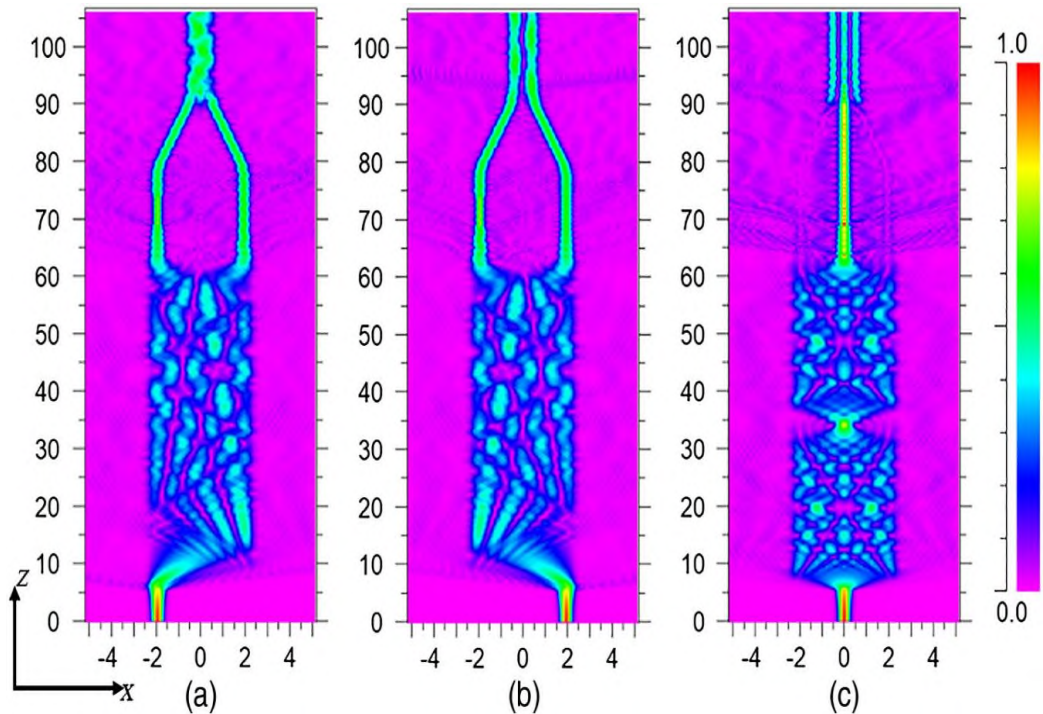


**Figure 2.23:** Optical field distribution of the proposed device when operating as a multiplexer for the input mode (a) TE<sub>0</sub>, (b) TE<sub>1</sub>, (c) TE<sub>2</sub>. Values on both axes are in  $\mu\text{m}$ .

The mode transverse cross-section profile at the input and output ends for both operations also confirm both operations of the designed device, as shown in Figure 2.24. The left and right are the input and output modes, respectively.

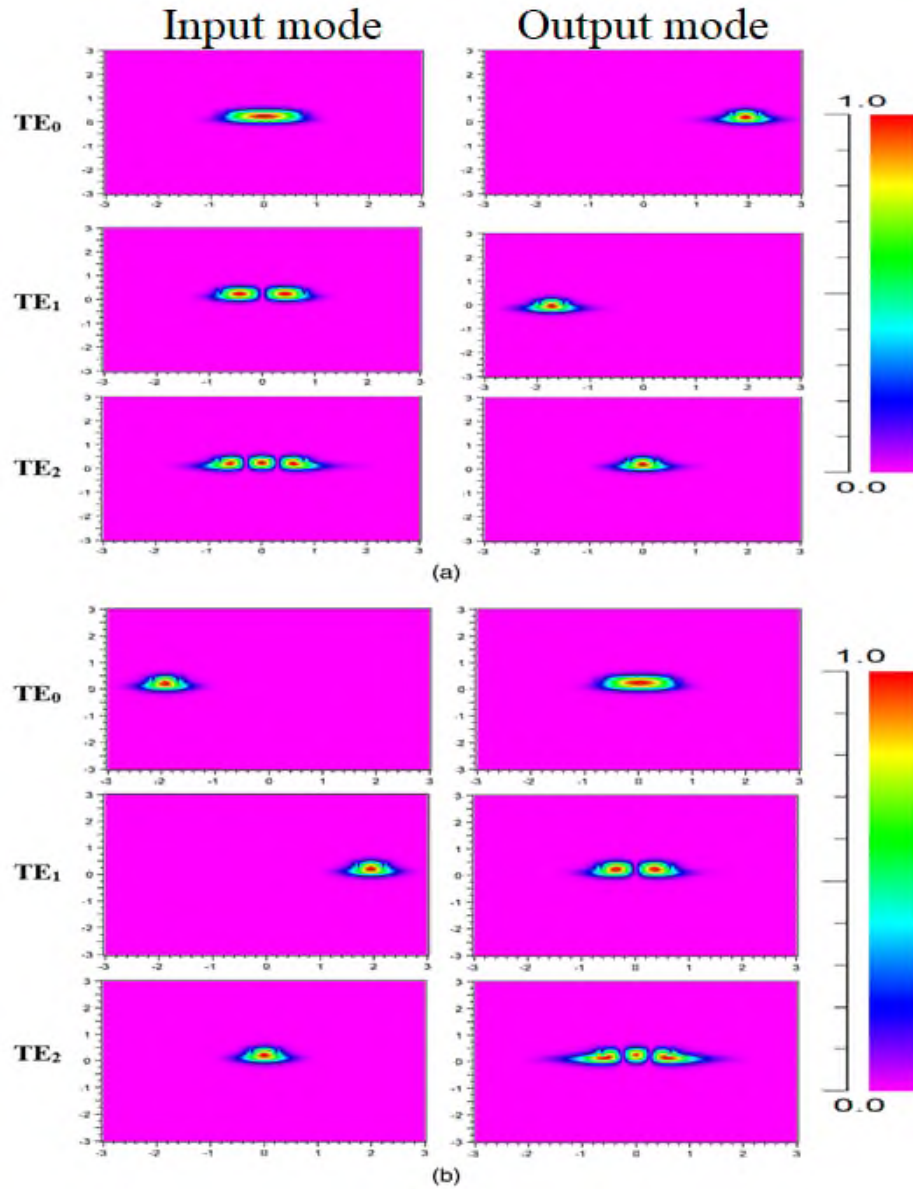


**Figure 2.24:** Transverse field profile of all-SWG  
(a) demultiplexer, (b) multiplexer.

The performance of the proposed device is evaluated through insertion loss ( $I.L$ ) and crosstalk ( $C.T$ ) parameters assessment using equations (2.21) and (2.22), respectively. The result is depicted in Figures 2.25 and 2.26. These

Figures show the calculated insertion loss and crosstalk as a function of the operating wavelength of the input mode extending over the range (1.470-1.630)  $\mu\text{m}$ , thus the 3-dB operating bandwidth is 160 nm. Table 2.5 gives device insertion loss and crosstalk at the design wavelength of 1.55  $\mu\text{m}$ .

**Table 2.5.** (De)multiplexer insertion loss and crosstalk at  $\lambda = 1.55 \mu\text{m}$ .

Parameter	TE <sub>0</sub> mode	TE <sub>1</sub> mode	TE <sub>2</sub> mode
I.L (dB)	-1.28	-1.38	-1.02
C.T (dB)	-25.02	-40.3	-25.7

A performance comparison between the proposed device with related (de)multiplexing devices in [73] and [86] and the reported designed SWG-assisted device reported in the thesis. The comparison results are listed in Table 2.6. The proposed device offers low losses. The operating bandwidth of the proposed device is 160 nm which means that the designed (de)multiplexer has 4 times wider bandwidth compared with these devices. It can be noticed that the designed device shows the minimum footprint among them too.

**Table 2.6** Performance comparison of the designed device with the previously reported devices.

Ref#	Structure	B.W ( $\mu\text{m}$ )	C.T(dB)	I.L(dB)	Area ( $\mu\text{m}$ ) <sup>2</sup>
73	2-TE mode Conventional (de)multiplexer	1.530-1.570	<-15	>-1.00	3×44
86	3-TE mode Conventional (de)multiplexer	1.525-1.565	<-17	>-0.90	5×400
This work (SWG-assisted device)	3-TE SWG- assisted (de)multiplexer	1.490-1.610	< -5	> -1.0	4.5×120
This work	3-TE-mode All-SWG (de)multiplexer	1.470-1.630	<-16	>-1.38	4×95

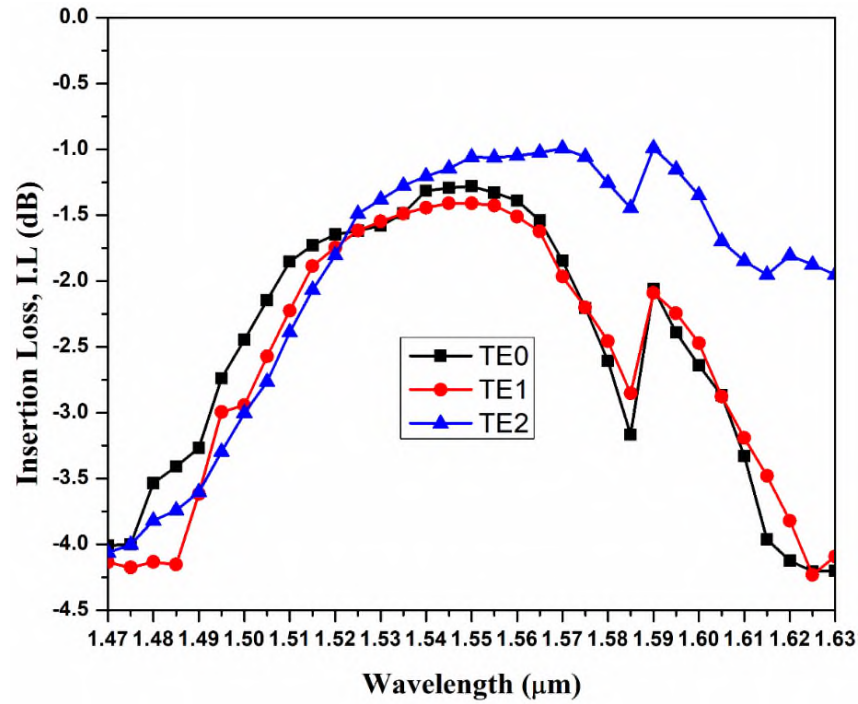


**Figure 2.25:** Insertion loss spectrum of the proposed all-SWG (de)multiplexer.

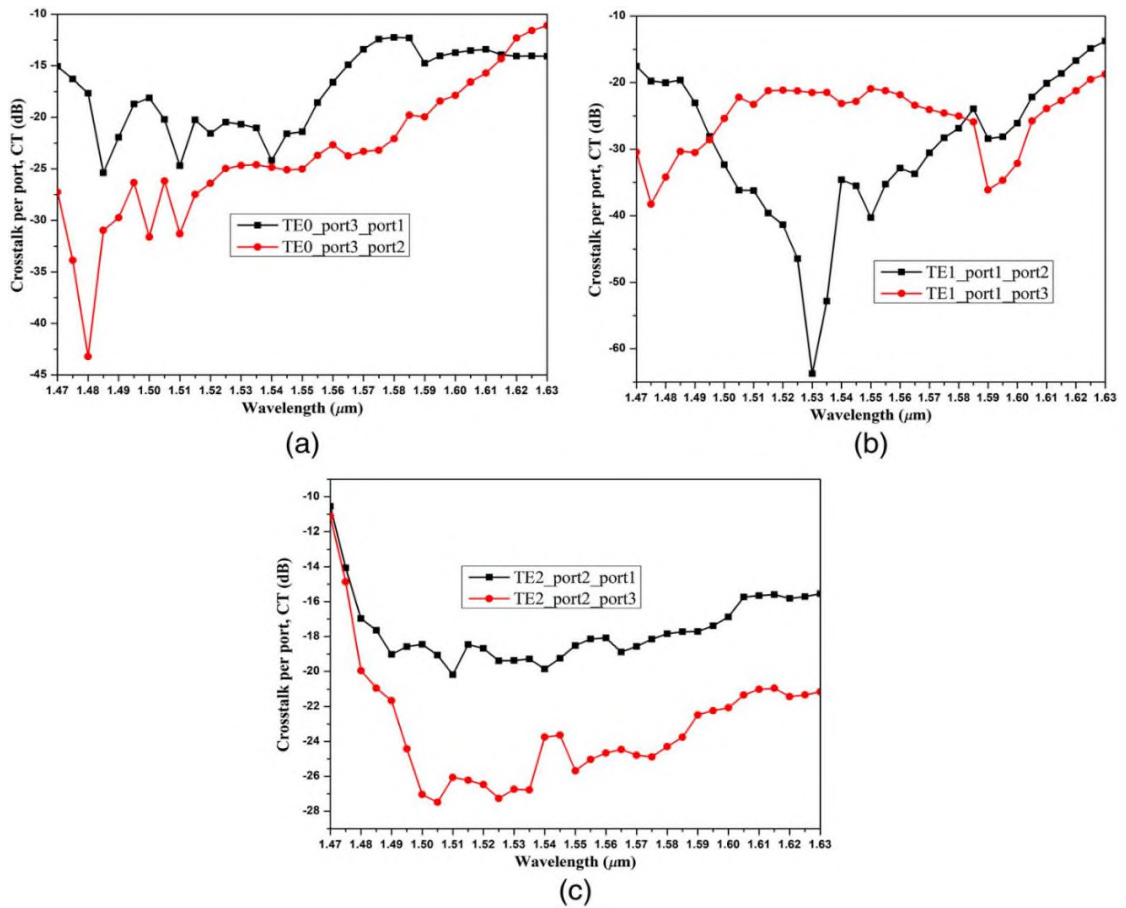


**Figure 2.26:** Crosstalk per port of the proposed all-SWG (de)multiplexer when excited by: (a)  $TE_0$ , (b)  $TE_1$ , (c)  $TE_2$ .

### 2.3.3. Operation Bandwidth Extension

This subsection presents how the designed devices are modified so that they can cover other optical communication wavelength bands e.g. O+C band, and C+L band while keeping the main demultiplexing operation and losses unchanged.

#### 2.3.3.1 O+C/C+L Band Operating (De)multiplexer

First, the device introduced in Figure 2.4 is modified to operate at the O+C bandwidth with wavelength extending over the range (1.260-1.565)  $\mu\text{m}$ , and central wavelength at  $\lambda=1.4125 \mu\text{m}$ . Based on equation (1.26), the shorter the wavelength is the longer the beat length becomes, and as a result, a longer SWG-MMI coupler is required while keeping the other parts of the (de)multiplexer the same of  $L_{MMI} = 65 \mu\text{m}$ . Figure 2.27 shows the optical field distribution of the guided mode across the new (de)multiplexer for each case of the input modes.

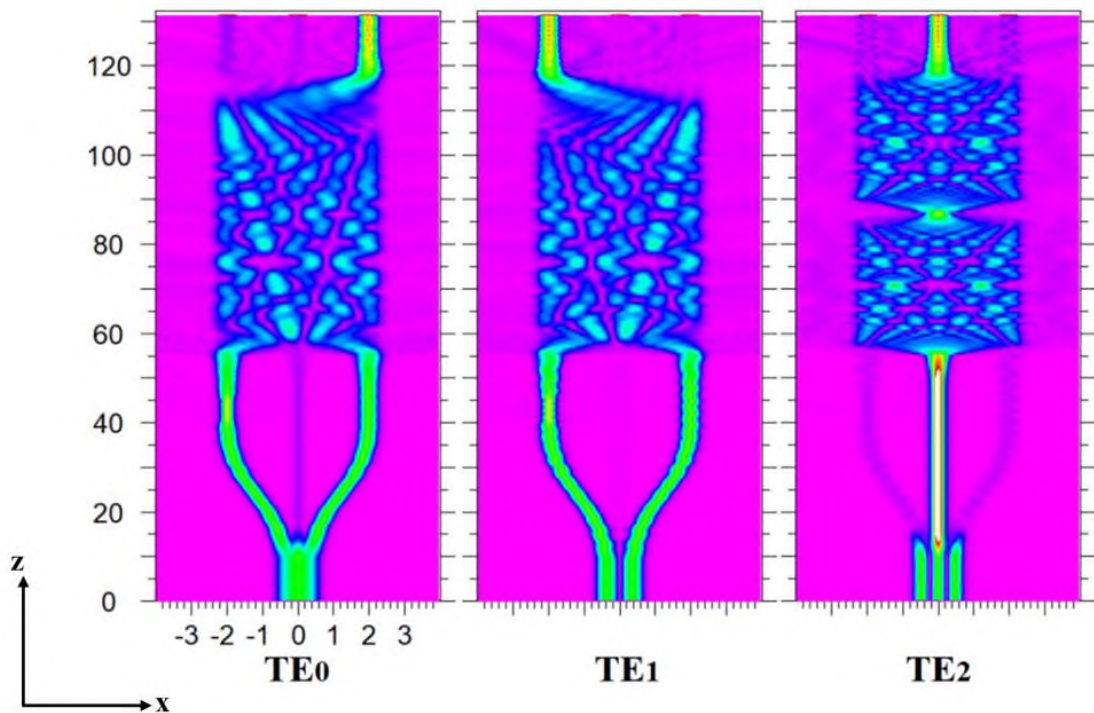


**Figure 2.27:** Optical field distribution of the guided mode along the O+C (de)multiplexer when the input mode is (a)  $TE_0$ , (b)  $TE_1$ , (c)  $TE_2$ . Values on both axes are in  $\mu\text{m}$ .

Next, the same concept is applied to employ this device to operate at the C+L bandwidth where the wavelength extends over the range (1.530-1.625)  $\mu\text{m}$ , and the central wavelength is  $\lambda=1.5775 \mu\text{m}$ . Note that the required SWG-MMI coupler is almost the same as the previously designed coupler with  $L_{MMI}=55 \mu\text{m}$ . Figure 2.28 shows the optical field distribution of the guided mode across the new (de)multiplexer for each case of the input modes. It is important to mention that the insertion loss and crosstalk are kept as minimum as possible for both devices.

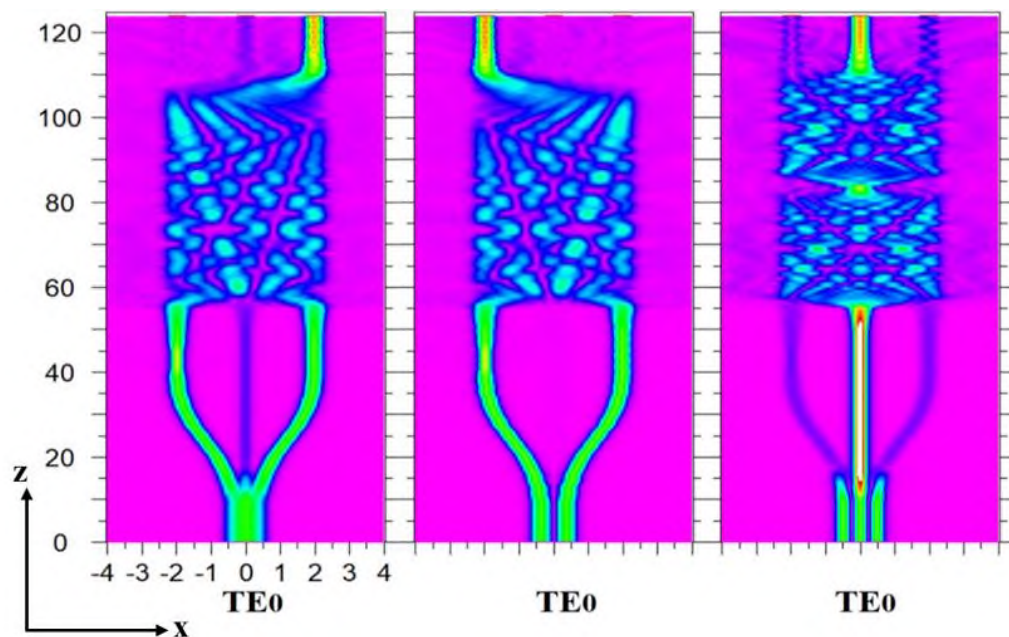


**Figure 2.28:** Optical field distribution of the guided mode along the C+L (de)multiplexer when the input mode is (a)  $TE_0$ , (b)  $TE_1$ , (c)  $TE_2$ . Values on both axes are in  $\mu\text{m}$ .

### 2.3.3.2 C+L Band Operating All-SWG (De)multiplexer

In MDM applications, it is required to design devices that operate over a wide bandwidth, i.e. extending the bandwidth to a range beyond the C-band towards the L-band allowing the use of current technologies to be used over the C+L band with no need to add new hardware resources. The reason for considering the L-band is both C and L bands' attenuation losses are almost the same, also the erbium-doped fiber amplifier can be tuned easily to

operate for the new C+L band. Based on the 100 GHz ITU wavelength grid issued for WDM, the L- and C- band covers 10 THz. The L-band covers 50 channels from 190.9 THz (1.57041  $\mu\text{m}$ ) to 186 THz (1.61178  $\mu\text{m}$ ), while The C-band covers 50 channels too, starting from 195.9 THz (1.53033  $\mu\text{m}$ ) to 191 THz (1.56959  $\mu\text{m}$ ). Thus C+L starts from 1.53033-1.61178  $\mu\text{m}$  with a central wavelength of 1.56959  $\mu\text{m}$  which is the new wavelength of the proposed device of the scheme shown in Figure 2.29. The SWG segments are of thickness  $a_i$  with duty cycle  $D.C = a_i/\Lambda_i$ . To satisfy the desired operation, numerical simulation is conducted for the optimum splitter dimensions including arm's widths, length, and pitch (duty cycle), denoted by  $w_1$ ,  $w_2$ ,  $L_s$ , and  $\Lambda_s$  ( $D.C$  %), respectively. The results are depicted in Figure 2.30 (a-c), which shows the normalized transmission of the splitter as a function of each of these parameters. Based on the results, the parameters can be set to 0.5  $\mu\text{m}$ , 0.27  $\mu\text{m}$ , 25  $\mu\text{m}$ , and 0.16 (70%)  $\mu\text{m}$  for  $w_1$ ,  $w_2$ ,  $L_s$ , and  $\Lambda_s$  ( $D.C$  %), respectively.

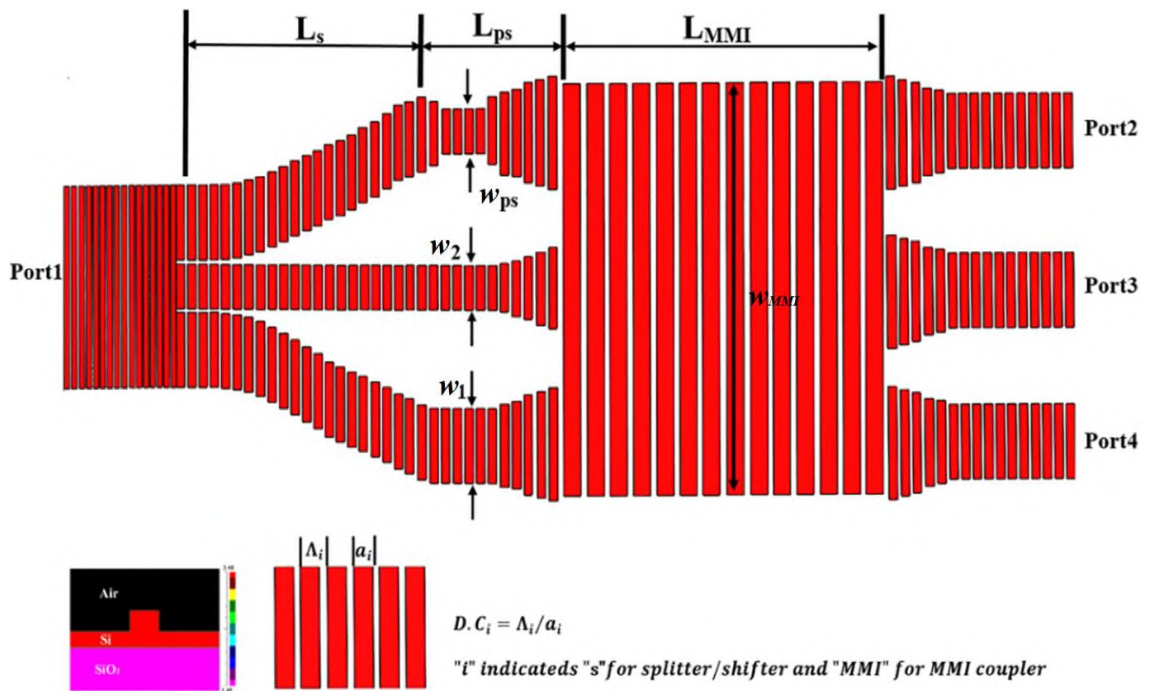


**Figure 2.29:** Schematic diagram of the C+L Band all-SWG (de)multiplexer. The inset is waveguide cross-section and SWG details.

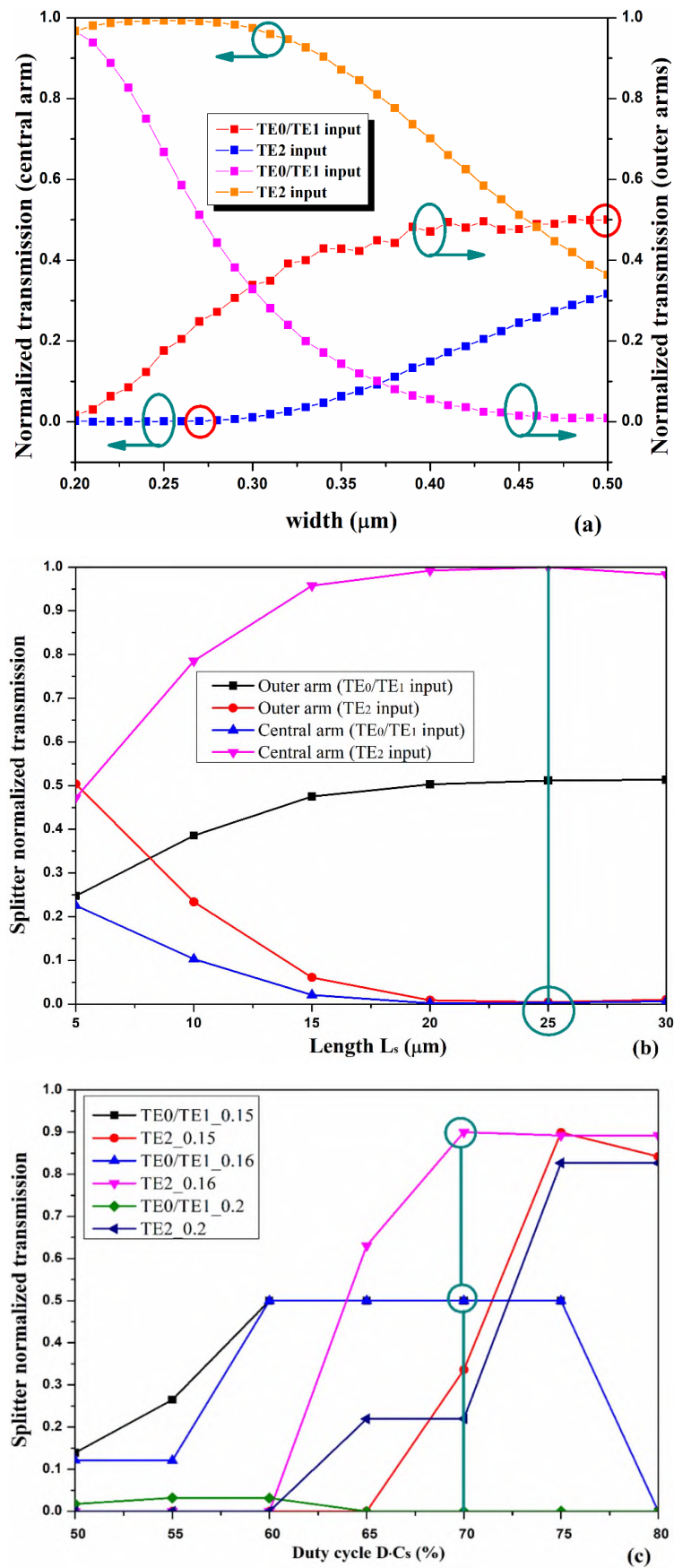


**Figure 2.30:** Splitter transmission as a function of arms (a) width (b) length (c) duty cycle.

Next, designing the dimensions of the shifter are which is distinguished by its main parameters, the length  $L_{ps}$  which is set to  $3 \mu\text{m}$  for compactness purposes, and the width  $w_{ps}$  chosen through numerical simulation to achieve a  $\pi/2$  phase shift. Figure 2.31 depicts the phase variation with the change of  $w_{ps}$ . The desired shift is achieved where  $w_{ps} = 0.31 \mu\text{m}$ .

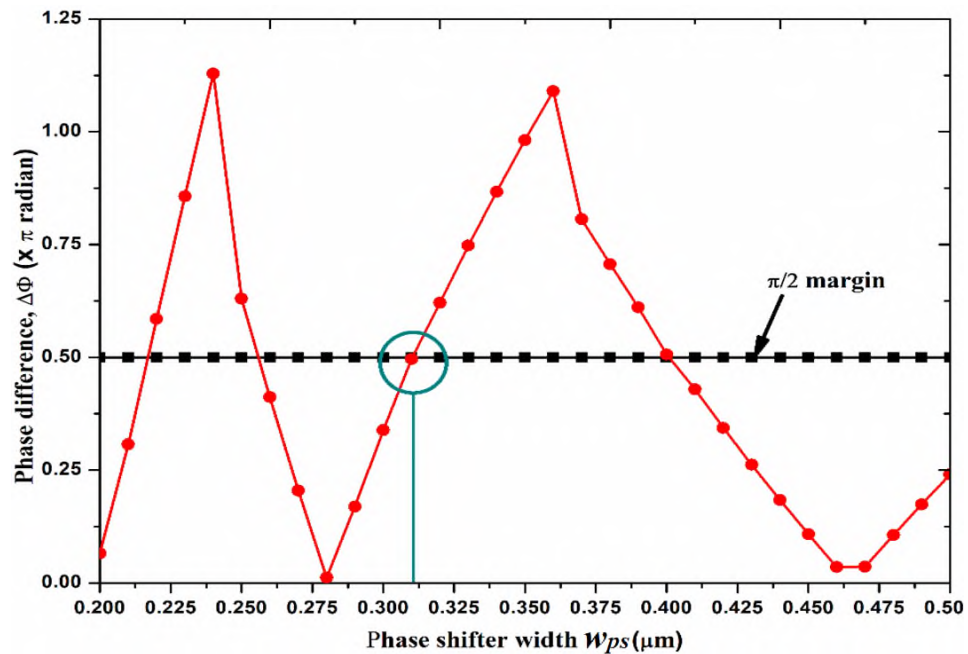


**Figure 2.31:** Phase difference as a function of shifter width  $w_{ps}$ .

The final section to be designed is the  $3 \times 3$  SWG-MMI coupler which acts as a 3-dB splitter for the case of  $\text{TE}_0$  and  $\text{TE}_1$  mode, and in the case of  $\text{TE}_2$  mode, it guides the field from the central input port to the central output port. This section is parameterized via three main parameters which are MMI length  $L_{MMI}$ , width  $w_{MMI}$ , pitch length  $\Lambda_{MMI}$  to satisfy these requirements. Initially,  $w_{MMI}$  and  $\Lambda_{MMI}$  (D.C %) are set to  $4 \mu\text{m}$ , and  $0.2 \mu\text{m}$  (50%). Numerical simulation is conducted to obtain the value of  $L_{MMI}$  where the described operation is satisfied. Figure 2.32 shows the normalized transmission of the SWG-MMI coupler in response to the change in its length. The results show that the suitable  $L_{MMI}$  value is  $45 \mu\text{m}$ .

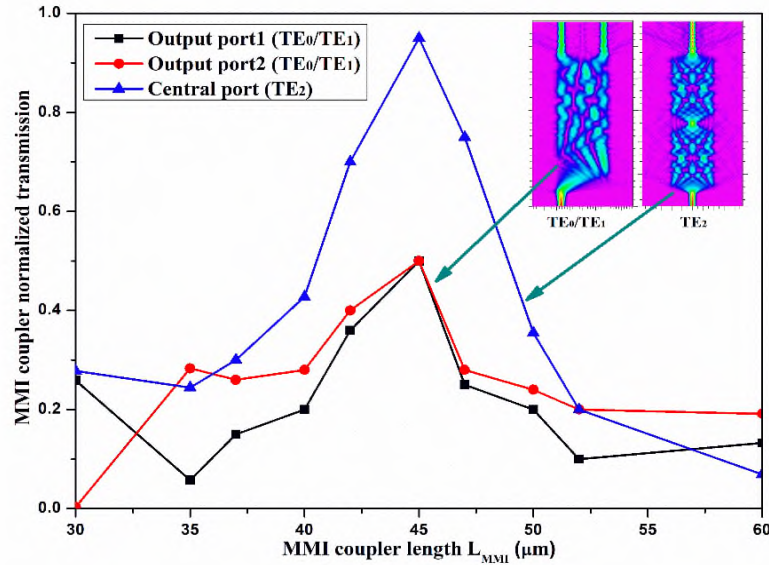


**Figure 2.32:** Coupler transmission as a function of the length  $L_{MMI}$ .

A numerical simulation is carried out to monitor the intensity distribution over the (de)multiplexer for each case of input modes at the operating wavelengths  $\lambda_{light} = 1.5696 \mu\text{m}$ ,  $1.5303 \mu\text{m}$ , and  $1.6118 \mu\text{m}$ , the results are shown in Figures 2.33, 2.34, and 2.35, respectively.

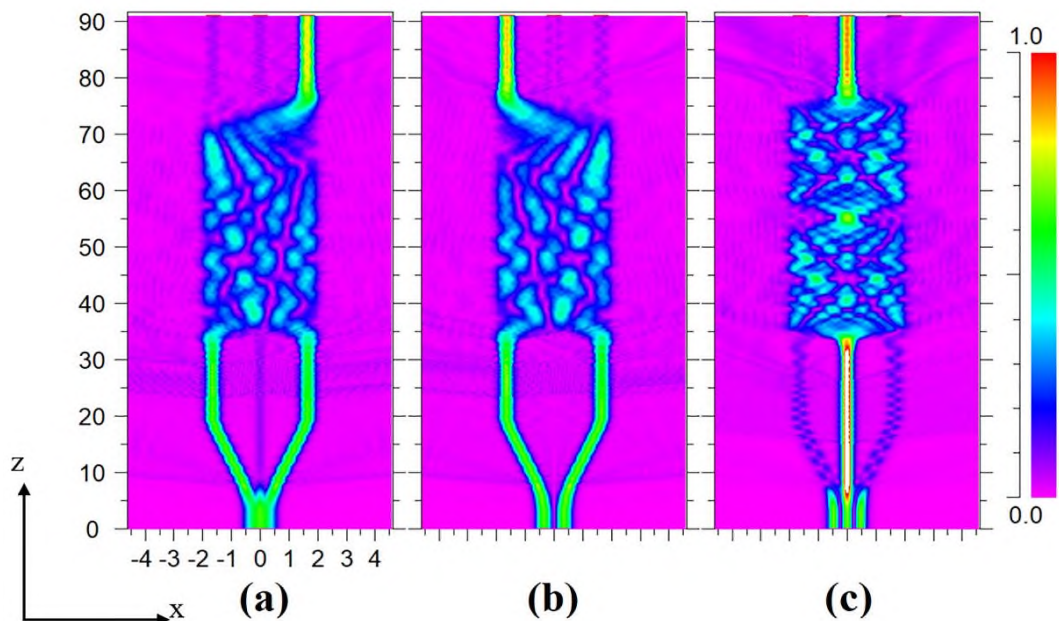


**Figure 2.33:** Intensity distribution across the C+L band all-SWG (de)multiplexer at  $1.5696 \mu\text{m}$  for input mode (a) TE<sub>0</sub>, (b) TE<sub>1</sub>, (c) TE<sub>2</sub>. Values on both axes are in  $\mu\text{m}$ .

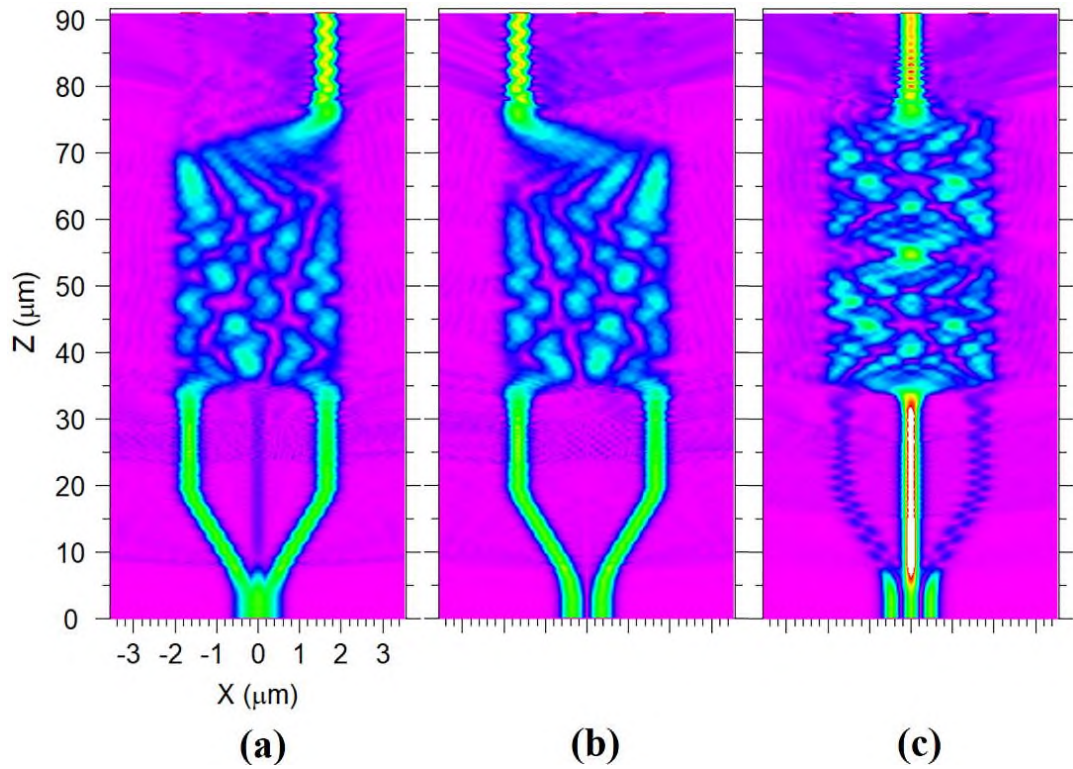


**Figure 2.34:** Intensity distribution across the C+L band all-SWG (de)multiplexer at  $1.5303 \mu\text{m}$  for input mode (a)  $\text{TE}_0$ , (b)  $\text{TE}_1$ , (c)  $\text{TE}_2$ . Values on both axes are in  $\mu\text{m}$ .

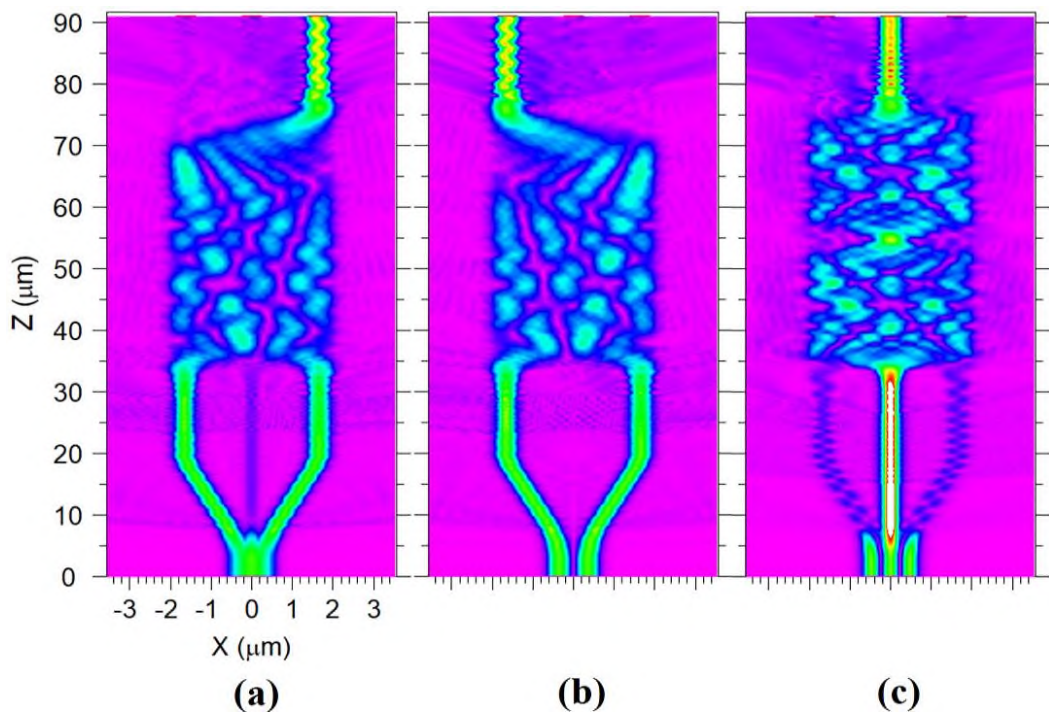


**Figure 2.35:** Intensity distribution across the C+L band all-SWG (de)multiplexer at  $1.6118 \mu\text{m}$  for input mode (a)  $\text{TE}_0$ , (b)  $\text{TE}_1$ , (c)  $\text{TE}_2$ . Values on both axes are in  $\mu\text{m}$ .

To evaluate the performance of the device, equations (2.21) and (2.22) are revisited to calculate the insertion loss (I.L), and crosstalk (C.T) dependency on the operating wavelength of the injected light. The results are presented in Figure 2.36.

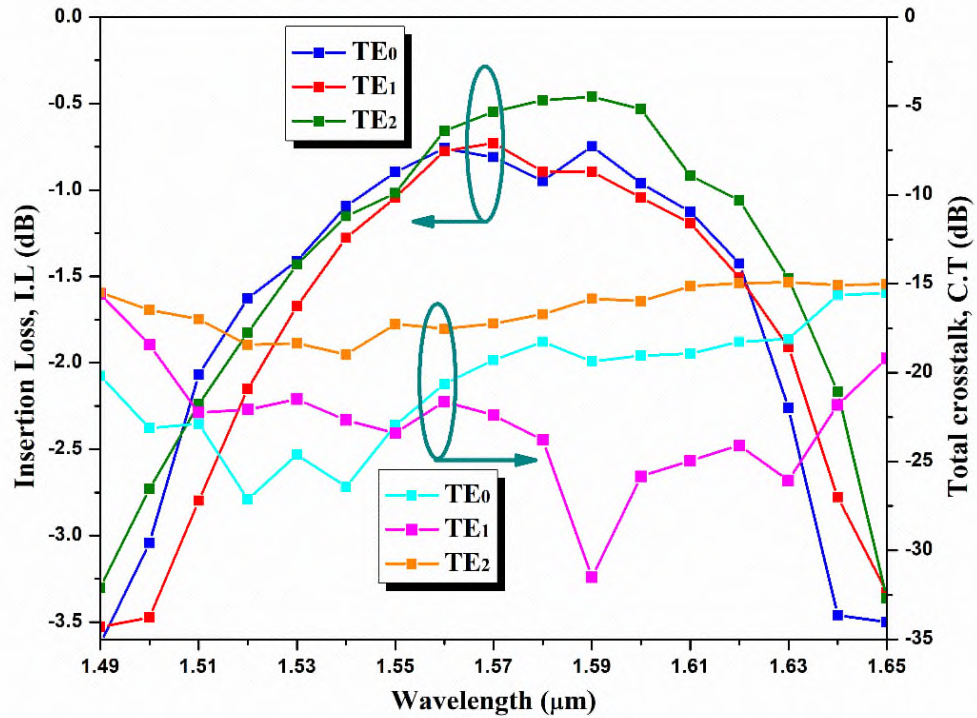


**Figure 2.36:** Device performance dependency on operating wavelength.

Table 2.7 lists the insertion loss and crosstalk readings of the proposed device for each of the input modes at the wavelengths 1.5303, 1.5696, and 1.6118  $\mu\text{m}$  which shows that the designed device offers performance with losses  $> -1.7$  dB and crosstalk lower than  $-17$  dB over the C+L band.

**Table 2.7** Device performance indicators for the C+L band all-SWG (de)multiplexer.

wavelength ( $\mu\text{m}$ )	I.L (dB)			C.T (dB)		
	TE <sub>0</sub>	TE <sub>1</sub>	TE <sub>2</sub>	TE <sub>0</sub>	TE <sub>1</sub>	TE <sub>2</sub>
1.5303	-1.4	-1.7	-1.4	-24	-23	-18
1.5696	-0.8	-0.73	-0.55	-19.3	-22.4	-17.3
1.6118	-1.17	-1.2	-1	-18	-25	-15

## 2.4 Proposed Four-TE Mode (De)multiplexer

This section presents the design and performance evaluation of the proposed 4-mode (de)multiplexer utilizing two different Si/SiO<sub>2</sub> platforms, first, the conventional waveguide, and second, the SWG-assisted waveguide.

### 2.4.1 Conventional Four-Mode (De)multiplexer

The first device is shown in Figure 2.37 which is the conventional 4-mode (de)multiplexer designed using a strip waveguide. It supports four input modes TE<sub>0</sub>, TE<sub>1</sub>, TE<sub>2</sub>, and TE<sub>3</sub>, and the structure consists of three main parts, a 1×4 beam splitter, a 4×4 MMI coupler, and two  $\pi/2$  phase shifters inserted at certain arms of the splitter to achieve the desired (de)multiplexing function. The waveguide structure is a rib/ridge based on the SOI platform with Si, SiO<sub>2</sub>, and air, as core, substrate, and cover materials with refractive indices at the operating wavelength of 1.55  $\mu\text{m}$  are 3.46, 1.45, and 1, respectively.

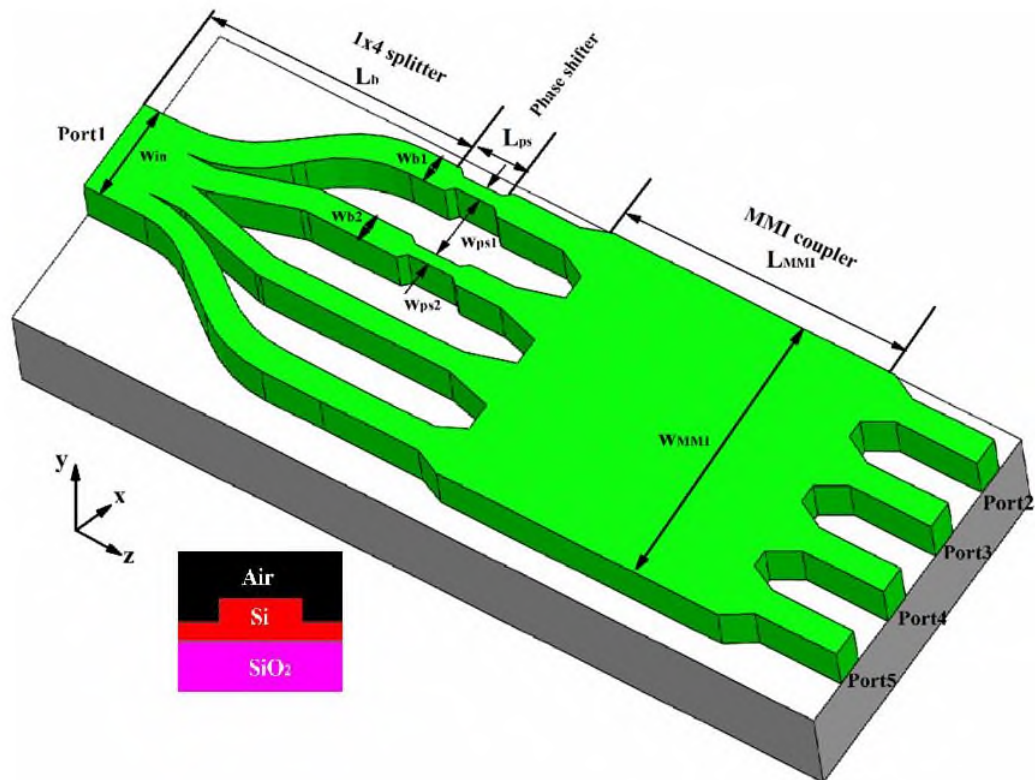


**Figure 2.37:** Conventional 4-TE mode (de)multiplexer scheme.

The demultiplexing operation can be described in two cases:

- a) If  $TE_0$  ( $TE_1$ ) mode is injected into the main stem, the mode is split and guided through the outer arms of the splitter, and the output is observed through port5 (port2) of the MMI coupler.
- b) If  $TE_2$  ( $TE_3$ ) mode, the mode is guided through the inner arms of the splitter, and the output is observed through port4 (port3) of the MMI coupler.

The parameters of each part to satisfy the desired operation are selected through numerical simulation. Starting with the  $1 \times 4$  splitter section which comprises the main stem of width  $w_{in}$  and four S-bend arms of length  $L_b$  attached to it. The outer arms are of width  $w_{b1}$ , and the inner ones of width  $w_{b2}$ . The splitter is designed to act as a 3-dB splitter where it splits the input mode between a specific set of arms equally. A numerical simulation is conducted for the splitter normalized transmission as a function of widths and length is carried out for the values where the desired operation is achieved and the results are depicted in Figures 2.38 (a and b). It is obvious that for the required splitter operation the widths  $w_{b1}$ ,  $w_{b2}$ , and  $w_{in}$  can be set to  $0.5 \mu\text{m}$ ,  $0.3 \mu\text{m}$ , and  $1.3 \mu\text{m}$ , respectively. Also the length  $L_b$  set to  $70 \mu\text{m}$ .

Next is to design two passive phase shifters both of equal length  $L_{ps}$  with widths denoted by  $w_{ps1}$ , and  $w_{ps2}$  corresponding to shifter 1 and shifter 2, respectively. Note that the length  $L_{ps}$  is set to  $(3 \mu\text{m})$  and numerical simulation is carried out for the optimum width  $w_{ps}$  at which the desired phase shift  $\pi/2$  is obtained. The result is depicted in Figure 2.39 where it is clear that  $w_{ps1}$  and  $w_{ps2}$  can be set to  $0.3 \mu\text{m}$  and  $0.22 \mu\text{m}$ , respectively.

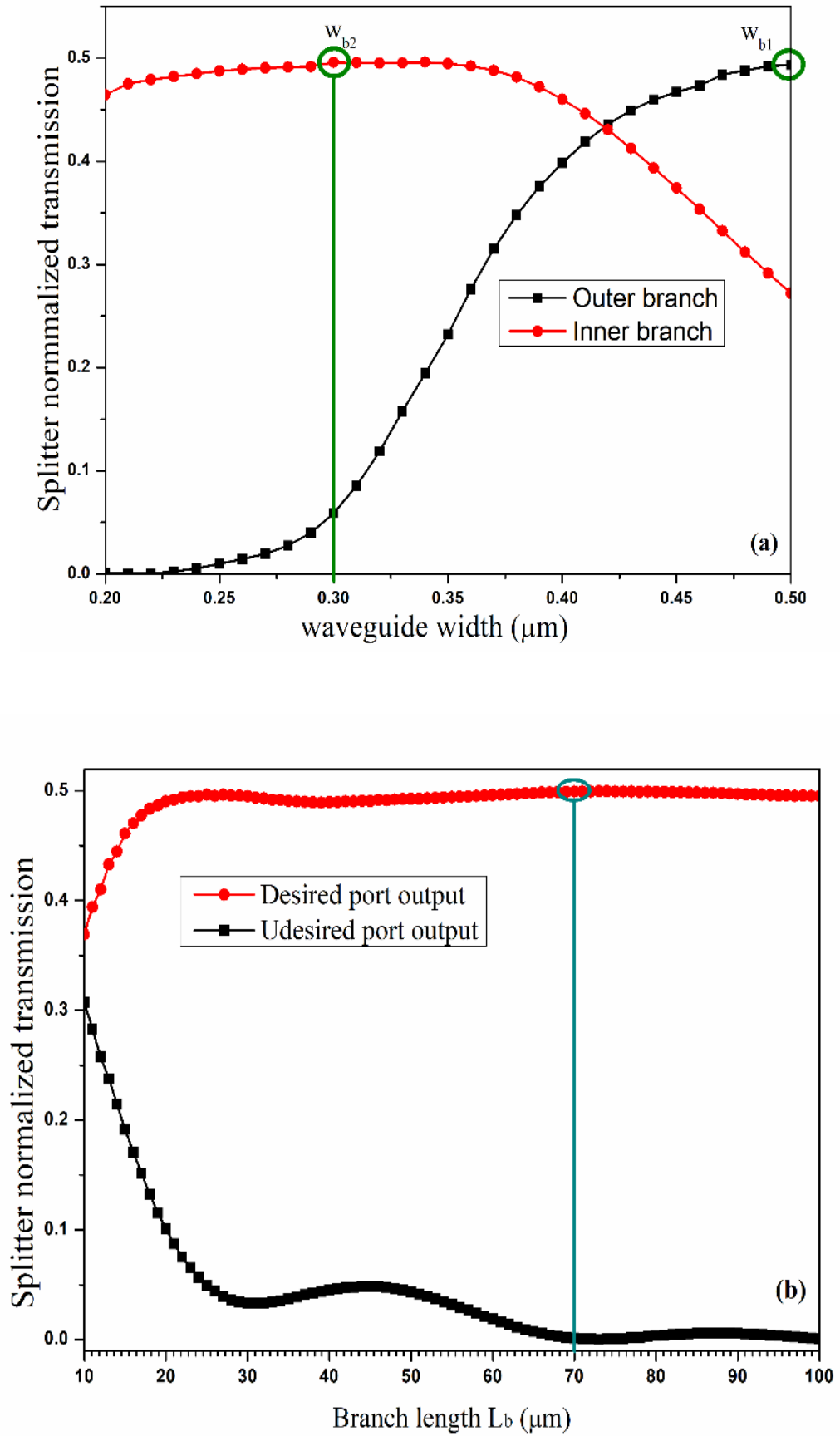


**Figure 2.38:** Splitter transmission evolution as a function of the branch (a) width (b) length.

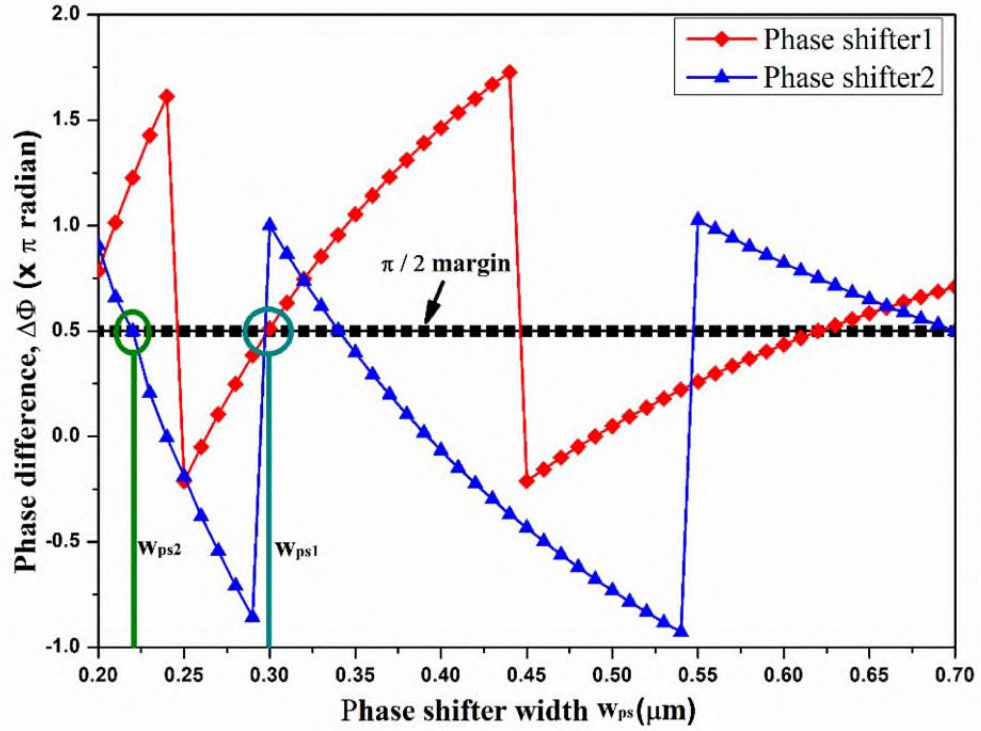


**Figure 2.39:** Phase difference as a function of the width  $w_{ps}$  for a phase shifter designed with  $L_{ps} = 3 \mu\text{m}$ .

To finalize this device, a  $4 \times 4$  MMI coupler is designed. This part is characterized via its main parameters, the width, and length denoted by  $w_{MMI}$ , and  $L_{MMI}$ , respectively. The MMI function is to operate as a 3-dB coupler for the field injected from any of its input ports located at position  $x$ , where  $x$  is given as below [78]

$$x_i = \frac{w_{MMI}}{N} (i + 0.5) - \frac{w_{MMI}}{2} \quad (2.23)$$

where  $i=0, 1, 2, \dots, N$ , and  $N$  is the number of ports. The width  $w_{MMI}$  is set to  $4.5 \mu\text{m}$ , while the MMI length is numerically simulated for the desired operation and the result is shown in Figure 2.40, depicting the normalized transmission of the coupler as a function of length variation and it is clear that the length should be set to  $L_{MMI}=100 \mu\text{m}$  for maximum output to be extracted from the coupler.

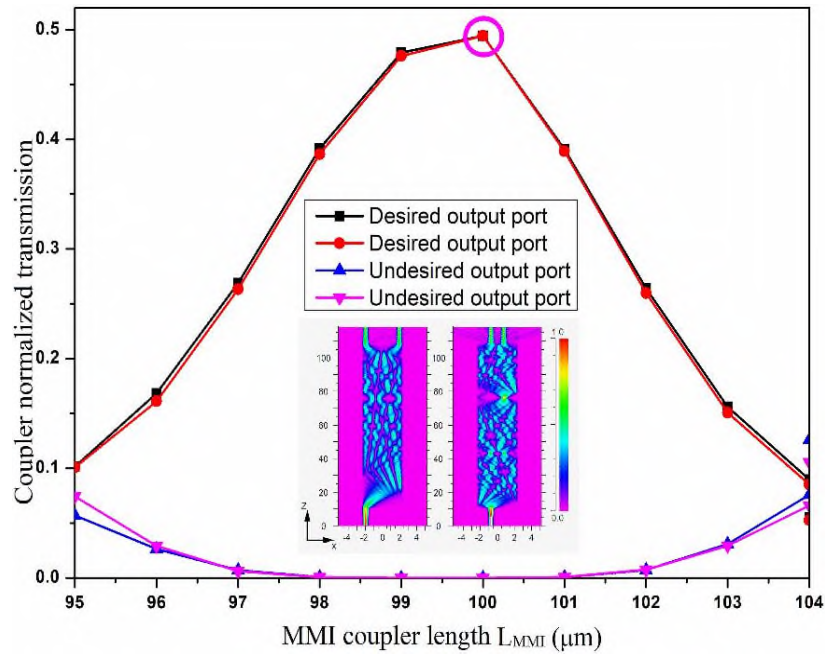


**Figure 2.40:** Conventional MMI coupler transmission as a function of  $L_{MMI}$ .

The performance of the device is evaluated through intensity distribution monitoring across the device and calculating both I.L and C.T for each case of the input modes. The results are shown in Figures 2.41 and 2.42 (a and b).

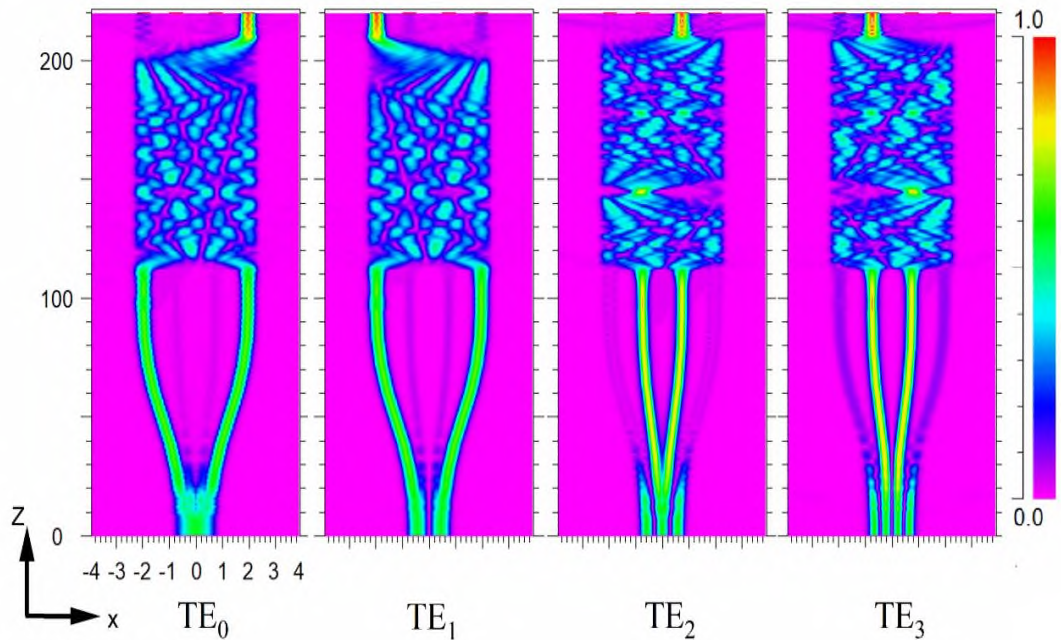


**Figure 2.41:** Intensity distribution of the guided mode along the (de)multiplexer with conventional MMI coupler. Values on both axes are in  $\mu\text{m}$ .

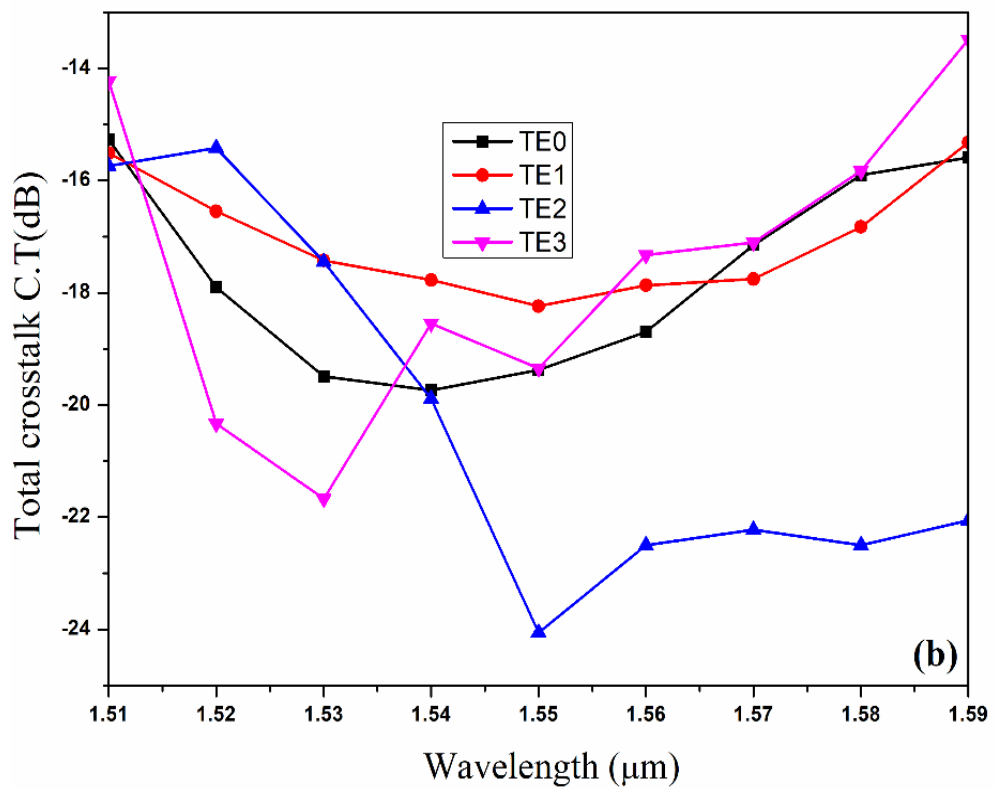
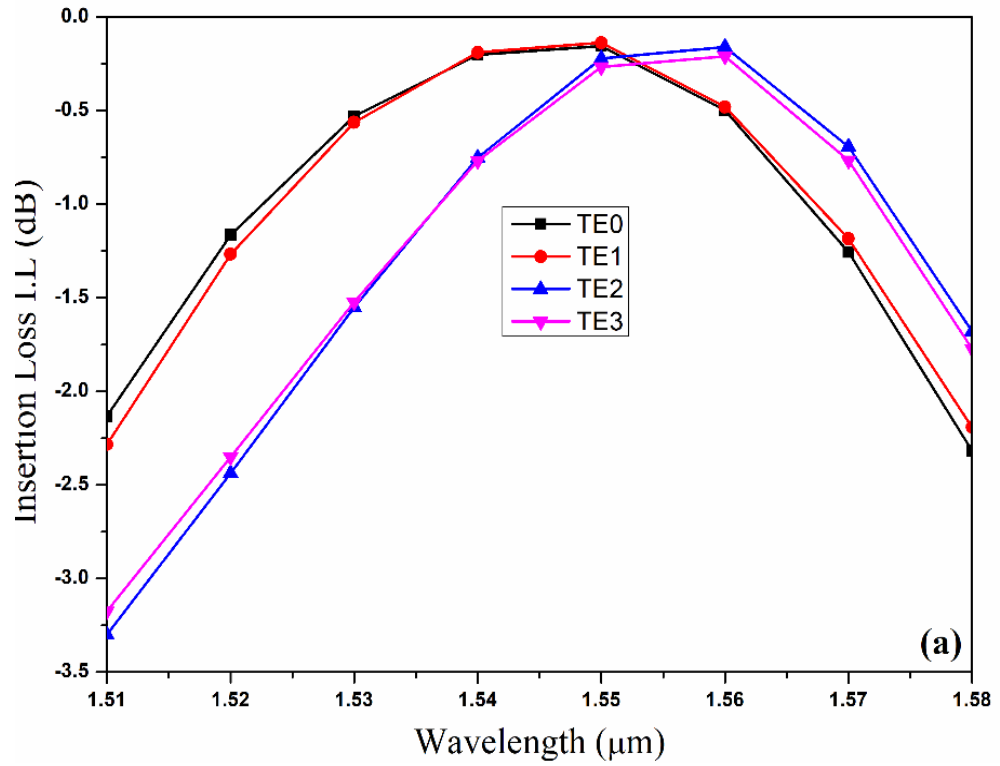


**Figure 2.42:** Conventional device performance as a function of wavelength  
(a) I. L (b) C. T.

It is obvious the device has an insertion loss is  $> -0.5$  dB and the crosstalk is lower than  $-15$  dB at  $\lambda=1.55$   $\mu\text{m}$ . The operating bandwidth is 80 nm (1.510-1.590)  $\mu\text{m}$ . The total footprint of the device is  $4.5 \times 173$  (779  $\mu\text{m}^2$ ). Table 2.6 gives a summary of the design and performance parameters of each device.

**Table 2.8** Conventional device geometrical and performance parameters.

Parameter	Value
Core index ( $n_{co}$ )	3.46
Cladding index ( $n_{cl}$ )	1.45
Cover index ( $n_{cover}$ )	1
Outer arm width ( $w_{b1}$ )	0.5 $\mu\text{m}$
Inner arm width ( $w_{b2}$ )	0.3 $\mu\text{m}$
Branch length ( $L_b$ )	70 $\mu\text{m}$
Phase shifter1 width ( $w_{ps1}$ )	0.34 $\mu\text{m}$
Phase shifter2 width ( $w_{ps2}$ )	0.2 $\mu\text{m}$
Phase shifter length ( $L_{ps}$ )	3 $\mu\text{m}$
MMI coupler width ( $w_{MMI}$ )	4.5 $\mu\text{m}$
MMI coupler length ( $L_{MMI}$ )	100 $\mu\text{m}$
Operating bandwidth (nm)	(1510-1590) $\mu\text{m}$
Overall area ( $\mu\text{m}^2$ )	$4.5 \times 173$ (780)
$I.L$ (dB)	TE <sub>0</sub> = -0.2, TE <sub>1</sub> = -0.2 TE <sub>2</sub> = -0.1, TE <sub>3</sub> = -0.3
$C.T$ (dB)	TE <sub>0</sub> = -19.4, TE <sub>1</sub> = -17.8 TE <sub>2</sub> = -22.1, TE <sub>3</sub> = -17.3

### 2.4.2 SWG-assisted (de)multiplexer

The conventional four-TE mode MMI coupler is replaced with an SWG-assisted counterpart. The new device scheme is shown in Figure 2.43. The splitter and the phase shifters are kept the same consideration for the conventional device. Also, the operation of the device is maintained and its performance is evaluated based on  $I.L$  and  $C.T$ . The SWG section of the same width  $w_{MMI}$  but different length  $L_{MMI(SWG)}$ . It comprises segments with  $(a)$  thickness,  $\Lambda$  pitch length, and  $D.C_{SWG} = a/\Lambda$  duty cycle. The values of  $\Lambda$  and  $D.C_{SWG}$  ( $a$ ) of the SWG section are set to  $0.2 \mu\text{m}$  and  $50\%$  ( $0.1 \mu\text{m}$ ), respectively, and the length is simulated at which the desired operation is satisfied. The results are depicted in Figure 2.44 which shows that maximum transmission can be obtained at  $L_{MMI(SWG)} = 50 \mu\text{m}$ .

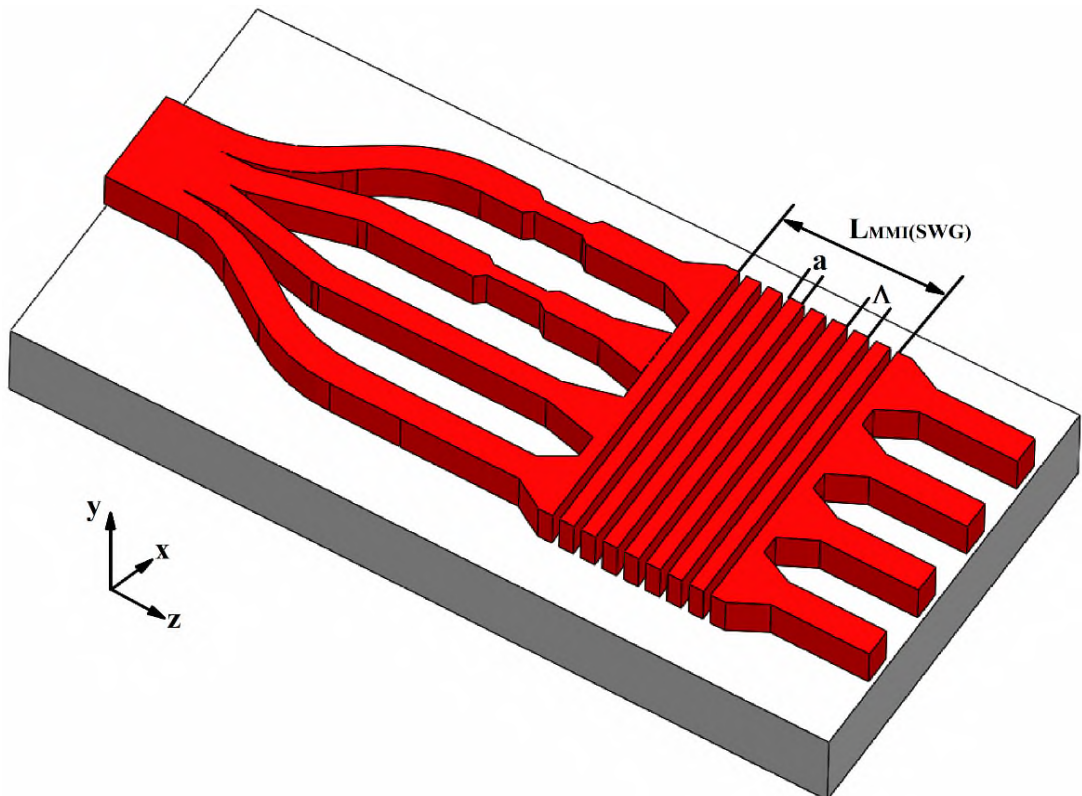


**Figure 2.43:** SWG-assisted 4-TE mode (de)multiplexer scheme.

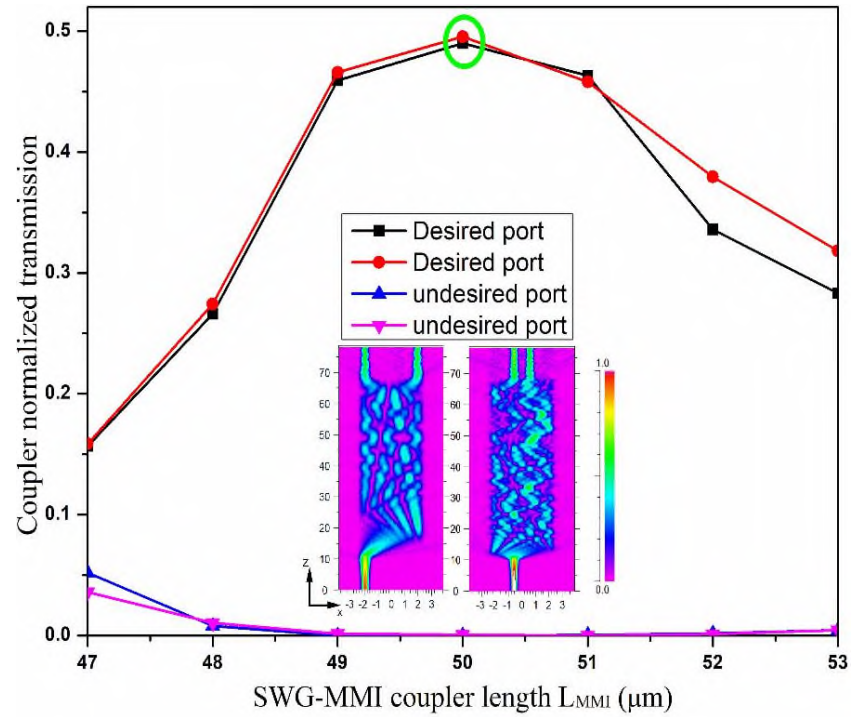


**Figure 2.44:** SWG-MMI coupler transmission as a function of  $L_{MMI(SWG)}$ .

Based on this result, the SWG offers 50% shortness in the length of the MMI than the conventional coupler. The performance evaluation results are done similarly to the conventional one and the results are shown in Figures 2.45 and 2.46.

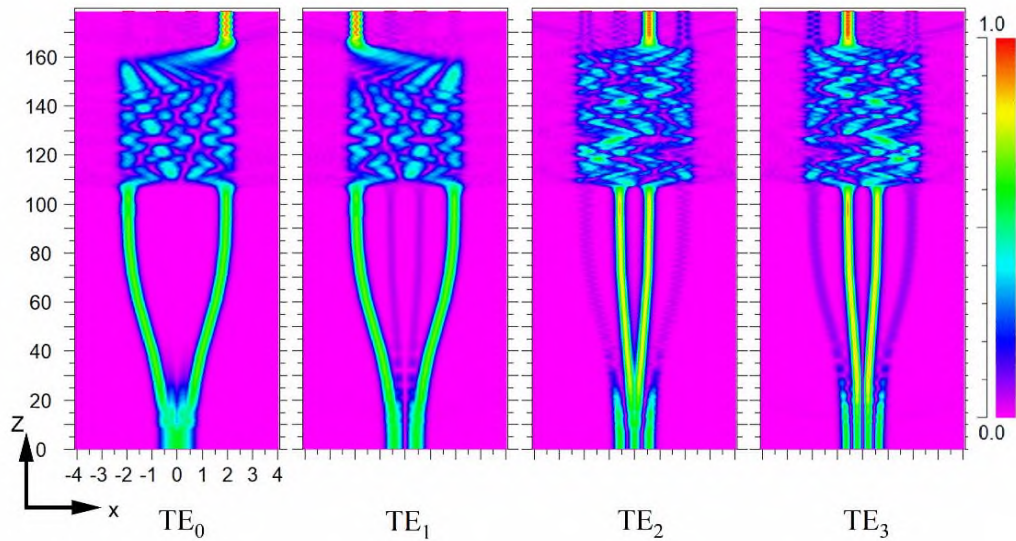


**Figure 2.45:** Intensity distribution of the guided mode along the (de)multiplexer with SWG MMI coupler. Values on both axes are in  $\mu\text{m}$ .

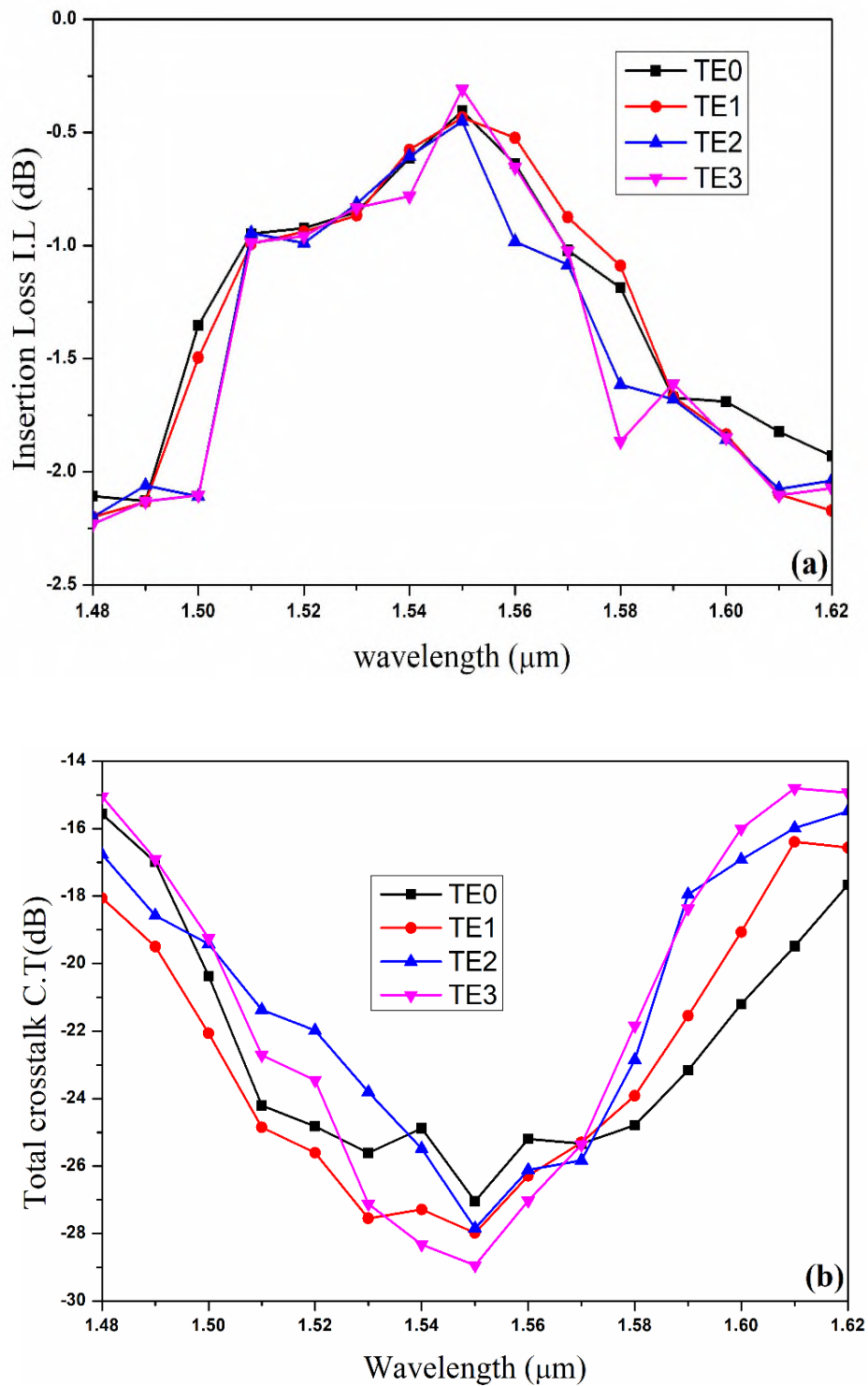


**Figure 2.46:** SWG-assisted device performance as a function of wavelength (a) *I.L* (b) *C.T*.

The insertion loss and crosstalk of the new device are maintained with  $I.L > -0.5$  dB and  $C.T < -15$  dB at 1.55 μm same as conventional. The

operating bandwidth is 140 nm (1.480-1.620)  $\mu\text{m}$ . Thus, extra bandwidth of 75% is gained from the design using the SWG technology. The footprint of the device is  $4.5 \times 100$  ( $553 \mu\text{m}^2$ ), which means the SWG offered a 30% shrink in the length of the device which in turn the overall footprint shrinks accordingly. Table 2.7 gives a summary of the design and performance parameters of each device.

**Table 2.9** SWG –assisted device geometrical and performance parameters.

Parameter	Value
Core index ( $n_{co}$ )	3.46
Cladding index ( $n_{cl}$ )	1.45
Cover index ( $n_{cover}$ )	1
Outer arm width ( $w_{b1}$ )	$0.5 \mu\text{m}$
Inner arm width ( $w_{b2}$ )	$0.3 \mu\text{m}$
Branch length ( $L_b$ )	$70 \mu\text{m}$
Phase shifter1 width ( $w_{ps1}$ )	$0.34 \mu\text{m}$
Phase shifter2 width ( $w_{ps2}$ )	$0.2 \mu\text{m}$
Phase shifter length ( $L_{ps}$ )	$3 \mu\text{m}$
MMI coupler width ( $w_{MMI}$ )	$4.5 \mu\text{m}$
MMI coupler length ( $L_{MMI}$ )	$50 \mu\text{m}$ (250 periods)
Period ( $\Lambda$ )	$0.2 \mu\text{m}$
Duty-cycle ( $D, C_{SWG}$ )	50%
Operating bandwidth (nm)	(1.480-1.620) $\mu\text{m}$
Overall area ( $\mu\text{m}^2$ )	$4.5 \times 123$ (550)
$I.L$ (dB)	TE <sub>0</sub> = -0.40, TE <sub>1</sub> = -0.39, TE <sub>2</sub> = -0.40, TE <sub>3</sub> = -0.30
$C.T$ (dB)	TE <sub>0</sub> = -24.9, TE <sub>1</sub> = -27.3, TE <sub>2</sub> = -25.5, TE <sub>3</sub> = -28.3

Performance comparison between the proposed 4-TE mode devices and their related counterparts reported in [49] and [86] and the comparison results are listed in Table 2.10. The proposed devices offer lower losses. Their operating bandwidth is wider than that reported in [86]. Further, The designed device

offers a 27% shrink in the footprint compared to that of [86] and a higher capacity than that of [49].

**Table 2.10** Performance comparison of the designed device with the previously reported devices.

Ref#	Structure	BW ( $\mu\text{m}$ )	C.T (dB)	I.L (dB)	Area ( $\mu\text{m}^2$ )
49	2-TE mode SWG-assisted (de)multiplexer	1.300-1.700	< -20	> -0.84	3.7×36
86	3-TE mode conventional (de)multiplexer	1.525-1.565	< -17	> -0.9	5×400
This work	4-TE mode conventional (de)multiplexer	1.510-1.590	< -15	> -0.5	4.5×173
	4-TE mode SWG-assisted (de)multiplexer	1.480-1.620			4.5×123

# Chapter Three

## Design of High-Order Mode (De)Multiplexer Using Cascaded Subwavelength Gratings

3.1 Introduction
3.2 Twelve-TE mode SWG-assisted ADC (De)multiplexer
3.2.1 General Description and Parameters Selection
3.2.2 Device Performance Evaluation
3.3 Fourteen-TE mode SWG-assisted (De)multiplexer
3.5 Twelve-TM-mode SWG-assisted ADC (De)multiplexer
3.4.1 Device Performance Evaluation
3.5 Dual-polarization SWG-assisted ADC (De)multiplexer

## CHAPTER THREE

### Design of High-Order Mode (De)Multiplexers Using Cascaded Subwavelength Gratings

#### 3.1 Introduction

This chapter presents the design and performance simulation of different mode (de)multiplexers based on cascaded asymmetric directional couplers (ADCs) and utilizing subwavelength grating (SWG) technology. First, two devices are designed to support 12 and 14-TE mode (de)multiplexing. The design later is modified for 12-TM mode and further expanded for 24-dual-polarization (12-TE/12-TM mode) operation.

#### 3.2 Twelve-TE mode SWG-assisted ADC (De)multiplexer

##### 3.2.1 General Description and Parameters Selection

In this section, a twelve ( $TE_0$ -to- $TE_{11}$ ) (de)multiplexer of the scheme shown in Figure 3.1 is designed based on cascaded ADCs geometry utilizing SWG technology. The proposed device comprises a main SWG multimode bus divided into six sections and eleven single-mode access waveguides coupled to it through SWG joints. Numerical simulation is carried out via Rsoft photonics CAD suite to design and optimize the device's main parameters and performance evaluation. The device is built based on an SOI platform in a rib/ridge waveguide form with 500 nm height and 220 nm slab height [85]. The waveguide consists of silicon (Si) as core material, silicon dioxide ( $SiO_2$ ) as cladding, and air as cover. These material refractive indices are 3.476, 1.444, and 1, for Si,  $SiO_2$ , and air, respectively. The SWG structure is Si/ $SiO_2$  segments of thickness  $a$  periodically repeated over pitch length  $\Lambda$ . The effective refractive index of the resultant section can be estimated using equations (1.21) and (1.22). The parameters  $\Lambda$  and  $D.C$  are chosen so that

the field can smoothly propagate through the structure with minimum losses and thus, maximum output transmission is achieved. The designed device comprises six SWG-assisted ADCs as sections of different widths  $w_i$  (with  $i=1,2,\dots,6$ ) connected through tapered waveguides of length  $L_t$ . each section has several single-mode access waveguides of width  $w_{gi}$  attached to it with a certain coupling length and gap denoted by  $L_c$  and  $g_i$ , respectively. To reduce possible crosstalk between these access waveguides are S-bended to separate them from each other and the SWG-bus.

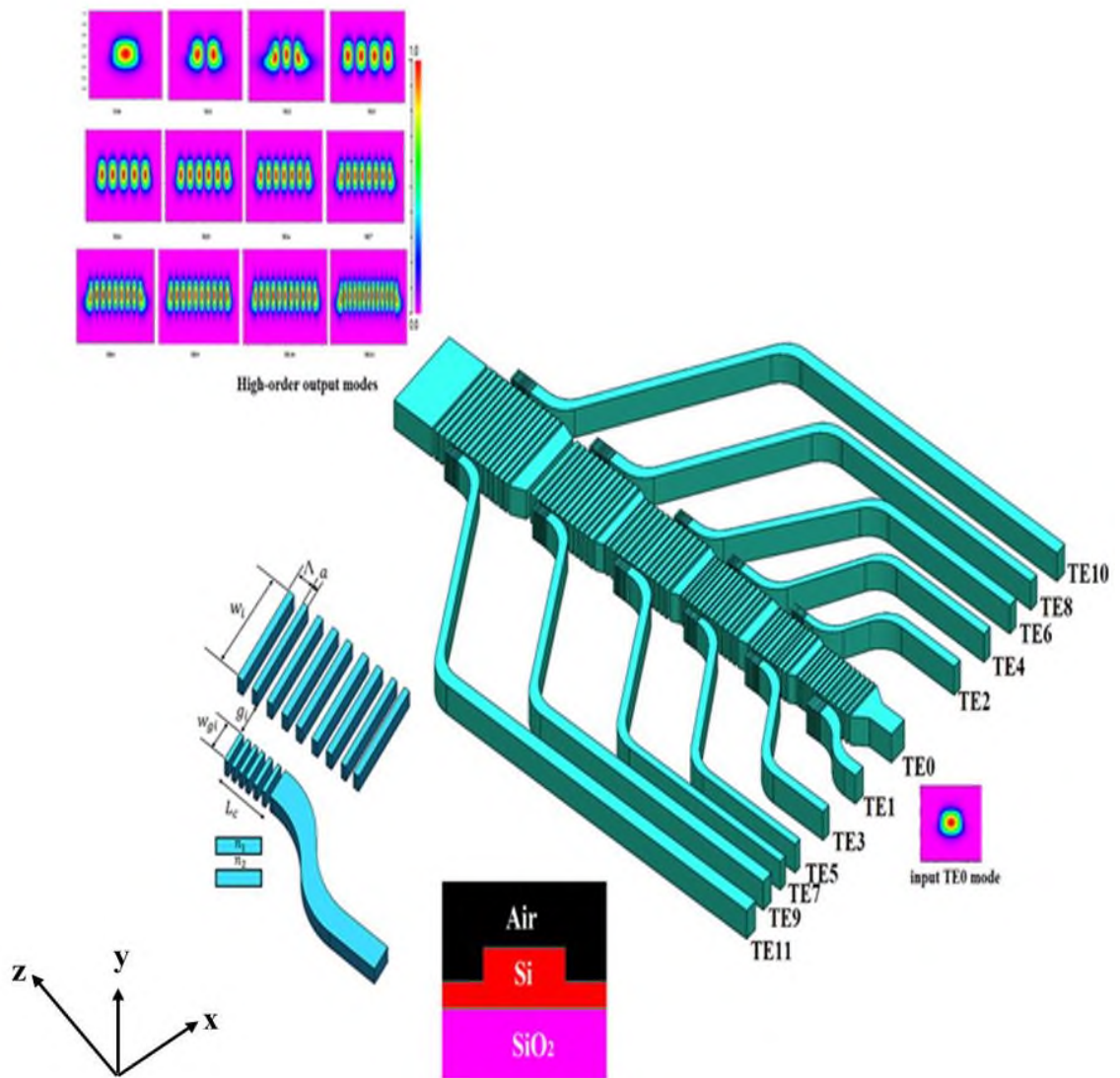


**Figure 3.1:** Schematic of the proposed 12-mode multiplexer. The inset shows the waveguide, input and output modes transverse cross-sections, the SWG, and coupling parameters.

For efficient mode coupling and thus high-order mode excitation where the fundamental  $TE_0$  input mode is converted into  $TE_n$  mode ( $n=1,2,\dots,11$ ), the phase-matching condition between the modes of the access waveguide and the SWG-bus must be achieved by adjusting their width and thus their effective indices to be almost equal [ $n_{eff}(w_{gi}) - n_{eff}(w_i) \approx 0$ ] to trigger the mode excitation process, where  $n_{eff}(w_i)$ , and  $n_{eff}(w_{gi})$ , are the effective index of the desired high-order mode excited in the  $i$ -th section and the fundamental mode of the access waveguide, respectively. as the desired effective index for mode coupling is achieved, the power from the access waveguide is coupled into the target bus section and transformed to the high-order mode. In the design of such structures, either several high-order modes to be excited share the same main bus width but different access waveguide widths or vice versa. In this device, for ease of fabrication and design dimensions stability, the main bus sections are selected to support as maximum allowed modes per section, while keeping the access waveguides dimensions the same as much as possible.

The first step is to choose the parameters of the SWG-bus distinguished as  $w_i$ ,  $\Lambda$ ,  $D.C$ , and  $L_t$ . Initially, the length  $L_t$  is set to  $10 \mu\text{m}$  for smooth transmission of the field between the sections of the main bus. Numerical simulation is carried out for  $\Lambda$  and  $D.C$  at where maximum transmission is achieved at the device output and the result is depicted in Figure 3.2, which depicts the normalized transmission as a function of  $\Lambda$  and  $D.C$  varied over the ranges ( $0.1\text{-}0.3 \mu\text{m}$ ), and ( $50\%\text{-}100\%$ ), respectively. For compactness and ease of fabrication, it is required to select  $\Lambda$ , and  $D.C$  to  $0.15 \mu\text{m}$ , and  $50\%$ , respectively. Next, calculating the effective index  $n_{eff}(w_i)$  for the allowed modes to propagate in the waveguide based on its width and the result is shown in Figure 3.3.

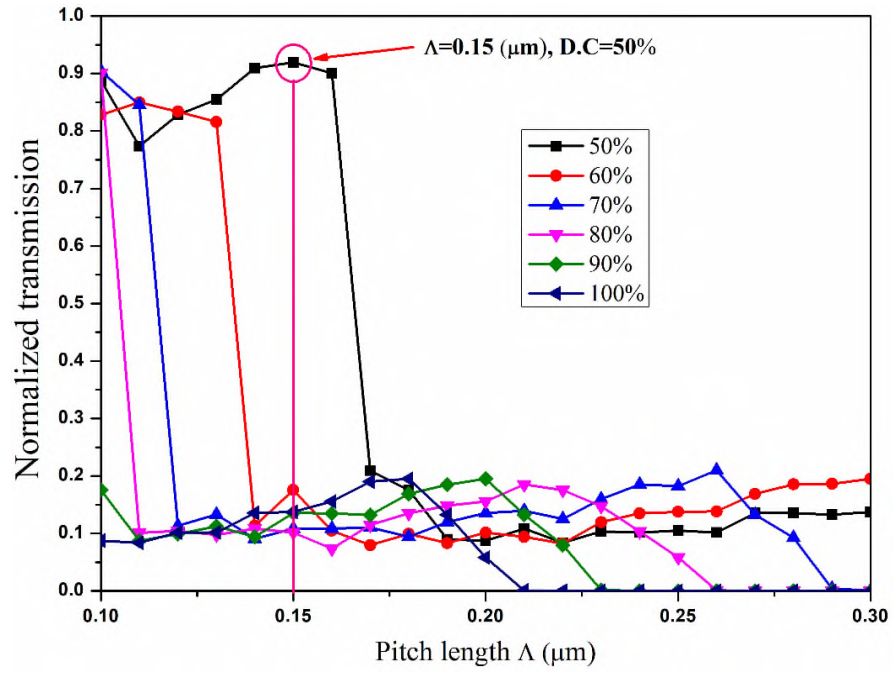


**Figure 3.2:** Normalized transmission as a function of  $\Lambda$  and  $D.C$  at  $1.55 \mu\text{m}$ .

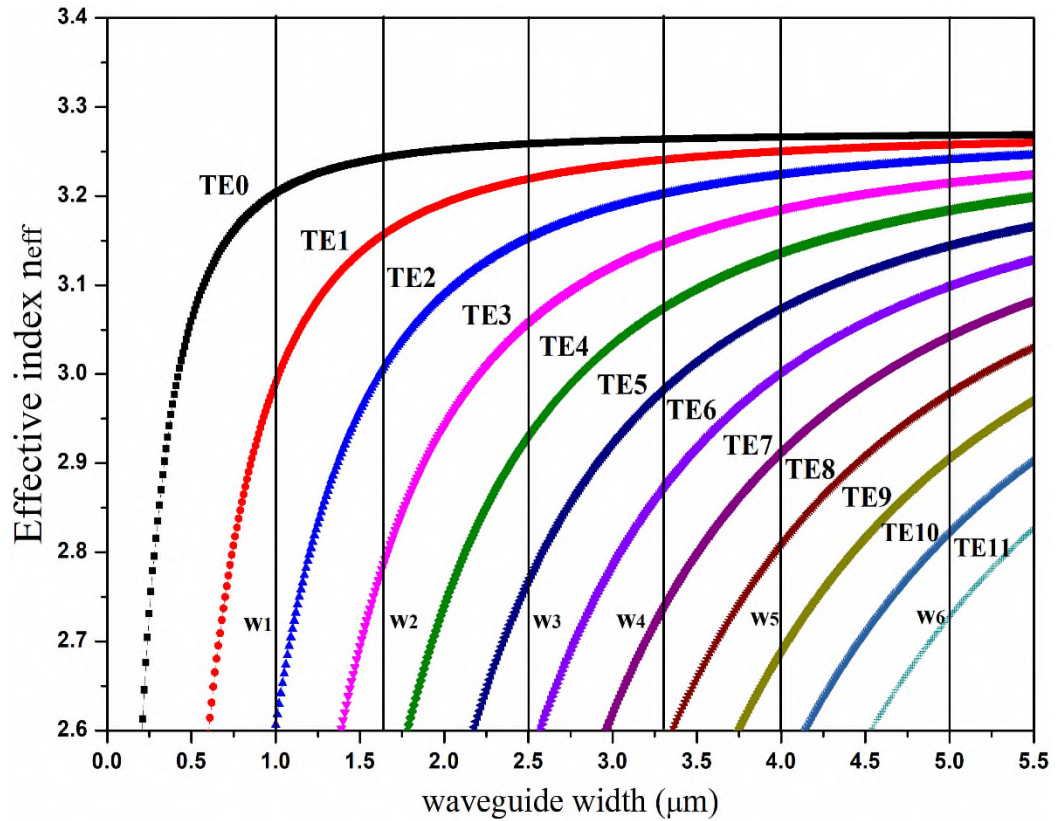


**Figure 3.3:** Effective index of the guided TE-mode as a function of waveguide width.

For the designed device, the widths are set as shown in Table 3.1 to support the desired mode configuration.

**Table 3.1** SWG-bus sections widths for the 12-TE mode device.

Mode	Waveguide ( $w_i$ )	Width ( $\mu\text{m}$ )
TE <sub>0</sub>	Directly inject	
TE <sub>1</sub>	$w_1$	1.00
TE <sub>2</sub>	$w_2$	1.63
TE <sub>3</sub>		
TE <sub>4</sub>	$w_3$	2.50
TE <sub>5</sub>		
TE <sub>6</sub>	$w_4$	3.30
TE <sub>7</sub>		
TE <sub>8</sub>	$w_5$	4.00
TE <sub>9</sub>		
TE <sub>10</sub>	$w_6$	5.00
TE <sub>11</sub>		

Moving to the next part to select the optimum width  $w_{gi}$  and coupling parameters  $L_c$  and  $g_i$  of the single-mode access waveguides that are attached to each section to achieve a robust phase-matching condition and excite the desired high-order TE-mode while keeping the ease of fabrication at a reasonable margin. Referring to Figure 3.2, the phase-matching condition for certain high-order mode excitation is satisfied at the point where the TE<sub>0</sub> and that high-order mode curves intersect and thus have the same effective index. Further, the width  $w_{gi}$ , the gaps  $g_i$  and the lengths  $L_c$  of the joints are optimized through numerical simulation so that high mode coupling and maximum transmission are achieved. The results are summarized in Table 3.2 where the geometrical parameters for each mode are given. During simulation, it is noticed that large gaps are associated with long coupling length, which means weak coupling and a large footprint, whereas smaller gaps are obtained with shorter coupling lengths, although this may be challenging from a fabrication point of view. Thus, to balance these

requirements, the gaps and lengths are designed in ranges of 80-100 nm, and 8-13  $\mu\text{m}$ , respectively.

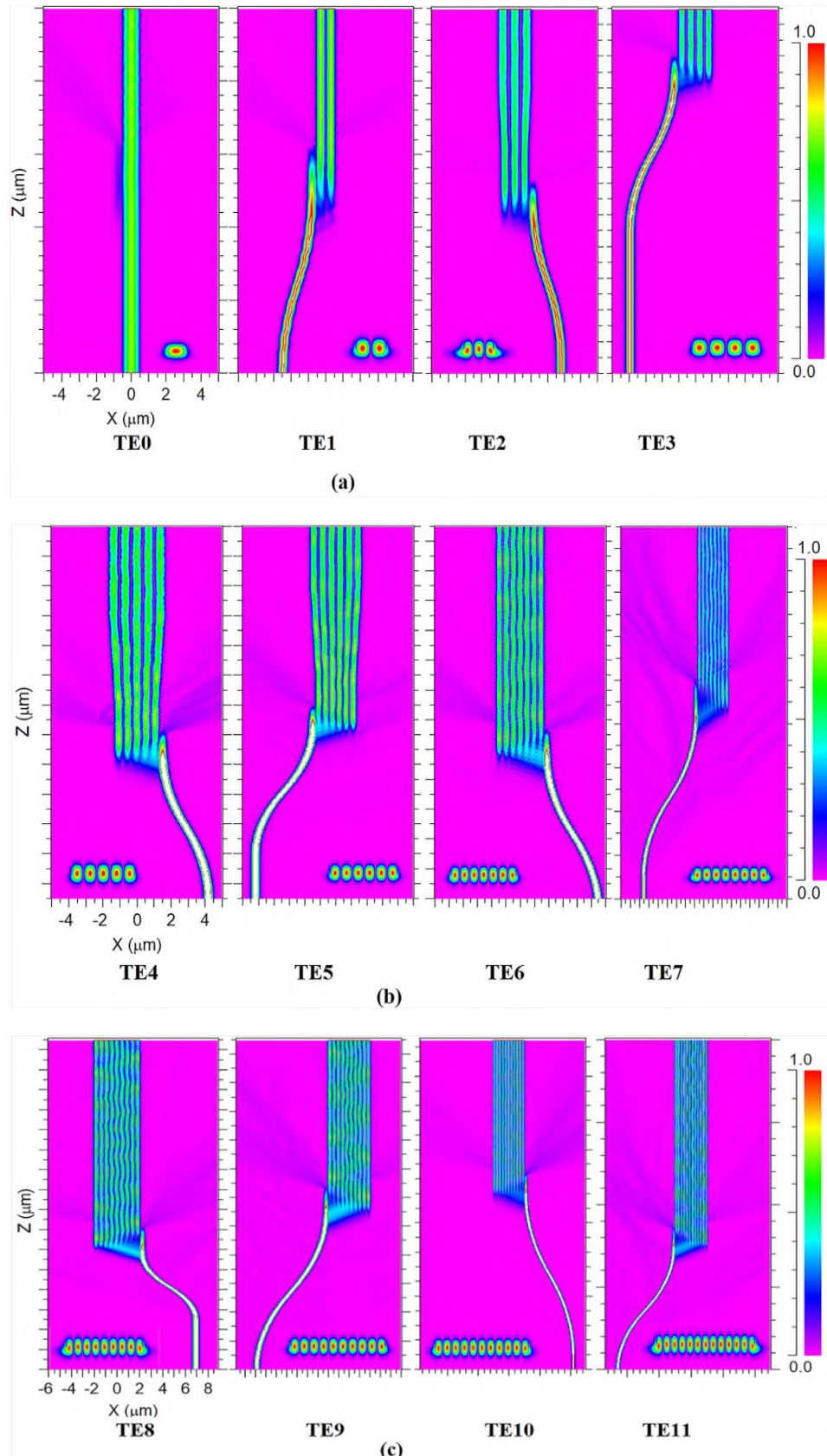
**Table 3.2** Access waveguide geometrical parameters for the 12-TE mode device.

Mode	$w_{gi}$ ( $\mu\text{m}$ )	$g_i$ (nm)	$L_c$ ( $\mu\text{m}$ )
TE <sub>0</sub>	Direct inject		
TE <sub>1</sub>	0.43	80	9
TE <sub>2</sub>	0.43	80	8
TE <sub>3</sub>	0.37	85	8
TE <sub>4</sub>	0.36	80	8
TE <sub>5</sub>	0.30	100	8
TE <sub>6</sub>	0.30	100	8
TE <sub>7</sub>	0.24	100	8
TE <sub>8</sub>	0.30	100	10
TE <sub>9</sub>	0.25	100	10
TE <sub>10</sub>	0.30	100	13
TE <sub>11</sub>	0.26	100	13

### 3.2.2 Device Performance Evaluation

Field propagation and the performance of the designed devices are investigated in each case of high-order mode excitation of the twelve modes. The propagation along the z-axis is simulated via the Rsoft photonics suit CAD and the results are shown in Figure 3.4 where the device operates as a multiplexer where an input TE<sub>0</sub> mode is injected into the access waveguide and converted to the phase-matched high-order mode. It is worth mentioning that the designed device is also capable to give the same results for the case of demultiplexing operation.

Next, device performance is checked based on insertion loss  $I.L$  and crosstalk  $C.T$  calculated at the designed wavelength of 1.55  $\mu\text{m}$  for each case of the excited high-order mode using equations (2.21) and (2.22), respectively. The  $I.L$  calculation results are given in Table 3.3 which is clear that the device offers an insertion loss  $> -0.6$  dB.

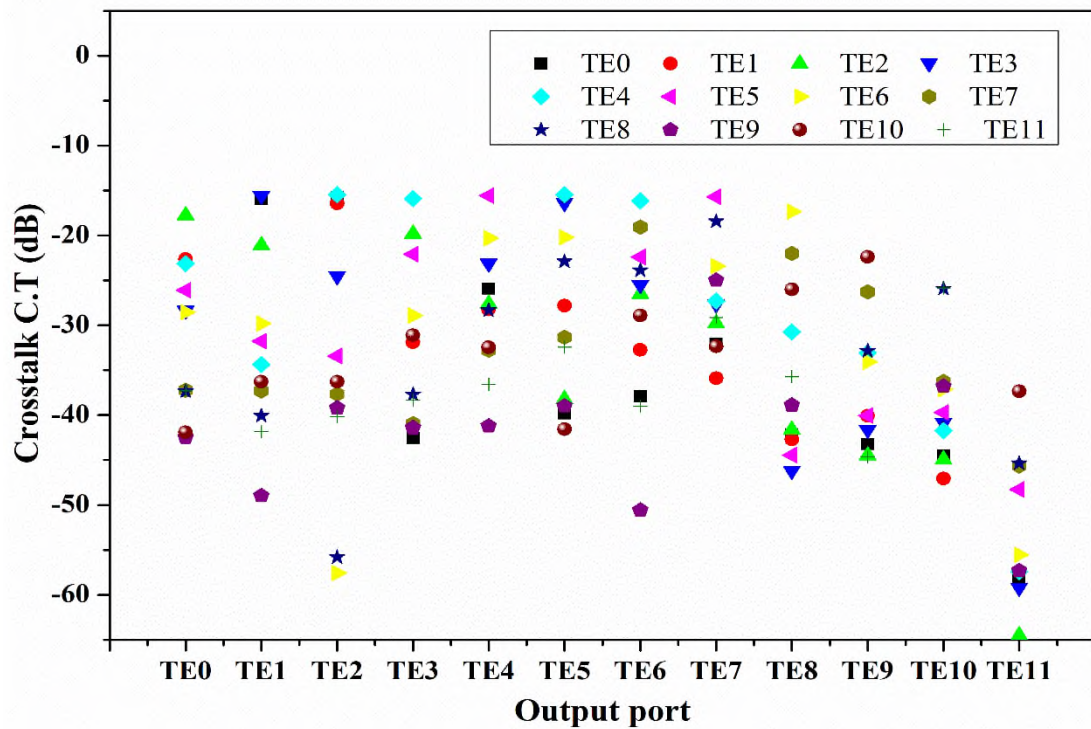


**Figure 3.4:** Intensity distribution across the 12-TE mode  
 (a) TE<sub>0</sub>-TE<sub>3</sub>, (b) TE<sub>4</sub>-TE<sub>7</sub>, (c) TE<sub>8</sub>-TE<sub>11</sub>.  
 The inset shows the output modes transverse cross-sections.  
 Values on both axes are in  $\mu\text{m}$ .

**Table 3.3** Device insertion loss (dB) at 1.55  $\mu\text{m}$ .

Output mode	I.L (dB)
TE <sub>0</sub>	-0.03
TE <sub>1</sub>	-0.55
TE <sub>2</sub>	-0.21
TE <sub>3</sub>	-0.60
TE <sub>4</sub>	-0.30
TE <sub>5</sub>	-0.42
TE <sub>6</sub>	-0.60
TE <sub>7</sub>	-0.50
TE <sub>8</sub>	-0.06
TE <sub>9</sub>	-0.30
TE <sub>10</sub>	-0.16
TE <sub>11</sub>	-0.04

The  $C.T$  is the measure of how much the output ports are affecting each other in the case of demultiplexing operation. Figure 3.5 depicts device crosstalk for each case of input high-order modes where it is always  $< -15$  dB.

**Figure 3.5:** Crosstalk of the proposed 12-TE mode device for demultiplexing operation.

The operating bandwidth of the device is determined at which the losses are maintained within 1-dB and/or 3-dB margins over a wavelength range of (1.400-1.700)  $\mu\text{m}$ . The results are shown in Figure 3.6 which confirms the ultra-broadband and low loss operation of the designed device. These results are also summarized in Table 3.4 which shows both 3-dB and 1-dB operating bandwidths.

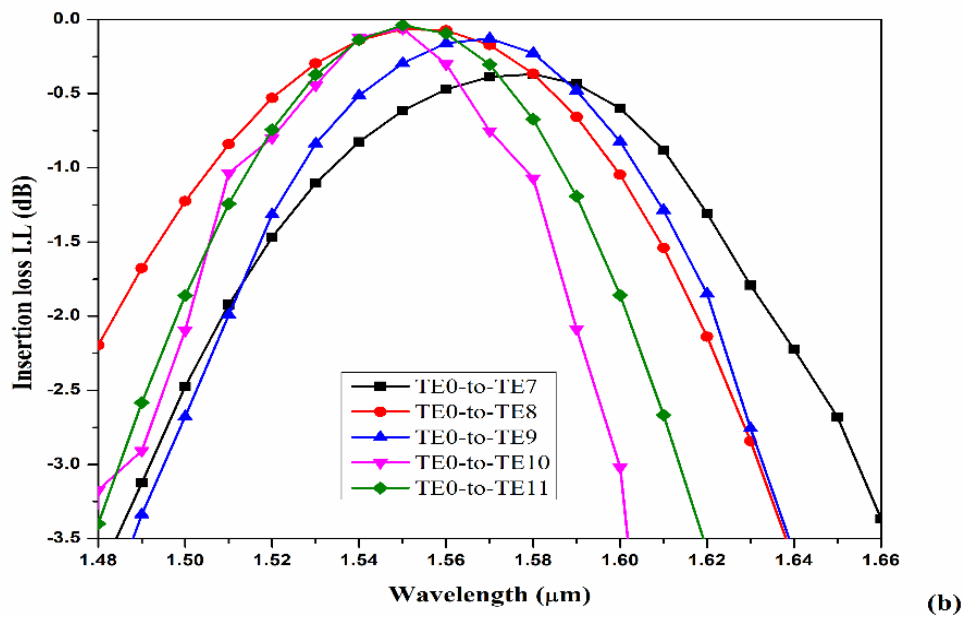
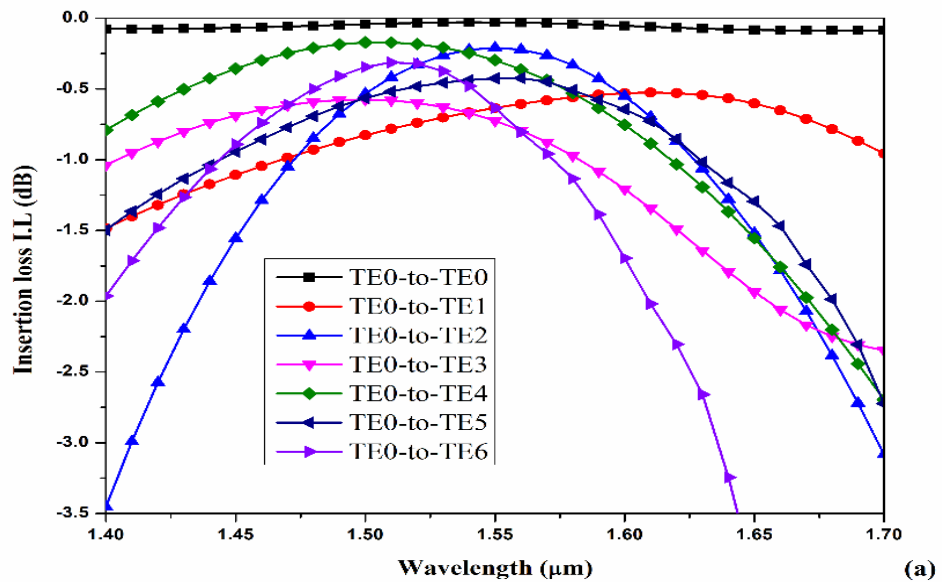


**Figure 3.6:** Insertion loss of the proposed 12-TE mode device as a function of wavelength TE<sub>0</sub>-TE<sub>6</sub>, (b) TE<sub>7</sub>-TE<sub>11</sub>.

**Table 3.4** 12-TE mode device operating bandwidths.

Mode	3-dB Bandwidth ( $\mu\text{m}$ )	1-dB Bandwidth ( $\mu\text{m}$ )
TE <sub>0</sub>	> 0.5	> 0.5
TE <sub>1</sub>	1.250-1.700	1.370-1.700
TE <sub>2</sub>	1.400-1.700	1.460-1.680
TE <sub>3</sub>	1.220-1.700	1.330-1.640
TE <sub>4</sub>	1.250-1.700	1.360-1.640
TE <sub>5</sub>	1.300-1.700	1.400-1.660
TE <sub>6</sub>	1.350-1.700	1.410-1.600
TE <sub>7</sub>	1.480-1.660	1.510-1.630
TE <sub>8</sub>	1.460-1.640	1.500-1.600
TE <sub>9</sub>	1.490-1.640	1.520-1.610
TE <sub>10</sub>	1.480-1.600	1.510-1.580
TE <sub>11</sub>	1.520-1.700	1.530-1.590

Furthermore, the results in Table 3.4 reveal that all modes are covering the entire C-band (1.530-1.565)  $\mu\text{m}$  in wavelength-division multiplexing (WDM) networks. Thus, the proposed device can be employed in the MDM-WDM network to achieve the hybrid multiplexing technology for further improvement in the link capacity.

Finally, errors during the fabrication process may occur which affect the quality of operation of the device. Fabrication tolerance is investigated by checking the performance stability in response to the deviation of the width of the access and SWG-assisted waveguides from their optimum values. The results are presented in Figure 3.7, where the device shows acceptable performance within the  $\pm\Delta w_i$  equals  $\pm 5\%$  around the desired value.

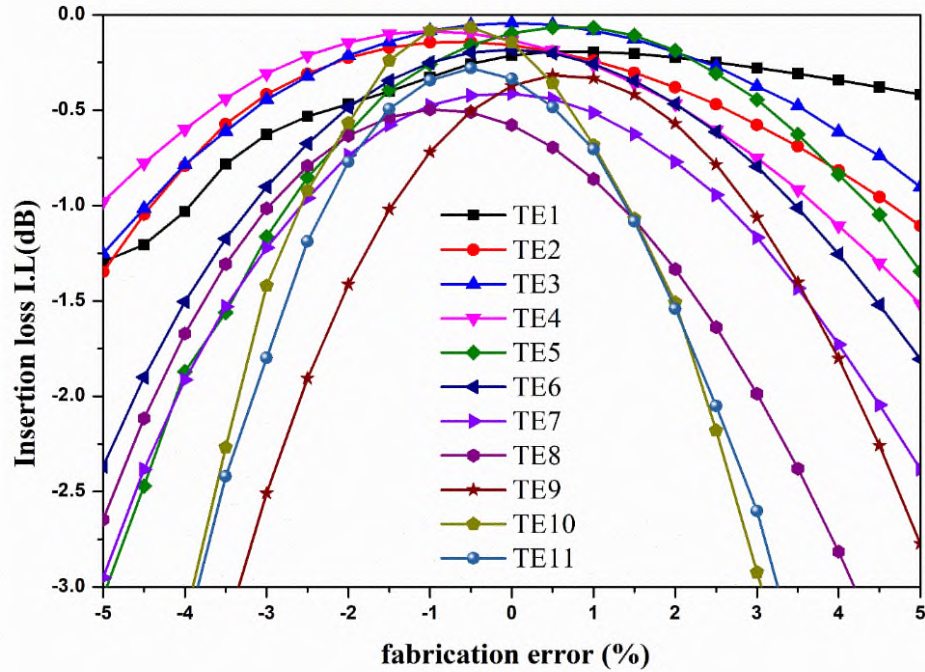


**Figure 3.7:** Effect of fabrication error on the insertion loss of the 12-TE modes device.

### 3.3 Fourteen-TE mode SWG-assisted (De)multiplexer

In the previous section, a 12-mode (de)multiplexer is designed with the main SWG-assisted bus and 11 access waveguides attached to it to excite the desired modes. In this section, the device is expanded to serve as a 14-TE mode ( $TE_0$ -to- $TE_{13}$ ) (de)multiplexer by adding a new SWG-bus section of width ( $w_7$ ). Figure 3.8 presents the effective index variation as a function of the new section width, which is possible to say that  $w_7$  can be set to  $5.5 \mu\text{m}$  to handle both  $TE_{12}$  and  $TE_{13}$ . The parameters of the new section are also summarized in Table 3.5.

**Table 3.5** Geometrical parameters of the added sections 14-TE mode device.

Mode	$w_{gi}$ ( $\mu\text{m}$ )	$w_7$ ( $\mu\text{m}$ )	$g_i$ (nm)	$L_c$ ( $\mu\text{m}$ )
$TE_{12}$	0.27	5.50	130	13
$TE_{13}$	0.24		130	13

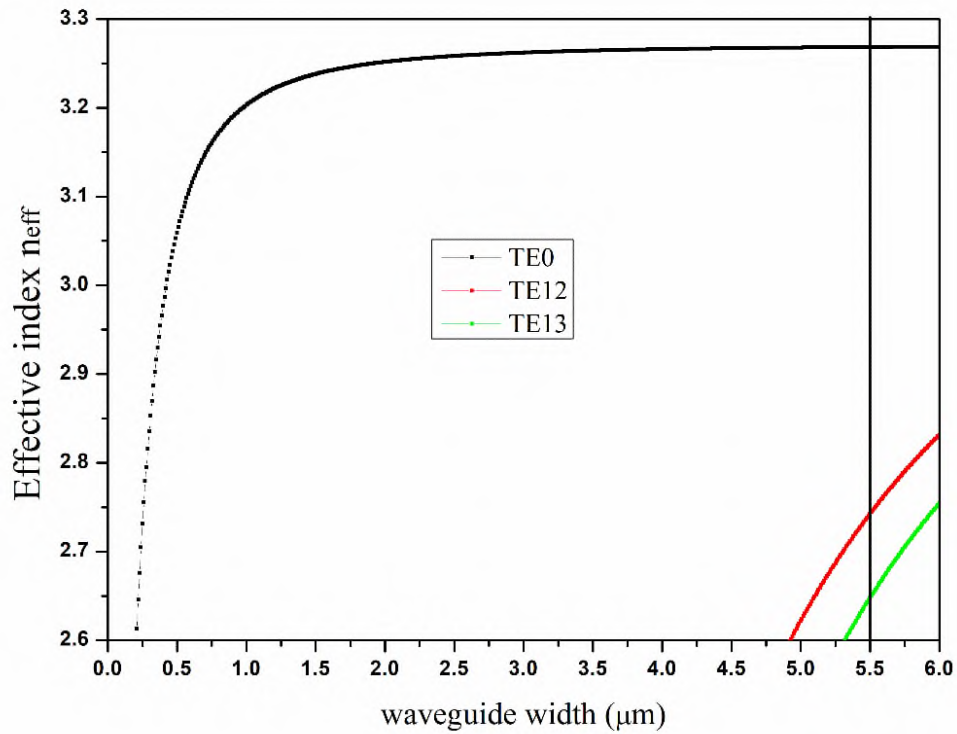


**Figure 3.8:** Effective index of the TE<sub>12</sub> and TE<sub>13</sub> modes as a function of waveguide width.

The performance of the new section is investigated by checking the intensity distribution across the device for each case of mode excitation. Also, the insertion loss, crosstalk, and operating bandwidth are calculated. The results are depicted in Figures (3.9-3.11), respectively. From Figure 3.9, it is clear that the device has losses  $> -0.4$  dB at the design wavelength of  $1.55 \mu\text{m}$ . The crosstalk of the demultiplexing operation is always  $< -30$  dB. The performance of the device is summarized in Table 3.6.

**Table 3.6** Added section performance parameters.

Mode	I.L (dB)	C.T (dB)	3-dB bandwidth ( $\mu\text{m}$ )
TE <sub>12</sub>	-0.30	$> -30$	(1.450-1.650)
TE <sub>13</sub>	-0.40		

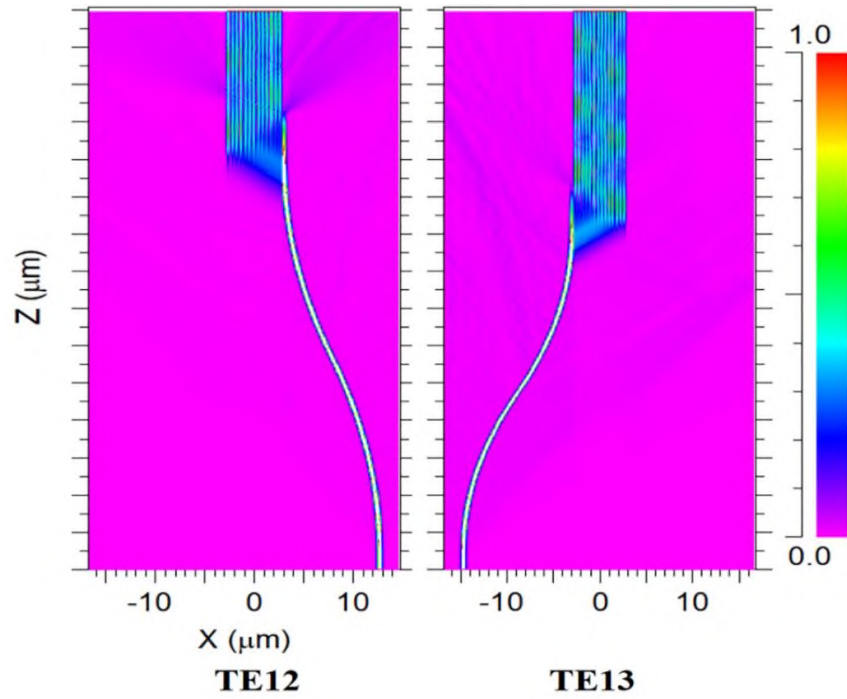


**Figure 3.9:** Intensity distribution across the device when exciting (left) TE<sub>12</sub>, (right) TE<sub>13</sub>. Values on both axes are in  $\mu\text{m}$ .

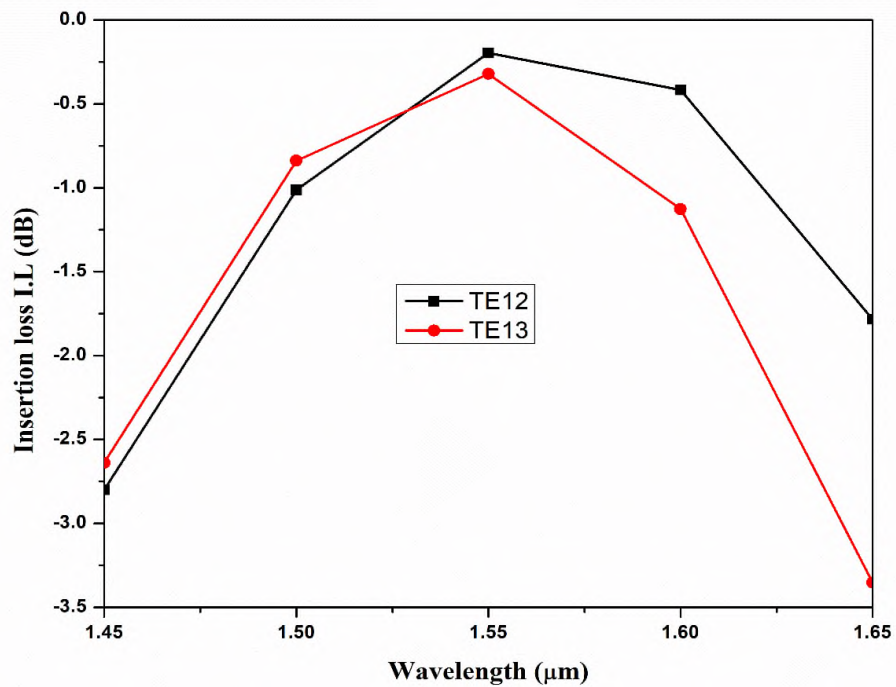


**Figure 3.10:** Insertion loss of the proposed 14-TE device as a function of wavelength.

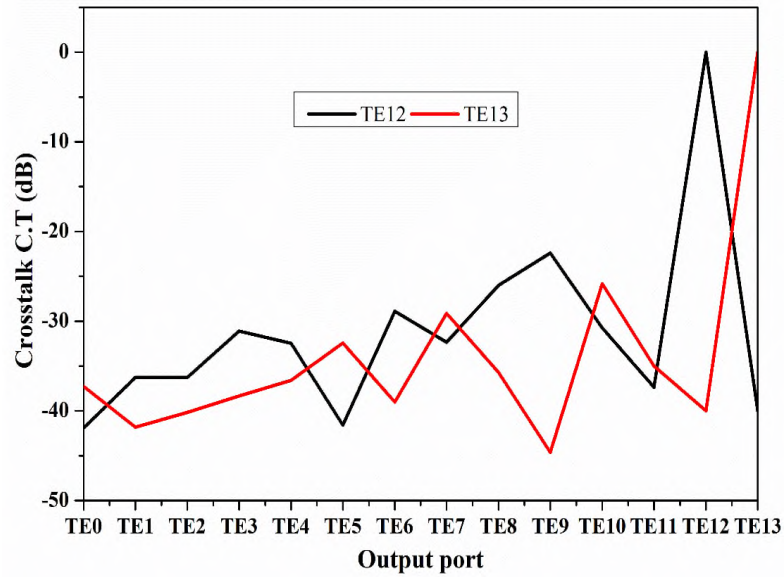


**Figure 3.11:** Crosstalk of the proposed 14-TE device as a function of wavelength.

Fabrication error for the new section is investigated in terms of maintaining low losses while deviating from the optimum value of the section width. The result is depicted in Figure 3.12 which shows that the performance remains within the 3-dB margin while the width deviates by  $\pm 3.5\%$  from the optimum value of the SWG-bus.

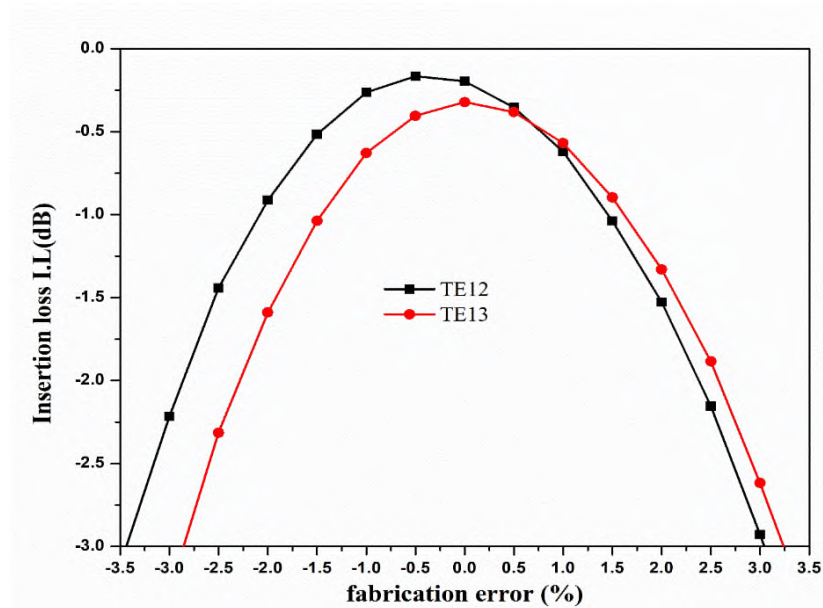


**Figure 3.12:** Effect of fabrication on the insertion loss of the 14-TE device.

### 3.4 Twelve-TM mode SWG-assisted ADC (De)multiplexer

In this section, a twelve TM-mode SWG-ADC-based (de)multiplexer of the scheme shown in Figure 3.13 is designed. The same concept presented in section 3.2 for TE polarization is applied here for the TM. The proposed device comprises a main SWG multimode bus divided into six sections and eleven single-mode access waveguides coupled to it through SWG joints. Numerical simulation is carried out to design and optimize the device's main parameters and to evaluate the performance.

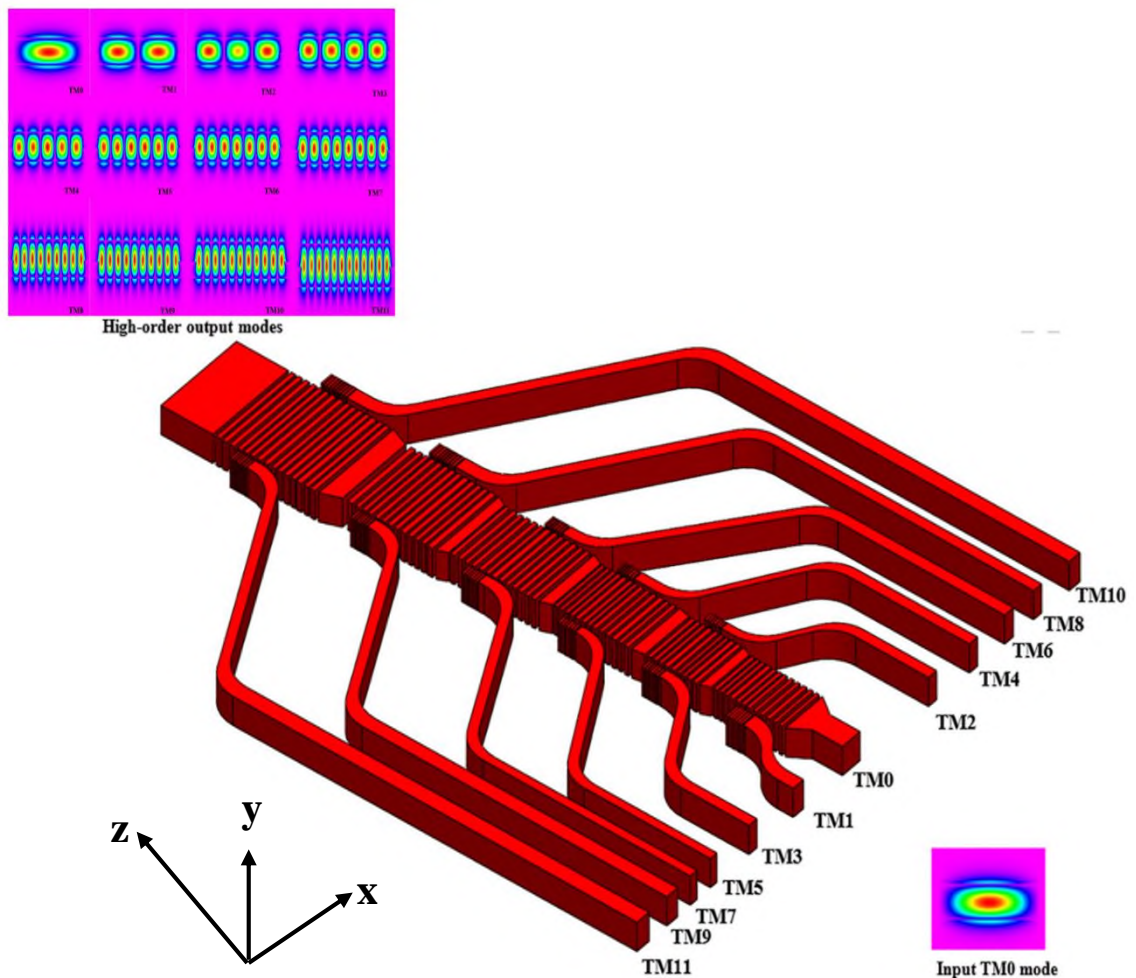


**Figure 3.13:** Schematic configuration of the proposed 12-TM mode multiplexer. The inset shows the input and output modes transverse cross-sections.

The same SWG-bus sections considered for TE-modes are used for the TM-modes as presented in Table 3.7. The modification applied via numerical

simulation on the parameters of the single-mode access waveguides  $w_{gi}$ ,  $L_c$  and  $g_i$  to excite the desired high-order mode at the designed SWG-bus section. The simulation results are presented in Table 3.8 and Figure 3.14.

**Table 3.7** SWG-bus sections widths of the proposed 12-TM device.

Mode	Waveguide ( $w_i$ )	Width ( $\mu\text{m}$ )
TM <sub>0</sub>	Directly inject	
TM <sub>1</sub>	$w_1$	1.00
TM <sub>2</sub>	$w_2$	1.63
TM <sub>3</sub>		
TM <sub>4</sub>	$w_3$	2.50
TM <sub>5</sub>		
TM <sub>6</sub>	$w_4$	3.30
TM <sub>7</sub>		
TM <sub>8</sub>	$w_5$	4.00
TM <sub>9</sub>		
TM <sub>10</sub>	$w_6$	5.00
TM <sub>11</sub>		

**Table 3.8** Access waveguide geometrical parameters of the proposed 12-TM mode device.

TM	$w_{gi}$ ( $\mu\text{m}$ )	$g_i$ (nm)	$L_c$ ( $\mu\text{m}$ )
TM <sub>0</sub>	Directly inject		
TM <sub>1</sub>	0.46	300.00	6.40
TM <sub>2</sub>	0.48	300.00	6.40
TM <sub>3</sub>	0.38	400.00	6.40
TM <sub>4</sub>	0.35	400.00	5.40
TM <sub>5</sub>	0.30	300.00	5.20
TM <sub>6</sub>	0.35	300.00	5.20
TM <sub>7</sub>	0.32	300.00	3.00
TM <sub>8</sub>	0.32	300.00	3.00
TM <sub>9</sub>	0.28	300.00	3.00
TM <sub>10</sub>	0.31	300.00	2.00
TM <sub>11</sub>	0.28	300.00	2.00

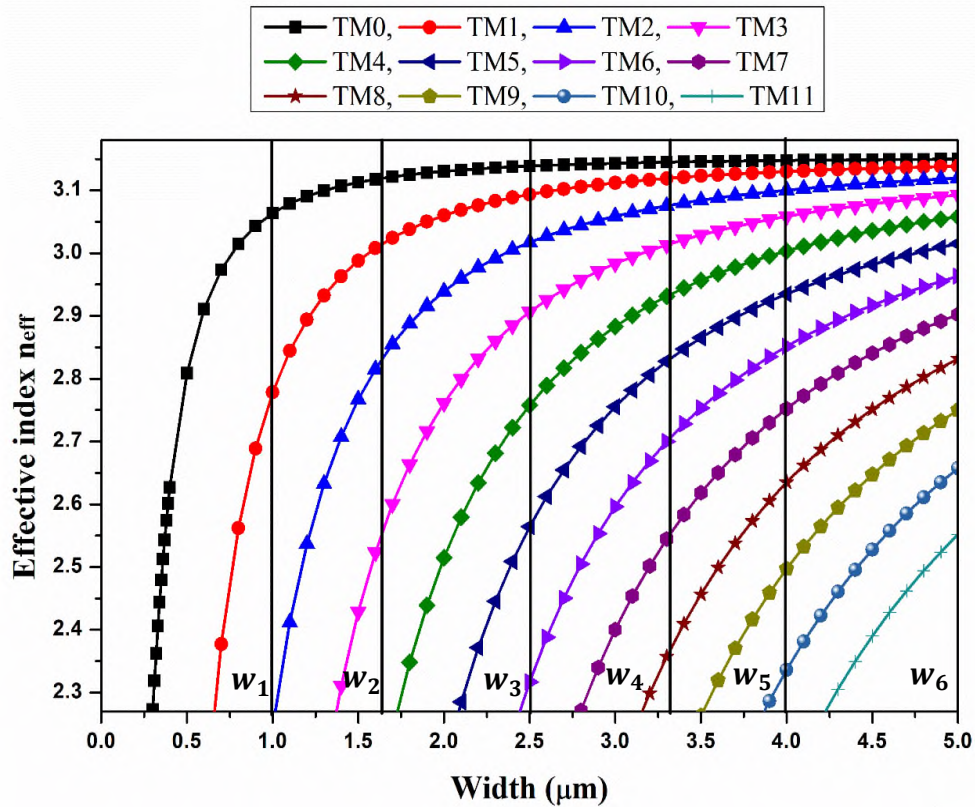


**Figure 3.14:** Effective index of the guided TM-modes as a function of waveguide width.

### 3.4.1 Performance Evaluation of the Proposed Device

The performance and field distribution along the proposed device for each case of the twelve TM output modes is investigated via the Rsoft photonics suit CAD. The results are shown in Figure 3.15, where the device operates as a multiplexer. The input exciting mode TM0 is injected into the specific port of the access waveguides and the phase-matched high-order mode is excited with the maximum transmission. The transverse cross-section of each of the output modes is presented in Figure 3.16. The performance of the designed device is checked based on insertion loss and crosstalk at the designed wavelength of  $1.55 \mu\text{m}$  given by equations (2.21) and (2.22), respectively.

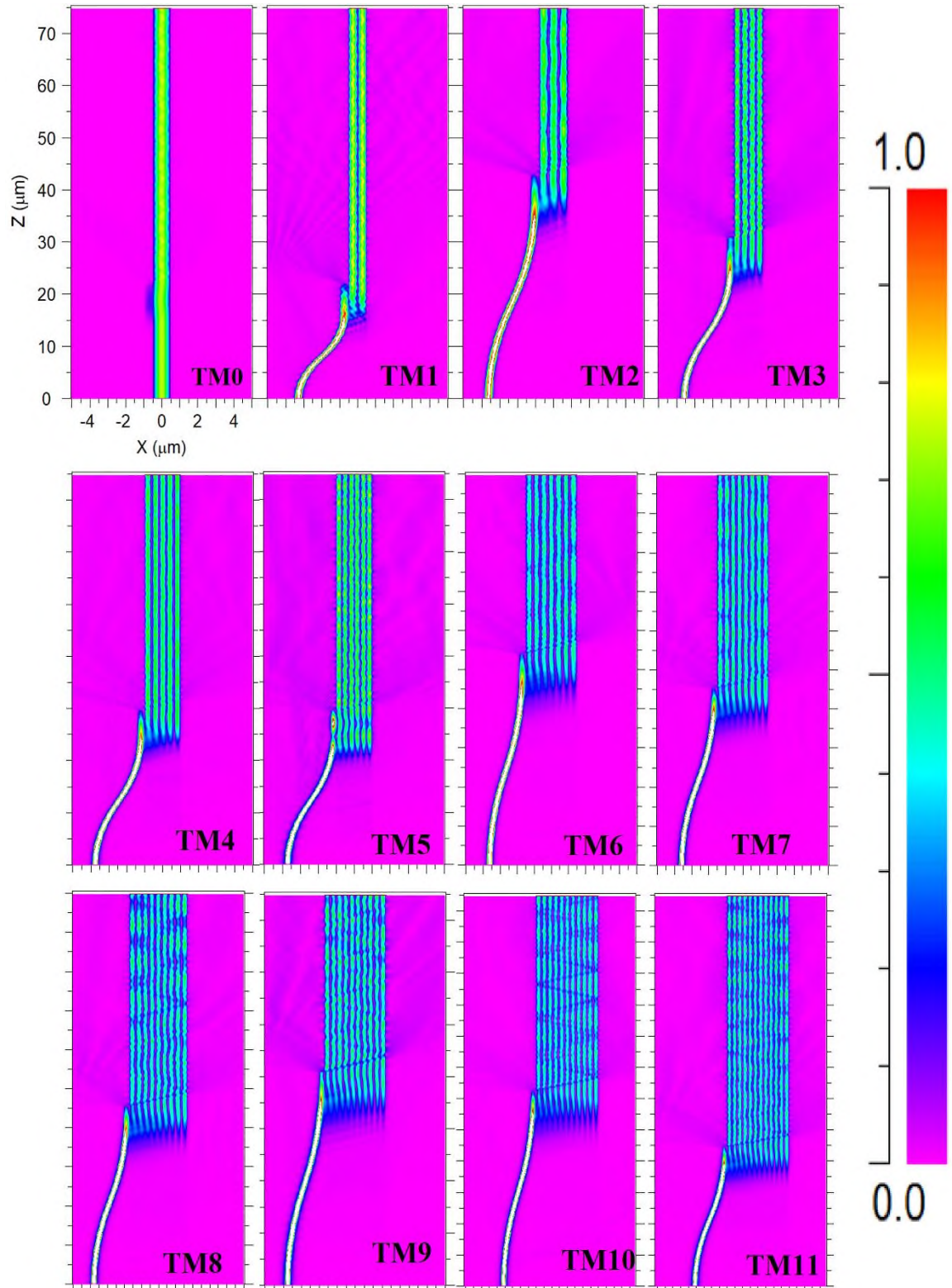


**Figure 3.15:** Intensity distribution across the 12 TM-mode device for each case of excited high-order mode. Values on both axes are in  $\mu\text{m}$ .

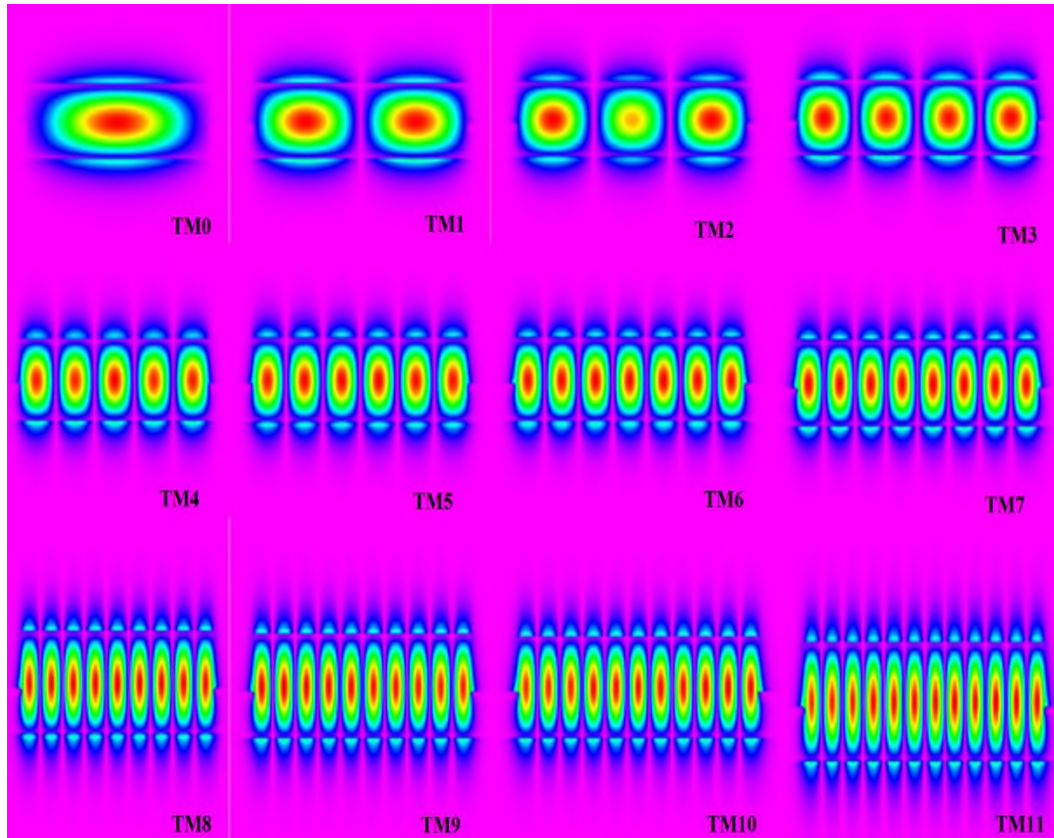


**Figure 3.16:** Excited high-order mode cross-section detected at the output end of the 12 TM-mode designed device.

**Table 3.9** 12-TM mode device insertion loss (dB) at  $1.55 \mu\text{m}$ .

Excited high-order mode	Insertion loss (I.L)
TM <sub>0</sub>	-0.00007
TM <sub>1</sub>	-0.27
TM <sub>2</sub>	-0.38
TM <sub>3</sub>	-0.63
TM <sub>4</sub>	-0.25
TM <sub>5</sub>	-0.61
TM <sub>6</sub>	-0.39
TM <sub>7</sub>	-0.40
TM <sub>8</sub>	-0.57
TM <sub>9</sub>	-0.72
TM <sub>10</sub>	-0.40
TM <sub>11</sub>	-0.50

The calculated insertion loss  $I.L$  (dB) is given in Table 3.9 which is obvious that the device shows a maximum insertion loss of -0.7 dB. The crosstalk  $C.T$  (dB) measures the effect of the output ports on each other in the case of demultiplexing operation, and the result is shown in Figure 3.17 where the device always shows crosstalk lower than -15 dB.

The 1-dB/3-dB operating bandwidths of the device are calculated over a wavelength range (1.400-1.700)  $\mu\text{m}$ . The results are depicted in Figure 3.18 (a and b) and shown numerically in Table 3.10. The device shows minimum operating bandwidth of 130 nm, and 190 nm for 1-dB and 3-dB, respectively.

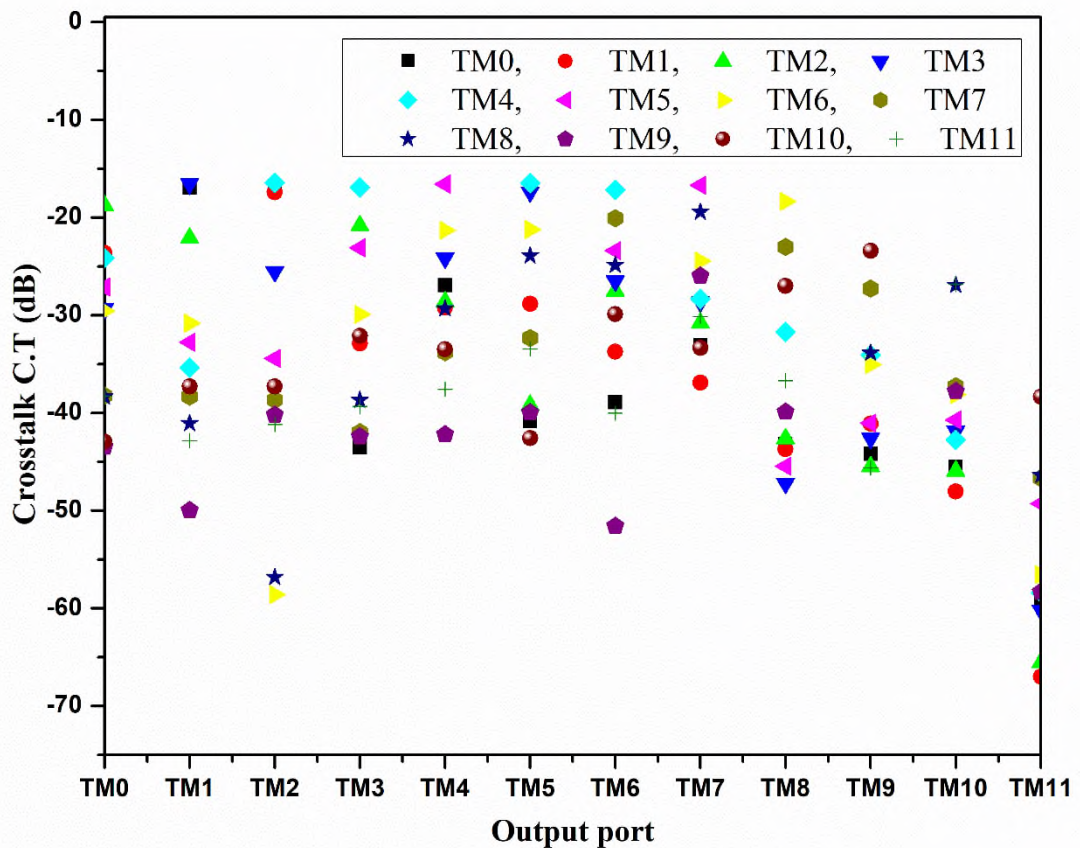
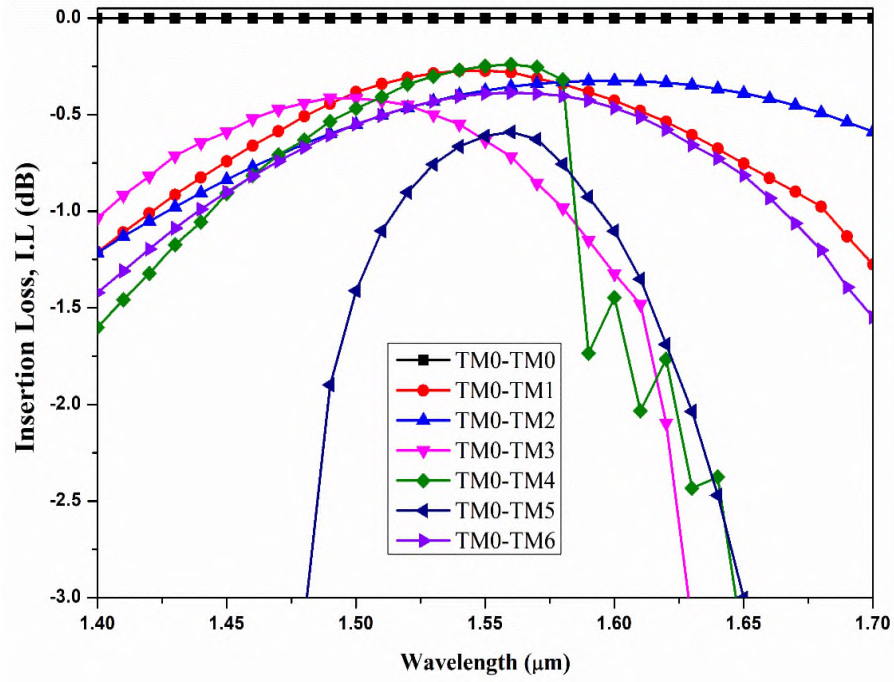
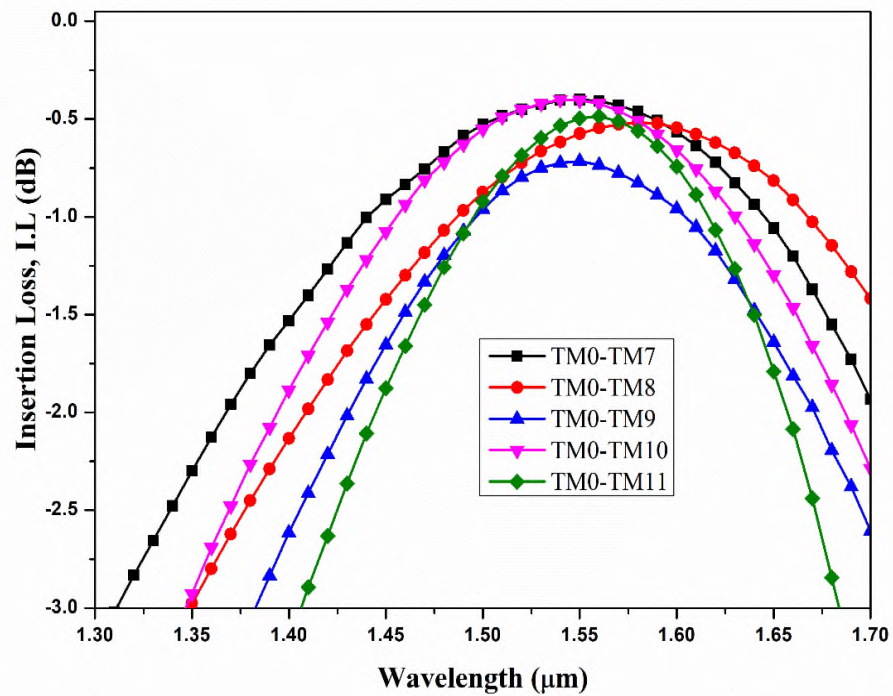


**Figure 3.17:** The proposed device crosstalk for demultiplexing operation.



(a)



(b)

**Figure 3.18:** Insertion loss spectrum of the 12-TM mode device operating bandwidth (a)  $TM_0$ - $TM_6$ , (b)  $TM_7$ - $TM_{11}$ .

**Table 3.10** 12-TM mode designed device operating bandwidths.

Mode	1-dB bandwidth ( $\mu\text{m}$ )	3-dB bandwidth ( $\mu\text{m}$ )
TM <sub>0</sub>	> 0.5	> 0.5
TM <sub>1</sub>	1.390-1.700	1.250-1.700
TM <sub>2</sub>	1.390-1.700	1.200-1.700
TM <sub>3</sub>	1.350-1.610	1.240-1.630
TM <sub>4</sub>	1.420-1.600	1.300-1.660
TM <sub>5</sub>	1.490-1.620	1.470-1.660
TM <sub>6</sub>	1.400-1.690	1.270-1.700
TM <sub>7</sub>	1.410-1.670	1.290-1.700
TM <sub>8</sub>	1.430-1.700	1.320-1.700
TM <sub>9</sub>	1.440-1.650	1.350-1.700
TM <sub>10</sub>	1.420-1.660	1.330-1.700
TM <sub>11</sub>	1.470-1.640	1.390-1.700

A comparison between the performance of the designed devices and the recently reported ADC-based (de)multiplexers is presented in Table 3.11. The proposed devices offer lower losses, higher-order modes, and wider operating bandwidths compared to those reported in both [88] and [91].

**Table 3.11** Performance comparison of the designed devices with the previously reported ones.

Ref#	Structure	No. of modes	I.L (dB)	C.T (dB)	B.W ( $\mu\text{m}$ )
88	Conventional ADC-based (de)multiplexer	5 TE	-0.24	< -33	(1.530-1.570)
91	SWG-assisted ADC-based (de)multiplexer	3 TE	> -1.7	< -15	(1.500-1.600)
This work	SWG-assisted ADC-based (de)multiplexer	12 TE	> -0.6	< -15	(1.480-1.600)
		12 TM	> -0.7	< -15	(1.490-1.620)

### 3.5 Dual-polarization SWG-assisted ADC (De)multiplexer

For the sake of capacity increase in the optical transmission system, hybrid systems supporting both mode- and polarization-division multiplexing (MDM-PDM) technology have proved their effectiveness. Such systems, multiplexes two differently polarized modes, the TE-modes and TM-modes. First, the system is made so that each polarization has its structure using the previously designed ones. Then the two structures are combined through a suitable polarization beam splitter (PBS) placed on certain pair of input  $TE_0/TM_0$  ports. The overall setup is shown in Figure 3.19, where the right side represents the TE- modes and the left side for the TM-modes. This setup can serve 24 modes in total, i.e. double the capacity of previously designed devices with the same performance characteristics in terms of losses and operating bandwidth. The field propagation along the structure for each case of excited mode is presented in Figure 3.20.

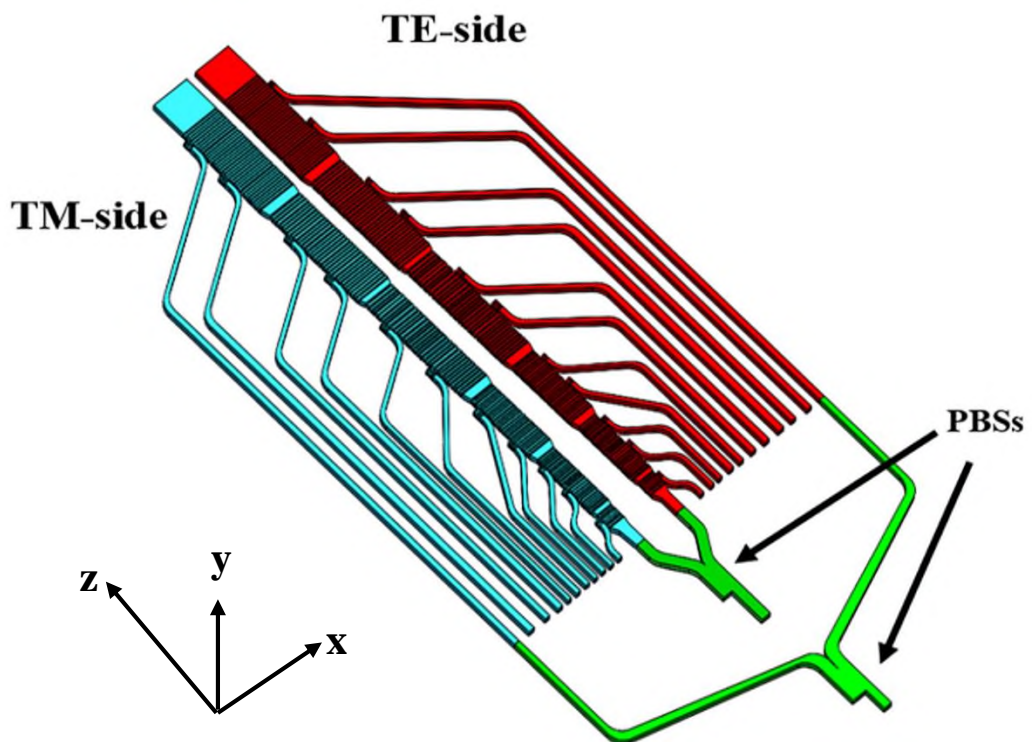


**Figure 3.19:** Schematic configuration of the proposed 24-mode multiplexer.

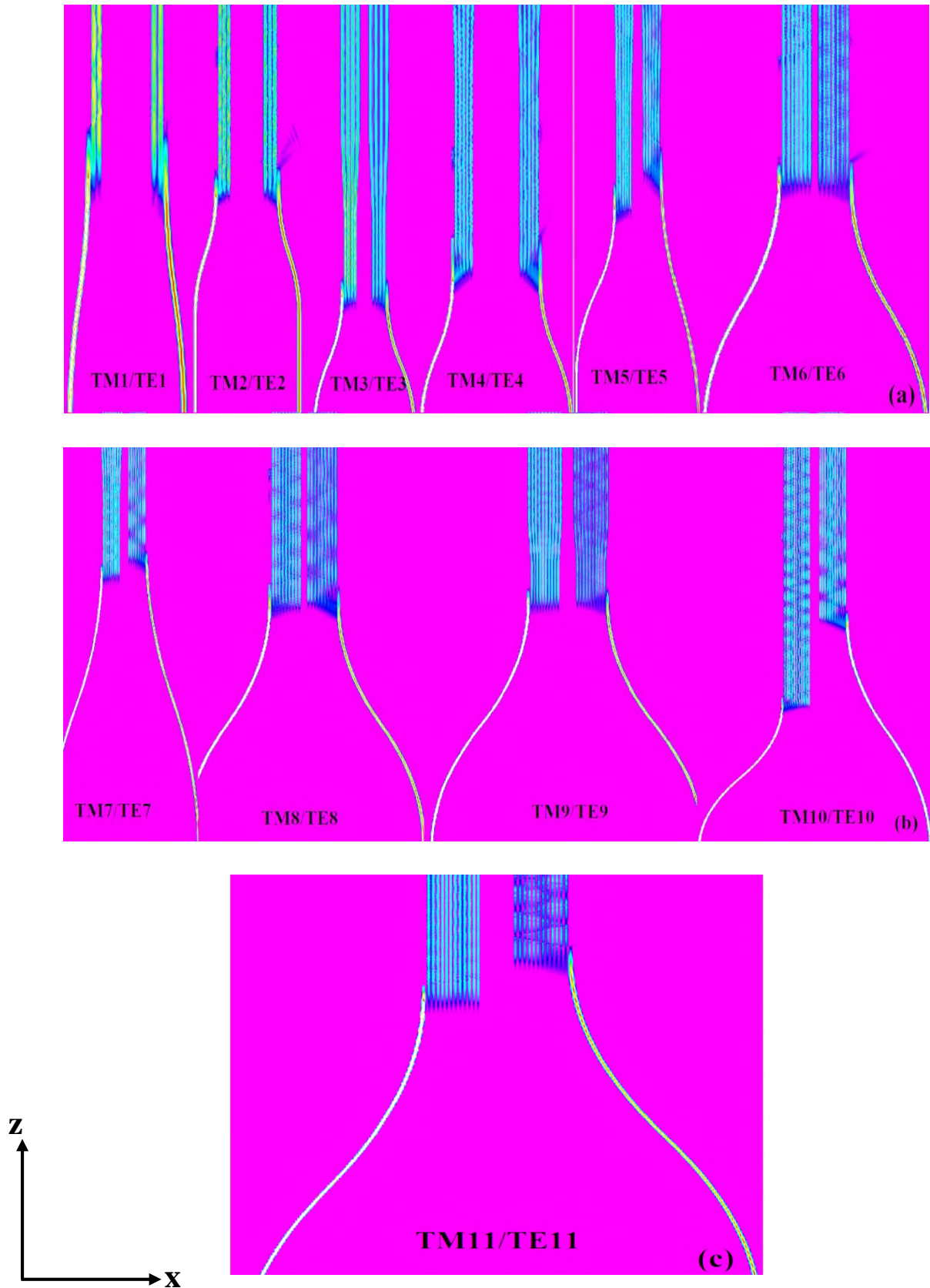


**Figure 3.20:** Field propagation of the proposed 24 modes across the designed structure (a) TE<sub>1</sub>/TM<sub>1</sub> to TE<sub>6</sub>/TM<sub>6</sub>, (b) TE<sub>7</sub>/TM<sub>7</sub> to TE<sub>10</sub>/TM<sub>10</sub>, (c) TE<sub>11</sub>/TM<sub>11</sub>. Values on both axes are in  $\mu\text{m}$ .

To combine the operation of the previously designed devices for 24 modes of expansion, their input ports are required to be connected through polarization beam splitters (PBSs) connecting the counterpart ports from each device. The schematic diagram of the designed MMI-based PBS is shown in Figure 3.21. The splitter consists of a main section of width and length denoted by  $w_{pbs}$  and  $L_{pbs}$ , respectively, and input and output ports of width  $w_a$ . The dimensions of the splitter are chosen through numerical simulation so that each port is assigned to a specific type of mode polarization with maximum transmission and minimum to the other one. In this device, the TE-mode is observed at the end of the left output port whereas the TM-mode is observed at the right one.

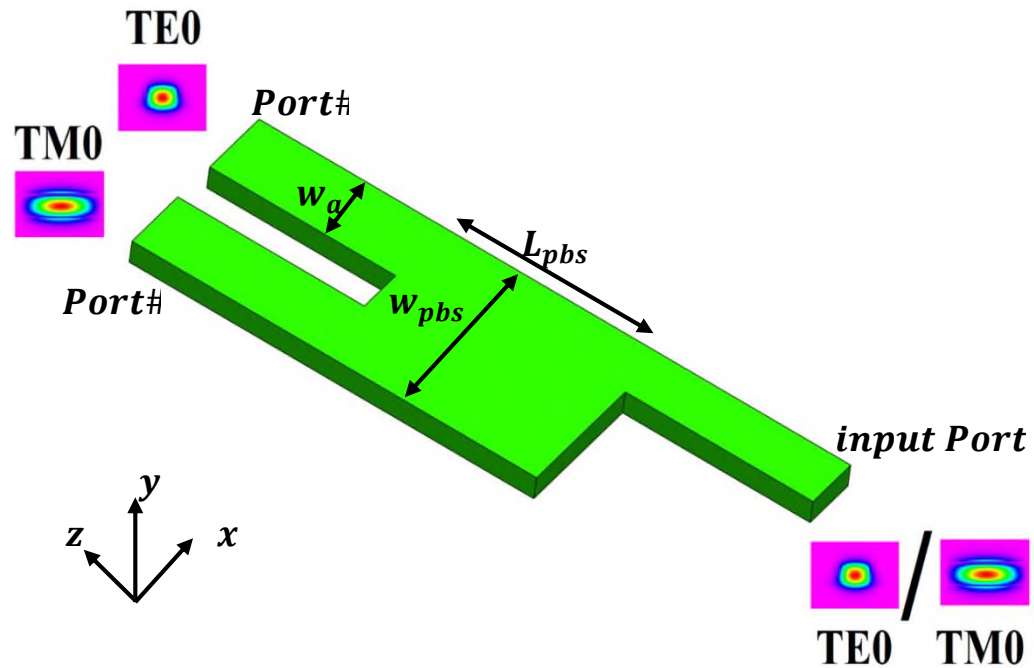


**Figure 3.21:** Schematic configuration of the polarization beam splitter.

The two main parameters of the splitter are simulated for the desired function where the length is scanned over the range (36-38  $\mu\text{m}$ ) and in parallel, the width is scanned over the range (0.9-1.3  $\mu\text{m}$ ), note that these ranges are chosen for compactness purposes and avoid adding additional complexity to

the structure. The results are depicted in Figures 3.22 and 3.23. From these results, it is obvious that the splitter shows acceptable performance at the values of  $1 \mu\text{m}$  and  $37.6 \mu\text{m}$  for  $w_{pbs}$  and  $L_{pbs}$ , respectively.

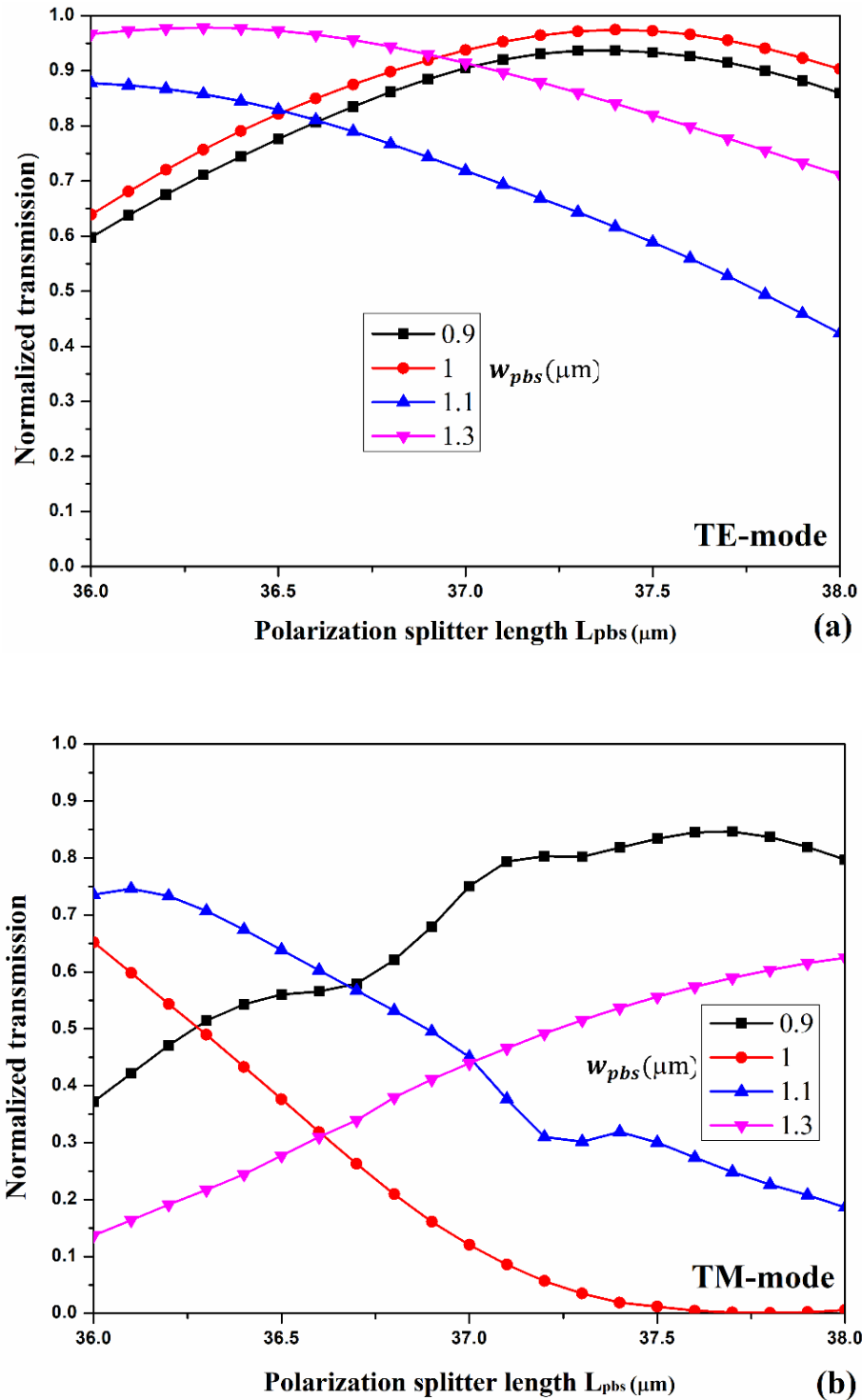


**Figure 3.22:** Splitter port#1 normalized transmission for the case of (a) TE modes, (b) TM modes.

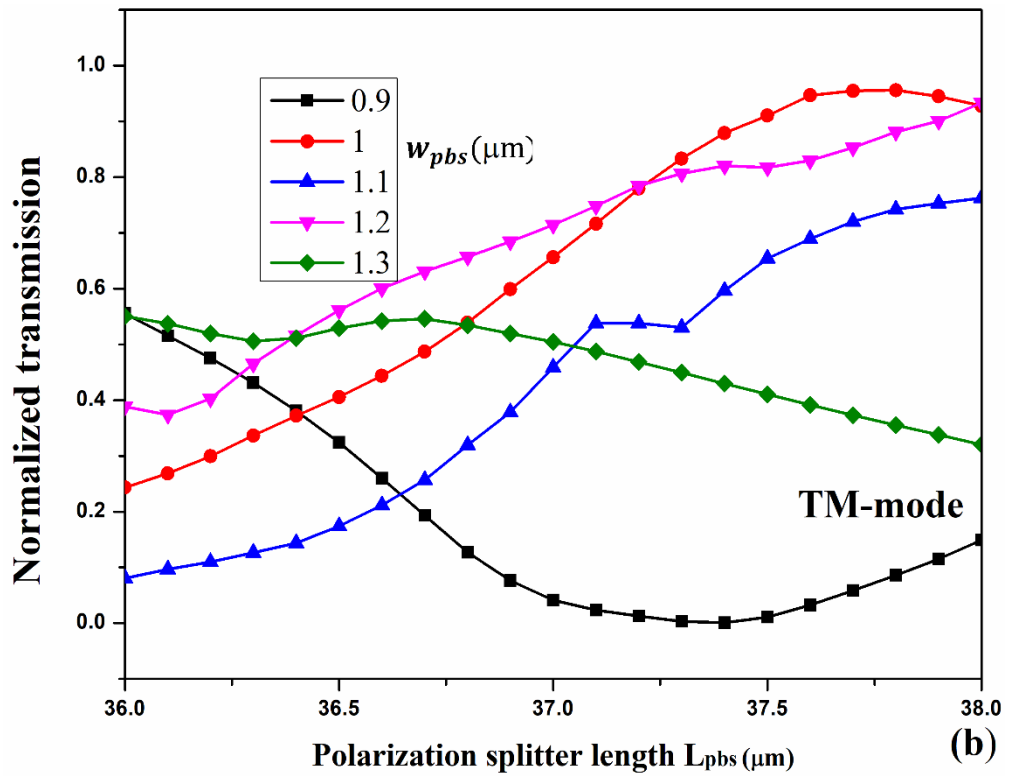
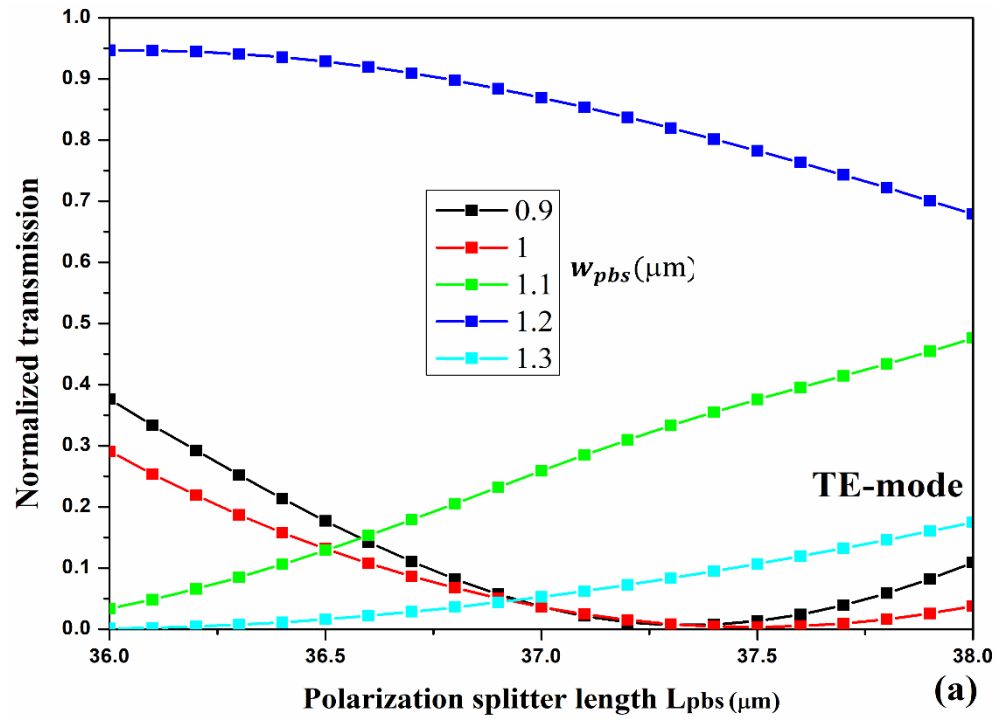


**Figure 3.23:** Splitter port#2 normalized transmission for the case of (a) TE modes, (b) TM modes.

After setting the desired values of the parameters, the designed polarization splitter is simulated and the results are depicted in Figure 3.24 for each case of the input polarization.

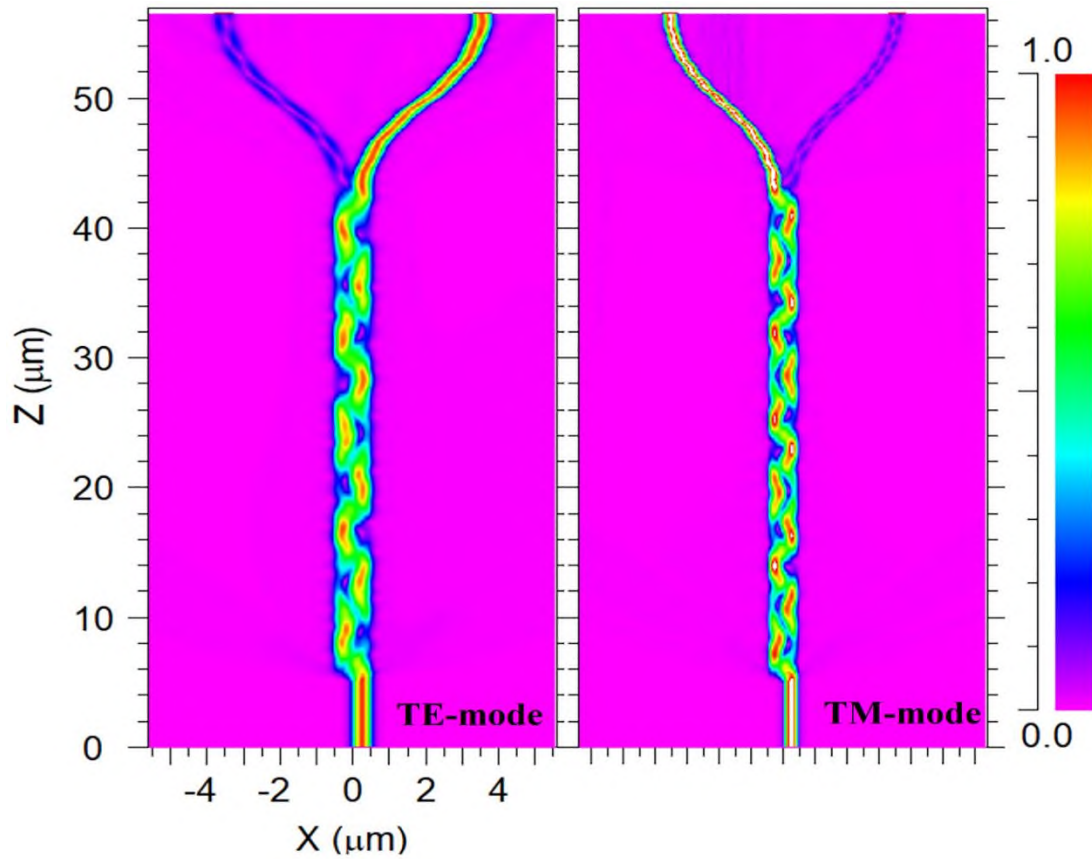


**Figure 3.24:** Field propagation of the proposed polarization beam splitter.

The left for TE mode and the right for TM mode.

Values on both axes are in  $\mu\text{m}$ .

# **Chapter Four**

## **Conclusions and Suggestions for Future Work**

4.1 Conclusions
4.2 Suggestions for Future Work

## CHAPTER FOUR

### Conclusions and Suggestions for Future Work

#### 4.1 Conclusions

This thesis has presented a work that focuses on the design and performance investigation of the multimode interferometer (MMI)-based and asymmetric directional coupler (ADC)-based (de)multiplexers built using subwavelength grating (SWG) technology and operating at the C-band wavelength range. The main goal is to obtain better compactness, performance, and operating bandwidth in comparison to the existing counterpart devices. The following points are the main conclusions drawn from the work

- i. A 3-TE mode (de)multiplexer using a  $3 \times 3$  SWG-assisted MMI coupler, phase shifter, and a tri-junction splitter has been successfully designed and operated. The numerical simulations obtained from device performance evaluations show that the device has an insertion loss  $> -1.3$  dB, crosstalk better than  $-15$  dB, and an operating bandwidth of 120 nm (1.490–1.610)  $\mu\text{m}$ . The designed device's overall footprint is as compact as  $4.5 \times 120 \mu\text{m}^2$  and can offer good performance even with fabrication imperfections.
- ii. A 3-TE mode (de)multiplexer presented in point (i) is later built completely using SWG technology and its performance is re-evaluated. Consequently, while maintaining low losses, a compact and ultra-wideband device has been obtained. The insertion loss of the device is  $> -1$  dB, crosstalk reaching  $-65$  dB over an operating bandwidth of 160 nm (1.470 to 1.630)  $\mu\text{m}$ . The footprint of the designed device is  $4 \times 95 \mu\text{m}^2$ , i.e. about 30% shrink in the overall area. Again, the new device shows a good performance in response to the errors that might occur during the fabrication process.

- iii. A 4-TE mode MMI-based (de)multiplexer has been presented for the first time, first using a conventional MMI coupler, then replaced with an SWG- assisted MMI coupler. The performance of both devices has been evaluated and compared to address the enhancements obtained from considering the SWG technology.
- iv. The conventional 4-mode MMI coupler device showed an 80 nm operating bandwidth (1.510–1.590)  $\mu\text{m}$  with insertion loss and crosstalk  $> -0.5$  dB and  $< -15$  dB, respectively. The overall footprint of the device is  $4.5 \times 173$  ( $780 \mu\text{m}^2$ ).
- v. While the insertion loss and crosstalk remain as low as the conventional device, the SWG-assisted MMI coupler device showed a 140 nm operating bandwidth (1.480–1.620)  $\mu\text{m}$ . The overall footprint of the new device is  $4.5 \times 123$  ( $550 \mu\text{m}^2$ ). Thus, the SWG technology offers low losses, a 30% enhancement in the compactness, and 75% additional operating bandwidth of the new device compared to the conventional counterpart.
- vi. An ultra-broadband and low loss 12-TE mode multiplexer has been designed based on SWG technology and waveguides cascading structure.
- vii. The designed device shows insertion loss and crosstalk  $> -0.6$  dB, and  $< -15$  dB respectively, and a minimum bandwidth of 120 nm (1.480-1.600)  $\mu\text{m}$ . Further, the device offered a good degree of compactness with a 300  $\mu\text{m}$  overall length.
- viii. A 12-TM mode multiplexer is designed based on SWG technology and waveguides cascading structure. the losses of the device obtained are  $> -0.7$  dB, and  $< -15$  dB for insertion loss and crosstalk, respectively. the minimum operating bandwidth of the designed device is 130 nm (1.490-1.620)  $\mu\text{m}$ .

- ix. For an extra capacity, a 24-mode (de)multiplexer has been obtained through the connection of previously designed 12-TE and 12-TM mode devices with carefully designed polarization beam splitters.
- x. Finally, these results confirm that the SWG technology serves the purpose to design wideband, low insertion loss, and fabrication tolerant devices that can be used in silicon photonic integrated circuits and WDM to expand the transmission data rate capacity.

## **4.2 Suggestions for Future Work**

The work in this thesis can be extended in the future to address the following points

- i. Fabricating of the proposed devices to investigate their performance practically.
- ii. Expanding the MMI-based devices to operate in the TM-mode.
- iii. Designing an all-SWG 4-TE mode device.
- iv. Using new material platforms for implementing the designed devices and investigating their performance in the new environment.
- v. Studying the nonlinear phenomena that might occur and their effect on the performance of the designed devices.

## References

- [1] S. E. Miller, “Integrated optics: an introduction,” *Bell Syst. Tech. J.* 48, 2059 (1969).
- [2] C. F. Lam, “Fiber to the home: getting beyond 10 Gb/s,” *Opt. Photonics News*, vol. 27, no. 3, pp. 22-29, 2016, doi: 10.1364/opn.27.3.000022.
- [3] H. Liu, C. F. Lam, and C. Johnson, “Scaling optical interconnects in datacentre networks opportunities and challenges for WDM,” in *18th IEEE Symposium on High Performance Interconnects*, p. 113-116, Mountain View (USA), Aug. 2010. doi: 10.1109/HOTI.2010.15..
- [4] J. A. Tatum *et al.*, “VCSEL-based interconnects for current and future data centers,” *J. Light. Technol.*, vol. 33, no. 4, pp. 727–732, 2015, doi: 10.1109/JLT.2014.2370633.
- [5] A. Polman and H. A. Atwater, “Photonic design principles for ultrahigh-efficiency photovoltaics,” *Nat. Mater.*, vol. 11, no. 3, pp. 174–177, 2012, doi: 10.1038/nmat3263.
- [6] D. A. B. Miller, “Attojoule optoelectronics for low-energy information processing and communications,” *J. Light. Technol.*, vol. 35, no. 3, pp. 346–396, 2017, doi: 10.1109/JLT.2017.2647779.
- [7] J. L. de Miguel *et al.*, “Experimental demonstration of low-uncertainty calibration methods for bragg grating interrogators,” *Sensors (Switzerland)*, vol. 18, no. 6, 2018, doi: 10.3390/s18061895.
- [8] A. V. Velasco *et al.*, “Optical fiber interferometer array for scanless Fourier-transform spectroscopy,” *Opt. Lett.*, vol. 38, no. 13, pp. 2262-2264, 2013, doi: 10.1364/ol.38.002262.
- [9] F. Rodríguez-Barrios *et al.*, “Distributed brillouin fiber sensor assisted by first-order raman amplification,” *J. Light. Technol.*, vol. 28, no. 15, pp. 2162–2172, 2010, doi: 10.1109/JLT.2010.2051141.
- [10] M. Lipson, “Guiding, modulating, and emitting light on Silicon - Challenges and opportunities,” *J. Light. Technol.*, vol. 23, no. 12, pp. 4222–4238, 2005, doi: 10.1109/JLT.2005.858225.
- [11] Q. Cheng, M. Bahadori, M. Glick, S. Rumley, and K. Bergman, “Recent advances in optical technologies for data centers: a review,” *Optica*, vol. 5, no. 11, pp. 1354-1370, 2018, doi: 10.1364/optica.5.001354.

- [12] Cisco Annual Internet Report (2018–2023), <https://www.cisco.com/c/en/us/solutions/collateral/executive-perspectives/annual-internet-report/white-paper-c11-741490.html>, Visited on 31-1-2022.
- [13] B. G. Lee *et al.*, “Ultrahigh-bandwidth silicon photonic nanowire waveguides for on-chip networks,” *IEEE Photonics Technol. Lett.*, vol. 20, no. 6, pp. 398–400, 2008, doi: 10.1109/LPT.2008.916912
- [14] Z. Liu *et al.*, “ $25 \times 50$  Gbps wavelength division multiplexing silicon photonics receiver chip based on a silicon nanowire-arrayed waveguide grating,” *Photonics Res.*, vol. 7, no. 6, pp. 659–663, 2019, doi: 10.1364/prj.7.000659.
- [15] D. Dai and J. E. Bowers, “Silicon-based on-chip multiplexing technologies and devices for Peta-bit optical interconnects,” *Nanophotonics*, vol. 3, no. 4–5, pp. 283–311, 2014, doi: 10.1515/nanoph-2013-0021.
- [16] C. Alessandri *et al.*, “ $5 \times 25$  Gbit/s WDM transmitters based on passivated graphene–silicon electro-absorption modulators,” *Appl. Opt.*, vol. 59, no. 4, pp. 1156–1162, 2020, doi: 10.1364/AO.383462.
- [17] C. R. Doerr *et al.*, “Monolithic Polarization and Phase Diversity Coherent Receiver in Silicon,” *J. Light. Technol.*, vol. 28, no. 4, pp. 520–525, 2010, doi: 10.1109/JLT.2009.2028656
- [18] S. Chen, Y. Shi, S. He, and D. Dai, “Compact monolithically-integrated hybrid (de)multiplexer based on silicon-on-insulator nanowires for PDM-WDM systems,” *Opt. Express*, vol. 23, no. 10, pp.12840–12849, 2015, doi: 10.1364/oe.23.012840.
- [19] W. Song *et al.*, “High-density waveguide superlattices with low crosstalk,” *Nat. Commun.*, vol. 6, no. 1, Article no.7027, 2015, doi: 10.1038/ncomms8027.
- [20] D. Dai, W. Zhao, and D. Liu, “Multimode silicon photonics devices,” *Opt. InfoBase Conf. Pap.*, vol. 8, no. 2, pp. 227–247, 2021, doi: 10.1364/oecc.2021.s3e.1.
- [21] Rene Daendliker "Concept of modes in optics and photonics", Proc. SPIE 3831, *Sixth International Conference on Education and Training in Optics and Photonics*, (16 June 2000), doi:10.1117/12.388718.

- [22] L. Gan *et al.*, “Investigation of channel model for weakly coupled multicore fiber,” *Opt. Express*, vol. 26, no. 5, pp. 5182-5519, 2018, doi: 10.1364/oe.26.005182.
- [23] K. S. Chiang, “Polymer optical waveguide devices for mode-division-multiplexing applications,” SPIE Optics and Optoelectronics, 2017, Prague, Czech Republic, Proceedings vol. 10242- Integrated. Opt. Phys. Simulations III, paper 102420R, 2017, doi: 10.1117/12.2265275.
- [24] G. Li, N. Bai, N. Zhao, and C. Xia, “Space-division multiplexing: the next frontier in optical communication,” *Adv. Opt. Photonics*, vol. 6, no. 4, pp. 413-48, 2014, doi: 10.1364/aop.6.000413.
- [25] C. Montero-Orille *et al.*, “Ion-exchanged glass binary phase plates for mode-division multiplexing,” *Appl. Opt.*, vol. 52, no. 11, pp. 2332–2339, 2013, doi: 10.1364/AO.52.002332.
- [26] A. Forbes, A. Dudley, and M. McLaren, “Creation and detection of optical modes with spatial light modulators,” *Adv. Opt. Photonics*, vol. 8, no. 2, pp. 200-227, 2016, doi: 10.1364/aop.8.000200.
- [27] C. Koebele *et al.*, “Two mode transmission at 2x100Gb/s, over 40km-long prototype few-mode fiber, using LCOS-based programmable mode multiplexer and demultiplexer,” *Opt. Express*, vol. 19, no. 17, pp. 16593–16600, 2011, doi: 10.1364/OE.19.016593.
- [28] J. F. Morizur *et al.*, “Efficient and mode-selective spatial multiplexer based on multi-plane light conversion,” *Opt. Fiber Commun. Conf. OFC 2015*, vol. 22, no. 13, pp. 488–496, 2015, doi: 10.1364/oe.22.015599.
- [29] S. G. Leon-Saval *et al.*, “Mode-selective photonic lanterns for space-division multiplexing,” *Opt. Express*, vol. 22, no. 1, pp. 1036–1044, 2014, doi: 10.1364/OE.22.001036.
- [30] A. M. Velázquez-Benítez *et al.*, “Scaling photonic lanterns for space-division multiplexing,” *Sci. Rep.*, vol. 8, no. 1, pp. 1–9, 2018, doi: 10.1038/s41598-018-27072-2.
- [31] J. Leuthold, R. Hess, J. Eckner, P. A. Besse, and H. Melchior, “Spatial mode filters realized with multimode interference couplers,” *Opt. Lett.*, vol. 21, no. 11, pp. 836-838, 1996, doi: 10.1364/ol.21.000836.
- [32] T. Uematsu, Y. Ishizaka, Y. Kawaguchi, K. Saitoh, and M. Koshiba, “Design of a compact two-mode multi/demultiplexer consisting of

multimode interference waveguides and a wavelength-insensitive phase shifter for mode-division multiplexing transmission,” *J. Light. Technol.*, vol. 30, no. 15, pp. 2421–2426, 2012, doi: 10.1109/JLT.2012.2199961.

[33] Y. Ding, J. Xu, F. Da Ros, B. Huang, H. Ou, and C. Peucheret, “On-chip two-mode division multiplexing using tapered directional coupler-based mode multiplexer and demultiplexer,” *Opt. Express*, vol. 21, no. 8, pp. 10376–10382, 2013, doi: 10.1364/oe.21.010376.

[34] N. Hanzawa, K. Saitoh, T. Sakamoto, T. Matsui, K. Tsujikawa, M. Koshihara, and F. Yamamoto, “Two-mode PLC-based mode multi/demultiplexer for mode and wavelength division multiplexed transmission,” *Opt. Express*, vol. 21, no. 22, pp. 25752–25760, 2013.

[35] D. Dai, J. Wang, and Y. Shi, “Silicon mode (de)multiplexer enabling high capacity photonic networks-on-chip with a single-wavelength-carrier light,” *Opt. Lett.*, vol. 38, no. 9, pp. 1422–1424, 2013, doi: 10.1364/ol.38.001422.

[36] N. Hanzawa *et al.*, “Mode multi/demultiplexing with parallel waveguide for mode division multiplexed transmission,” *Opt. Express*, vol. 22, no. 24, pp. 29321–29330, 2014, doi: 10.1364/oe.22.029321.

[37] J. Wang, S. He, and D. Dai, “On-chip silicon 8-channel hybrid (de)multiplexer enabling simultaneous mode- and polarization-division-multiplexing,” *Laser Photonics Rev.*, vol. 8, no. 2, pp. 18–22, 2014, doi: 10.1002/lpor.201300157.

[38] M. Greenberg and M. Orenstein, “Multimode add-drop multiplexing by adiabatic linearly tapered coupling,” *Opt. Express*, vol. 13, no. 23, pp. 9381–9387, 2005, doi: 10.1364/opex.13.009381.

[39] L. Han, S. Liang, H. Zhu, L. Qiao, J. Xu, and W. Wang, “Two-mode de/multiplexer based on multimode interference couplers with a tilted joint as phase shifter,” *Opt. Lett.*, vol. 40, no. 4, pp. 518–521, 2015, doi: 10.1364/ol.40.000518.

[40] F. Guo *et al.*, “An MMI-based mode (DE) MUX by varying the waveguide thickness of the phase shifter,” *IEEE Photonics Technol. Lett.*, vol. 28, no. 21, pp. 2443–2446, 2016, doi: 10.1109/LPT.2016.2599934.

[41] D. Dai, “Advanced passive silicon photonic devices with asymmetric waveguide structures,” *Proc. IEEE*, vol. 106, no. 12, pp. 2117–2143, 2018, doi: 10.1109/JPROC.2018.2822787.

[42] Liu, J., “Photonics devices”, Cambridge University Press, 2010.

- [43] G. P. Agrawal, “Lightwave Technology: Components and Devices,” John Wiley, 2004.
- [44] K. Tanvir and A. Rony, “Waveguide devices for mode division multiplexing optical communication”, Ph.D., City University of Hong Kong, 2019.
- [45] A. Sosa, “Design of silicon photonic multimode interference couplers,” Ph.D., Research Center of Microperipheric Technologies, 2012.
- [46] L. Sun, Y. Zhang, Y. He, H. Wang, and Y. Su, “Subwavelength structured silicon waveguides and photonic devices,” *Nanophotonics*, vol. 9, no. 6, pp. 1321–1340, 2020, doi: 10.1515/nanoph-2020-0070.
- [47] L. Sun, Y. Zhang, Y. He, H. Wang, and Y. Su, “Subwavelength structured silicon waveguides and photonic devices,” *Nanophotonics*, vol. 9, no. 6, pp. 1321–1340, 2020, doi: 10.1515/nanoph-2020-0070.
- [48] W. Zhou, Z. Cheng, X. Chen, K. Xu, X. Sun, and H. Tsang, “Subwavelength engineering in silicon photonic devices,” *IEEE J. Sel. Top. Quantum Electron.*, vol. 25, no. 3, Article no. 2900113, 2019, doi: 10.1109/JSTQE.2019.2899757.
- [49] D. González-Andrade *et al.*, “Ultra-Broadband Mode Converter and Multiplexer Based on Sub-Wavelength Structures,” *IEEE Photonics J.*, vol. 10, no. 2, 2018, doi: 10.1109/JPHOT.2018.2819364.
- [50] H. Xu, D. Dai, and Y. Shi, “Ultra-Broadband and Ultra-Compact On-Chip Silicon Polarization Beam Splitter by Using Hetero-Anisotropic Metamaterials,” *Laser Photonics Rev.*, vol. 13, no. 4, pp. 1–7, 2019, doi: 10.1002/lpor.201800349.
- [51] J. Xiao and Z. Guo, “Ultracompact Polarization-Insensitive Power Splitter Using Subwavelength Gratings,” *IEEE Photonics Technol. Lett.*, vol. 30, no. 6, pp. 529–532, 2018, doi: 10.1109/LPT.2018.2801337.
- [52] Y. Zhang, Y. Cheng, K. Zhang, C. Li, and W. Kong, “Broadband polarization beam splitter based on subwavelength grating in Terahertz,” in *Proc.SPIE*, Jul. 2019, vol. 11064, doi: 10.1117/12.2535633.
- [53] A. Herrero-Bermello *et al.*, “Experimental demonstration of metamaterial anisotropy engineering for broadband on-chip polarization beam splitting,” *Opt. Express*, vol. 28, no. 11, pp. 16385–16393, 2020, doi: 10.1364/oe.389070.

- [54] J. M. Luque-González *et al.*, “Tilted subwavelength gratings: controlling anisotropy in metamaterial nanophotonic waveguides,” *Opt. Lett.*, vol. 43, no. 19, pp. 4691-4694, 2018, doi: 10.1364/ol.43.004691.
- [55] S. Masui, S. Kadoya, M. Michihata, and S. Takahashi, “Theoretical model of a subwavelength grating polarization beam splitter,” *Appl. Opt.*, vol. 59, no. 30, pp. 9469–9475, 2020, doi: 10.1364/AO.405660.
- [56] H. Sattari *et al.*, “Silicon Photonic MEMS Phase-Shifter,” *Opt. Express*, vol. 27, no. 13, pp. 18959–18969, 2019, doi: 10.1364/OE.27.018959.
- [57] D. González-Andrade *et al.*, “Ultra-broadband nanophotonic phase shifter based on subwavelength metamaterial waveguides,” *Photonics Res.*, vol. 8, no. 3, pp. 359-367, 2020, doi: 10.1364/prj.373223.
- [58] W. Chang *et al.*, “Ultra-compact mode (de) multiplexer based on subwavelength asymmetric Y-junction,” *Opt. Express*, vol. 26, no. 7, pp. 8162-8170, 2018, doi: 10.1364/oe.26.008162.
- [59] R. Halir *et al.*, “Subwavelength-Grating Metamaterial Structures for Silicon Photonic Devices,” *Proc. IEEE*, vol. 106, no. 12, pp. 2144–2157, 2018, doi: 10.1109/JPROC.2018.2851614.
- [60] N. L. Kazanskiy, M. A. Butt, and S. N. Khonina, “Silicon photonic devices realized on refractive index engineered subwavelength grating waveguides-A review,” *Opt. Laser Technol.*, vol. 138, Article no. 106863, 2021, doi:10.1016/j.optlastec.2020.106863.
- [61] S. Farhadi, M. Miri, and A. Alighanbari, “Design and simulation of a compact and ultra-wideband polarization beam splitter based on sub-wavelength grating multimode interference coupler,” *Appl. Phys. B Lasers Opt.*, vol. 126, no. 7, 2020, doi: 10.1007/s00340-020-07468-7.
- [62] L. Xu *et al.*, “Compact high-performance adiabatic 3-dB coupler enabled by subwavelength grating slot in the silicon-on-insulator platform,” *Opt. Express*, vol. 26, no. 23, pp. 29873-29885, 2018, doi: 10.1364/oe.26.029873.
- [63] D. Gonzalez-Andrade *et al.*, “Dispersion-engineered nanophotonic devices based on subwavelength metamaterial waveguides,” *2020 IEEE Photonics Conf. IPC 2020 - Proc.*, pp. 15–16, 2020, doi: 10.1109/IPC47351.2020.9252329.
- [64] M. G. Floquet, “Sur les équations différentielles linéaires a coefficients périodiques (On linear differential equations with periodic coefficients),” *Ann. Sci. Éc. Norm. Supér.* vol. 2, no. 12, pp. 47-88, 1883.

- [65] F. Bloch, “Über die quantenmechanik der elektronen in kristallgittern (On the quantum mechanics of electrons in crystal lattices),” *Z. Phys.* Vol. 52, pp. 555-600, 1928.
- [66] S. G. Davison and M. Stęślicka, “Basic theory of surface states”, Oxford: Clarendon Press, 1992.
- [67] R. Sumi, N. Das Gupta, and B. K. Das, “Integrated Optical Linear Edge Filters Using Apodized Sub-Wavelength Grating Waveguides in SOI,” *IEEE Photonics Technol. Lett.*, vol. 31, no. 17, pp. 1449–1452, 2019, doi: 10.1109/LPT.2019.2931520.
- [68] D. G. Andrade, "Subwavelength metamaterials for high-performances photonic micro devices," Ph.D. Thesis, Complutense University of Madrid, 2021.
- [69] I. Molina-Fernández *et al.*, “Subwavelength grating metamaterial structures for integrated photonics,” in *Proc.SPIE*, Feb. 2020, vol. 11284, doi: 10.1117/12.2545061.
- [70] Y. Wang *et al.*, “Ultra-Compact Sub-Wavelength Grating Polarization Splitter-Rotator for Silicon-on-Insulator Platform,” *IEEE Photonics J.*, vol. 8, no. 6, pp. 1–9, 2016, doi: 10.1109/JPHOT.2016.2630849.
- [71] J. Zhang, “Subwavelength engineering of silicon waveguides and cavities for nonlinear photonics,” Ph.D. Thesis, Paris Saclay University (COMUE), 2020.
- [72] P. Cheben, R. Halir, J. H. Schmid, H. A. Atwater, and D. R. Smith, “Subwavelength integrated photonics,” *Nature*, vol. 560, no. 7720, pp. 565–572, 2018, doi: 10.1038/s41586-018-0421-7.
- [73] Y. Zhou and J. Sun, “Silicon-based mode converter and demultiplexer for wavelength division multiplexing transmission by using multimode interference couplers,” *Opt. Photonics J.*, vol. 10, no. 06, pp. 117–124, 2020, doi: 10.4236/opj.2020.106012.
- [74] L. Xu *et al.*, “Ultra-Broadband and Compact Two-Mode Multiplexer Based on Subwavelength-Grating-Slot-Assisted Adiabatic Coupler for the Silicon-on-Insulator Platform,” *J. Light. Technol.*, vol. 37, no. 23, pp. 5790–5800, 2019, doi: 10.1109/JLT.2019.2939260.
- [75] Y. Shi, D. Dai, and S. He, “Improved performance of a silicon-on-insulator-based multimode interference coupler by using taper structures,” *Opt. Commun.*, vol. 253, no. 4–6, pp. 276–282, 2005, doi: 10.1016/j.optcom.2005.04.078.

- [76] J. López, “Design and fabrication of photonic devices Based on multimode interference,” Ph.D. Thesis, National Institute of Astrophysics, Optics and Electronics, 2008.
- [77] D. Q. Duy, H. D. T. Linh, T. C. Dung, N. T. Hung, D. H. Bac, and L. C. Duan, “Three lowest optical modes simultaneous generator based on silicon multimode interference and Y-junction couplers,” in *2019 6th NAFOSTED Conference on Information and Computer Science (NICS)*, 2019, pp. 285–291, doi: 10.1109/NICS48868.2019.9023840.
- [78] L. B. Soldano and E. C. M. Pennings, “Optical multi-mode interference devices based on self-imaging: principles and applications,” *J. Light. Technol.*, vol. 13, no. 4, pp. 615–627, 1995, doi: 10.1109/50.372474.
- [79] J. Wang *et al.*, “Subwavelength grating enabled on-chip ultra-compact optical true time delay line,” *Sci. Rep.*, vol. 6, no. 1, Article no. 30235, 2016, doi: 10.1038/srep30235.
- [80] N. C. Harris *et al.*, “Efficient, compact and low loss thermo-optic phase shifter in silicon,” *Opt. Soc. Am.*, vol. 22, no. 9, pp. 83–85, 2014, doi: 10.1364/OE.22.010487.
- [81] H. Xu, D. Dai, and Y. Shi, “Silicon integrated nanophotonic devices for on-chip multi-mode interconnects,” *Applied Sciences*, vol. 10, no. 18, Article no. 6365, Sep. 2020. doi: 10.3390/app10186365.
- [82] B. Paredes, Z. Mohammed, J. Villegas, and M. Rasras, “Dual-band (O & C-Bands) two-mode multiplexer on the SOI platform,” *IEEE Photonics J.*, vol. 13, no. 3, Article no. 6600309, 2021, doi: 10.1109/JPHOT.2021.3075292.
- [83] D. Dai *et al.*, “10-Channel mode (de)multiplexer with dual polarizations,” *Laser Photonics Rev.*, vol. 12, no. 1, pp. 1–9, 2018, doi: 10.1002/lpor.201700109.
- [84] Y. Xiong, “Silicon Photonic Devices for Sensing , Switching , Polarization and Mode Control,” Ph.D. Thesis, Carleton University, 2014.
- [85] Z. Jafari, A. Zarifkar, and M. Miri, “Compact fabrication-tolerant subwavelength-grating-based two-mode division (de)multiplexer,” *Appl. Opt.*, vol. 56, no. 26, pp. 7311, 2017, doi: 10.1364/ao.56.007311.
- [86] C. D. Truong, T. H. Nguyen, Q. T. Pham, M. T. Trinh, and K. Vu, “Three-mode multiplexer and demultiplexer utilizing trident and multimode couplers,” *Opt. Commun.*, vol. 435, pp. 334–340, 2019, doi: 10.1016/j.optcom.2018.11.003.

- [87] A. Herrero-Bermello et al., “Design of a broadband polarization splitter based on anisotropy-engineered tilted subwavelength gratings,” *IEEE Photonics J.*, vol. 11, no. 3, 2019, DOI: 10.1109/JPHOT.2019.2912335.
- [88] . P. Nath, N. Dhingra, G. J. Saxena, and E. K. Sharma, “Compact Mode Division (de)Multiplexer Based on Collaterally Coupled SOI Waveguides,” *IEEE Photonics Technol. Lett.*, vol. 32, no. 10, pp. 595–598, 2020, DOI: 10.1109/LPT.2020.2985959.
- [89] D. González-Andrade et al., “Experimental demonstration of a broadband mode converter and multiplexer based on subwavelength grating waveguides,” *Opt. Laser Technol.*, vol. 129, no. January, p. 106297, 2020, DOI: 10.1016/j.optlastec.2020.106297.
- [90] H. Shiran, G. zhang, and O. Liboiron-Ladouceur, “Dual-mode broadband compact  $2 \times 2$  optical power splitter using sub-wavelength metamaterial structures,” *Opt. Express*, vol. 29, no. 15, pp. 23864, 2021, DOI: 10.1364/oe.423882.
- [91] W. Jiang et al., “Broadband Silicon Four-Mode (De)Multiplexer Using Subwavelength Grating-Assisted Triple-Waveguide Couplers,” *J. Light. Technol.*, vol. 39, no. 15, pp. 5042–5047, 2021, DOI: 10.1109/JLT.2021.3079911.

## Publications

1. Zaid Lateef Hussain, Raad S. Fyath, “**Design and simulation of a compact three-mode (de)multiplexer based on a subwavelength grating multimode interference coupler,**” *Photonics Nanostructures - Fundam. Appl.*, vol. 47, pp. 100966, 2021, DOI: 10.1016/j.photonics.2021.100966.
2. Zaid Lateef Hussain, Raad S. Fyath, “**All-subwavelength grating compact three-mode (de)multiplexer using multimode interference coupler: design and simulation,**” *Opt. Eng.*, vol. 60, no. 08, pp. 1–22, 2021, DOI: 10.1117/1.oe.60.8.086107.
3. Zaid Lateef Hussain, Raad S. Fyath, “**Design and simulation of 4-mode (de)multiplexers implemented in conventional and subwavelength grating Si/SiO<sub>2</sub> platforms,**” *Optik* , vol. 251, pp. 168449, 2022, DOI: 10.1016/j.ijleo.2021.168449.
4. Zaid Lateef Hussain, Raad S. Fyath, “**Twelve TE-mode (De)Multiplexer using Cascaded Subwavelength Grating Waveguides,**” *Optik*, *Accepted*.
5. Zaid Lateef Hussain, Raad S. Fyath, “**Towards C+L Band Three-Mode (De)Multiplexer Using Subwavelength Grating (SWG) Technology,**” *Iraqi Journal of Laser*, *Accepted*.

# Appendix A

## Rsoft Photonics Suit package

The RSoft CAD is the core program in the RSoft Photonic Device Tools and acts as a control program for the passive device simulation modules BeamPROP BPM, FullWAVE FDTD, BandSOLVE, GratingMOD, DiffractMOD RCWA, FemSIM FEM, and ModePROP EME. It is used to define the most important input required by these simulation modules: the material properties and structural geometry of a photonic device. A user will typically first design a structure in the CAD interface and then use one or more simulation engines to model various aspects of the device performance.

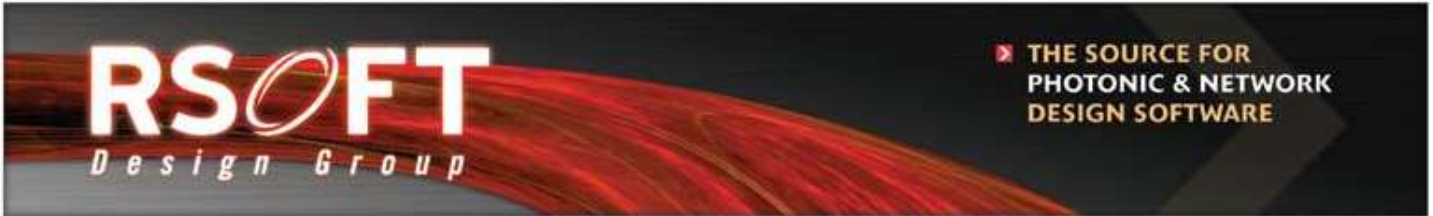


rsoftdesign.com

## Table of Contents

About RSoft Design Group.....	2		
Academic Programs.....	3		
<b>&gt; Photonics Component Design Suite .....</b>	<b>4</b>		
<b>PASSIVE DEVICE</b>			
RSoft CAD Environment™.....	6		
BeamPROP™.....	8		
FullWAVE™.....	10		
BandSOLVE™.....	12		
ModePROP™.....	14		
DiffractMOD™.....	16		
GratingMOD™.....	18		
FemSIM™.....	20		
<b>ACTIVE DEVICE</b>			
LaserMOD™.....	22		
		<b>OPTIONS AND UTILITIES</b>	
		MOST™.....	24
		Solar Cell Utility™.....	26
		Multi-Physics Utility™.....	28
		Tapered Laser Utility™.....	29
		<b>&gt; Optical Communication Design Suite .....</b>	<b>30</b>
		<b>SYSTEM</b>	
		OptSim™.....	32
		ModeSYS™.....	34
		<b>NETWORK</b>	
		MetroWAND™.....	36
		Artifex™.....	38
		Professional Services and Programs.....	40
		Offices, Distributors, System Requirements...	41

30 day evaluations are available upon request.  
 Please contact [sales@rsoftdesign.com](mailto:sales@rsoftdesign.com) for further information.



## About RSoft Design Group

---



**RSoft Design Group** is the worldwide leader in photonic design automation software, and serves several industries including optical communication, optoelectronics, and semiconductor manufacturing. Within optical communications, RSoft is the only company to provide a full range of design, optimization, and planning tools. Within the physical layer, RSoft provides the most extensive collection of award-winning design tools for passive and active optoelectronic components and subsystems.

### History

RSoft Design Group, Inc. is a pioneer in the field of photonic design and simulation software. RSoft released its first software package for the integrated optics industry in 1990. In 2001 RSoft merged with NDTI, a spin off from Telcordia Technologies, and two years later, acquired Artis Srl.. In an effort to capitalize on this growth and provide the highest level of customer service, RSoft has anchored offices in the US, Japan, and Europe, as well as established distributors worldwide. RSoft has been committed to meeting the needs for passive and active device design as well as optical communication systems simulation since 1990, and looks forward to providing solutions well into the future.

### Government *Contracts*

RSoft has participated in multiple government contracts including a NIST ATP titled PCAD. PCAD was a joint consortium dedicated to Photonics CAD Software and included Telcordia, SAIC, Agilent, Nortel, IBM, JDS Uniphase (SDL), Columbia University, and others. The ambitious five year R&D project created technology included in many of RSoft Design Group's products today.

RSoft has won other government contract awards including multiple SBIRs and STTRs which have resulted in commercialized technology.

### Business *Partners*

We have established partnerships with both hardware and software companies to broaden the capabilities of our software. Hardware companies such as Luna Technologies have partnered with us to integrate our software tools into test and measurement applications. MATLAB®, Cadence, and other software manufacturers, have added extended software benefits to the end user. For additional information about these partnerships, please visit [www.rsoftdesign.com/aboutus](http://www.rsoftdesign.com/aboutus).

## Academic Programs



As the global leader in photonic design automation software, RSoft Design Group is committed to support academic research and education. RSoft's academic program provides professors, researchers, and students at several hundred academic institutions all over the world access to its world-class design tools for photonic components, optical communication systems, and optical network design and planning. This creates an infrastructure in which the next generation of optical engineers can be trained, new ideas can be transformed into reality through advanced research, and RSoft's tools are ensured to meet the latest R&D needs through collaborations with leading research groups.

### Benefits

- › Available single/multi-user license at a discounted price for research and classroom teaching.
- › Collaboration with university research groups to develop advanced simulation features and algorithms.
- › Partnership in government funded research programs.
- › Commercialization of in-house developed models/software and IP licensing.
- › Well developed course tutorials with simulation examples.
- › Demo software with leading text books.
- › Hundreds of application notes and simulation samples.
- › Student scholarships to encourage research of novel modeling and simulation techniques.
- › Practical training and internship program.
- › Joint research publications.
- › Hundreds of published articles, white papers and journals for reference.
- › Well represented in standard organizations and industry associations.

*For more information on our academic program, please contact an RSoft Design Group representative or e-mail: [info@rsoftdesign.com](mailto:info@rsoftdesign.com).*



## RSOFT's Photonic Component Design Suite

RSOFT's Photonic Component Design Suite allows users to design and simulate both passive and active photonic devices for optical communications, optoelectronics, and semiconductor manufacturing.

RSOFT currently addresses both passive and active devices through two design suites: a Passive Device Suite and an Active Device Suite. Each suite includes a CAD environment, simulation engines, and an optimization utility.

### Key Features

- \* Highly accurate algorithms allow for rapid virtual prototyping reducing the need for costly and lengthy physical prototyping increasing productivity and decreasing time-to-market.
- \* Assists in the discovery of new products by creating "what if" product scenarios.
- \* Each algorithm engine shares a common CAD interface; the software can utilize multiple RSOFT packages without having to import designs from one software to the next.
- \* Scripting can be done with any programming language.
- \* Includes automated parameter scanning via MOST.
- \* Each simulation engine is licensed separately, allowing users to choose only those that are relevant to their work.



**PASSIVE DEVICE** ▶

***RSOFT CAD Environment***  
Layout and control program shared by all RSOFT's passive device simulators

***BeamPROP***  
Simulates waveguides and fiber applications

***FullWAVE***  
Simulates PBG nanotechnology applications, and biophotonic

***BandSOLVE***  
Computes band structures of photonic bandgap devices

***ModePROP***  
Eigenmode propagation tool

***DiffractMOD***  
Simulates diffractive gratings, semiconductor surface gratings, and metrology applications

***GratingMOD***  
Provides the response of optical gratings and fiber Bragg gratings

***FemSIM***  
Transverse and cavity mode solver for arbitrary structures

**ACTIVE DEVICE** ▶

***LaserMOD***  
Simulates active device applications

## Options & Utilities



RSoft's Options and Utilities extend the capability of RSoft's software tools to provide a complete simulation solution. These tools provide additional simulation options and can be used to combine multiple tools to study advanced application areas.

## Key Features

- \* Provide an easy and simple method to incorporate additional simulation capabilities with RSoft's simulation tools.
- \* Combine the strengths of multiple simulation tools to meet the needs of specific application areas.
- \* Each simulation engine is licensed separately, allowing users to choose only those that are relevant to their work.
- \* Certain options and utilities are included in a limited form with some of RSoft's simulation tools. See product descriptions for complete licensing details.

### OPTIONS AND UTILITES



#### ***MOST***

A design optimization utility for all of RSoft's passive device design tools

#### ***Solar Cell Utility***

Simulates solar cells

#### ***Multi-Physics Utility***

Extends passive device simulator capabilities to include index perturbations from physical effects

#### ***Tapered Laser Utility***

Models tapered laser cavities



The RSoft CAD Environment is the core program of the RSoft Passive Device Suite, and allows researchers and engineers to create systems for the design of waveguide devices, optical circuits, and other photonic devices. It acts as a control program for RSoft's passive device modules, including BeamPROP, FullWAVE, BandSOLVE, ModePROP, DiffractMOD, GratingMOD, and FemSIM, and defines the important input required by these programs: the material properties and structural geometry of the device to be studied.

## Benefits

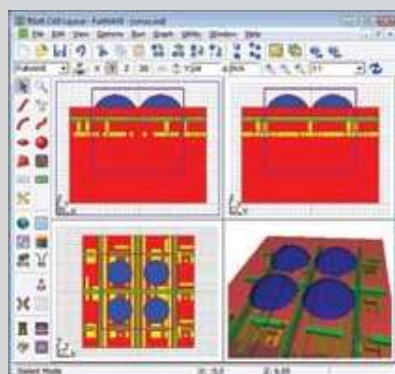
- > Highly flexible design environment allows virtually any geometry to be created.
- > Included with each of RSoft's passive component simulation tools.
- > Provides a unified platform for RSoft's passive component simulation tools; designs do not need to be imported from one software package to another to use different simulation algorithms.
- > Easy to use, streamlined user interface that allows fine control over device layout and simulation.

## Layout Capabilities

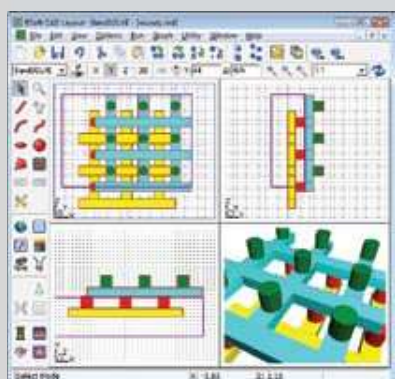
The RSoft CAD Environment has been designed from the ground up to accommodate the special needs of photonic devices and circuits. Fundamental objects such as straight, tapered, and curved components, lenses, and polygons can easily be selected from the toolbar and graphically added to the circuit using the mouse. In addition to standard objects, the CAD allows for the creation of customized components using mathematical equations or data files. Component positions may be specified directly, either absolutely or through relative offsets with respect to any other component. At any time, one or several components may be selected and moved, scaled, deleted, or reinserted. This unique design approach provides an extremely flexible system in which the desired logical arrangement can be maintained.

## Object-Oriented Design

Each individual component can have its own set of properties that can be accessed with a right click of the mouse. Parameters include shape information and optical properties such as refractive index profile type and value. This unique object-oriented input model is extremely flexible. Furthermore, each parameter of a component (e.g. position coordinates, width, index) can be specified by an arithmetic expression involving user-defined variables, rather than simply being a constant number. This allows an entire design to be easily modified by using formulas to define each component's angle, the entire circuit can be modified by simply changing the value of a single variable without having to edit multiple parts of the structure.



Multi-pane view of 3D CMOS design in CAD showing views along the X, Y, and Z axes as well as 3D view.



Multi-pane view of 3D PBG in CAD.

## FEATURES

- \* 3D editing options allow the structure to be viewed along the X, Y, and Z axis.
- \* A multi-pane mode where the X, Y, Z, and rotatable 3D views are shown at once.
- \* Object-oriented design environment (*see previous page*).
- \* Hierarchical Layout allows arbitrarily complicated structures to be built from smaller components.
- \* Mask files in CIF, DXF, and GDS-II formats can be directly imported into the CAD interface. Design files can be exported in both DXF and GDS-II files for mask fabrication.
- \* Includes layout utilities for common periodic structures, grating structures, and AWG structures.
- \* Includes WinPLOT, RSoft's technical graphing program.
- \* Includes DataBROWSWER which allows users to quickly browse and view results.
- \* Several utilities are included for custom pre- and post-processing capabilities including interfaces with popular ray-tracing software packages.

# BeamPROP

COMPONENT DESIGN  
Passive Device



BeamPROP is the industry-leading design tool based on the Beam Propagation Method (BPM) for the design and simulation of integrated and fiber-optic waveguide devices and circuits. The software has been commercially available since 1994, and is in use by leading researchers and development engineers in both university and industrial environments worldwide.

## Benefits

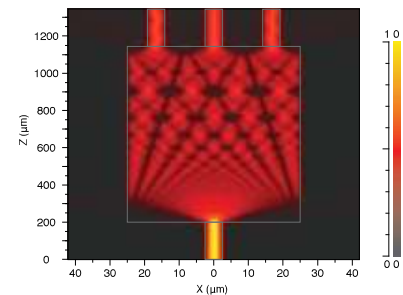
- > Industry-proven BPM algorithm for fast and accurate device design.
- > Built-in advanced AWG utility for simplifying router and demultiplexer design.
- > Advanced capabilities allow for the simulation of complicated devices.
- > Fully integrated into the RSoft CAD Environment (Page 6).

## Applications

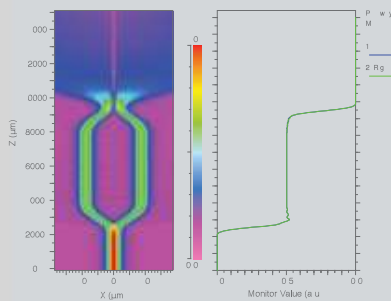
*BeamPROP has applications in a wide range of integrated and fiber-optic devices including, but not limited to:*

- \* WDM devices such as arrayed waveguide grating (AWG) routers
- \* Switches, e.g. directional coupler-based or digital-y type
- \* Modulators, e.g. Mach-Zehnder type
- \* Multimode interference devices
- \* Passive 1 x N or N x N splitters
- \* Laser structure transverse mode analysis
- \* Standard and specialty fiber design
- \* Gratings
- \* Sensor structures

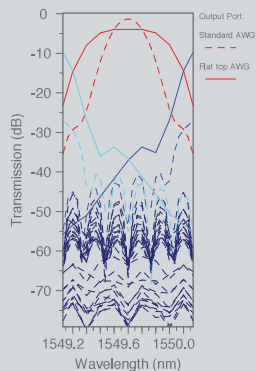
## Featured Application



BeamPROP simulation of a 1 x 3 MMI device. The length of the MMI was optimized so that the three output waveguides contained equal power.



BeamPROP simulation of a Mach-Zehnder modulator operating completely out of phase. The power in each arm is shown on the right.



BeamPROP simulation of a flat-top AWG. The taper on the input port was designed to produce the flat-top response shown. The standard AWG output is also shown as reference.

## FEATURES

- \* Superior, robust and efficient results via an implementation of the Beam Propagation Method (BPM) based on an implicit finite-difference scheme.
- \* 2D and 3D simulation capabilities.
- \* Non-uniform mesh.
- \* Anisotropic and non-linear materials.
- \* Fully integrated with Multi-Physics Utility (Page 28).
- \* Polarization effects and coupling via a full-vectorial BPM implementation.
- \* Wide-angle propagation can be improved by multistep Padé approximation techniques, a variable reference wave number, and conformal index mapping of bends to allow for accurate and efficient off-axis propagation.
- \* Bidirectional BPM formulation for considering reflection along the propagation direction to be considered.
- \* Two BPM-based mode-solvers for the computation of modal propagation constants and profiles for both guided and radiation modes for 2D and 3D geometries.
- \* Comprehensive measurement tools to compute fields, power distribution, loss, etc.
- \* Automated parametric studies and design optimization using MOST (Page 24).

# FullWAVE

COMPONENT DESIGN  
Passive Device



FullWAVE is a highly sophisticated simulation tool for studying the propagation of light in a wide variety of photonic structures including integrated and fiber-optic waveguide devices as well as circuits and nanophotonic devices such as photonic crystals. The software employs the Finite-Difference Time-Domain (FDTD) method for the full-vector simulation of photonic structures. FullWAVE's award winning innovative design and feature set has made it the market leader among optical device simulation tools.

## Benefits

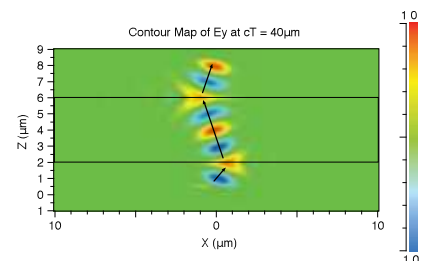
- › Cutting edge implementation of mature FDTD algorithm allows for a wide range of simulation and analysis capabilities.
- › Advanced capabilities allow for clustered simulation environment for massive computational increases in speed and efficiency.
- › Fully integrated into the RSoft CAD Environment (Page 6).

## Applications

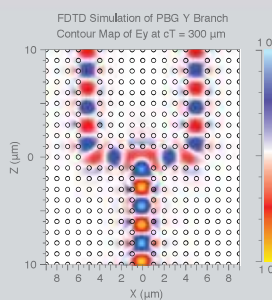
*FullWAVE has applications in a wide range of integrated and nano-optic devices including, but not limited to:*

- \* WDM devices such as ring resonators
- \* Photonic bandgap circuits & applications
- \* Grating structures, surface normal gratings, and other diffractive structures
- \* Cavity computations and extractions
- \* Nano- and micro-lithography
- \* Biophotonics
- \* Light scattering
- \* Metrology
- \* LED extraction analysis
- \* Sensor and bio-sensor designs
- \* Plasmon propagation effects
- \* Surface plasmons
- \* Negative refractive index materials

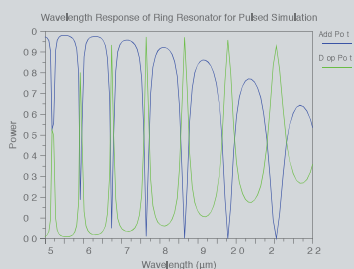
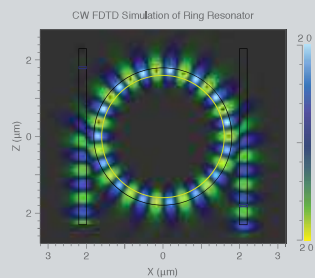
## Featured Application



Demonstration of negative index refraction with the propagation of a beam through a left handed material bounded by air.



FullWAVE CW simulation of photonic bandgap y-branch structure.



Top: CW response of ring resonator run at a wavelength resonance of  $1.593\mu\text{m}$ .

Bottom: Wavelength response of a pulsed simulation of the same resonator.

## FEATURES

- \* Advanced and robust FDTD implementation allowing for full-vector field solutions in arbitrary structures and materials.
- \* 2D, radial, and 3D simulation capabilities.
- \* Non-uniform mesh.
- \* Full control of dispersion, non-linear ( $X^2$  and  $X^3$ ), and anisotropic effects.
- \* Frequency-dependent saturable gain model.
- \* Includes Perfectly Matched Layer (PML), periodic, and symmetric/anti-symmetric boundary conditions.
- \* Advanced excitation options for multiple launch fields, each with different spatial and temporal characteristics such as position, wavelength, direction, polarization, and temporal excitation. Point sources and white light sources are also available.
- \* Total-field/scattered-field formulation for scattering problems.
- \* A wide range of analysis and monitoring features to measure common electromagnetic quantities such as power flux, energy densities, overlap integrals, far fields, and the Poynting Vector. Additionally, both FFT and DFT options are included for frequency analysis.
- \* Includes Q-Finder, a utility that automates the search for cavity modes and Q-factors.
- \* Automated parametric studies and design optimization using MOST (Page 24).
- \* Increased performance through parallel processing via multi-cpu/core machines and/or clustering across a network of computers. Contact RSoft for licensing policies regarding this feature.
- \* A native 64-bit version of FullWAVE is available that takes advantage of modern 64-bit CPUs that support additional system memory (RAM).

SEE PAGE 41 FOR SYSTEM REQUIREMENTS

# BandSOLVE

COMPONENT DESIGN  
Passive Device



BandSOLVE is the first commercially available design tool to automate and simplify the modeling and calculation of photonic band structures for all photonic crystal (PC) devices. The BandSOLVE simulation engine employs the Plane Wave Expansion (PWE) algorithm to perform band computations, and also provides a graphical display of the electromagnetic fields and other quantities of interest for further analysis.

## Benefits

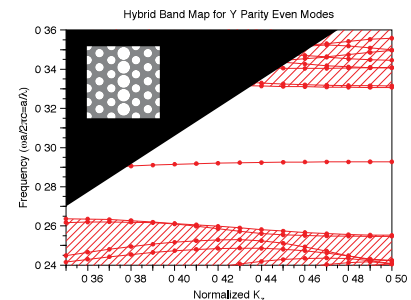
- > Advanced implementation of PWE and FDTD (for FullWAVE users only) algorithms allows for a wide range of simulation and analysis capabilities for different types of PBG devices & materials.
- > Built-in array layout utility as well as layout hierarchy offers a convenient way to create both standard and custom PBG structures.
- > A large number of real application examples.
- > Fully integrated into the RSoft CAD Environment (Page 6).

## Applications

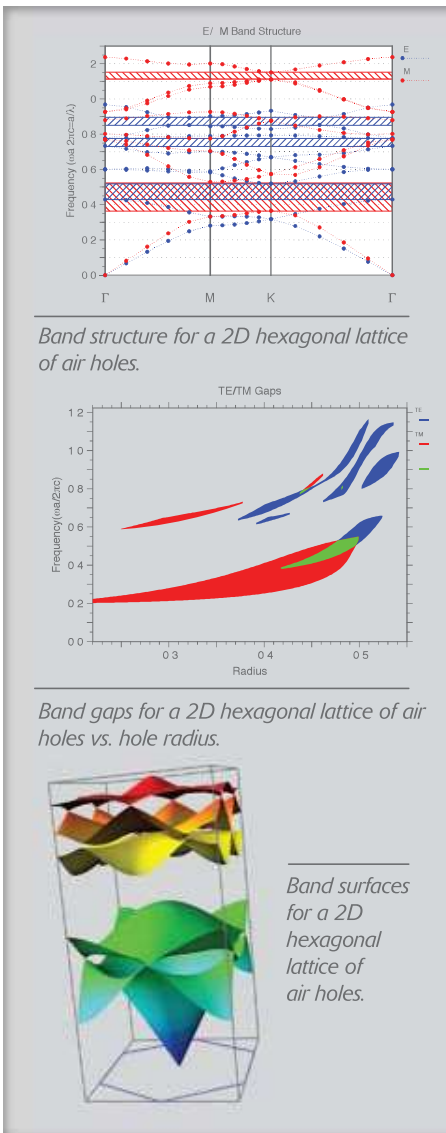
*BandSOLVE can be used to optimize the band structure of new photonic crystal geometries before fabricating the device and to determine the performance of existing components. BandSOLVE can be applied to a wide range of PC components, including but not limiting to:*

- \* 2D and 3D PC slab and waveguides
- \* 2D and 3D cavity problems
- \* Photonic crystal fibers, both band-gap guiding and conventional guiding
- \* Defect modes of non-strictly periodic structures
- \* Metallic and anisotropic structures

## Featured Application



Band diagram for even modes of a waveguide in a lattice of air holes in a photonic crystal slab as computed by a 3D BandSOLVE simulation. The black area represents the leaky mode region, the shaded red regions represent the slab modes, and the red line represents guided modes in the waveguide. The waveguide was formed by enlarging one row of holes as shown.



**FEATURES**

- \* Employs a very efficient and robust Plane Wave Expansion (PWE) algorithm that can solve for the band gaps of most 1D, 2D, and 3D PBG devices.
- \* Includes several advanced simulation features for more efficient, fast band computations, such as inversion symmetry, mode seeding, and parity for 3D calculations.
- \* Includes a Finite-Difference Time-Domain (FDTD) engine (for FullWAVE users only) for situations in which the PWE algorithm is not applicable, such as metallic and non-linear systems.
- \* Employs complete and powerful post-processing tools for the calculation of a wide range of data and graphs. BandSOLVE's analysis features include:
  - Band gaps, band maps, and gap maps
  - Mode computation including Bloch and defect modes
  - Wide range of measurements such as effective and group index, group velocity, and dispersion
  - Equi-frequency plots for analysis of the entire Brillouin zone
  - Light cone filters for photonic crystal slab applications
  - Fixed-frequency analysis to incorporate material dispersion

SEE PAGE 41 FOR SYSTEM REQUIREMENTS

# ModePROP

COMPONENT DESIGN  
Passive Device



ModePROP is an Eigenmode expansion propagation tool that accounts for both forward and backward propagation and radiation modes. It provides a rigorous steady-state solution to Maxwell's equations that is based on the highly-stable Modal Transmission Line Theory. A full array of analysis and simulation features make this tool flexible and easy to use.

## Benefits

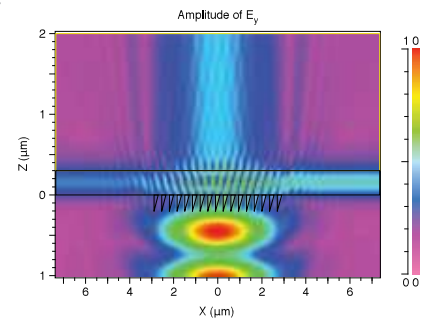
- > Rigorous full-vector analysis.
- > Solves for both forward and backward traveling modes.
- > Fully integrated into the RSoft CAD Environment (Page 6).

## Applications

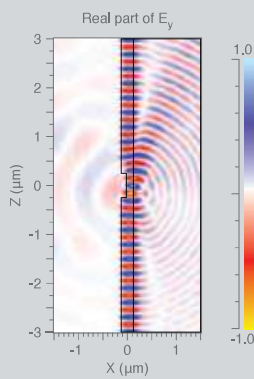
*ModePROP has applications including, but not limited to:*

- \* Waveguide/Fiber-based systems
- \* Surface-normal grating couplers
- \* Plasmonic devices
- \* Sensors
- \* Filters
- \* Mode converters
- \* Photonic bandgap
- \* Computing coupling efficiency

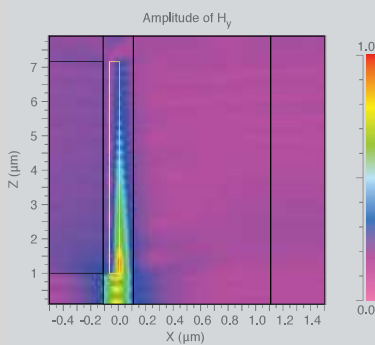
## Featured Application



ModePROP simulation results of a blazed finite surface grating. An incident Gaussian beam is coupled into a waveguide by a surface grating.



Simulation results that show the field scattered by an air groove.



Simulated field within a surface plasmon based interferometer that is operating out of phase.

## FEATURES

- \* Full-vectorial analysis for both Cartesian and cylindrical (azimuthally symmetric) structures in 2D and 3D.
- \* Modal Transmission Line (MTL) framework to ensure that the simulation is unconditionally stable.
- \* Accounts for reflections.
- \* User-defined initial field.
- \* Accommodates complex index for lossy materials and high index contrast profiles.
- \* Robust meshing scheme which conforms to the structure.
- \* PML boundary conditions.
- \* Output information includes transmission/reflection of individual modes as well as total values, and the Poynting Vector.
- \* Sophisticated output options allow user to calculate and display field profiles and other electro-magnetic quantities at any position.
- \* Automated parametric studies and design optimization using MOST (Page 24).

SEE PAGE 41 FOR SYSTEM REQUIREMENTS

# DiffractMOD

COMPONENT DESIGN  
Passive Device



DiffractMOD is a design and simulation tool for diffractive optical structures such as diffractive optical elements, subwavelength periodic structures, and photonic bandgap crystals. It is based on the Rigorous Coupled Wave Analysis (RCWA) technique that has been implemented using advanced algorithms including fast Fourier factorization and generalized transmission line formulation. Already a market leader, the tool has extensive applications in a broad range of areas including semiconductor manufacturing and wave optics.

## Benefits

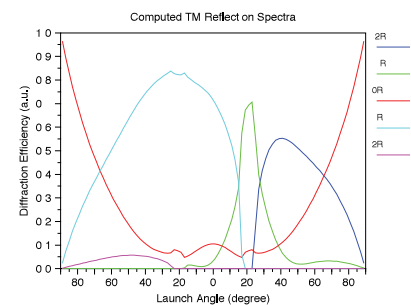
- > Incorporates advanced algorithm options that extend the basic RCWA technique to improve its robustness, efficiency, and user-friendliness.
- > Fully integrated into the RSoft CAD Environment (Page 6).

## Applications

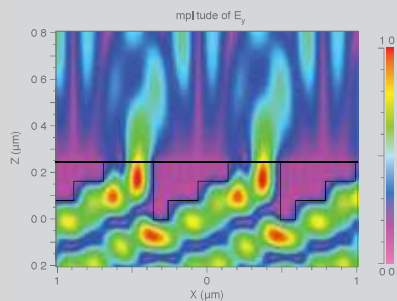
*DiffractMOD can handle complicated periodic structures containing both dielectric and metallic components with lossy or dispersive materials. It has application to a wide-range of devices including, but not limited to:*

- \* Waveguide resonance gratings
- \* Diffractive Optical Elements (DOEs)
- \* Surface relief and volume index gratings
- \* Wavelength filters
- \* Optical metrology
- \* Nano-lithography
- \* Polarization sensitive devices
- \* Artificial dielectric coatings
- \* Photovoltaic systems
- \* 3D displays
- \* Optical interconnections
- \* Optical data storage
- \* Spectroscopy

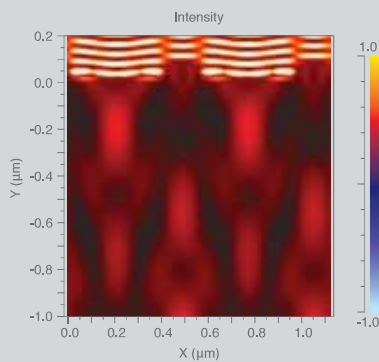
## Featured Application



Computed spectra for TM reflected diffraction orders for a 2D metallic grating.



*Field profile of metallic grating structure.*



*Simulation of a Phase Shift Mask with DiffractMOD.*

## FEATURES

- \* Advanced algorithm options are used to improve convergence.
- \* Modal Transmission Line (MTL) framework to ensure that the simulation is unconditionally stable.
- \* Full vector simulations for both 2D and 3D. Additionally, conical incidence is allowed.
- \* An inverse rule is used to improve the convergence of TM fields. For 3D simulation, DiffractMOD can choose appropriate algorithms depending on structures.
- \* Account for material dispersion and complex refractive index for metals.
- \* Calculate, display, and output spectra of diffraction efficiency for any diffraction order.
- \* Calculate total reflected power, transmitted power, and absorbed power.
- \* Sophisticated field output options allow the user to calculate and display field profiles at any position.
- \* Spectrums vs. wavelength, angle and polarization for any diffraction efficiency can easily be computed.
- \* Output common metrology parameters directly.

# GratingMOD

COMPONENT DESIGN  
Passive Device



GratingMOD is a general design tool for analyzing and synthesizing complicated grating profiles in optical fibers and integrated waveguide circuits for a wide variety of photonic applications. The software is based on the Coupled Mode Theory (CMT) algorithm for fast simulation as well as sophisticated multiple mode algorithms for advanced applications. GratingMOD also provides a general platform for simulation of various coupling mechanisms.

## Benefits

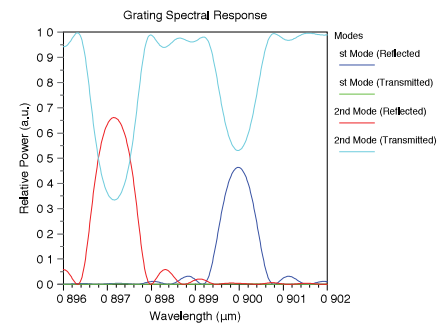
- > Incorporates advanced algorithms to improve its robustness, efficiency, and user-friendliness
- > Fully integrated into the RSoft CAD Environment (Page 6).

## Applications

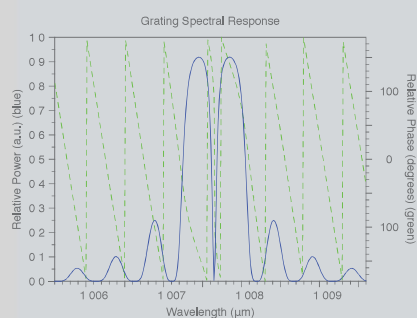
*GratingMOD can handle various grating structures for both fiber and integrated waveguides. It has applications to a wide range of integrated and fiber-optic devices including, but not limited to:*

- \* Dispersion compensation Fiber Bragg Grating
- \* Multiplexing/Demultiplexing
- \* Add/Drop filtering
- \* Gain equalization in optical amplifiers
- \* Grating assisted couplers
- \* Long period grating sensors

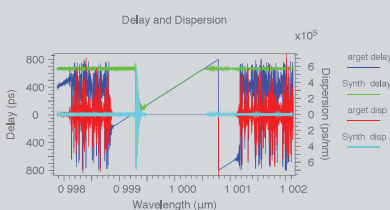
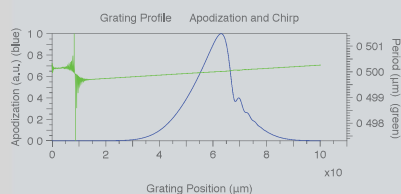
## Featured Application



Results for multimode simulation of a grating assisted coupler. Spectra are shown for both forward & backward propagation for both modes in the structure.



*Simulation results showing the phase and amplitude.*



*Synthesis results of a grating with constant dispersion compensation.*

## FEATURES

- \* Bragg condition searching to find both the period from the specified modes and the modes from a specified period.
- \* Sophisticated orthogonality relations for both lossless and lossy waveguide are included.
- \* Optimal modes are used to reduce error.
- \* Analytical mode calculations can be used when applicable.
- \* An arbitrary number of gratings at arbitrary positions in both 2D and 3D structures can be used to study coupling mechanisms. Coupling mechanism includes fiber core coupling, fiber core to cladding coupling, long period fibers, as well as side coupling and vertical coupling for integrated circuits.
- \* Multi-mode grating systems can be analyzed via a multi-mode CMT implementation.
- \* An advanced synthesis tool utilizes a state-of-the-art synthesis technique to solve the 'inverse' problem.
- \* Both waveguide and material dispersion can be included.
- \* Transmitted and reflected spectra for each mode can be determined.
- \* Calculation of phase, dispersion, and time delay.
- \* Generation of mode, apodization, chirp, and grating profiles.
- \* Automated calculation of band width for primary order reflection.
- \* Spectrum analysis and Bragg condition analysis.

SEE PAGE 41 FOR SYSTEM REQUIREMENTS



FemSIM is a generalized mode solver based on the Finite Element Method (FEM) that can calculate any number of transverse or cavity modes of an arbitrary structure on a non-uniform mesh. FemSIM employs a full-vector implementation and has been enhanced with many features to compute complex modes. The tool is flexible and extendable to a wide range of problems such as high index contrast, plasmonic, and photonic bandgap based waveguides.

## Benefits

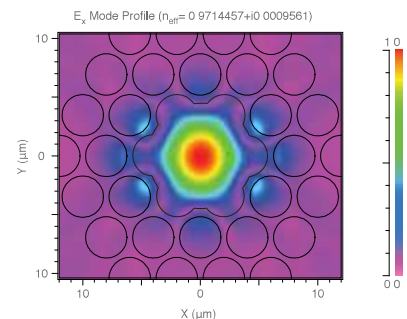
- > Advanced implementation of the FEM algorithm allows for a wide range of simulation and analysis capabilities for different types of devices.
- > Can be used in conjunction with other RSoft tools to solve for modes and then propagate them through a device.
- > Fully integrated into the RSoft CAD Environment (Page 6).

## Applications

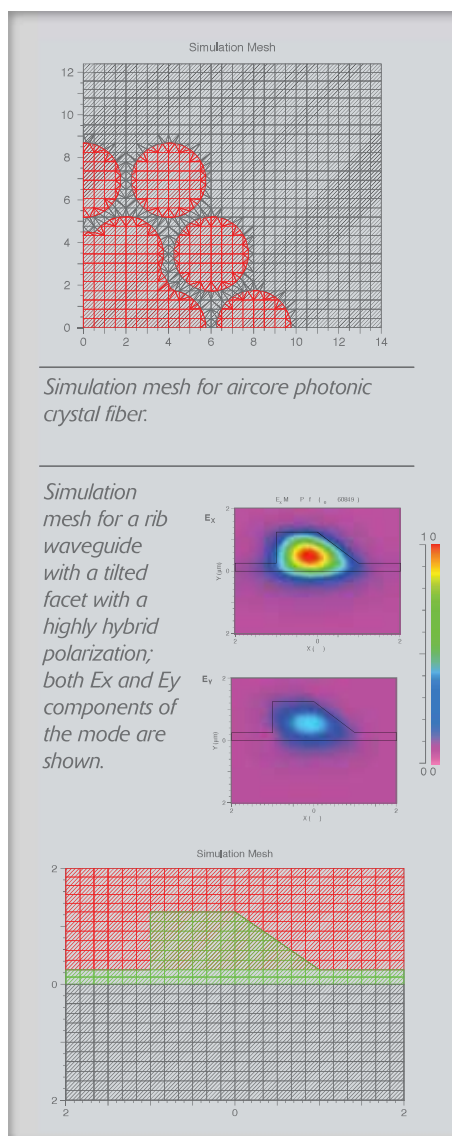
*FemSIM has applications for mode solving to a wide range of integrated and nano-optic devices including, but not limited to:*

- \* Structures with arbitrary profiles, including those with curved or uncommon shapes
- \* Structures with high index contrast and/or small feature sizes
- \* Air or solid core photonic fibers
- \* Lossy structures
- \* Silicon-based devices such as SOIs
- \* Polarization rotators
- \* Plasmonic waveguides
- \* Laser and PBG defect cavities

## Featured Application



Computed mode profile for an aircore photonic crystal fiber. Symmetric boundary conditions were used in the calculation to provide a speedy solution. The simulation mesh can be seen on the next page.



## FEATURES

- \* Full-vector analysis for both Cartesian (1D, 2D) and cylindrical (azimuthally symmetric) structures.
- \* Accommodates complex index for lossy materials and high index contrast profiles.
- \* Robust meshing scheme which conforms to the index profile using hybrid triangular and rectangular mesh elements.
- \* First and second order elements used to avoid spurious modes.
- \* PML and symmetric/anti-symmetric boundary conditions.
- \* Determination of propagating, leaky, and cavity modes.
- \* Higher order modes can be found with minimal additional computational expense.
- \* Computation of dispersion diagrams.
- \* Output information includes field profiles, propagation constants, overlap integrals, confinement factors, and diagnostics.
- \* Automated parametric studies and design optimization using MOST (Page 24).

# LaserMOD

COMPONENT DESIGN  
Active Device



LaserMOD is a photonic device design software tool for simulating the optical, electronic, and thermal properties of semiconductor lasers and similar active devices. In these devices, thermal flux and carrier transport can strongly affect overall performance through spatial hole burning and self-heating. LaserMOD accounts for these and other important processes within a self-consistent scheme.

## Benefits

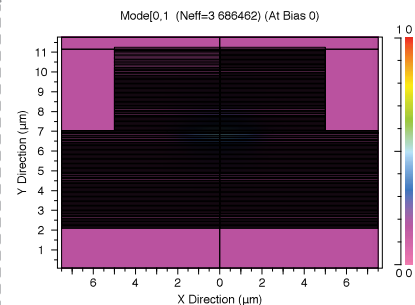
- > Versatile, user friendly, parametric CAD interface.
- > All simulation modules included in a single package.
- > Integrated with both passive device and system tools from RSoft Design Group.

## Applications

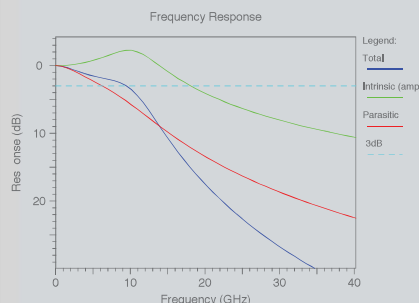
*LaserMOD applications include the following device families:*

- \* Edge emitting lasers, such as Fabry-Perot (FP), Distributed Feedback (DFB), and Distributed Bragg Reflector (DBR)
- \* Cylindrical Vertical Cavity Surface Emitting Lasers (VCSEL)
- \* Silicon modulators (Electro-absorptive, electro-refractive, and thermo-optic modulators in silicon and other semiconductor materials)
- \* Hybrid & Multilevel applications when combined with other tools in the RSoft suite

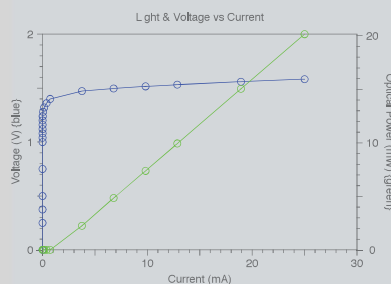
## Featured Application



Fundamental cavity mode of an oxide-aperture VCSEL calculated via finite-element method (FEM).



Computed light-current and current-voltage (LIV) characteristics indicating the progress of a steady-state simulation.



Frequency response to a small pulse applied at the steady-state operating point. Parasitic effects can be included to account for packaging.

**FEATURES**

- \* 1D, 2D and cylindrical (quasi-3D)
- \* Advanced physics based models
- \* Self-consistent solution of optics, quantum mechanical gain, and electro-thermal transport
- \* Steady-state and time dependent simulation
- \* 8x8 KP band calculation for gain
- \* Lock up table base gain model
- \* Integrated BPM and FEM mode solvers
- \* Integrated mesh generator
- \* Extensible material libraries
- \* Numerous tutorial examples
- \* Standard and custom plot generation
- \* Scanning of design parameters

SEE PAGE 41 FOR SYSTEM REQUIREMENTS

# MOST

COMPONENT DESIGN  
Options and Utilities



**MOST**<sup>†</sup>, RSoft's Multi-variable Optimization and Scanning Tool, is an exciting solution to the critical problem of design optimization for photonic devices. During the research or design cycle, it becomes vital to understand the full parameter space of the system. Acting as an automated driver for RSoft's physics-based simulators, MOST takes the drudgery out of these important operations by streamlining the definition, calculation and analysis of scans and optimizations. Moreover, if you own multiple copies of RSoft products, MOST can automate the distribution of work across your entire network with virtually a single mouse click.

## Benefits

- > Automatically scans and optimizes devices with minimal user interaction.
- > Automates the design process to take out tedious work.
- > A wide range of output and analysis features available through measurement and user-defined metric techniques.
- > Fully integrated into the RSoft CAD Environment and with all of the component simulation tools. (Page 6).

## Applications

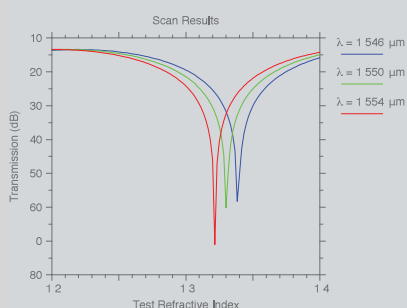
*MOST is applicable to any situation where a range of parameters need to be looked at or optimized including, but not limited to:*

- \* Perform parameter scans over any design parameter in any number of dimensions
- \* Perform single and multiple variable local and global automated optimization
- \* Perform global optimization by genetic algorithm
- \* Automated distributed computation of scans and some optimizations

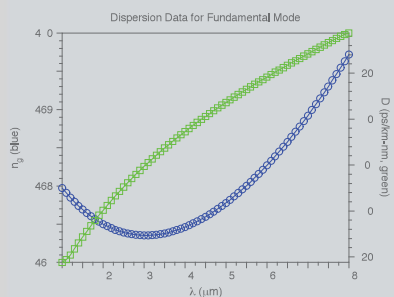
## Simulation Technology

MOST provides the most flexible scanning/optimization environment available today. Measurements are generalized so that any type of data produced by any simulator can be treated in a uniform fashion. Thus, scanning modal effective indices calculated with BeamPROP is identical to scanning diffraction efficiencies calculated with Diffract-MOD. In addition, vector and matrix quantities such as reflection spectra or modal profiles are scanned just as easily. Literally, any quantity produced by any RSoft tool can be the target of a scan or optimization.

<sup>†</sup> The scanning portion of MOST is included with all passive device simulation tools; optimization and distributed scanning are licensed separately.



ModePROP scan results showing surface plasmon resonance locations for different operating wavelengths as a function of the refractive index of the test material.



Computed dispersion parameters for a fiber found using BeamPROP and the scanning/post-processing capabilities of MOST.

## FEATURES

- \* Any quantity produced by any RSoft tool can be the target of a scan or optimization.
- \* Scans and optimizations can be performed over an arbitrary number of parameters.
- \* Automatic generation of line, contour, and 3D volume plots.
- \* “Data sliced” plots showing behavior in particular planes of the parameter space.
- \* Real time convergence plots to track the performance of optimizations.
- \* Data conveniently accessed and viewed within RSoft’s customized DataBROWSER environment.
- \* Instantly reprocess existing data in different plot styles.
- \* Complete data dumps to file of any scanned quantity.
- \* Several optimization algorithms available for different types of convergence.
- \* Custom post-processing of simulation output to produce scans/optimizations of any parameter.
- \* Define new optimization algorithms with MOST through custom modules.

# SOLAR CELL UTILITY

COMPONENT DESIGN  
Options and Utilities



The Solar Cell Utility<sup>†</sup> provides an optical and electronic simulation solution for solar cell devices. The utility simplifies common tasks associated with solar cell design and aids in the rigorous computation of J-V curves, quantum efficiency spectra, and overall cell-efficiency. The basic version of the Solar Cell Utility uses a simple electronic model and operates with one or more RSoft optical simulation tools<sup>††</sup>. If a rigorous electronic modeling solution is desired, LaserMOD can be used. The Solar Cell Utility LaserMOD option provides a limited license of LaserMOD for this purpose.

## Benefits

- > Rigorous optical simulation is performed by one of RSoft's passive optical design tools.
- > Can use either a simple electronic model or RSoft's rigorous LaserMOD simulation tool.
- > Fully integrated into the RSoft CAD Environment (Page 6).

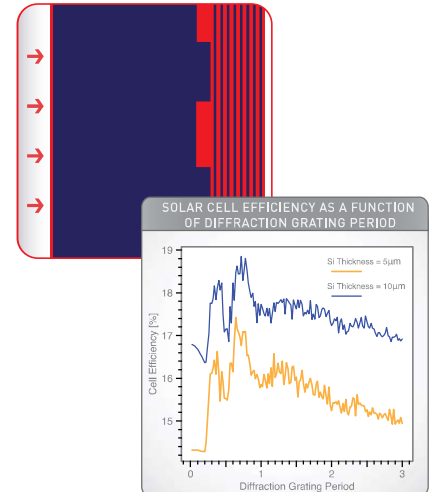
<sup>†</sup>The Solar Cell Utility provides owners of some of RSoft's optical simulation tools the functionality described here. All simulation tools are licensed separately.

<sup>††</sup>Consult an RSoft representative to determine which combinations of products are currently supported.

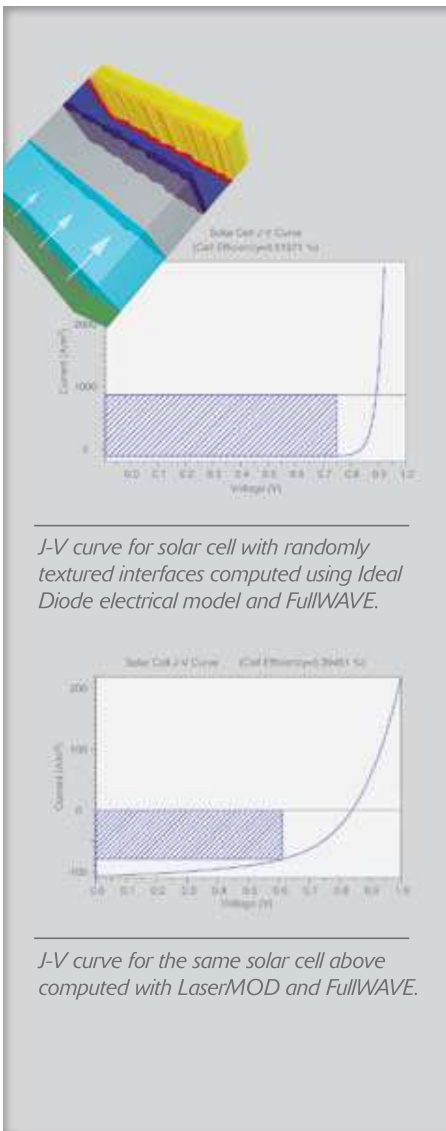
## Applications

- \* Solar cell design
- \* Solar cells with diffractive optical elements (DOEs)
- \* Solar cells with randomly textured material interfaces
- \* Ideal for investigating the electronic nature of solar cells

## Featured Application



Schematic of solar cell structure along with solar cell efficiency computed by DiffractMOD as a function of the period of a diffractive optical element within the cell.



## FEATURES

- \* Arbitrary solar cell geometry can easily be created in the RSoft CAD.
- \* Important material properties such as frequency-dependent complex refractive indexes can be used to correctly model absorptive materials.
- \* Simple electronic modeling via modified Ideal Diode equation; rigorous modeling via RSoft's LaserMOD tool.
- \* Uses the AM1.5 Solar Spectrum as incident spectrum by default; a user-specified spectrum can also be used.
- \* Direct user control over shadowing, filling-factor, and collection efficiency.
- \* Accounting of parasitic resistances in both simple and rigorous electronic models.
- \* Outputs include cell efficiency, J-V curves, and quantum efficiency spectra in addition to the standard output from the simulation tool(s) used (DiffractMOD, FullWAVE, and/or LaserMOD).
- \* Automated parametric studies and design optimization using MOST (Page 24).

# Multi-Physics

UTILITY

COMPONENT DESIGN  
Options and Utilities



The **Multi-Physics Utility**<sup>†</sup> is designed to be used in conjunction with any of RSoft's passive device simulation tools. It provides a convenient interface from which perturbations of the refractive index profile of a structure may be included in the simulation. These perturbations can be due to advanced physical processes in the material, such as electro-optic effects, thermo-optic effects, stress-optic effects (i.e. strain), and carrier-induced effects. All material parameters needed to describe these effects can be defined in RSoft's Material Library.

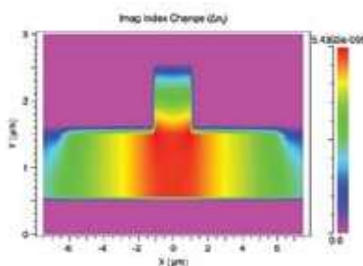
## Benefits

- Expands the power of all of RSoft's passive device simulation tools.
- Fully integrated into the RSoft CAD Environment (Page 6).

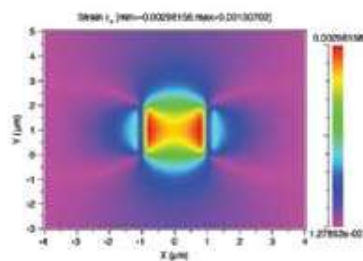
## Applications

- \* Electro-absorptive/electro-refractive modulators
- \* Thermo-optic switches
- \* Electrically biased modulators
- \* Birefringence in waveguides and fibers
- \* Stress effects caused by cooling during device fabrication.

## Featured Applications



Change in refractive index, due to carrier effects, in a silicon ridge waveguide buried in SiO<sub>2</sub>.



X component of strain in a silicon ridge waveguide buried in SiO<sub>2</sub>.

## Features

- \* Fully integrated with all of RSoft's passive device simulation tools.
- \* Leverages RSoft's material library for all model parameters.
- \* Computes index perturbation by solving Poisson's equation (electro-optic effect), thermal equation (thermo-optic effect), stress-strain equation (stress effect), and by using LaserMOD to model carrier-based effects.
- \* Automated parametric studies and design optimization using MOST (Page 24).

<sup>†</sup> The basic Multi-Physics Utility with electro-optic and thermo-optic effects is included with all passive device tools; the stress and carrier effects are offered as options that are licensed separately.

# Tapered Laser

UTILITY



The **Tapered Laser Utility**<sup>†</sup> provides an efficient and accurate design tool for analyzing and optimizing tapered semiconductor laser diodes. It essentially combines, two of RSoft's most powerful and mature simulation tools BeamPROP and LaserMOD, to provide a full 3D simulation of tapered laser diodes. The quasi-3D electrical, quantum mechanical gain and thermal calculations are performed via LaserMOD, whereas the optical field is propagated via BeamPROP.

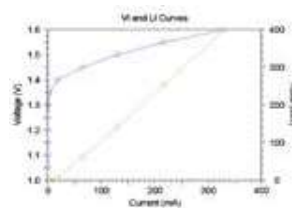
## Benefits

- > Leverages the power of RSoft's BeamPROP and LaserMOD simulation tools for use with tapered semiconductor laser diode applications.
- > Fully integrated into the RSoft CAD Environment (*Page 6*).

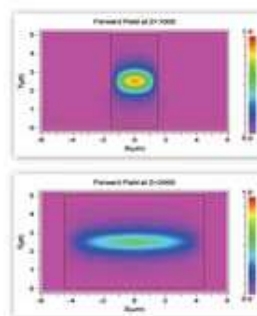
## Applications

- \* Tapered laser diode design.

## Featured Application



Computed light-current and current-voltage characteristics.

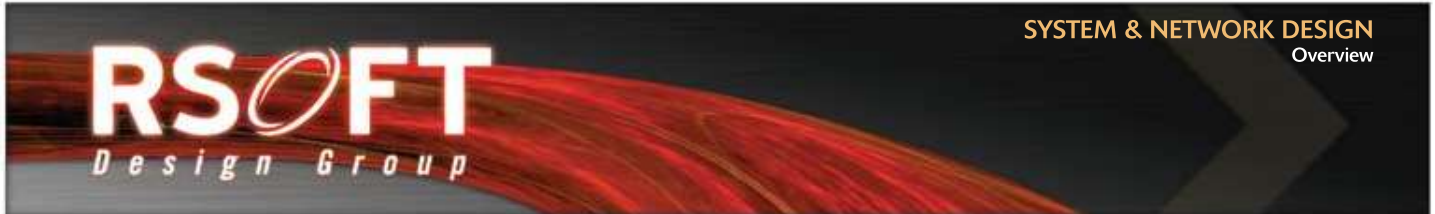


TL Utility computed stabilized field profiles along different sections of the tapered laser.

## Features

- \* Fully integrated with RSoft's BeamPROP and LaserMOD simulation packages to automatically compute tapered laser characteristics.
- \* Self-consistent optical, electronic and thermal simulation.
- \* Extensible material libraries.
- \* Output information includes L-I curves, I-V curves, spatial field plots, farfields etc.
- \* Capable of simulating physical effects like spatial hole burning, filamentation, over pumping etc.

<sup>†</sup> The Tapered Laser Utility provides owners of BeamPROP and LaserMOD the functionality described here. All simulation tools are licensed separately.



## RSOFT's Optical Communication Design Suite



RSOFT's Optical Communication Design Suite allows users to design and simulate current and next generation optical communication systems at the signal-propagation, network-architecture, and packet level. Currently four software packages are part of the suite: OptSim, ModeSYS, MetroWAND, and Artifex. These advanced tools enhance and accelerate user-modeling capabilities and provide real field design scenarios using extensive industry specifications. The customer base includes optical component and equipment manufacturers, system integrators, service providers, as well as government labs and academic institutions. Whether you are interested in maximizing performance, minimizing costs, reducing time-to-market, fast-prototyping, or analyzing multiple what-if scenarios for optical communication networks, these tools will become an inseparable partner and the secret of your success.

## OptSim & ModeSYS Key Features

- \* Enable the user to design and simulate single mode (OptSim) and multimode (ModeSYS) optical communication systems at the signal-propagation level.
- \* Virtual prototyping reduces the need for costly and lengthy physical prototyping for increased productivity and decreased time-to-market.
- \* Optimization of the design for enhanced performance and reduced cost.
- \* Common graphical interface but separate licenses allows users to choose only the simulation engine that is relevant to their work.
- \* Assist in the discovery and analysis of next generation optical communication systems deploying new modulation formats.
- \* Interfaces with 3rd party tools such as MATLAB®, Cadence Spectre, Liekki Application Designer, and the Luna Optical Vector Analyzer.
- \* Advanced electrical modeling with embedded Spice engine.

## MetroWAND Key Features

- \* Plan Ring and Mesh Architectures.
- \* Highly efficient network design algorithms.
- \* Design rules incorporate fiber topology, traffic demands and equipment constraints.
- \* Quick analysis of 'what-if' scenarios.
- \* Optical link layer performance estimations.
- \* Failure analysis with rerouting options.
- \* Customize Vendor equipment library.

## Artifex Key Features

- \* Design and simulate discrete event systems using the Petri Net formalism.
- \* Graphical object-oriented language and event-driven simulation ensures scalability to high degrees of complexity.
- \* Integrated platform with tools to create, validate, simulate, measure and deploy the system.
- \* Dynamic visualization of events and states supports iterative model development.
- \* Real-time and virtual-time simulation with full user control of model's execution.
- \* Simulation data analysis and representation.
- \* Automatic ANSI C and C++ code generation to build custom simulators and control software.
- \* Networking tool-kit for protocol simulations.



### SYSTEM

#### *OptSim*

Simulates a broad range of optical communication systems

#### *ModeSYS*

Simulates multimode optical communication systems

### NETWORK

#### *MetroWAND*

Models network design, network engineering, and network-planning

#### *Artifex*

Simulates discrete event networks through the Petri Nets formalism applications



OptSim is RSoft's award-winning software tool for the design and simulation of optical communication systems at the signal propagation level. With state-of-the-art simulation techniques, an easy-to-use graphical user interface and lab-like measurement instruments, OptSim provides unmatched accuracy and usability. The software has been commercially available since 1998 and is in use by leading engineers in both academic and industrial organizations worldwide.

## Benefits

- > Virtual prototyping of the optical communication systems for increased productivity and reduced time-to-market.
- > Optimization of the design for enhanced performance and/or reduced cost.
- > Interfaces with 3rd party tools such as MATLAB®, Cadence Spectre, Liekki Application Designer, and the Luna Optical Vector Analyzer.
- > Advanced electrical modeling with embedded SPICE engine.

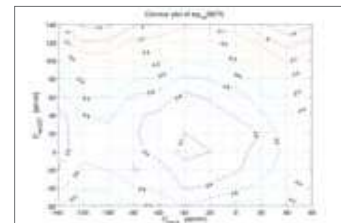
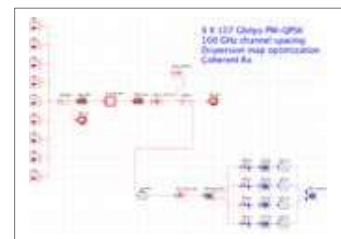
## Applications

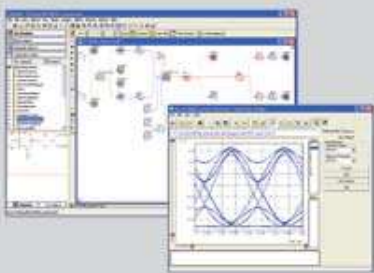
*OptSim is ideally suited for computer-aided design of optical communication systems including, but not limited to:*

- |  |  |   |
|--|--|---|
| * DWDM / CWDM systems with optical amplification, e.g. EDFA, Raman, SOA, OPA | * Coherent Optical Communication Systems, e.g. PM-QPSK, OFDM | * EDC   |
| * Advanced Modulation Formats, e.g. DQPSK, Duobinary, etc.                   | * OCDMA / OTDM   | * FSO   |
| * FTTx / PON   | * CATV Digital/Analog  | * Soliton                                       |
|  | * Optical Interconnects                                      | * Interferometric Fiber Optic Gyroscope (I-FOG) |

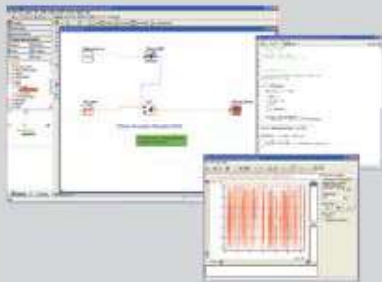
### Featured Application

- \* Synchronous PolMUX-QPSK system with 9 channels at 107 Gbit/s, 20x100 Km SMF fiber, and a DSP-based digital coherent receiver.
- \* Direct error counting on 262,144 simulated bits.
- \* OptSim's unique capability of simulating arbitrarily long bit sequences makes it the tool of choice to design systems where the direct error counting is required to assess the system performance, such as systems using FEC, MLSE, EDC, and DSP-based digital coherent receivers.





*OptSim project layout of a DQPSK system. OptSim includes an advanced BER estimator specific for D(Q)PSK systems based on Karhunen-Loeve series expansion.*



*OptSim - MATLAB cosimulation project layout. An Electro-Absorption Modulator with Chirp is modeled using the MATLAB m-file programming language. The MATLAB engine is automatically invoked by OptSim at runtime to simulate the EAM model.*

## FEATURES

- \* Only design tool with multiple engines implementing both the Time Domain Split Step and the Frequency Domain Split Step for the most accurate and efficient simulation of any optical link architecture.
- \* MATLAB® interface makes it easy to develop custom user models using the m-file language and/or the Simulink® modeling environment.
- \* Interfaces with laboratory test equipment such as Agilent and Luna to merge simulation with experiment.
- \* Interfaces with device-level design tools such as BeamPROP, and LaserMOD provide a powerful mixed-level design flow for optoelectronic circuits and systems.
- \* Co-simulation with embedded SPICE engine, and interfaces with EDA tools such as Cadence Virtuoso Spectre, and Synopsys HSPICE for a mixed-domain electrical and optical simulation.
- \* Interfaces with EDA tools such as Berkeley SPICE, Cadence Virtuoso Spectre, and Synopsys HSPICE for a mixed-domain electrical and optical simulation.
- \* Application Programming Interface (API) for programming languages such as C/C++ for the development of custom user models.
- \* Best Fit Laser Toolkit™ makes customizing powerful rate-equation laser model parameters to fit desired performance characteristics easy.
- \* Extensive library of predefined manufacturer components makes it easy to model commercially available devices.
- \* Intuitive and flexible measurement post-processing graphical interface acts like a virtual laboratory instrument.

# ModeSYS

OPTICAL COMMUNICATION DESIGN  
System



ModeSYS supports the design and simulation of multimode fiber optic systems. With a primary focus on data communication applications, ModeSYS allows users to evaluate both temporal and spatial attributes of optical signal propagation. ModeSYS can be used as a standalone tool or combined with OptSim to form a comprehensive single-mode and multimode optical communication system design suite.

## Benefits

- > Simulates both temporal waveform and spatial modes of multimode systems combining system-level speed with device-level representation accuracy
- > Virtual prototyping of the multimode optical communication system for increased productivity and reduced time-to-market
- > Fully supports yield analysis through statistical models of multimode fiber defects such as Cambridge 81 and 108 fiber models
- > Interfaces with device-level tools such as RSoft's BeamPROP to simulate at the system level custom components designed at the device level

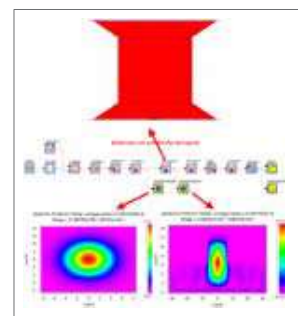
## Applications

*ModeSYS is ideally suited for computer-aided design of multimode optical communication systems including, but not limited to:*

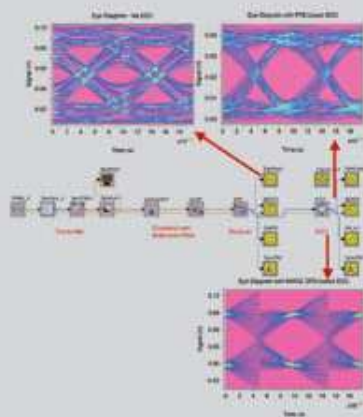
- \* Gigabit Ethernet, e.g. 1GbE, 10GbE
- \* 10GBASE- systems, e.g. SX, LX-4 and LRM
- \* Serial / WDM
- \* FTTx / PON
- \* EDC
- \* Optical Interconnects
- \* FSO

## Featured Application

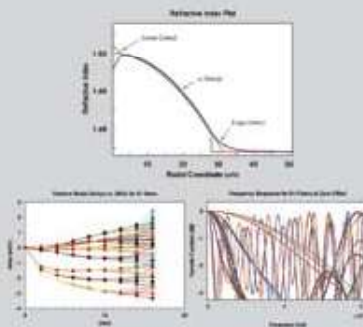
- \* ModeSYS - BeamPROP co-simulation enables the user to simulate in the context of a ModeSYS multimode system simulation a component designed at the device level in BeamPROP
- \* BeamPROP uses the Beam Propagation Method (BPM) to simulate custom components such as waveguides, lenses, couplers, gratings, etc.
- \* The figure depicts a 6-mm long waveguide with an input/output width of  $14\mu\text{m}$  that tapers to  $8\mu\text{m}$  within the 4-mm long central region. The substrate, core (index = 3.5) and layer (index = 1.5) materials have different indexes.



*Using BeamPROP's SOI-based rib waveguide design in ModeSYS to analyze its system level performance*



*Modeling of Electronic Dispersion Compensation (EDC) in ModeSYS. ModeSYS and OptSim include FFE- and DFE-based EDC with MMSE-based optimization.*



*Studying the impact of refractive index profile perturbations using Cambridge-81 and Cambridge-108 models in ModeSYS.*

## FEATURES

- \* Multimode fiber model includes Helmholtz equation solver supporting arbitrary index profile and index profile perturbations.
- \* Extensive set of measurement tools enables the user to analyze key-characteristics of multimode optical communication systems such as:
  - Transverse mode profiles
  - Signal over time
  - Signal spectra
  - Eye diagrams
  - BER
  - Effective modal bandwidth (EMB)
  - Differential Mode Delay (DMD)
  - Encircled Flux (EF)
  - Radial power distributions
- \* Mode-propagation model supports modal dispersion and Differential Mode Attenuation (DMA).
- \* Comprehensive spatial model using distinct transverse mode profiles supports launch-condition, optical-coupling, and alignment-tolerances analysis.
- \* Extensive library of predefined manufacturer components makes it easy to model commercially available devices.
- \* Deterministic and statistical component parameter sweeping.
- \* Powerful encryption capabilities make protecting your schematics and model parameters easier than ever.
- \* Application Programming Interface (API) for programming languages such as C/C++ for the development of custom user models.

# MetroWAND

OPTICAL COMMUNICATION DESIGN  
Network



**MetroWAND** is a network planning/design platform for SONET/SDH and WDM technologies. As a network-modeling tool, MetroWAND is used to simulate various network configuration scenarios, routing methods, failure scenarios, and traffic load analysis. MetroWAND may also be used to obtain various statistics like system utilization, wavelength utilization, throughput rates, and equipment capacity. MetroWAND's optical engineering module simulates the optical channel propagation and calculates the end-to-end link performance of a particular optical channel. End-to-End link performance is validated using the numerical measures of total attenuation, accumulated dispersion, accumulated dispersion slope, optical SNR, BER and Q.

## Benefits

- > Uses cost-optimization algorithm to locate WDM or SONET ring networks by considering equipment, topology, and traffic.
- > Considers any transport rate including gigabit Ethernet, SONET/SDH, and user-defined rates.
- > All Optical network design objectives like wavelength routing, wavelength assignment, and physical layer performance simulation are featured in a single tool.
- > Vendor-neutral tool.
- > Flexible equipment models enable evaluation of different technologies.
- > Mesh Routing and Restoration.
- > Intuitive GUI.

## Applications

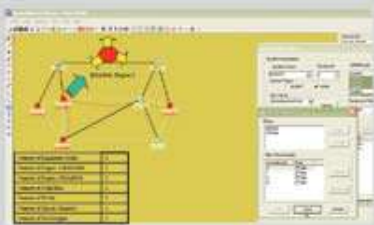
- \* Design and optimization of UPSR, 2-fiber BLSR, 4-fiber BLSR, SNCP, and MSSP rings.
- \* Optical channel performance simulations and placement of amplifiers and regenerators.
- \* Obtain the minimum network cost by optimizing fiber, structure, cable, amplifier, and regenerator usage along with ring ADMs.
- \* Model and analyze the existing rings together with planned rings as well as with new rings for the expansion of the network.
- \* Model multiple equipment types (ADM, Cross-connects, and MSPPs) and design the network.
- \* Optical network link engineering and analysis covering both linear effects as well as non-linear effects.

## Feature Application

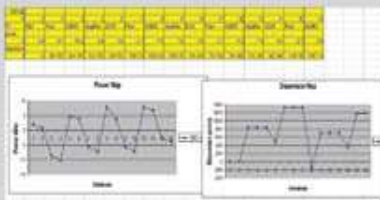
A comprehensive network-planning tool that gives flexibility in modeling wavelength routing and wavelength assignments. It accurately simulates the performance of the system under various network conditions. The tool performs analysis on the simulation results and recommends the most suitable hardware components.



*Multiple views of the optical network in MetroWAND. Physical layer topology view and traffic demand view.*



*During the capacity design stage, the software creates an optical ring, it grooms the traffic into optical channels, assigns wavelengths, and places Optical Add Drop Multiplexers (OADMs).*



*For each wavelength, power, dispersion, OSNR and Q values are plotted and shown for each optical component instances. This will allow the planner to a) adjust amplifier gain b) adjust variable attenuator and c) select a dispersion compensation module. This analysis can be carried out in Terminal-Terminal, Terminal-OADM, or OADM-OADM configurations.*

## FEATURES

- \* Design and plan metropolitan mesh and ring networks.
- \* Capacity planning and optical layer performance simulation in one engine.
- \* Optical layer optimization by adding amplifiers, dispersion compensators and regenerators based on OSNR and Q values.
- \* Quick validation of network design scenarios.
- \* Model next-generation SONET/WDM equipment.
- \* Model network growth scenarios.
- \* Determine hub locations and optimum cross-connect locations.
- \* Partition the network into sub-networks and design core and access rings.
- \* Analyze disaster recovery under multi-failure scenarios.
- \* Optical link engineering and Analysis.



Artifex is a development platform for discrete event simulation. It uses a graphical modeling and simulation environment to model, design, simulate, and analyze discrete event systems. Artifex is widely used to simulate optical network protocols, control plane architecture, and switching mechanisms.

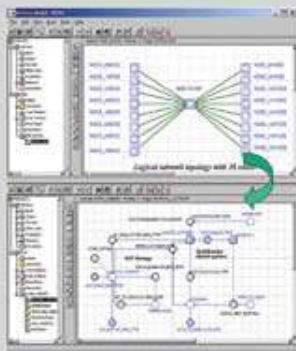
## Benefits

- > An integrated platform to design, develop, validate, and simulate models and systems
- > Quick development of models using the graphical language Petri Net
- > C/C++ code integration with the models
- > Deploy simulation as a multi-node and/or a multi-threaded application
- > Automatic report generation
- > Automatic measurements

## Applications

*Artifex's open and extensible modeling approach is utilized in many industries like Transport, Defense, Telecom, and Finance. Listed below are a few applications from the Telecom industry:*

- \* Model, simulate, and analyze networking protocols like TCP, UDP, IP, Ethernet, OSPF, and MPLS.
- \* Develop, design, and validate new and emerging protocols.
- \* Conceptualize a complex system's behavior, prototype, and develop strategies for its implementation.
- \* Model, simulate, and analyze network elements like routers, switches, optical-Cross Connects (OXC) and Optical Add/Drop Multiplexers (OADMs) for their logical behavior and protocol implementation.
- \* Model various traffic generators.
- \* Design and analyze network performance and quality of services (QoS) using the logical models of traffic generators, protocols, and network elements.
- \* Design network architectures like rings or meshes, specify network type (optical-access metro or transport), and study the network level behaviors like network through-put, blocking probability, and wavelength assignment.
- \* Model buffering, memory, and Integrated Circuits (IC).
- \* Develop, validate, and analyze protection switching or restoration switching protocols.



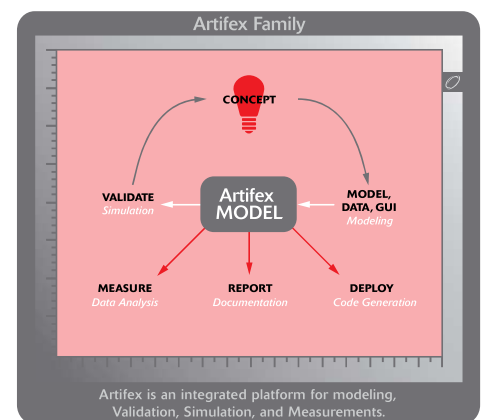
Shows logical view (mesh) of a WDM Ring and the view of schemes implemented in a ring node. Each node generates packets according to a Poisson process stored in a distinct transmission queue, one associated with each destination/channel. The objective is to study the transmission queue latency time of packets sent to client nodes from client nodes; for example from NODE\_2 to NODE\_1, NODE\_3, NODE\_6, NODE\_9, NODE\_12 and from NODE\_9 to NODE\_14.

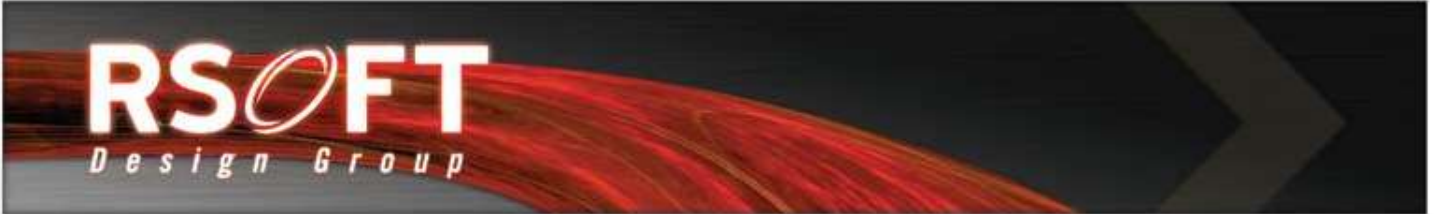


Shows the transmission queue latency times – client to client analysis for the WDM network.

## FEATURES

- \* Graphical modeling and simulation environment to model, design, simulate, and analyze discrete event systems.
- \* User can draw the system dynamic behavior through an intuitive graphical language based on the Petri Nets formalism.
- \* Validates the Petri Net model and generates code in C/C++ language.
- \* Models can be compiled and run in the Artifex environment or compiled and executed as standalone applications.
- \* Objects can be dragged and dropped from a library to the drawing canvas and connected to create system models.
- \* Networking tool-kit consists of library of traffic generators, protocols, and optical and non-optical network elements.





## Professional Services & Programs



RSoft Design Group provides a variety of professional services and programs that supplement and support our client's need for a total solution. These services include:

### Training *Seminars*

RSoft organizes product training seminars every year. Seminars are either hosted at the RSoft offices or by a host sponsor, including many prominent universities. Private seminars are also available at an additional cost.

### Customized *Solutions*

In order to address the needs of specialized applications, RSoft offers consulting services to extend the current capabilities of its software tools. Customized solutions accelerate product development and reduce client time to market.

### Design *Services*

RSoft offers a range of supplemental consulting services, ranging from application design optimization to full product design. Typical applications include promoting a faster learning curve with the software tools and exploring possible what-if concepts. This can be especially useful if company manpower is limited.

*For more information on our professional services and programs, please contact an RSoft Design Group representative or e-mail: [info@rsoftdesign.com](mailto:info@rsoftdesign.com).*

## Offices & Distributors

---

RSoft Design Group is currently headquartered in Ossining, NY USA. Our sales offices can be reached through the contact information on the right. In addition, RSoft has a significant number of distributors who market and sell our software. A full list of our distributors can be obtained at our website, [www.rsoftdesign.com](http://www.rsoftdesign.com).

## System Requirements

---

Most RSoft products have 32-bit and 64-bit versions for both Windows and Linux systems. Please check the 'System Requirements' section of the relevant product on RSoft's website for a list of the specific OS versions we currently support.

## Products & Services

---

For additional information on RSoft's Products & Services, please contact us at [info@rsoftdesign.com](mailto:info@rsoftdesign.com).



### UNITED STATES

*Corporate Headquarters*



**RSoft Design Group, Inc.**

400 Executive Boulevard, Ste. 100  
Ossining, NY 10562, USA

Phone: 1.914.923.2164

Fax: 1.914.923.2169

E-mail: [info@rsoftdesign.com](mailto:info@rsoftdesign.com)

### JAPAN



**RSoft Design Group Japan KK**

Matsura Building 2F, 1-9-6 Shiba  
Minato-ku, Tokyo, 105-0014 Japan

Phone: +81.3.5484.6670

Fax: +81.3.5484.2288

E-mail: [info@rsoftdesign.co.jp](mailto:info@rsoftdesign.co.jp)

### EUROPE



**RSoft Design UK Ltd.**

11 Swinborne Drive  
Springwood Industrial Estate  
Braintree, Essex CM7 2YP

Phone: +44 (0) 1376.528556

Fax: +44 (0) 1376.528651

E-mail: [info@rsoftdesign.co.uk](mailto:info@rsoftdesign.co.uk)



NOTES



## الخلاصة

تمثل الضوئيات السليكونية المعتمدة على تقنية السيليكون على العازل (SOI) الحل الأمثل لتصميم الدوائر الضوئية المتكاملة و (PICs) التي هي جوهر التوصيلات البينية الضوئية. باستخدام هذه التقنية أمكن الحصول على ذات خسائر منخفضة ، حجم صغير ، ونطاق ترددي تشغيلي واسع. في الآونة الأخيرة ، جذبت التقنيات الجديدة اهتمامًا كبيرًا في تصميم الهياكل الضوئية للسيليكون لقدرتها على تحسين أداء و ابعاد الأجهزة الموجودة سلفاً إضافة الى إدخال أجهزة جديدة بأشكال جديدة. إحدى هذه التقنيات هي باستخدام المحرز مادون الطول الموجي.

يتكون العمل في هذه الأطروحة من جزأين رئيسيين. الجزء الأول ، تم تصميم مضاعفات ارسال باستخدام مقياس التداخل متعدد الوسائط (MMI) مدعوما بتقنية SWG. أولاً تم تنفيذ مُضاعفٍ ثلاثي النمط باستخدام SWG في قسم MMI فقط. ثم تم توسيع تصميم الجهاز و بناءه كلياً باستخدام تقنية الـ SWG . تم مقارنة أداء كلا الجهازين مع بعضهما البعض بالإضافة إلى المقارنة مع نظيرهما التقليدي حيث لوحظ الحفاظ الاجهزة المصممه على نسبة خسائر منخفضة مصحوبه بزيادة في النطاق الترددي للاجهزة المصممه حيث وصلت الى 160 نانومتر و تقلص في المساحة الكلية تصل الى 70% مقارنة مع تلك الخاصه بالجهاز المعتمد على الدليل الموجي من النوع التقليدي. ثانياً ، تم تصميم اثنين من مضاعفات رباعية النمط باستخدام مقرن MMI التقليدي و آخر مدعوم بتقنية الـ SWG. تم مقارنة أداء الجهازين لبيان مزايا التقنية المستخدمة حيث لوحظ تحسين كبير في أداء الجهاز من خلال الحفاظ على أداء منخفض الخسائر (< 0.5- ديسيبل) مع زياده في عرض النطاق الترددي التشغيلي الى (140 نانومتر) وتقلص في حجم الجهاز الجديد الى (4.5x123) ميكرومتر مربع.

في الجزء الثاني من الأطروحة ، تم تصميم مضاعفات الإرسال على أساس المقرنات الاتجاهية المتتالية غير المتماثلة مدعومة بمحزر مادون الطول الموجي (SWG-ADC) حيث تم تصميم ثلاثة أجهزة. الجهاز الاول يدعم 12 نمط كهربائي TE مستعرض و الجهاز الثاني يدعم 12 نمط مغناطيسي مستعرض TM و الثالث يدعم 24 نمط هجين عن طريق ربط الجهازين الاول و الثاني. الجهاز ذو 12 نمط عبارة عن هيكل مكون من ست مراحل كل مرحلة تدعم عددًا معينًا من الانماط بناءً على التصميم المطلوب. تم تحسين الاقتران بين الناقل الرئيسي النواقل الفراعية عن طريق استخدام وصلات مدعومه بتقنية الـ SWG. الاجهزة المصممه تعتبر مضاعفات ذات ترتيب أعلى بالإضافة إلى كونها منخفضة الخسائر بنطاق ترددي تشغيلي واسع مقارنة مع تلك من النوع التقليدي التشغيلي. أخيرًا ، يتم توصيل كل من الأجهزة ذات الوضع TE و TM من خلال فواصل الاستقطاب لأغراض توجيه الوضع ، مما يؤدي إلى جهاز جديد ذي وضع مزدوج لتعدد الإرسال. تم تصميم جميع معدات الإرسال المقترحة ومحاكاتها باستخدام برنامج Rsoft photomics CAD ver 2020.0 .



وزارة التعليم العالي والبحث العلمي

جامعة بغداد

معهد الليزر للدراسات العليا

## تصميم جهاز منضد النمط مدمج مدعوم بمحزر مادون الطول الموجي لأنظمة التنضيد بتقسيم النمط

أطروحة مقدمة الى

معهد الليزر للدراسات العليا / جامعة بغداد / لاستكمال متطلبات نيل شهادة  
دكتوراه فلسفة في الليزر / الهندسة الالكترونية والاتصالات

من قبل

زيد لطيف حسين

بكالوريوس هندسة الليزر و الالكترونيات البصرية - 2002

ماجستير هندسة الليزر و الالكترونيات البصرية - 2005

بإشراف

الاستاذ الدكتور رعد سامي فياض